Passive control of thermoacoustic instabilities in idealised combustion systems using heat exchangers

Aswathy Surendran

Submitted in partial fulfilment of the requirements of the degree of Doctor of Philosophy in Applied Mathematics

Faculty of Natural Sciences
Keele University, United Kingdom

October 2017

Keele University

Declaration Part 1. To be bound in the thesis

SUBMISSION OF THESIS FOR A RESEARCH DEGREE

Part I. DECLARATION by the candidate for a research degree. To be bound in the thesis

Degree for which thesis being submitted Doctor of Philosophy in Applied Mathematics

Title of thesis Passive control of thermoacoustic instabilities in idealised combustion systems using heat exchangers

This thesis contains confidential information and is subject to the protocol set down for the submission and examination of such a thesis.

NO

Date of submission 29 June 2017 Original registration date 11 October 2013
(Date of submission must comply with Regulation 2D)

Name of candidate Aswathy Surendran

Research Institute Faculty of Natural Sciences Name of Lead Supervisor Prof. Maria A. Heckl

I certify that:

(a) The thesis being submitted for examination is my own account of my own research
(b) My research has been conducted ethically. Where relevant a letter from the approving body confirming that ethical approval has been given has been bound in the thesis as an Annex
(c) The data and results presented are the genuine data and results actually obtained by me during the conduct of the research
(d) Where I have drawn on the work, ideas and results of others this has been appropriately acknowledged in the thesis
(e) Where any collaboration has taken place with one or more other researchers, I have included within an 'Acknowledgments' section in the thesis a clear statement of their contributions, in line with the relevant statement in the Code of Practice (see Note overleaf).
(f) The greater portion of the work described in the thesis has been undertaken subsequent to my registration for the higher degree for which I am submitting for examination
(g) Where part of the work described in the thesis has previously been incorporated in another thesis submitted by me for a higher degree (if any), this has been identified and acknowledged in the thesis
(h) The thesis submitted is within the required word limit as specified in the Regulations

Total words in submitted thesis (including text and footnotes, but excluding references and appendices) ……32500……

Signature of candidate ……Aswathy Surendran…… Date……20 July 2017……

Note
Extract from Code of Practice: If the research degree is set within a broader programme of work involving a group of investigators – particularly if this programme of work predates the candidate's registration – the candidate should provide an explicit statement (in an 'Acknowledgments' section) of the respective roles of the candidate and these other individuals in relevant aspects of the work reported in the thesis. For example, it should make clear, where relevant, the candidate's role in designing the study, developing data collection instruments, collecting primary data, analysing such data, and formulating conclusions from the analysis. Others involved in these aspects of the research should be named, and their contributions relative to that of the candidate should be specified (*this does not apply to the ordinary supervision, only if the supervisor or supervisory team has had greater than usual involvement*).

Acknowledgements

First of all, I would like to express my deepest gratitude to my lead supervisor Prof. Maria Heckl for her great support, guidance and encouragement. I would also like to thank our project administrators Ms. Fenella Webster and Ms. Jemma Sharrock for their support with the administrative tasks and the smooth running of the TANGO project, Mr. Ian Marr and the IT support team at the School of Computing and Mathematics for their prompt support with the computing facilities, Dr. Shailesh Naire and his family for the nice time spent in their company and the HR at Keele, especially Ms. Sue Stone for the all the help with the contracts and visa applications.

Next, I would like to thank all the TANGO fellows and senior academics for all the wonderful time spent together and the helpful discussions. I thoroughly enjoyed the travelling to various countries, the unique mixture of cultures and professions. Special mention to Dr. Alessandra Bigongiari (Keele) and Ms. Wei Na (KTH) for their companionship, Prof. Avraham Hirschberg (TU/e) for the insights into quasi-steady modelling, Mr. Naseh Hosseini (Bekaert and TU/e) and Dr. Joàn Teerling (Bekaert) for their help with my secondment at Bekaert, Dr. Susann Boij (KTH), Prof. Hans Bodén (KTH), Mr. Luck Peerlings (KTH) and Mr. Danilo Prelevic (KTH) for their help with my secondment at KTH. I would also like to acknowledge the decadelong association with and the invaluable support and encouragement I received from my mentor, Prof. R. I. Sujith (IIT Madras).

I take this opportunity to thank my parents, sister and my loving husband Sreenath for their encouragement and support for all my endeavours in life. I would like to especially thank Sreenath for all the thought provoking discussions, the help with preparing this thesis in LaTeX and for being a good listener and encouraging me to dream high and reach for my goals. I would also like to thank all my friends, particularly Sagar, Vinid and Vinod, for their constant support, advice and good wishes they had showered upon me.

I would also like to take this opportunity to thank the open source community for LaTeX and Inkscape without which my thesis will not be what it is today.

The work presented in this thesis is part of the Marie Curie Initial Training Network "Thermoacoustic and Aeroacoustic Nonlinearities in Green combustors with Orifice structures" (TANGO), and I gratefully acknowledge the financial support from the European Commission under call FP7-PEOPLE-ITN-2012.

Last, but not the least, I thank Lord Almighty for being so benevolent and kind as to bestow upon me with such wonderful gifts like my teachers, my family and friends, who were responsible for shaping my life. I also thank Him for giving me the strength and patience to complete this project.

Abstract

Thermoacoustic instabilities pose a great threat to combustion systems, as they could cause severe structural damage, if they are unchecked and uncontrolled. These instabilities are caused due to the existence of a positive feedback loop between the pressure oscillations and heat release rate oscillations. To prevent these instabilities, one can adopt active or passive control strategies.

The aim of the present work is to passively control thermoacoustic instabilities in a domestic boiler system. To this end, the boiler is modelled as a 1D quarter-wave resonator (open at one end and closed at the other) containing a heat source and a heat exchanger (*hex*). The heat source follows a simple time-lag law for its heat release rate. The hex is modelled as an array of circular tubes in cross flow, and it is placed near the closed end of the resonator, causing it to behave like a cavity-backed tube row. The hex acts as both heat sink and acoustic scatterer. The heat transfer response is obtained from numerical simulations (transfer function approach) and the acoustic scattering or the aeroacoustic response is modelled through a quasi-steady approach. The combination of these two responses at the hex along with the cavity backing gives the effective reflection coefficient of the downstream end of the combustor.

Stability maps are constructed for various system parameters. A classical eigenvalue method is used to obtain the complex eigenfrequencies of the first mode of the combustor. From the growth rate (imaginary part of the eigenfrequencies) obtained for different parameter combinations, it is observed that for the eigenfrequency range of interest, an increase in the mean cross flow velocity, in cavity length, or in hex tube diameter, and a decrease in the gap between the hex tubes, all favoured stability.

Contents

Acknowledgements i

Abstract iii

List of Tables viii

List of Figures ix

List of Symbols xv

1. Introduction 1

1.1. Combustion systems and instabilities 1

1.2. Passive control strategies 6

1.2.1. Cavity-backed acoustic liners with bias flow 8

1.2.2. Acoustic liners in combustors 11

1.3. Research Motivation 13

1.3.1. Sound dissipation in tube banks 13

1.4. Scope of Research 14

1.5. Structure of thesis 15

2. The modelled configuration 18

2.1. Introduction 18

2.2. Description of the model 20

2.2.1. Acoustic field 21

2.2.2. Heat Source 22

2.2.3. Heat Exchanger or Hex 22
2.3. Conclusions 23

3. Heat Source or Sink **24**
3.1. Introduction 24
3.2. Rayleigh Criterion 26
3.3. Some factors affecting the heat release rate fluctuations 30
3.4. Heat release rate models 32
3.4.1. Time-Lag $(n-\tau)$ laws 33
3.4.2. Transfer Function (TF) 35
3.5. Acoustic field across the heat source/sink 37
3.6. Conclusions 38

4. Modelling of Heat Exchanger **39**
4.1. Introduction 39
4.2. Numerical modelling of heat transfer at hex 41
4.2.1. Transfer Function approach 43
4.2.2. Approximations to Transfer Functions 45
4.3. Theoretical and experimental modelling of acoustic scattering at hex . 46
4.3.1. Theoretical modelling 47
4.3.2. Experimental validation 52
4.3.3. Reasons for discrepancy between theoretical and measured results 57
4.4. Total scattering matrix of hex 58
4.5. Acoustic properties of hex 62
4.5.1. Influence of heat sink coefficient (α) 62
4.5.2. Influence of impedance ratio (ζ_{32}) 63
4.5.3. Influence of frequency (f) 65
4.5.4. Influence of mean flow velocity $(\bar{u}_2)$ 65
4.5.5. Influence of open area ratio (η) 66
4.5.6. Influence of hex tube diameter (d) 67

4.6. Conclusions 68

5. Cavity-backed Heat Exchanger **70**

5.1. Introduction 70

5.2. Cavity-backed hex 71

5.3. Cavity backing and resonance 73

5.4. Acoustic properties of cavity-backed hex 74

5.4.1. Influence of frequency (f) 75

5.4.2. Influence of mean flow velocity ($\bar{u}_2$) 75

5.4.3. Influence of open area ratio (η) 76

5.4.4. Influence of hex tube diameter (d) 78

5.5. Conclusions 79

6. Stability Analysis **80**

6.1. Introduction 80

6.2. Eigenvalue Method 82

6.2.1. Boundary and jump conditions 83

6.2.2. Methodology 83

6.2.3. Growth rate determination 84

6.3. Stability maps for various combustor properties 84

6.3.1. Influence of frequency (f) 87

6.3.2. Influence of cavity length (l_c) 87

6.3.3. Influence of mean flow velocity ($\bar{u}$) 88

6.3.4. Influence of impedance ratios (ζ) 88

6.3.5. Influence of hex tube diameter (d) 91

6.3.6. Influence of open area ratio (η) 92

6.4. Conclusions 94

7. Conclusions **96**

7.1. Summary and Conclusions 96

7.2. Scope for future work 99

A. List of Publications **102**

B. Transfer Function Approximations **122**

C. Flow separation point calculation **127**

C.1. von Kármán equation 128

C.2. Thwaites' Method 129

C.3. Flow separation location 130

C.3.1. Comparison with simulations 132

D. Derivation of Scattering Matrix **133**

E. Huang and Heckl model **137**

E.1. Experimental results 138

F. Schlömilch Series **141**

References **143**

List of Tables

4.1. $\bar{T}_3$ and ζ_{32} for $d = 3$mm and $\eta = 0.1$, evaluated from numerical simulations 64

6.1. Properties of the combustion system. 85

6.2. $\bar{T}_3$ and ζ_{32} evaluated from numerical simulations. 87

C.1. Flow separation locations obtained from both FLUENT® simulations and Thwaites' method. y_S is calculated from the centreline of hex. 132

List of Figures

1.1. Schematic for combustion instability 3

1.2. Methods used to model and predict combustion instabilities. Reproduced from Poinsot (2017) 5

1.3. Schematic of combustor with acoustic dampers. Reproduced from Lieuwen and Yang (2005) 7

1.4. Schematic of baffles used in rocket motors. Reproduced from Culick (2006) 8

1.5. Schematic of (a) acoustic liners with perforations and (b) vortex shedding at the perforation edges 9

1.6. Typical conventional type combustion chamber. (Rolls-Royce, 1996) . . 11

1.7. A simplified domestic boiler with heat exchanger 15

1.8. Outline of thesis (image source: www.wolf-heiztechnik.de) 17

2.1. Sectional view of a domestic boiler 19

2.2. The modelled combustion system 21

2.3. Burner head 23

3.1. Rayleigh criterion and analogy to forced oscillation 27

3.2. Control volume for Rayleigh criterion 28

3.3. Factors affecting the heat release rate fluctuations 31

3.4. Modelling of Q' 34

3.5. $n - \tau$ law from Flame Transfer Function 36

3.6. Control volume for matching conditions 37

4.1. Schematic of the heat exchanger acting as both heat sink and acoustic scatterer. 41
4.2. Meshed geometry with boundary conditions. 42
4.3. Profiles of input velocity perturbation and the resulting heat absorption rate fluctuation. 44
4.4. (a) |HTF| and (b) Φ(HTF) obtained from numerical simulations, for d = 3mm, h_g = 0.3mm and different mean velocities, $\bar{u}$. 45
4.5. Comparison of |HTF| and Φ(HTF) obtained from numerical simulations ((a) and (c)) with their approximations ((b) and (d)), for d = 3mm, h_g = 0.3mm and different mean velocities, $\bar{u}$. 46
4.6. Tube row and its approximation 47
4.7. Schematic of the flow within the domain. 49
4.8. Quasi-steady model results for (a) d = 20mm, h_g = 5mm (*Sample 1*) and (b) d = 16mm, h_g = 4mm (*Sample 2*) 52
4.9. Schematic of the experimental setup 53
4.10. Measured and theoretical values for $|T_t^{\pm}|$ and $|R_t^{\pm}|$ vs. Strouhal number for *Sample 1*, and three velocities. The vertical broken line shows the Strouhal number limit till which the quasi-steady model is assumed to be valid. 55
4.11. Measured and theoretical values for $|T_t^{\pm}|$ and $|R_t^{\pm}|$ vs. Strouhal number for *Sample 2*, and three velocities. The vertical broken line shows the Strouhal number limit till which the quasi-steady model is assumed to be valid. 56
4.12. Measurements for (a) d = 20mm, h_g = 5mm (Sample 1) and (b) d = 16mm, h_g = 4mm (Sample 2) 57
4.13. Measured and theoretical values for $|T_t^{\pm}|$ and $|R_t^{\pm}|$ vs. frequency for *Sample 1*, and three velocities 58
4.14. Measured and theoretical values for $|T_t^{\pm}|$ and $|R_t^{\pm}|$ vs. frequency for *Sample 2*, and three velocities 59

4.15. Schematic of the network modelling approach used on hex 60

4.16. Variation of the elements of $[\mathrm{SM}]_{hex}$ as a function of frequency (f), for fixed velocities $\bar{u}$ (or $\bar{u}_2$), d = 3mm and η = 0.1. Solid markers indicate the results obtained by including α and curves indicate the results obtained by using $\alpha = 0$. 63

4.17. Variation of the elements of $[\mathrm{SM}]_{hex}$ as a function of ζ_{32}, for fixed velocities $\bar{u}$ (or $\bar{u}_2$), f = 100Hz, d = 3mm and $\eta = 0.1$. Solid markers indicate the results obtained by including α and curves indicate the results obtained by using $\alpha = 0$. 64

4.18. Variation of the elements of $[\mathrm{SM}]_{hex}$ as a function of frequency (f), for fixed velocities $\bar{u}$ (or $\bar{u}_2$), d = 3mm, $\eta = 0.1$ and $\zeta_{32} = 1.936$ when $\bar{T}_3$ = 400K. The curves are obtained using Eq. (4.36). 66

4.19. Variation of the elements of $[\mathrm{SM}]_{hex}$ as a function of the incoming velocity ($\bar{u}_2$), for fixed frequencies, d = 3mm, $\eta = 0.1$ and $\zeta_{32} = 1.936$ when $\bar{T}_3$ = 400K. The curves are obtained using Eq. (4.36). 67

4.20. Variation of the elements of $[\mathrm{SM}]_{hex}$ as a function of open area ratio (η), for fixed velocities $\bar{u}$ (or $\bar{u}_2$), f = 100Hz, d = 3mm and $\zeta_{32} = 1.936$ when $\bar{T}_3$ = 400K. The curves are obtained using Eq. (4.36). 68

4.21. Variation of the elements of $[\mathrm{SM}]_{hex}$ as a function of hex diameter (d), for fixed velocities $\bar{u}$ (or $\bar{u}_2$), f = 100Hz, $\eta = 0.1$ and $\zeta_{32} = 1.936$ when $\bar{T}_3$ = 400K. The curves are obtained using Eq. (4.36). 69

5.1. Schematic of cavity-backed hex. Here, R_L is the effective reflection coefficient at $x = L$. 72

5.2. Variation of $|R_L|$ and Δ_L as functions of the cavity length (l_c), for fixed frequencies, d = 3mm, $\eta = 0.1$, $\zeta_{32} = 1.936$, $R_p = 1$ and $\bar{u}_2$ = 2.0m/s. . 74

5.3. Variation of $|R_L|$ and Δ_L as functions of the cavity length (l_c), for fixed frequencies, d = 3mm, $\eta = 0.1$, $\zeta_{32} = 1.936$, R_p = -1 and $\bar{u}_2$ = 2.0m/s. . 74

5.4. Variation of $|R_L|$ and Δ_L as functions of frequency (f), for fixed velocities $\bar{u}$ (or $\bar{u}_2$), $d = 3$mm, $\eta = 0.1$, $\zeta_{32} = 1.936$ and $l_c = 0.25$m. 75

5.5. Variation of $|R_L|$, Δ_L and $\Re(R_L)$ as functions of the mean flow velocity ($\bar{u}_2$), for fixed frequencies, $d = 3$mm, $\eta = 0.1$, $\zeta_{32} = 1.936$ and $l_c = 0.25$m. 77

5.6. Variation of $|R_L|$ and Δ_L as functions of open area ratio (η), for fixed velocities $\bar{u}$ (or $\bar{u}_2$), $f = 100$Hz, $d = 3$mm, $\zeta_{32} = 1.936$ and $l_c = 0.25$m. 77

5.7. Variation of $|R_L|$ and Δ_L as functions of open area ratio (η), for fixed frequencies, $\bar{u}_2 = 2.0$m/s, $d = 3$mm, $\zeta_{32} = 1.936$ and $l_c = 0.25$m. . . . 77

5.8. Variation of $|R_L|$ and Δ_L as functions of hex diameter (d), for fixed velocities $\bar{u}$ (or $\bar{u}_2$), $f = 100$Hz, $\eta = 0.1$, $\zeta_{32} = 1.936$ and $l_c = 0.25$m. . 78

5.9. Variation of $|R_L|$ and Δ_L as functions of hex diameter (d), for fixed frequencies, $\bar{u}_2 = 2.0$m/s, $\eta = 0.1$, $\zeta_{32} = 1.936$ and $l_c = 0.25$m. 79

6.1. Schematic of typical time response of a system undergoing (a) stable oscillations, and (b) unstable oscillations, in the variable $y(t)$. 82

6.2. (a) Stability maps obtained for the case without hex and bias flow, and (b) contour map for the eigenfrequencies, ω_1 (in Hz) encountered. The properties of the system are given in Table 6.1. 86

6.3. Expected trend for increase in stability, as l_c, l_f and $\bar{u}$ vary. 88

6.4. Stability maps obtained for $d = 3$mm, $\eta = 0.1$ and incoming velocity of (a) $\bar{u} = 0.5$m/s, (b) $\bar{u} = 1.0$m/s and (c) $\bar{u} = 1.5$m/s. 89

6.5. Variation of Δ_L with impedance ratio (ζ_{32}) and mean velocity ($\bar{u}$) for $d = 3$mm, $\eta = 0.1$, $l_c = 0.25$m and frequencies $f = 60$, 100, 140 and 180Hz. 90

6.6. Stability maps obtained for $d = 5$mm, $\eta = 0.1$ and mean velocity of (a) $\bar{u} = 0.5$m/s, (b) $\bar{u} = 1.0$m/s and (c) $\bar{u} = 1.5$m/s. 91

6.7. Stability maps obtained for $d = 3$mm, $\eta = 0.2$ and incoming velocity of (a) $\bar{u} = 0.5$m/s, (b) $\bar{u} = 1.0$m/s and (c) $\bar{u} = 1.5$m/s. Dashed lines indicate the boundary between the stable and unstable regions shown in Fig. 6.4(a). 92

6.8. Variation of Δ_L with open area ratio (η) and impedance ratio (ζ_{32}) for $d = 3$mm, $l_c = 0.25$m, $f = 100$Hz and mean velocities $\bar{u} = 0.5$, 1.0 and 1.5m/s. 93

6.9. Stability maps obtained for $d = 5$mm, $\eta = 0.2$ and incoming velocity of (a) $\bar{u} = 0.5$m/s, (b) $\bar{u} = 1.0$m/s and (c) $\bar{u} = 1.5$m/s. 94

7.1. Thesis in a nutshell 100

B.1. Comparison of |HTF| and Φ(HTF) obtained from numerical simulations ((a) and (c)) with their approximations ((b) and (d)), for $d = 3$mm, $h_g = 0.3$mm and different mean velocities, $\bar{u}$. 123

B.2. Comparison of |HTF| and Φ(HTF) obtained from numerical simulations ((a) and (c)) with their approximations ((b) and (d)), for $d = 3$mm, $h_g = 0.6$mm and different mean velocities, $\bar{u}$. 124

B.3. Comparison of |HTF| and Φ(HTF) obtained from numerical simulations ((a) and (c)) with their approximations ((b) and (d)), for $d = 5$mm, $h_g = 0.5$mm and different mean velocities, $\bar{u}$. 125

B.4. Comparison of |HTF| and Φ(HTF) obtained from numerical simulations ((a) and (c)) with their approximations ((b) and (d)), for $d = 5$mm, $h_g = 1$mm and different mean velocities, $\bar{u}$. 126

C.1. Schematic of the boundary layer formed on a solid surface 127

C.2. Schematic of streamlines and velocity profiles near the flow separation point S 130

C.3. Schematic of the discretised flow domain 131

E.1. Geometry of a tube row 137

E.2. Magnitude of transmission and reflection coefficients for Sample 1 with no bias flow. 139

E.3. Phase of transmission and reflection coefficients for Sample 1 with no bias flow. 139

E.4. Magnitude of transmission and reflection coefficients for Sample 2 with no bias flow. 140

E.5. Phase of transmission and reflection coefficients for Sample 2 with no bias flow. 140

List of Symbols

Roman

$\bar{Q}$	mean heat release/absorption rate	$[W]$
$\bar{T}$	temperature	$[K]$
$\bar{u}$	mean velocity	$[m/s]$
$\Im$	imaginary part.	
$\mathcal{S}$	source.	
$\mathcal{G}$	Rayleigh index.	
$\mathcal{N}$	a constant.	
$\mathcal{R}$	specific gas constant	$[J/kg/K]$
$\mathcal{T}$	time period	$[s]$
$\mathcal{V}$	volume	$[m^3]$
$\Re$	real part.	
A	amplitude of forward travelling pressure wave.	
B	amplitude of backward travelling pressure wave.	
c	speed of sound	$[m/s]$
C_p	specific heat at constant pressure	$[J/kg/K]$
C_v	specific heat at constant volume	$[J/kg/K]$
d	diameter	$[m]$
e	total energy	$[J/kg]$
f	frequency	$[Hz]$
H, h	enthalpy	$[J/kg]$
h_g	gap height	$[m]$
h_p	duct height	$[m]$
J	diffusion flux of species.	

k wavenumber $[rad/m]$

L length or location $[m]$

l length or location $[m]$

M Mach number.

n interaction index $[kg/m/s^2]$

p pressure $[Pa]$

Q heat release/absorption rate $[W]$

q heat release/absorption rate per mass $[W/kg]$

R reflection coefficient.

S cross-sectional area $[m^2]$

T transmission coefficient.

t time $[s]$

u velocity $[m/s]$

u_g bias flow velocity $[m/s]$

x location along x-axis.

Y mass fraction of species.

Greek

α heat sink coefficient.

$\bar{\bar{\tau}}$ stress tensor.

$\bar{\rho}$ mean density $[kg/m^3]$

Δ absorption coefficient.

δ growth rate.

η open area ratio.

γ ratio of specific heats.

κ heat conductivity $[W/m/K]$

ν kinematic viscosity $[m^2/s]$

Ω complex eigenfrequency.

ω natural frequency $[rad/s]$

Φ phase $[rad]$

ϕ phase shift $[rad]$

ρ density $[kg/m^3]$

τ time-lag $[s]$

Θ open end correction factor.

ζ impedance ratio.

Superscript

$+$ forward travelling waves for pressure and velocity; upstream coefficients when used with scattering.

$-$ backward travelling waves for pressure and velocity; downstream coefficients when used with scattering.

$\prime$ fluctuating quantity in time domain.

$\wedge$ frequency domain quantity.

Subscript

0 at location $x = 0$.

c cavity.

d downstream.

f flame or heat source.

g gap.

h,hex hex.

hs,s heat sink.

j jet.

L at location $x = L$.

m mode.

p piston.

r region within the combustor e.g. 1, 2, 3 etc.

ref reference location.

t,tr tube row.

u upstream.

w wire.

Acronyms

HTF	Heat exchanger Transfer Function.
SM	Scattering Matrix.
He	Helmholtz number.
HR	Helmholtz resonator.
R	resonator.
St	Strouhal number.
c.v.	control volume.
hex	heat exchanger.
r.h.s.	right hand side.
TF	Transfer Function.

Chapter 1

Introduction

In this chapter, we provide a background on combustion instabilities along with a literature review on some of the passive control strategies utilised. This is followed by the research motivation and the scope of the work undertaken in this thesis. The chapter is concluded with an overview and outline of the thesis.

1.1. Combustion systems and instabilities

The period post Industrial Revolution saw and still continues to witness tremendous advancements in all aspects of our lives, be it the standard of living, rapid economic growth or the unprecedented technological and scientific progress. A major contributor to these advancements is the energy production and management sector. Gas turbine engines, steam engines and other power generation units including industrial burners and furnaces, are the backbone of several industries like metalllurgy, chemical, manufacturing, transportation etc. Hence, there is an ever increasing demand for energy.

Unfortunately, this rapid progress came with a downside: the depletion of environment through pollution from these power generation units. Traditionally, in industrial power generators, diffusion-flame type combustors were used. In these combustors,

there is no premixing of the fuel and air before combustion, and such a combustion will lead to high levels of pollutants like NO_x and other green house gases.

To combat pollution and to reduce the NO_x production in gas turbine engines and other power generation units like industrial burners, furnaces, boilers etc., stringent emission laws were passed. One of the many ways to reduce NO_x emissions is by having a lean premixed combustion, where the fuel and air are mixed prior to combustion. Since the fuel and air are premixed, any small variation in the equivalence ratio or any other perturbation in the incoming premixture, will drastically effect the heat released in the combustor, leading to combustion instability or thermoacoustic instability.

Combustion instability is a consequence of the interactions between flame/heat source, flow and acoustics, of which thermoacoustic instabilities occur due to the presence of positive feedback between the unsteady heat release rates and the acoustic oscillations. The latter is characterised by large amplitude, low frequency self-excited oscillations that can be detrimental. If unchecked, these instabilities can cause vibrations of mechanical parts, unsteady and enhanced heat fluxes to walls, concentrated thermal and pressure loads leading to fatigue and in extreme cases severe structural damage. Typical combustion instability mechanism can be summarised as shown in Fig. 1.1. The figure shows the key elements participating in the feedback mechanism: flow, acoustics and heat release rate. The black arrows indicate the feedback loop.

The earliest observation of thermoacoustic instability was made by Higgins (Raun et al., 1993, Richardson, 1922) as early as 1777, when he reported the emittance of musical note while placing a hydrogen diffusion flame inside a closed/open ended tube. For the early part of the last century, combustion instability research was mostly within the academic community. But these instabilities became very important research topics when the instabilities hindered the operations of industrial power generation units like gas turbine engines, rocket motors, industrial furnaces, boilers etc. Notable cases for the detrimental side of combustion instabilities include the failure of the F1 engine during the Apollo program in the 1960s. A detailed historical background of combustion

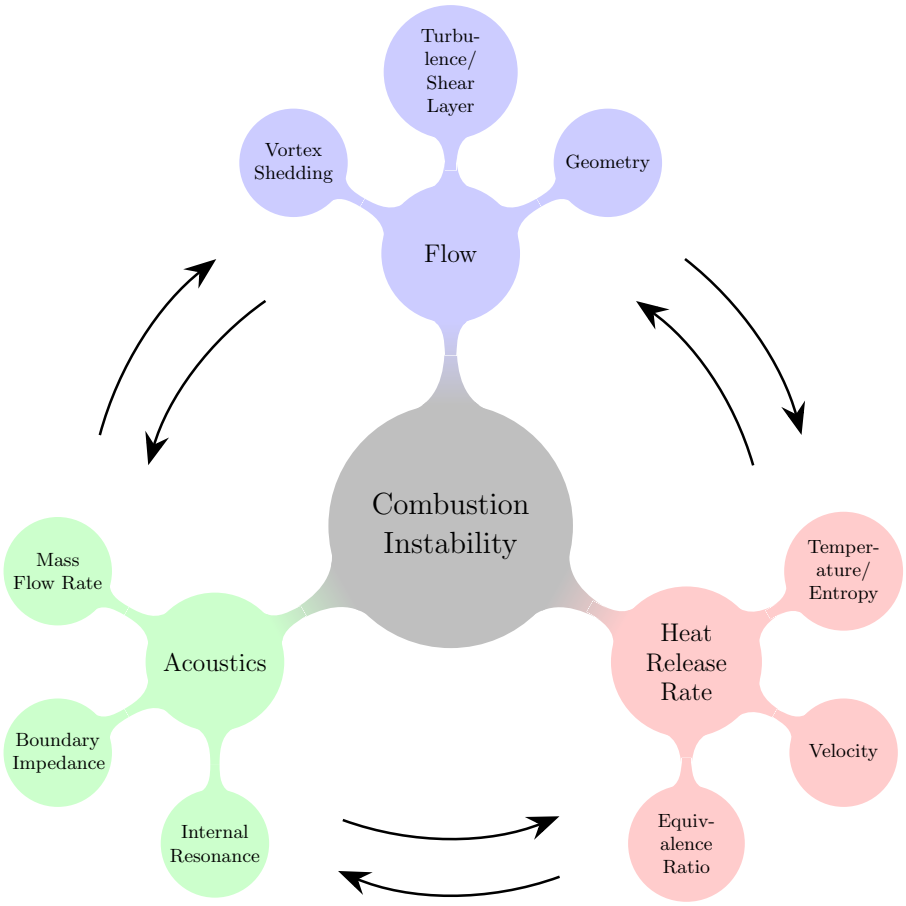

Figure 1.1: Schematic for combustion instability

instability research up until the 2000s can be found in the books by Culick (2006) and Lieuwen and Yang (2005).

Over the last few decades there has been a lot of advancements in the field of combustion instability modelling and instability predictions. A major contributor is the ability of simulation techniques like DNS and LES to produce high fidelity numerical computations of combustors, gas turbine engine, rocket motors etc., having complex geometries and operating under various conditions that cannot be imitated in laboratory conditions. The techniques used for instability predictions fall under two classes, as shown in Fig. 1.2 (Poinsot, 2013, 2017).

- DNS and LES simulations: The full Navier-Stokes equation is solved numerically to get stability predictions (Laera et al., 2016, Polifke et al., 2001). Here, the flow dynamics and the flame dynamics are coupled, and we get accurate predictions for the stability behaviour of real combustion units. Even though the *brute force* LES is a straightforward tool to analyse stability behaviour, the implementation of this method is computationally very expensive and time consuming. Moreover, to fully understand the combustion phenomenon and behaviour of combustion units, we have to conduct parametric studies by varying different parameters in the system. This will lead to a high number of DNS or LES simulations, and in turn to a very cumbersome analysis.
  To overcome this difficulty in analysis, some researchers use the LES method to simulate flame dynamics and obtain the flame response to acoustic perturbations. The flame response is modelled in the form of a transfer function (FTF or FDF) and then used in low order acoustic models and thermoacoustic codes (refer to the red arrow in Fig. 1.2) (Flohr et al., 2003, Han et al., 2015, Jaensch et al., 2017).

- Themoacoustic codes: Thermoacoustic (*TA*) codes do not solve the full Navier-Stokes equation. In this modelling approach, the mean flow is assumed to be frozen and only the wave equation is solved throughout the computational domain. The flame is modelled as an active acoustic element that act is an input to the wave equation through transfer functions (FTFs and FDFs) (Tay-Wo Chong and Polifke, 2012). Since only the wave equation is solved, *TA* codes can accommodate complex geometries in the computational domain.

- Low order network models: The combustion system is simplified through various assumptions to form a network of acoustic elements. Each of the components

in the combustion system such as duct, orifice, burner, duct termination etc. are treated as acoustic elements that are related to each other through transfer matrices or scattering matrices. These transfer matrices are combined to form the *system matrix* of the complete system and the matrix is then algebraically solved to predict the stability behaviour (Polifke, 2010, Stow and Dowling, 2009).

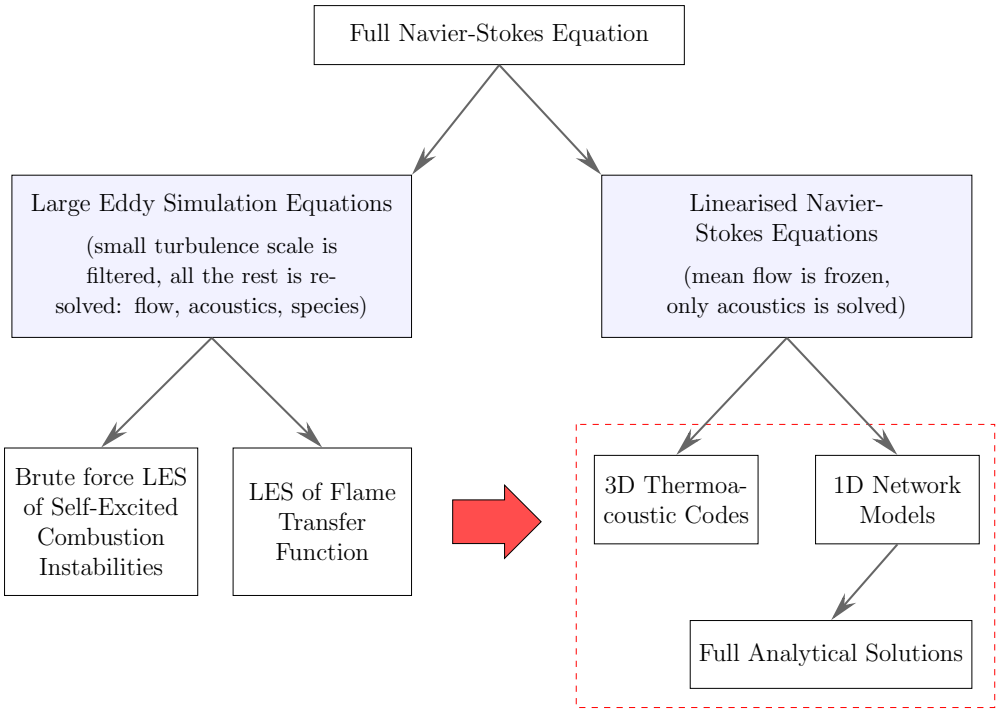

Figure 1.2: Methods used to model and predict combustion instabilities. Reproduced from Poinsot (2017)

Computational methods can predict instability. However, to understand the underlying physics and to find the means to control instabilities, one need to resort to theory and simplified models. To control or eliminate thermoacoustic instabilities, the feedback loop existing between the unsteady heat release rates and the acoustic fluctuations must be broken. This can be done in two ways: by use of active or passive control strategies. In active control, the operating conditions of the systems are modified through external means. These involve continuous monitoring of the system with time and modifying the system parameters dynamically, to prevent the setting in of instabilities. A review on active control of combustion instabilities can be found in Candel (1992) and McManus et al. (1993), where they provide broad overview of the underlying mechanisms of combustion instabilities coupled with pressure oscilla-

tions, active control principles, role of hydrodynamic instabilities like vortex shedding and vortex roll-up in exacerbating the existing instability, and also the usefulness of pressure oscillations in pulsed combustion engines.

In contrast to active control, the passive control strategies do not have dynamic component. Their behaviour is fixed in time. They include changes to hardware and other design modifications like changes to combustion chamber geometry or the injector geometry, inclusion of acoustic dampers or even changes in the reactant composition etc. In the present work we aim to passively control thermoacoustic instabilities and hence the literature covered will be based on these considerations.

1.2. Passive control strategies

Some of the most commonly used passive control components are Helmholtz resonators, quarter-wave and half-wave tubes, baffles etc. The Helmholtz resonator consists of a large cavity with a short neck. A schematic of a combustion chamber equipped with a Helmholtz resonator and a quarter-wave tube is shown in Fig. 1.3 . The fluid within the resonator interacts with the fluid in the combustion chamber through this neck. When the pressure oscillates in the combustion chamber, the fluid enters and exits the resonator, causing the fluid within the resonator to compress and expand. This results in an oscillatory motion of the mass of fluid in the resonator neck, and consequently some acoustic energy may dissipate at the neck entrance. The resulting damping is effective for frequencies close to the natural frequency (resonance) of the Helmholtz resonator. The natural frequency is given by

$$\omega_{HR} = c_0 \sqrt{\frac{S}{\mathcal{V}\, l_{HR}}}, \tag{1.1}$$

where c_0 is the speed of sound, S is the cross-sectional area of the neck, l_{HR} is the length of the neck and $\mathcal{V}$ is the volume of the cavity (Dowling and Ffowcs Williams, 1983).

In quarter-wave and half-wave tubes (Fig. 1.3), the damping mechanism is mainly the viscous damping at the resonator walls and the vortex shedding and turbulence dissipation at the resonator inlet. The resonant frequencies are given by

$$\omega_R = \frac{2\pi c_0}{\mathcal{N}(l_R + \Theta)}, \tag{1.2}$$

where Θ denotes the open end correction factor, l_R is the length of the resonator and $\mathcal{N}$ is a constant. $\mathcal{N} = 2$ for a half-wave tube and $\mathcal{N} = 4$ for a quarter-wave tube. These resonating tubes effectively dampen those combustion instability frequencies that are close to the resonant frequencies given by Eq. (1.2). A more detailed comparison between the damping efficiencies of Helmholtz resonators, quarter-wave and half-wave tubes can be found in Sohn and Park (2011).

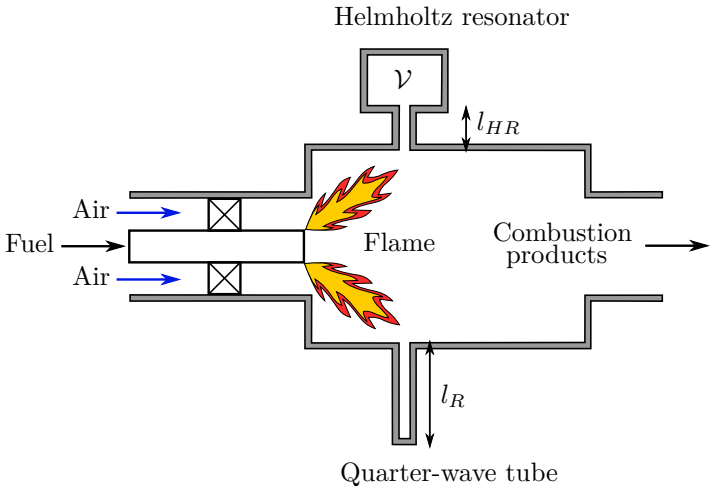

Figure 1.3: Schematic of combustor with acoustic dampers. Reproduced from Lieuwen and Yang (2005)

Baffles are structures placed within the combustion chambers, especially in rocket motors, to mitigate thermoacoustic instabilities. Some of the commonly used baffle configurations in rocket motors are shown in Fig. 1.4. The baffle configuration is chosen based on the resonant mode shapes within the rocket motor, so as to interrupt the pressure oscillations by modifying the acoustic mode shapes within the motor. In addition to altering the mode shapes, baffles also induce vortex shedding, leading to enhanced acoustic absorption (Zhao and Li, 2015). Culick (2006) provides a concise

yet rich overview of the various passive control strategies used in rocket engines for eliminating combustion instabilities.

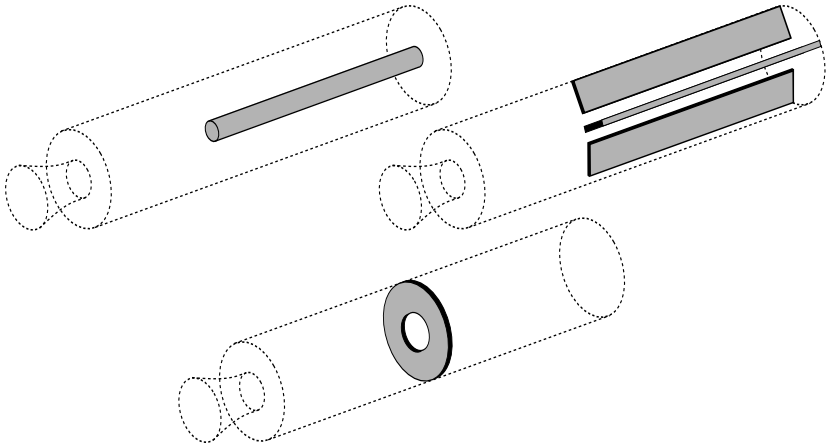

Figure 1.4: Schematic of baffles used in rocket motors. Reproduced from Culick (2006)

Eventhough the aforementioned passive control components are effective in damping thermoacoustic instabilities, there are some disadvantages associated with them. Firstly, most of these dampers are effective in a very limited frequency range that is close to their respective resonant frequencies. To have broadband mitigation, we may have to use more than one damper. Secondly, thermoacoustic instabilities are typically low frequency excitations and hence larger dampers are needed to eliminate instabilities. Since the dampers become bulky and heavy, they increase the overall weight of the damping component, and are usually avoided. Moreover accommodating them into an engine is very difficult.

1.2.1. Cavity-backed acoustic liners with bias flow

An alternative passive control strategy is the use of acoustic liners with bias flow. These liners are metallic sheets with perforations. In the case of liners with bias flow, the acoustic damping is caused by the vortices shed from the edges of the perforations. A schematic showing the typical perforations used and the vortex shedding process from the perforation edge is provided in Fig. 1.5. The acoustic energy is converted into vortex energy, which is then dissipated. Bechert (1980) experimentally showed this

mechanism of sound absorption in a jet flow from a nozzle.

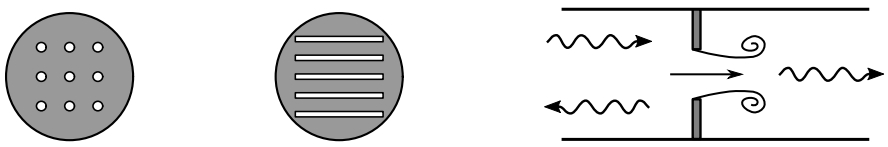

(a) (b)

Figure 1.5: Schematic of (a) acoustic liners with perforations and (b) vortex shedding at the perforation edges

There is a vast amount of literature available on sound absorption by vortices induced by bias flow through orifices, slit-plates and nozzle exits. Leppington and Levine (1973) developed mathematical expressions for the reflection and transmission at a plane perforated screen with circular or elliptical apertures. However, they did not consider the effect of bias flow through the perforations. The influence of bias flow and the sound absorption mechanism by vortex shedding was mathematically described in the work by Howe (1979). He derived expressions for the absorptive properties of circular perforated plates in unsteady high Reynolds number flows, where the main contributor to the acoustic dissipation is the shed vortices from the edges of the perforations.

Hughes and Dowling (1990) extended the modelling of the absorption properties of perforated plates to include the effect of a cavity. These models were later verified experimentally by Jing and Sun (1999). The latter also investigated the effect of plate thickness and the influence of the bias flow direction, on the absorptive properties of the perforated plate.

Instead of circular or elliptical perforations, one can also use slit-plates with bias flow (Dowling and Hughes, 1992, Howe, 1980). In both these liner configurations, it was observed that the absorption capability can be enhanced greatly by including a cavity backing (Dowling and Hughes, 1992, Monkewitz, 1985, Smits and Kosten, 1951). The acoustic response of acoustic liners i.e., the transmission, reflection and absorption properties, largely depend on their geometries and also on the bias flow velocities. A detailed discussion on the influence of different liner parameters on the

acoustic behaviour of bias flow liners can be found in Lahiri (2014), Lahiri and Bake (2017).

There is also an extensive literature on high fidelity numerical simulations of the acoustics of perforated liners and slit-resonators (Eldredge et al., 2007, Mendez and Eldredge, 2009). Hofmans et al. (2001a), Hofmans (1998), Hofmans et al. (2001b, 2003) utilised a vortex-blob method to simulate the flow through an in-duct orifice as well as the flow through in vitro models of vocal folds. The numerical results obtained for the scattering matrix of the orifice and the numerical results obtained for the pressure variations within the vocal folds were then compared to their respective models (quasi-steady model and boundary layer model, respectively) as well as experiments. Tam et al. (2005, 2010) conducted extensive DNS studies and subsequent experimental validation to explore the flow-acoustic interactions in slit-resonators. The simulations were conducted to compute the impedances of slits with different geometries, slit widths and different incident frequencies, and also to obtain detailed visualisation of the flow dynamics and dissipation mechanism in slit-resonators. Zhang and Bodony (2012) conducted LES simulations for orifices backed by hexagonal cavities. These acoustic liners are used for aeroengine noise reduction. The high fidelity results were then used to construct a time-domain model to describe the flow dynamics through the orifice.

In order to have less expensive and less computationally demanding numerical methodology (compared to DNS or LES), Na (2015), Na et al. (2016) proposed a 'unified LNSE approach' to predict the acoustic properties of a hybrid liner consisting of a perforated plate, a back cavity and a metallic foam. In the unified LNSE approach, they have combined the LNSE with a fluid equivalent model, a commonly used method to model sound propagation in porous materials. Their proposed method gave good agreement with experimental results for the hybrid liner.

Researchers have also examined the acoustic behaviour of perforated plates under the influence of high amplitude fluctuations, both in the absence and presence of bias flow. Cummings and Eversman (1983), Salikuddin and Ahuja (1983) conducted theoretical investigations on the effect of high amplitude acoustic fluctuations on the acoustic

behaviour of duct terminations (in the absence of bias flow), whereas the experimental investigations on the influence of medium and high amplitude fluctuations on the acoustic behaviour of orifices in the absence and presence of bias flow was carried out by Zhou and Bodén (2014). Tam et al. (2001) investigated the dissipation mechanisms in resonant acoustic liners through DNS. In all these studies, they found that when high intensity acoustic waves are incident on perforated liners, they induce vortex shedding, and vortex dissipation is the dominant damping mechanism in such liners.

1.2.2. Acoustic liners in combustors

In conventional diffusion flame type combustors, like the one shown in Fig. 1.6, there are dilution holes on the combustor casing to provide secondary cooling of the combustion liner. These dilution jets enhance the effective acoustic attenuation inside the combustion chamber. Unfortunately, such a control strategy is not acceptable in lean premixed combustion systems. The lean premixed combustors already operate near the lean blowout limit and any further dilution of the fuel-air mixture will lead to blowout.

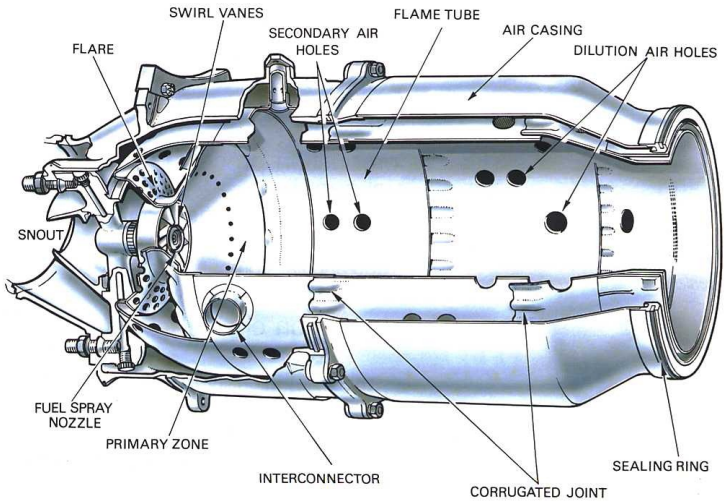

Figure 1.6: Typical conventional type combustion chamber. (Rolls-Royce, 1996)

However, in recent years, researchers have developed methods to use acoustic liners as dampers in lean premixed combustors. One such example is the work by Scarcini (Huang and Yang, 2009, Lieuwen and Yang, 2005), where a modified premixer con-

figuration was included in the Rolls Royce Trent 60 Aeroderivative gas turbine engine to effectively mitigate combustion instabilities. Instead of using a premixed mixture, the fuel was injected at the head of the premixer. The premixer walls had perforations through which air entered the premixer in the form of numerous jets, and facilitated for thorough mixing prior to combustion. Such a liner configuration was found to be effective in damping thermoacoustic instabilitites. However, the employability of acoustic liners as passive control elements in lean premixed combustion systems is still in the developmental phase, and presently a rapidly evolving field of research.

There are several theoretical, numerical and experimental works that have implemented cavity-backed perforations to control thermoacoustic instability in laboratory based test combustors. Tran et al. (2009a,b) successfully incorporated a cavity-backed perforated plate to annul the thermoacoustic instability in a swirl combustor. The cavity-backed perforated plate was placed at the upstream end of the swirl burner, and the control was achieved by varying the cavity length. Tran's work was continued by Scarpato et al. (2013, 2012) with the aim of investigating the influence of Strouhal number on the absorption mechanism of the cavity-backed perforate. Stability predictions of Tran's combustor were carried out by Heckl and Kosztin (2013), using a Green's function approach and a generic time-lag law for the heat source. They predicted that control can be achieved for a wide range of cavity lengths and also examined the effectiveness of the control for different time-lags.

Zhao et al. (2011) utilized the aforementioned method to study the damping properties of perforated liners fitted along the bounding walls of a combustion chamber. They observed that the combustion chamber length and the bias flow through the perforations are important parameters for passive control. They also developed a real-time tuning scheme for the perforated liners, which was implemented to obtain optimum damping for a broad frequency range.

Rehman and Eldredge (2007) investigated the influence of perforated liners on the stability of a simplified combustion system by modelling the scattering properties of the acoustic liners in terms of transfer matrices (using the model proposed by Eldredge and

Dowling (2003)) and then by using this model in a heuristic gain-delay flame model. They found that stability could be achieved by varying the porosity of the orifices as well as the bias flow velocity.

1.3. Research Motivation

Passive control strategies like cavity-backed acoustic liners with bias flow and bulky acoustic dampers like Helmholtz resonator or half-wave and quarter-wave tubes, are all viable control options in large power generation units, especially stationary ones (Lieuwen and Yang, 2005). Unfortunately, these passive control strategies are undesirable in small and compact power generation units like domestic boilers. Due to the strict emission laws, the latter systems also operate in the lean premixed regime and are therefore susceptible to thermoacoustic instabilities.

The amount of literature concerning the combustion instability control in small combustion systems like domestic burners is very limited, and this motivated us to look for alternative control strategies to suppress thermoacoustic instabilities in domestic boilers. One of the main differences between the gas turbine engines or other large power generators and small power generation units like domestic boilers, is the presence of heat exchangers in the latter. In a domestic boiler, the heat exchanger is housed within the combustion chamber along with the flame, and so requires no additional space. With this as the basis, we propose to use heat exchangers as a viable alternative to control thermoacoustic instabilities in combustion systems like domestic boilers.

1.3.1. Sound dissipation in tube banks

Heat exchangers are periodic structures that consist of arrays of tubes in a cross flow. It is evident from literature survey that tube rows or tube banks in cross flow can effectively damp acoustic oscillations. Some of the relevant works are mentioned below. If sound passes through an array of tubes, it is attenuated due to viscous, thermal and

turbulent losses. We aim to utilise this attenuation property of tube arrays to control thermoacoustic instabilities.

Kristiansen and Fahy (1972, 1974) have developed a simple theory for the prediction of sound dissipation in tube banks subjected to steady cross flow. They treated the tube bank as a special homogeneous medium whose characteristic properties or parameters were determined from the mean flow data. They observed that the attenuation within the tube bank increased with increasing mean flow velocity.

Quinn and Howe (1984) derived the dispersion relation for sound propagation through a bank of rigid circular tubes in cross flow. They observed that the attenuation of sound increases with decreasing Strouhal number. In other words, for a given incident acoustic frequency and tube diameter, the sound attenuation increases with increasing mean cross flow velocity. However, the approach by Quinn and Howe utilises a highly idealised flow modelling and hence provides only a qualitative description of the acoustic behaviour of the tube bank.

1.4. Scope of Research

The scope of the present work is to investigate the passive control capability of heat exchangers and to effectively use them to suppress the thermoacoustic instability in an idealised domestic boiler system.

In order to achieve this goal, the complex boiler system is simplified as shown in Fig. 1.7(a). The boiler is assumed to consist of its very basic components : (1) burner, (2) heat exchanger or *hex* and (3) outer casing with provisions for the flow of fuel-air mixture, exhaust and coolant.

A section of the boiler (Fig. 1.7(b)) taken from axis of symmetry and along the radial direction will resemble the combustion system that consists of a 1-D duct with a compact heat source. The upstream end is open and the downstream end is fitted with a cavity-backed heat exchanger tube row. In our study, we use the 1-D acoustic assumption because we focus on the instability in the *radial* direction and also assume

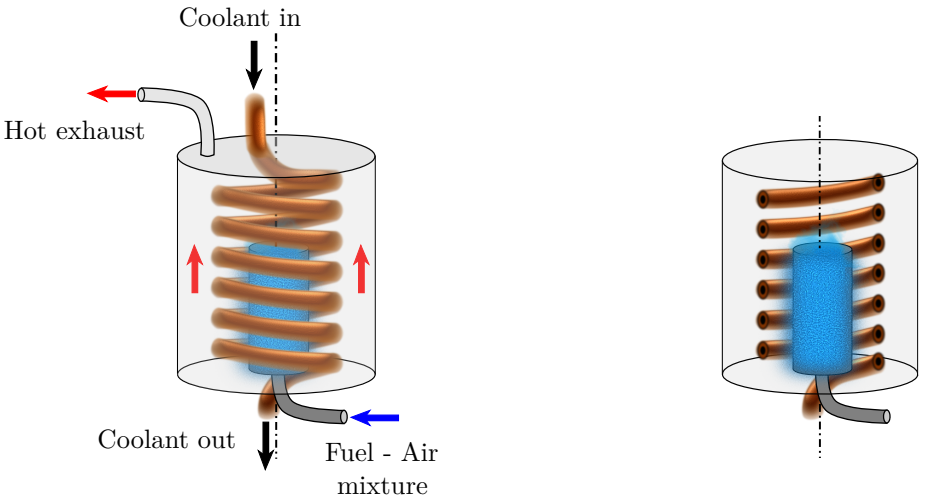

(a) Full view (b) Sectional view

Figure 1.7: A simplified domestic boiler with heat exchanger

that the system properties are uniform along the axis of the burner (z direction in cylindrical coordinates). The heat source is modelled using a time-lag law. The heat exchanger is modelled by taking into account both the heat transfer and the acoustic scattering aspects. We also take into account the jumps in mean temperature across both the heat source and the heat exchanger. In order to examine the instability control potential of the cavity-backed heat exchanger, we undertake a stability analysis by constructing stability maps for a wide range of downstream end boundary conditions.

1.5. Structure of thesis

The work presented in this thesis can be broadly divided into the following chapters

- Chapter 2 describes the thermoacoustic system being investigated. The practical combustion system like the domestic boiler is simplified to its most essential components and the overall acoustic field within such a combustion system is provided
- In Chapter 3, the different modelling approaches for the heat source or sink are presented. This chapter mainly focuses on the assumptions involved and the modelling of the heat sources using time-lag laws. A discussion on the acoustic jump or acoustic matching conditions across a compact heat source/sink is also provided in the chapter

- The modelling of the heat exchanger tube row is given in Chapter 4. The heat transfer response of the heat exchanger is obtained through numerical simulations, and formulated as a transfer function in the frequency domain (Surendran et al., 2016b). This is followed by the quasi-steady modelling of the aeroacoustic response of the heat exchanger tube row (Surendran et al., 2016a). In the last part of the chapter, the total acoustic response of the heat exchanger is derived and a parametric study is conducted to examine the influence of different system parameters on this response

- The influence of cavity backing on the acoustic response of the heat exchanger tube row is provided in Chapter 5. Again, a parametric analysis is done to investigate the additional influence of the cavity backing, along with other system parameters

- In Chapter 6, stability analysis of the complete combustion system is undertaken. Stability maps are constructed for various system parameters and the influence of these parameters on the instability control are discussed

- In the final chapter, Chapter 7, a brief summary of the work is presented. The key findings are highlighted along with the scope for future work

A concise representation of the thesis structure is shown in Fig. 1.8. Another relevant and complementary work related to this thesis (but not included in the thesis) is the representation of heat exchanger tube row by a row of narrow sharp-edged rods with rectangular cross-section, treating the hex effectively as a slit-plate. Details on this work can be found in Surendran and Heckl (2015, 2016, 2017).

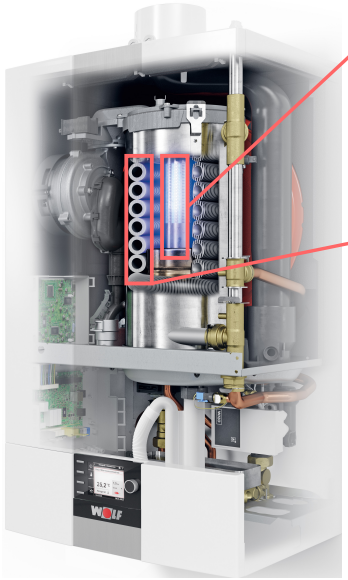

Chapter 2

- Simplifications to geometry
- Assumptions and acoustic field involved

Chapter 3

- Heat source modelling
- Time-lag laws
- Acoustic jump conditions

Chapter 4

- Heat exchanger modelling - heat sink and acoustic scatterer
- Numerical simulation of heat sink and transfer functions
- Analytical modelling and experimental verification of acoustic scattering
- Total scattering matrix at heat exchanger
- Parametric study - influence of system parameters

Chapter 5

- Influence of cavity backing
- Parametric study - influence of cavity and system parameters

Chapter 6

- Stability maps
- Influence of system parameters on passive instability control

Chapter 7

- Conclusions
- Key findings and scope for future work

Figure 1.8: Outline of thesis (image source: www.wolf-heiztechnik.de)

Chapter 2

The modelled configuration

The objective of this chapter is to introduce the thermoacoustic system being investigated. The main focus is to analytically model an idealised combustion system with heat exchanger and examine the influence of heat exchangers on the stability of such combustion systems. In this chapter, a practical combustion system like a domestic boiler is first reduced to a simple geometry. The assumptions involved and the form of the acoustic field within the combustor is given in this chapter.

2.1. Introduction

Due to strict emission laws to reduce NO_x production, power generation and combustion systems are required to operate in lean premixed combustion regime, often leading to thermoacoustic instabilities in these systems. The need to produce compact and clean combustion systems that are less prone to thermoacoustic instabilities have presented researchers and engineers with many design challenges. One such challenge is the inclusion of passive control components and dampers like quarter-wave resonators and Helmholtz resonators into the system configuration. These dampers are usually bulky and cannot be easily accommodated into the already intricate geometry of power

generation systems. In this work, we focus on passive instability control in domestic boilers.

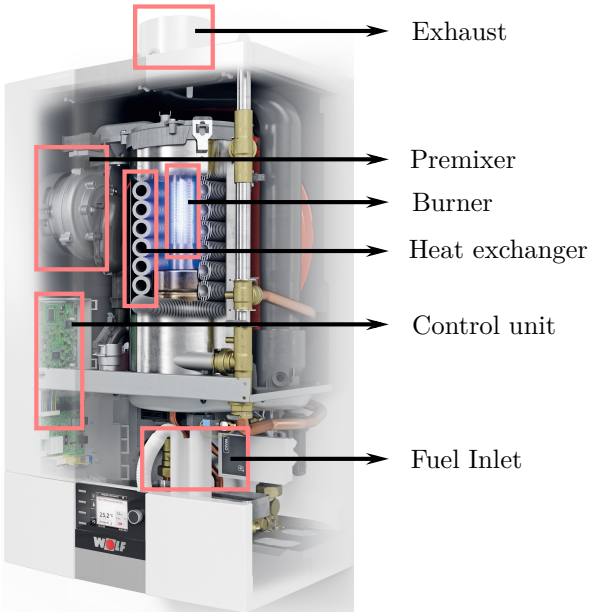

Figure 2.1: Sectional view of a domestic boiler (image source: www.wolf-heiztechnik.de)

A typical domestic boiler is as shown in Fig. 2.1. The main components are burner, heat exchanger, premixer, inlets for fuel, air and water, exhaust for flue gases and its associated control unit. Prior to combustion, the fuel enters the premixer where it mixes with air. The premixture then goes to the combustion chamber. The combustion chamber houses the burner and the heat exchanger. The fuel-air mixture burns at the burner surface and the hot combustion products or flue gases then exit the combustion chamber and subsequently the boiler through the exhaust. As the flue gases escape from the combustion chamber, they transfer their heat to the water present within the heat exchanger. This hot water is circulated around to radiators and hot water storage units.

Incomplete combustion of the fuel within the combustion chamber leads to the production of oxides of carbon and nitrogen that are deadly pollutants. To reduce this pollution, the fuel is premixed with excess air to form a lean mixture and is then burnt in the combustion chamber. Lean mixtures have low adiabatic flame temperatures and this affects flame stabilization on the burner (Glassman and Yetter, 2008). In addition to these, when the heat source (flame in the case of boiler) is placed in a closed environment, there will be close interaction between the heat release from the source

and the local acoustics. When this interaction transforms into a feedback mechanism, thermoacoustic instability ensues.

It is this instability and its suppression using passive components that is of interest in our present study. This doctoral work, which is part of the Marie Curie ITN TANGO, explores the usability of heat exchangers as passive control elements in domestic boilers. Heat exchanger being an integral component in any heat or power generation system, it is advantageous to modify or redesign the heat exchangers to mitigate thermoacoustic instabilities, rather than having additional damping components in the system. Our aim is to study, analytically, the mitigation potential of heat exchangers in the low frequency regimes, where quarter-wave resonators and Helmholtz resonators are practically not viable.

2.2. Description of the model

As mentioned in Chapter 1, the domestic boiler configuration is simplified to its basic components. However, for the analytical modelling purposes, we discard the fuel-air mixture and exhaust gas compositions, the chemical kinetics associated with combustion as well as the flux of coolant through the hex. Instead, we assume a homogeneous medium encompassing the burner and the hex, having different mean temperature values at different regions within the boiler. The hex is assumed to be maintained at constant temperature. After all these simplifying assumptions, the modelled combustion system reduces to that shown in Fig. 2.2. It consists of a long duct, open at one end and closed at the other, forming a quarter-wave resonator. Even though the geometrical complexities in a real boiler calls for modelling a duct with varying area of cross section, in our simplified case, we assume a duct with constant area of cross section. The open end at $x = 0$ denotes the line of symmetry and acts as an inlet for the unburnt fuel-air mixture[1] and the closed end denotes the outer casing of the

[1]In domestic boilers, the burner is mounted over a base of significant volume, which can act as a buffer region to dissipate any pressure build up within the burner. In such situations, the volume within the base leading up to the symmetry line of the burner can be treated as a pressure release boundary, where $p' = 0$. Hence, we are justified in assuming an open end at $x = 0$.

boiler. The open end is characterised by its reflection coefficient $R_0 = -1$ and the closed end by the corresponding reflection coefficient of $R_p = 1$. We are treating the downstream end of the combustor as a movable rigid backing (or a piston) in order to vary the distance between the hex and the backing wall. This distance is referred to as the cavity length (l_c) and is one of the key parameters in our study. The heat source, which denotes the flame front at the burner, is located at a distance l_f from the upstream end, dividing the resonator into a cold upstream region (Region *1*) and a hot downstream region (Region *2*). The speeds of sound ($c_{1,2}$) and mean temperatures ($\bar{T}_{1,2}$) are uniform in both regions, where $\bar{T}_1 < \bar{T}_2$ and subsequently $c_1 < c_2$. The hex is located at a distance $x = L$ from the open end.

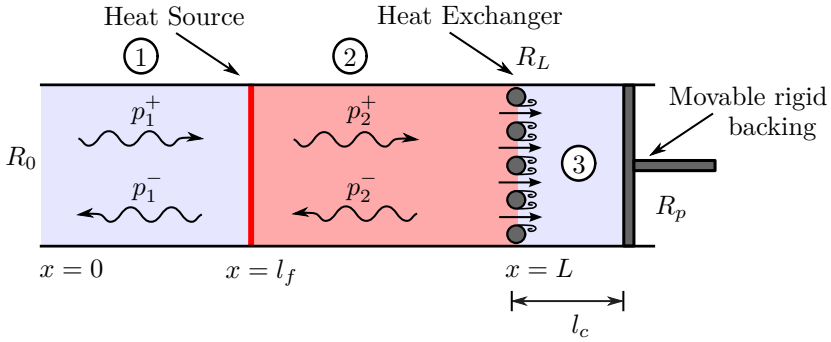

Figure 2.2: The modelled combustion system

2.2.1. Acoustic field

The acoustic field within the combustor is modelled as one-dimensional acoustic waves propagating perpendicular to the hex (normal incidence), as shown in Fig. 2.2. It consists of forward (p^+) and backward (p^-) travelling waves, with amplitudes A_1 and B_1 respectively in Region *1* and amplitudes A_2 and B_2 respectively in Region *2*. The acoustic pressure and velocity fields inside the combustor may be written as (Rienstra and Hirschberg, 2014)

Region r:

$$\hat{p}_r(x) = p_r^+ + p_r^- = A_r e^{ik_r(x-l_f)} + B_r e^{-ik_r(x-l_f)} \tag{2.1}$$

$$\hat{u}_r(x) = u_r^+ + u_r^- = \frac{1}{\rho_r c_r}\left\{A_r e^{ik_r(x-l_f)} - B_r e^{-ik_r(x-l_f)}\right\} \tag{2.2}$$

where $\hat{p}$ and $\hat{u}$ are the acoustic pressure and acoustic velocity respectively, A and B are the pressure amplitudes to be determined and u^+ and u^- are the acoustic velocity components corresponding to p^+ and p^- respectively. The subscript 'r' denotes the region within the combustor, ω is the frequency of the incoming acoustic wave, ρ is the density of the fluid and $k_r = \omega/c_r$ is the wave number in the region 'r'. In our analysis, the mean flow velocity is very small ($\sim \mathcal{O}(1\,\mathrm{m/s})$) compared to the speed of sound and hence can be neglected in the mathematical formulation. The factor of $e^{-i\omega t}$ is omitted throughout the analysis. Formulation of boundary conditions and the complete system is taken up in Chapter 6.

2.2.2. Heat Source

In typical burners, the heat source is the surface stabilised flame front composed of multiple flames as shown in Fig. 2.3. However, the lengths of individual flames are much smaller than the acoustic wavelengths encountered within the combustion system. Therefore, we can assume the heat source to be compact and confined to an infinitesimally thin region at the location $x = l_f$. We also assume that the heat release rate fluctuations $\left(\hat{Q}\right)$ at the heat source location is influenced by the acoustic velocity perturbation $(\hat{u})$ at that location. The relation between $\hat{u}$ and $\hat{Q}$ is given by heat release rate models and flame transfer functions. Chapter 3 addresses the modelling of heat sources and sinks in detail.

2.2.3. Heat Exchanger or Hex

The hex consists of an array of tubes with bias flow through the gaps, denoted by its Mach number, M. The Mach numbers considered in our analysis are very small (i.e. $M \ll 1$) and hence we could neglect them while describing the acoustic field within the combustor. The mean flow Mach number becomes relevant only in those regions close to the hex where hydrodynamic effects outweigh the acoustic effects. The influence of the hex and the backing wall, on the acoustic field within the combustor is given by

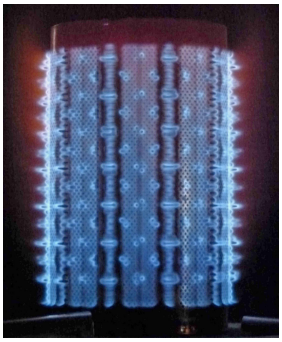

(a) Surface stabilised flames (image source: http://www.scm.keele.ac.uk/Tango/)

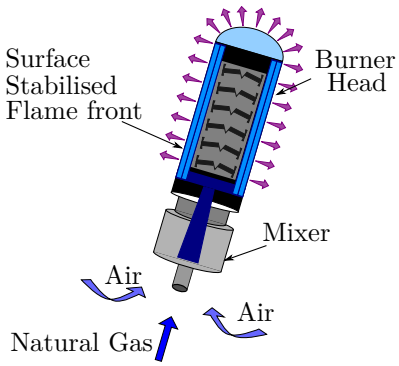

(b) Schematic of burner (Reproduced from www.alzeta.com)

Figure 2.3: Burner head

the reflection coefficient R_L at $x = L$. The details pertaining to the modelling of hex and derivation of R_L are given in Chapters 4 and 5 respectively.

2.3. Conclusions

Passive instability control using heat exchangers is a viable alternative for domestic boilers and other power generation systems, susceptible to thermoacoustic instabilities. To this end, the effect of heat exchangers on combustion systems need to be studied. In this chapter, we have introduced a practical boiler and its simplification to an idealised combustion system. The idealised system consists of a quarter-wave resonator (a constant area duct with open-closed ends) with a heat source and a heat exchanger. The acoustic field within the resonator is modelled as 1-D waves and the heat source is assumed to be compact. Even though there is a mean flow in the system, it is neglected due to its magnitude being much smaller than the speed of sound.

Chapter 3

Heat Source or Sink

This chapter gives an overview of the modelling of the response of heat sources and sinks to incoming perturbations. The derivation of Rayleigh criterion for heat sources/sinks, shows that a system undergoes instability if there is net acoustic energy growth in the system, and is greatly influenced by the phase difference between the acoustic perturbations and heat release rate perturbations. Since thermoacoustic instability is a manifestation of the feedback loop between acoustic perturbations and heat release rate perturbations, it is important to understand and model the responses of heat sources and sinks. Time-lag laws and Flame Transfer Functions are the most commonly used models. In the present study, we use a simple time-lag law to model the response of a compact heat source. Lastly, the acoustic pressure continuity and acoustic velocity jump conditions across the heat source/sink is formulated.

3.1. Introduction

Thermoacoustic instabilities in combustion systems manifest as a result of positive feedback mechanism existing between acoustic perturbations and heat release rate fluctuations. It is, therefore, appropriate to have a chapter dedicated solely to the

understanding of the physics and the subsequent modelling of the responses of heat sources and sinks to oncoming acoustic perturbations. In this chapter, we first derive the Rayleigh criterion to facilitate the prediction of thermoacoustic instabilities, followed by the discussions on heat release rate models and eventually their influence on the acoustic field within the combustion system.

The phenomenon of thermoacoustic instability was observed centuries ago by glass blowers while blowing hot bulbs at the end of narrow tubes (Lord Rayleigh, 1896). This behaviour was later experimentally studied by Sondhauss (1850). He observed that the frequency of the sound produced depend on the dimensions of the tube, especially the length and the volume of the bulb at the end of the tube. Another example of a simple combustion system to exhibit thermoacoustic instability is the Rijke tube. This system was extensively studied by Rijke (1859). He had a vertical glass tube with a wire gauze positioned at one-quarter length from the bottom end. The wire gauze was heated to red hot using hydrogen flame. The glass tube was open at both ends and the hot wire gauze induced an upward convective flow through the tube. He observed that a clear tone was produced seconds after the hydrogen flame was removed. As soon as the top end of the tube was covered, the sound stopped. Thermoacoustic instability can also be triggered when there is hot flow over a heat sink, as observed by Bosscha (Lord Rayleigh, 1896) and Riess (1859), and can be viewed as a '*reverse*' Rijke effect. They observed amplified pressure oscillations when a cold wire gauze or a heat sink was placed at the upper extremity of a Rijke tube. Even though there were similar observations made by various other researchers, it was Lord Rayleigh (1896) who gave well-founded explanations for these thermoacoustic behaviours. As will be explained in Section 3.2, Rayleigh attributed the sound production to the coupling of unsteady heat release fluctuations and pressure fluctuations.

3.2. Rayleigh Criterion

Lord Rayleigh, in his book *The Theory of Sound* (Lord Rayleigh, 1896), gave the reason for thermoacoustic instability as:

> "*If heat be periodically communicated to, and abstracted from, a mass of air vibrating (for example) in a cylinder bounded by a piston, the effect produced will depend upon the phase of the vibration at which the transfer of heat takes place. If heat be given to the air at the moment of greatest condensation, or be taken from it at the moment of greatest rarefaction, the vibration is encouraged. On the other hand, if heat be given at the moment of greatest rarefaction, or abstracted at the moment of greatest condensation, the vibration is discouraged.*"

This essentially means that for an instability to occur, the unsteady heat release fluctuations and the acoustic pressure fluctuations must be in phase. To draw an analogy to the Rayleigh criterion, consider the forced oscillations of a pendulum. Assume that the pendulum is analogous to the acoustic pressure fluctuations and the forcing to the heat release rate fluctuations. Let us first consider the case when heat is added at the pressure maxima. This corresponds to the forcing situation shown in Fig. 3.1(a), where the pendulum is forced from point A to B and the forcing is said to be in phase with the displacement. Such a forcing will increase the amplitude of oscillation. Repeated forcing at the maximum results in the amplification shown in Fig. 3.1(b). On the other hand, consider the case of heat addition to pressure minima. This corresponds to the forcing situation shown in Fig. 3.1(c). Here, the pendulum is displaced from point C to D i.e., the forcing is out of phase with the displacement of the pendulum, leading to damping (Fig. 3.1(d)). Similar analogies can be drawn for the cases with heat removal from a pressure maximum or minimum leading to damping or amplification of the oscillations.

As for the frequency of oscillation, Rayleigh noted that the frequency remained unaffected for the situations where the heat addition/removal occurred at the pressure

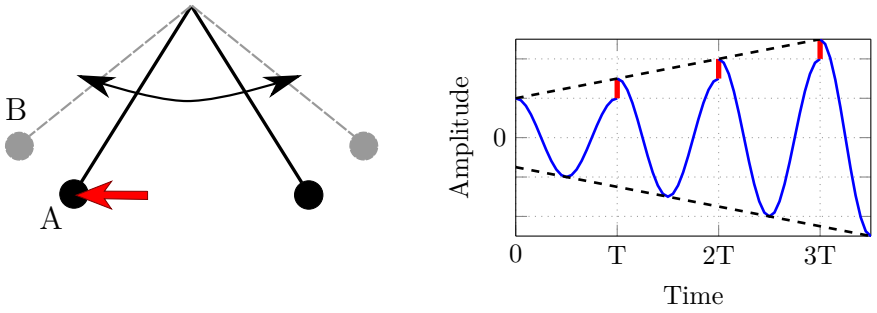

(a) Forcing (b) Amplification

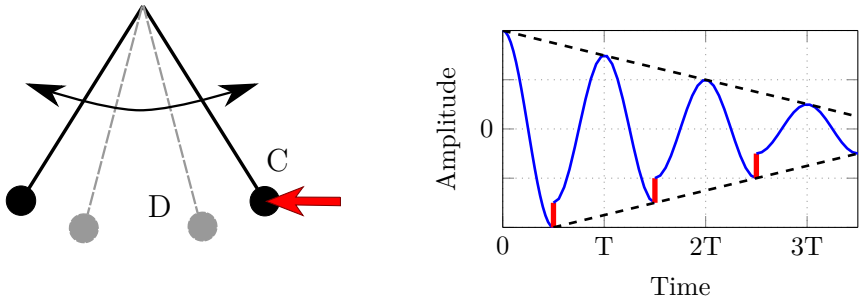

(c) Forcing (d) Damping

Figure 3.1: Rayleigh criterion and analogy to forced oscillation

maximum/minimum. The frequency was affected when heat addition/removal occurred at the mid-point of the oscillation. The frequency of pressure oscillation increased when heat was added quarter period before pressure maxima; and the frequency decreased when heat was added quarter period after pressure maxima. But, in such a situation the amplitude of oscillation was unchanged.

The mathematical formulation for the Rayleigh criterion can be derived using a control volume approach. Consider a control volume (*c.v.*) of length Δl and cross-sectional area S, enclosing the heat source, as shown in Fig. 3.2. Assuming an inviscid flow with no mass sources within the *c.v.*, no body forces and viscous forces acting on the *c.v.* and negligible heat transfer across the *c.v.*, we can write the mass and momentum equations as

$$\frac{D\rho}{Dt} + \rho \nabla \cdot \mathbf{u} = 0, \tag{3.1}$$

$$\rho \frac{D\mathbf{u}}{Dt} = -\nabla p, \tag{3.2}$$

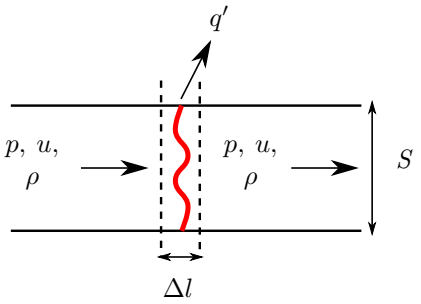

Figure 3.2: Control volume for Rayleigh criterion

where ρ is the density, $\mathbf{u}$ is the velocity vector and p is the pressure. In order to obtain the acoustic perturbation equations, we linearise Eqs. (3.1) and (3.2) using the mean and perturbed quantities of p, ρ and $\mathbf{u}$: $p = \bar{p} + p'$, $\rho = \bar{\rho} + \rho'$ and $\mathbf{u} = \bar{\mathbf{u}} + \mathbf{u}'$. With the assumption of quiescent medium ($\bar{\mathbf{u}}$ does not change with time or space), we can neglect the effect of the mean flow velocity: $\bar{\mathbf{u}} = \mathbf{0}$, and also the assumption that the perturbation quantities $\ll$ mean quantities, the 1-D conservation equations for the perturbed quantities are obtained as

$$\frac{\partial \rho'}{\partial t} + \bar{\rho}\,\frac{\partial u'}{\partial x} = 0, \tag{3.3}$$

$$\bar{\rho}\,\frac{\partial u'}{\partial t} = -\frac{\partial p'}{\partial x}. \tag{3.4}$$

Multiplying Eq. (3.4) with u' and substituting Eq. (3.3) in it, we obtain

$$\bar{\rho}\left[\frac{\partial}{\partial t}\left(\frac{1}{2}u'^{\,2}\right)\right] + \frac{\partial}{\partial x}\left(p'u'\right) = p'\left(\frac{-1}{\bar{\rho}}\,\frac{\partial \rho'}{\partial t}\right) \tag{3.5}$$

When heat is added to the fluid inside the *c.v.*, we can assume that the density variations are influenced by the variations in pressure and enthalpy (denoted by h) i.e., $\rho = \rho\,(p, h)$[1]. Hence, using chain rule of differentiation, we can write

$$\frac{\partial \rho}{\partial t} = \left(\frac{\partial \rho}{\partial p}\right)\Big|_h \frac{\partial p}{\partial t} + \left(\frac{\partial \rho}{\partial h}\right)\Big|_p \frac{\partial h}{\partial t}. \tag{3.6}$$

The isenthalpic relation gives $(\partial\rho/\partial p)|_h = 1/c^2$ and thermodynamic property relation $(\partial h/\partial T)_p = C_p = \gamma\mathcal{R}/(\gamma - 1)$ (Moran and Shapiro, 2004) combined with the ideal

[1]We could also use variations in entropy instead of enthalpy i.e., $\rho = \rho\,(p, s)$.

gas law $p = \rho \mathcal{R} T$, gives $(\partial\rho/\partial h)_p = (\partial\rho/\partial T) \times (\partial T/\partial h)_p = -\bar{\rho}\,(\gamma-1)/c^2$, where C_p is the specific heat at constant pressure, $\mathcal{R}$ is the specific gas constant and γ is the ratio of specific heats. Hence, substituting these relations in Eq. (3.6), we get [2]

$$\frac{\partial \rho'}{\partial t} = \frac{1}{c^2}\frac{\partial p'}{\partial t} + \frac{-\bar{\rho}\,(\gamma-1)}{c^2}\frac{\partial h}{\partial t}. \tag{3.7}$$

In the control volume, where heat is added, the only contribution to the rate of change of enthalpy i.e., $\partial h/\partial t$, is the heat release rate fluctuation (per unit mass) q'. Therefore, by substituting Eq. (3.7) in Eq. (3.5) and using $\partial h/\partial t = q'$, we obtain

$$\frac{\partial}{\partial t}\left[\frac{p'^{\,2}}{2\bar{\rho}c^2} + \frac{\bar{\rho}u'^{\,2}}{2}\right] + \frac{\partial}{\partial x}\left(p'u'\right) = \frac{(\gamma-1)}{c^2}\,p'\,q'. \tag{3.8}$$

Equation (3.8) is the local form of the acoustic energy balance in the control volume. The first term in Eq. (3.8) is the rate of change of potential and kinetic energies across the control volume, the second term is the rate of net outflux of energy from the control volume, or in other words, the rate of energy loss and the right hand side denotes the acoustic energy gained from the heat release. When integrated over the total volume, we obtain the global form of the acoustic energy balance.

$$\frac{\partial}{\partial t}\iiint_{\Delta\mathcal{V}}\left[\frac{p'^{\,2}}{2\bar{\rho}c^2} + \frac{\bar{\rho}u'^{\,2}}{2}\right] d\mathcal{V} + \iiint_{\Delta\mathcal{V}}\frac{\partial}{\partial x}\left(p'u'\right)\,d\mathcal{V} = \frac{(\gamma-1)}{c^2}\iiint_{\Delta\mathcal{V}} p'\,q'\,d\mathcal{V}. \tag{3.9}$$

Time averaging of Eq. (3.9) gives an indication of the stability of the combustion system under consideration. There will be net growth in the acoustic energy stored in the system, leading to instability, if the energy gained through heat addition is larger than the energy lost within the system. Many researchers (McManus et al., 1993) denote the time average of the integral term in the *r.h.s* of Eq. (3.9) as the *Rayleigh index* ($\mathcal{G}$), with

$$\mathcal{G} = \frac{1}{\mathcal{T}}\int_0^{\mathcal{T}} Q'(t)\,p'(t)\,dt, \tag{3.10}$$

[2] If we assume $\rho = \rho\,(p,s)$, $\partial\rho/\partial t = (\partial\rho/\partial p)_s\;\partial p/\partial t + (\partial\rho/\partial s)_p\;\partial s/\partial t$. Here, $(\partial\rho/\partial p)_s = 1/c^2$, from isentropic relation and $\partial s/\partial t = q'/T$, from 2nd Law of Thermodynamics, where q' is the rate of heat added or removed. $(\partial\rho/\partial s)_p$ can be evaluated from the ideal gas law as $-\bar{\rho}\,(\gamma-1)T/c^2$

where $\mathcal{T}$ is the time period of oscillation and $Q' = \iiint_{\Delta\mathcal{V}} \bar{\rho}\, q'\, d\mathcal{V}$ is the global unsteady heat release fluctuation. For systems with negligible acoustic losses, $\mathcal{G} > 0$ indicates amplification of the thermoacoustic instability and $\mathcal{G} < 0$ indicates damping. For situations with non-negligible acoustic losses, the condition for instability will be $\mathcal{G} > \iiint_{\Delta\mathcal{V}} \frac{\partial}{\partial x}(p'u')\, d\mathcal{V}$. Applying Eq. (3.10) to a harmonic pressure perturbation of the form $p'(t) = \hat{p}\cos(\omega t)$ and a heat release perturbation with a phase shift ϕ i.e., $Q' = \hat{Q}\cos(\omega t + \phi)$, predicts the phase difference to be $-\pi/2 < \phi < \pi/2$ for $\mathcal{G}$ to be positive. Hence, it is important to know the phase difference between p' and Q' to predict thermoacoustic instabilities.

3.3. Some factors affecting the heat release rate fluctuations

The prediction of thermoacoustic instabilities in real systems is not always straight forward. Even though the primary mechanism for the instability is the feedback loop between Q' and p', there are other secondary mechanisms that could affect Q' and trigger instability (McManus et al., 1993). Some of these factors are shown as a schematic in Fig. 3.3(a). Firstly, we consider the effect of equivalence ratio fluctuations in the incoming fuel-air mixture (Lieuwen and Zinn, 1998). Although we assume the incoming mixture to be fully premixed, it is not perfectly homogeneous in composition. This causes variations in the equivalence ratio, both temporally and spatially, leading to unsteady and non-uniform heat release rates and consequently a phase difference between p' and Q'.

Secondly, the heat released is proportional to the amount of fuel-air mixture being burnt at the flame surface. Therefore, Q' is influenced by the fluctuations in the mass flux at the combustor inlet. The fluctuations in the inlet mass flux is proportional to u' and hence we can deduce that Q' is proportional to u'.

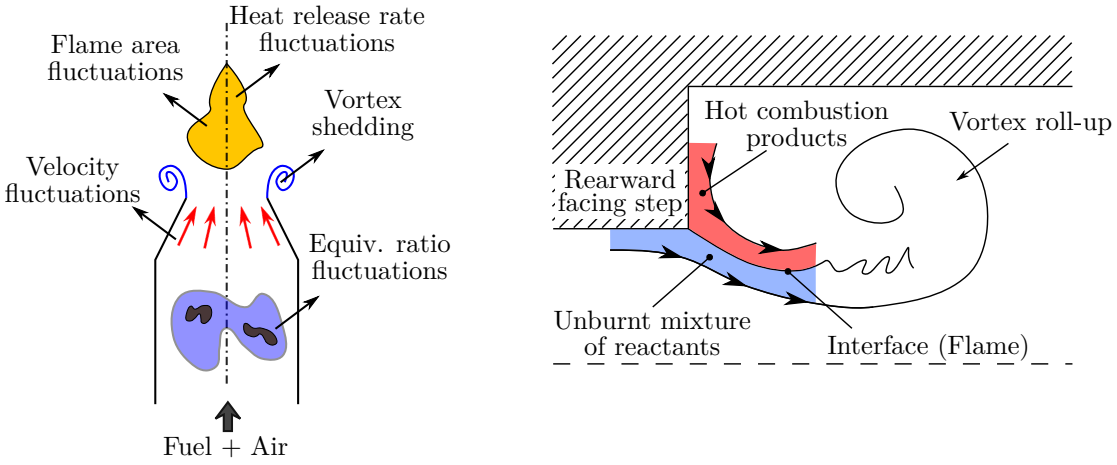

(a) Causes for fluctuations in the heat release rate

(b) Vortex roll-up. Reproduced from Schadow and Gutmark (1992)

Figure 3.3: Factors affecting the heat release rate fluctuations

Another factor that influences the heat release rate fluctuations is the presence of hydrodynamic instabilities, like vortex shedding and shear layers, in the source region (Schadow and Gutmark, 1992). Vortex structures and shear layers are formed when there is interaction between high and low speed streams. Typically in combustors, this occurs near the inlet or near flame holders where we have the high speed stream of unburnt fuel-air mixture and the low speed stream of the burnt gases, and the flame is formed at this interface between the two streams. The vortex development and vortex roll-up process causes unburnt mixture to be trapped within the vortices, and are then convected downstream along with the incoming flow (Fig. 3.3(b)). As the vortices convect, they grow due to the entrainment from the surrounding medium or by merging with adjacent vortices, and eventually breakdown into fine-scale turbulent structures (Pope, 2000). At this stage, there will be enhanced mixing of the previously trapped unburnt mixture with the surroundings, leading to sudden combustion at the flame interface, thereby causing a sudden heat release. The mechanism of vortex roll-up and the subsequent disintegration leading to heat release is a periodic process and when this periodic heat release is in phase with p', it can trigger thermoacoustic instability.

The amount of heat released is also dependent on the surface area of the heat source. The larger the surface area, the higher the heat released. Hence for flames, wrinkled

flame surfaces/fronts release more heat. The wrinkling of the flame front is indirectly influenced by u' and aforementioned hydrodynamic instabilities.

3.4. Heat release rate models

The response of a heat source to upstream acoustic perturbations is given by the heat release rate models. The most commonly used models are *Time-Lag* $(n-\tau)$ models and *Transfer Functions* (TF). Recalling from the Rayleigh criterion, we see that it is the phase difference between p' and Q' which is crucial in triggering instability. In the time domain, this phase difference can be interpreted as a *time delay* or a *time-lag*, and has strong influence on the stability behaviour of the combustion system. As mentioned in Section 3.3, there are many factors contributing to the phase difference between Q' and p', with each factor having its own associated time-lag.

It is usually convenient to model Q' in terms of time-lags when the underlying physics and the sources of time-lags in the system are known. However, when we are investigating thermoacoustic systems with complex sources and multiple time-lag contributions, we use the concept of Transfer Functions.

An important factor that contributes to the heat release rate modelling in a system, is the compactness of the heat source. Compactness can be based on either the acoustic field (acoustic compactness) or the hydrodynamic flow field (convective compactness) present in the system. For an acoustically compact heat source, the characteristic length of the heat source is much smaller than the acoustic wavelength, and hence we can apply the thin sheet approximation to describe the acoustic behaviour of the heat source. For a convectively compact heat source, we assume the heat source to be confined to a very small spatial region, with respect to the mean convected flow, such that there is no spatial variation in the heat source properties. In the case of a convectively non-compact heat source, there will be a spatial distribution of the heat source properties, namely the heat released. This will create phase differences between

the heat released and the mean flow velocity fluctuations at different spatial locations along the heat source. These phase differences can generate additional time-lags.

In our analysis, we restrict ourselves to acoustically and convectively compact heat sources (and sinks). Hence, the heat source is assumed to be confined to an infinitesimally thin plane, across which we can derive the jump conditions for the acoustic field (as will be shown in Section 3.5), as well as model the heat release rate laws.

3.4.1. Time-Lag ($n-\tau$) laws

As mentioned in Section 2.2.2, in our study we model Q' solely as a function of u'. Q' at the heat source location $x = l_f$ depends on the velocity perturbations from the upstream side, but with a certain time delay τ (Fig. 3.4). This formulation is based on the early research works conducted in rocket motors by Crocco and Cheng (1956), where they related the Q' to p' through a time-lag model. The rationale behind the time-lag concept is that in real life events, there is a small time lapse between the injection of the propellant to the final burnt products. Following a similar justification, we also assume a small time-lag between the acoustic velocity fluctuations at a reference position $x = x_{ref}$ (upstream of the heat source) and the heat released at $x = l_f$. Using this assumption, we can model the heat release rate for a compact and planar heat source, confined to an infinitesimal region at $x = l_f$ as

$$Q'(t) = n_1 \, u'_{ref}(t-\tau) \, , \tag{3.11}$$

where n_1 is the coupling coefficient or interaction index, $u'_{ref}(t)$ is the acoustic velocity fluctuation at x_{ref} and τ is the time-lag associated with the convection of the acoustic perturbations from x_{ref} to l_f. In our study, we refer to Eq. (3.11) as ***Simple n-τ law***. In the frequency domain, this corresponds to

$$\hat{Q}(\omega) = n_1 \, \hat{u}(x_{ref}) \, e^{i\omega\tau}, \tag{3.12}$$

Additionally, an extended form of the simple $n-\tau$ law, referred to as ***Extended n-τ law*** (Heckl and Kosztin, 2013), can also be employed. Here, the heat release rate

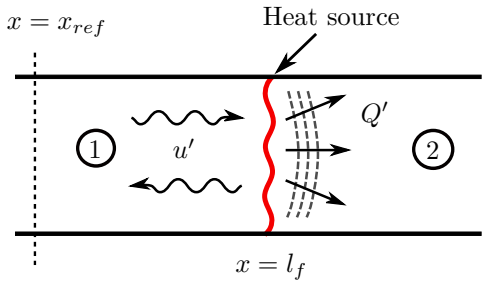

Figure 3.4: Modelling of Q'

fluctuation at the location $x = l_f$ is assumed to depend on both instantaneous ($u'(t)$) and time-lagged acoustic velocity fluctuations ($u'(t-\tau)$). The extended time-lag law in the time domain is given by

$$Q'(t) = \left\{ n_1 \, u'_{ref}(t-\tau) \; - n_0 \, u'_{ref}(t) \right\} , \tag{3.13}$$

where $n_{0,1}$ are the coupling coefficients relating $Q'(t)$ and $u'_{ref}(t)$. In the frequency domain, this relation becomes

$$\hat{Q}(\omega) = \left\{ n_1 \, e^{i\omega\tau} - n_0 \right\} \, \hat{u}(x_{ref}) \, . \tag{3.14}$$

For heat sources like hot gauzes, in unsteady flow, the time-lag models are constructed empirically from experimental data and numerical simulations. These empirical models are usually non-linear and are then linearised to resemble simple time-lag laws. For example, ***King's Law*** (King, 1914),

$$Q'(t) = L_w \, \left(\bar{T}_w - \bar{T} \right) \, \left(\kappa + 2 \sqrt{\pi \kappa C_v \bar{\rho} \, (d/2) \, |u|} \right) , \tag{3.15}$$

relates the heat transfer from the hot wire gauze with the upstream acoustic velocity fluctuations. L_w is the length of the wire, $\bar{T}_w$ is the temperature of the wire, d is he diameter of the wire. $\bar{T}$ is the temperature, κ is the heat conductivity and C_v is the specific heat per unit mass at constant volume of the surrounding fluid. We can convert this non-linear expression into its corresponding simple time-lag law by linearising it. Upon linearisation, we get $Q'(t) = \beta u'_{ref}(t-\tau)$, where $\beta = L_w \, \left(\bar{T}_w - \bar{T} \right) \, \sqrt{(\pi \kappa C_v \bar{\rho}/\bar{u}) \, (d/2)}$. The time-lag between the heat transfer from the hot wire and the velocity is given by $\tau = 0.2 \, d/\bar{u}$, and is present due to thermal inertia. Lighthill (1954) found that this time-lag is applicable for low frequencies ($\omega < 20 \, \bar{u}/d$) and those flow speeds where

boundary layer approximation is valid (Reynolds number > 10). King's Law can be applied to a heat sink if we assume the surrounding temperature $\bar{T}$ to be greater than the wire gauze temperature $\bar{T}_w$. In such a situation, the wire gauze will absorb heat rather than release it.

3.4.2. Transfer Function (TF)

Transfer Functions (TF) portray the response of heat sources or sinks to external perturbations, in the frequency domain. They can be obtained analytically (Schuller et al., 2003), experimentally (Noiray, 2007) and even numerically through simulations (Andreini et al., 2014, Selimefendigil et al., 2012). TF, denoted as $\mathcal{F}(\omega)$ in Eq. (3.16), is a complex quantity in the frequency domain, formed by taking the ratio of non-dimensional heat release rate fluctuations ($\hat{Q}/\bar{Q}$) to non-dimensional acoustic velocity fluctuations ($\hat{u}/\bar{u}$).

$$\frac{\hat{Q}(\omega)}{\bar{Q}} = \mathcal{F}(\omega)\,\frac{\hat{u}(\omega)}{\bar{u}} = G(\omega)\,e^{i\Phi(\omega)}\,\frac{\hat{u}(\omega)}{\bar{u}}, \tag{3.16}$$

where $\hat{Q}(\omega)$ and $\hat{u}(\omega)$ are heat release rate and acoustic velocity fluctuations in the frequency domain respectively, $\bar{Q}$ is the mean heat release rate and $\bar{u}$ is the mean velocity. The magnitude of $\mathcal{F}(\omega)$ is called *gain* ($G(\omega)$) and the argument of $\mathcal{F}(\omega)$ is called *phase* ($\Phi(\omega)$). Gain is a measure of the change in heat release rate caused by a change in the velocity and phase gives the phase difference between Q' and u'. $\mathcal{F}(\omega)$ is a linear response function and depends on the frequency. When we deal with flames and their heat release rate fluctuations, the TF is also called *Flame Transfer Function* (FTF).

TFs are very important in the modelling of thermoacoustic systems and their instability predictions since the information regarding the heat source (or sink) and its response is contained within the TF. In real life applications, it is relatively easy to obtain TFs from experiments or numerical simulations, than formulating time-lag models. The latter require apriori knowledge of the underlying physical processes that affect Q'. However, in some situations, we could construct simple time-lag models from TFs.

As an illustration, consider a hypothetical FTF as shown in Fig. 3.5. The intention is to express the low frequency behaviour of the flame in terms of a simple $n-\tau$ law. From the given FTF, it is evident that the flame behaves like a low pass filter with very high gain in the low frequency region i.e., for those frequencies less than f_b. Here f_b is the limit to which we intend to construct a time-lag model. The $G(\omega)$ appears to be almost a constant in the frequency range of interest, and $\Phi(\omega)$ appears to have a constant slope in this frequency range. Comparing Eqs. (3.12) and (3.16), we can assume $n_1 = \left(\bar{Q}\, G(\omega)/\bar{u}\right)$ and $\tau = \Phi(\omega)/\omega$. Hence, we can argue that linear time-lag laws can be viewed as time domain equivalents of transfer functions, under specific conditions like the one discussed before. However, in reality, the FTFs obtained experimentally or numerically, are not as elementary as the hypothetical one considered, and formulating time-lag models is very cumbersome. This is a topic that is currently being pursued by researchers.

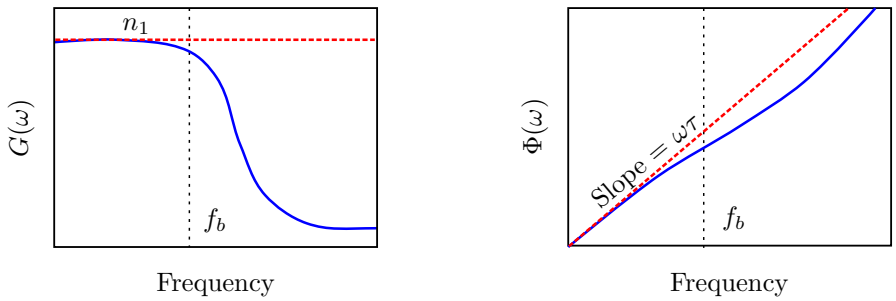

Figure 3.5: $n-\tau$ law from Flame Transfer Function

The concept of time-lag models and transfer functions are not restricted to flames and heat sources alone. They are applicable to heat sinks also. In the latter case, we have heat absorption rate laws instead of heat release rate laws. In our study, we use the transfer function approach to model the heat transfer process occurring at the heat exchanger, which acts as a heat sink.

3.5. Acoustic field across the heat source/sink

Once the heat release/absorption law is formulated, we can now relate the acoustic fields upstream and downstream of the heat source/sink by deriving matching conditions across an infinitesimally thin control volume (Culick, 2006). Consider a control volume of length $2\Delta x$ and cross-sectional area S as shown in Fig. 3.6, with the heat source/sink located at $x = l_f$. The matching conditions for the acoustic pressure and velocity fields across the heat source/sink are derived by integrating the conservation equations over this control volume, in the limit $\Delta\, x \to 0$.

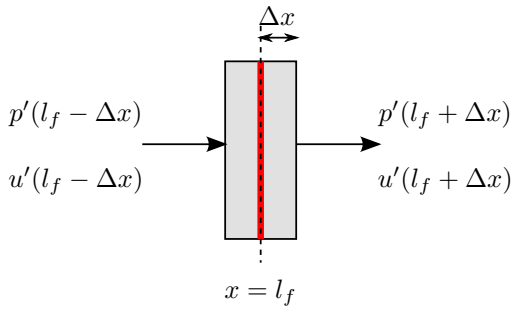

Figure 3.6: Control volume for matching conditions

Integrating the conservation of momentum (Eq. (3.4)) for small $\Delta\, x$ gives

$$\lim_{\Delta\, x \to 0} \int_{l_f - \Delta\, x}^{l_f + \Delta\, x} \left(\bar{\rho}\, \frac{\partial u'}{\partial t} + \frac{\partial p'}{\partial x} \right) dx = 0, \tag{3.17}$$

$$p'|_{l_f + \Delta\, x} = p'|_{l_f - \Delta\, x}\,, \tag{3.18}$$

showing the continuity of the acoustic pressure fluctuations across the control volume. The first term in Eq.(3.17) is a finite quantity whose volume integral in the limit of $\Delta x \to 0$, is zero. In order to integrate the acoustic energy equation, we simplify Eq. (3.7) to

$$\frac{\partial p'}{\partial t} + \bar{p}\, \gamma\, \frac{\partial u'}{\partial x} = (\gamma - 1)\, \bar{\rho}\, q', \tag{3.19}$$

and then apply the procedure aforementioned. This will provide us with the matching condition for the acoustic velocity field across the control volume.

$$\lim_{\Delta x \to 0} \int_{l_f - \Delta x}^{l_f + \Delta x} \left(\frac{\partial p'}{\partial t} + \bar{p}\,\gamma\,\frac{\partial u'}{\partial x} \right) dx = \lim_{\Delta x \to 0} \int_{l_f - \Delta x}^{l_f + \Delta x} \left((\gamma - 1)\,\bar{\rho}\,q' \right) dx, \tag{3.20}$$

$$u'|_{l_f + \Delta x} - u'|_{l_f - \Delta x} = \frac{(\gamma - 1)\,Q'}{\bar{\rho} c^2 S}. \tag{3.21}$$

In Eq.(3.20), the integral of the first term tends to zero, it being a finite quantity. From Eq. (3.21), we can conclude that there is a jump in the acoustic velocity fluctuation across the heat source/sink.

3.6. Conclusions

Thermoacoustic instabilities are caused due to the feedback loop between heat release rate fluctuations Q' and acoustic pressure fluctuations p'. Therefore, it is important to identify and properly model the interaction between Q' and p'. According to Rayleigh criterion, an instability is triggered when the phase difference between p' and Q' favours a net acoustic energy growth in the system, and apart from the direct interaction between p' and Q', there are other secondary mechanisms within the system that can bring about this phase difference. The collective influence of all these factors on the heat source is referred to as its *r*esponse, and is usually manifested in the form of fluctuations in the heat release rate. These responses are modelled using time-lag laws (in time or frequency domains) or transfer functions (in frequency domain). In our work, we model the response of a compact heat source as a time-lag law and the response of a hex as a transfer function, both modelled in the frequency domain.

Chapter 4

Modelling of Heat Exchanger

In this chapter, the thermoacoustic response of the hex is modelled in terms of the two physical processes occuring at hex: (1) the heat transfer across the hex (heat sink), and (2) the acoustic scattering due to the hex tube row. The heat transfer response of the hex, in the form of a transfer function, is evaluated through unsteady numerical simulations, and subsequently modelled as approximate functions in frequency, with the help of curve-fitting techniques. The transfer function is used to obtain the acoustic matching conditions across the hex. The acoustic scattering at the hex is modelled through a quasi-steady approach. The combination of these two physical phenomena at hex gives the total scattering response of the hex. Parametric study conducted on the total scattering response indicates the dependency on incoming mean flow velocity, incident wave frequency, geometry of the tube row and ratio of impedances across the heat sink.

4.1. Introduction

Heat exchangers are widely used in heat generation systems, refrigeration and air conditioning units etc., for effectively transporting the heat generated which in turn helps in cooling these systems. In domestic heating systems like boilers, the hex transfers the

heat produced within the combustion chamber to the coolant being circulated around, and then to radiators. As the hex is placed in a closed setting containing a heat source as mentioned in Chapter 2, there is thermoacoustic interaction occurring at the hex location. This thermoacoustic interaction can be regarded as an overall effect of two physical processes happening at the hex. The first process is the aeroacoustic response of the hex to incoming velocity perturbations, which is modelled as the acoustic scattering by the hex. The second process is the heat transfer response of the hex. In the latter case, we treat the hex as a heat sink and then model the heat transfer response as the interaction between the heat absorption rate fluctuations and incoming velocity fluctuations.

For simplicity and ease of analysis, we treat these two physical processes at the hex as two individual and independent processes, separated by an infinitesimal distance Δx as shown in Fig. 4.1. We also assume that the heat transfer phenomenon precedes the acoustic scattering, and is presumed to occur at $x = l_s$, while the acoustic scattering occurs at $x = L$. Such an assumption is based on the comparison between the thermal and momentum diffusivities of air. For air, the *Prandtl number* or the ratio of momentum diffusivity to thermal diffusivity is less than 1. This means that heat diffuses quicker than momentum (or velocity) and hence the thermal boundary layer will be larger than the velocity boundary layer. Once the individual processes are modelled independent of each other, we can derive the effective or net response of the hex by combining the heat transfer and aeroacoustic responses, similar to network modelling approach, and letting the infinitesimal distance to tend to zero i.e., in the limit $\Delta x \to 0$.

We obtain the heat transfer response of the hex through numerical simulations, and the procedure is detailed in Section 4.2. In Section 4.3, we develop a quasi-steady model to characterise the aeroacoustic response of the hex tube row. This model is then validated with measurements. The mathematical formulation for the net response of the hex is provided in Section 4.4, followed by a parametric analysis in Section 4.5,

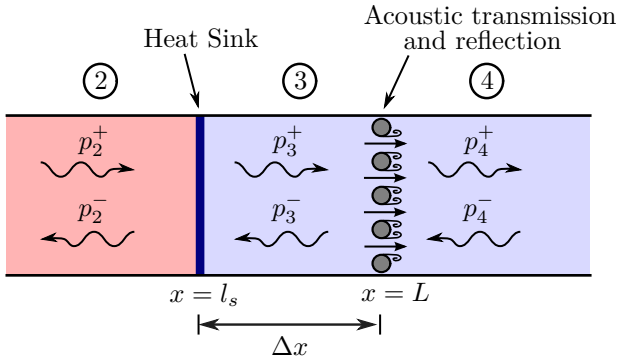

Figure 4.1: Schematic of the heat exchanger acting as both heat sink and acoustic scatterer.

to study the variation of the net acoustic response of the hex to different system parameters.

4.2. Numerical modelling of heat transfer at hex

The heat absorption rate fluctuation at the hex, due to the incoming velocity fluctuation, is obtained using the transfer function approach mentioned in Hosseini et al. (2015). Numerical simulations for the heat absorption or heat transfer response of the hex were conducted using the transient CFD solver ANSYS FLUENT® 15.0. on the geometry shown in Fig. 4.2. Rather than modelling an array of circular tubes, we have limited the computational domain to that of a semi-circular tube and half the gap height, with symmetry boundary conditions on either sides. At the inlet and outlet, '*velocity inlet*' and '*pressure outlet*' boundary conditions were imposed, respectively and on the hex surface, constant temperature with no-slip boundary conditions were imposed. Using the velocity inlet boundary condition, the magnitude, direction and temperature of the incoming flow are prescribed. This boundary condition enables us to impose fluctuations in the magnitude of the incoming velocity. Through the pressure outlet boundary condition, the pressure at the outlet is equated to the atmospheric pressure, indicating that there is no pressure build-up beyond the hex. A 2-D, laminar and incompressible flow was assumed in the computational domain. The hex was maintained at a constant temperature of 340K whereas the incoming flow was at 1500K. Simulations were conducted for diameters 3mm and 5mm, open area ratios (η)

0.1 and 0.2, and inlet velocities 0.5, 1.0 and 1.5m/s. Open area ratio (η) is the ratio of the gap height h_g to the diameter d.

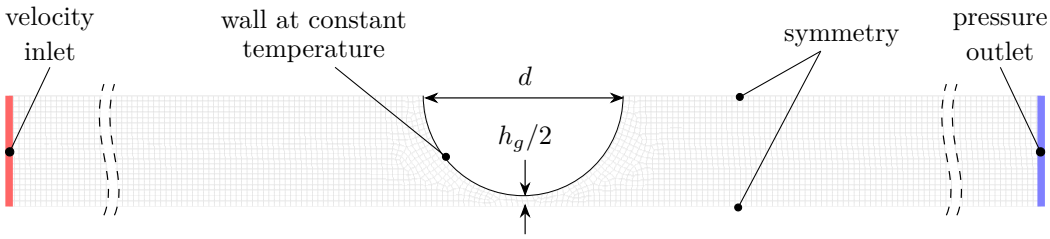

Figure 4.2: Meshed geometry with boundary conditions.

FLUENT® (ANSYS Inc., 2013) solves the mass conservation and momentum conservation equations for all flow problems. When there is heat transfer, an additional conservation equation for energy is also solved. The continuity equation or the mass conservation equation is given by

$$\frac{\partial \rho}{\partial t} + \nabla \cdot (\rho \mathbf{u}) = \mathcal{S}_{\mathbf{m}}. \tag{4.1}$$

This form of the mass conservation equation is valid for both incompressible and compressible flows. Here, $\mathcal{S}_{\mathbf{m}}$ is the mass source term and it denotes the mass added to the continuous phase flow, from any other user-defined sources or from the dispersed second phase like mass added due to vapourisation etc. In our study, $\mathcal{S}_{\mathbf{m}} = 0$ as we do not have any mass sources in our domain.

The momentum conservation equation in an inertial reference frame is given by

$$\frac{\partial}{\partial t}(\rho \mathbf{u}) + \nabla \cdot (\rho \mathbf{u}\mathbf{u}) = -\nabla \mathbf{p} + \nabla \cdot \left(\bar{\bar{\tau}}\right) + \rho \mathbf{g} + \mathbf{F} \tag{4.2}$$

where, $\mathbf{p}$ is the static pressure, $\bar{\bar{\tau}}$ is the stress tensor and $\rho\mathbf{g}$ and $\mathbf{F}$ are the gravitational body force and external body force terms.

The generalised energy conservation equation used in FLUENT® is given by

$$\frac{\partial}{\partial t}(\rho \mathbf{e}) + \nabla \cdot (\mathbf{u}(\rho \mathbf{e} + \mathbf{p})) = \nabla \cdot \left[\underbrace{k_{eff} \nabla T}_{\text{Conduction}} - \underbrace{\sum_j h_j J_j}_{\text{Species Diffusion}} + \underbrace{\left(\bar{\bar{\tau}}_{eff} \cdot \mathbf{u}\right)}_{\text{Viscous Dissipation}} \right] + \mathcal{S}_{\mathbf{h}} \tag{4.3}$$

where $e = h - (p/\rho) + (u^2/2)$ is the total energy per unit mass, $h = \sum_j Y_j\, h_j - (p/\rho)$ is the total enthalpy per unit mass (for incompressible flows), Y_j is the mass fraction of species j, h_j is the enthalpy of the species j, J_j is the diffusion flux of species j and k_{eff} is the effective thermal conductivity.

In our analysis, we use the pressure-based solver along with a laminar viscous model with no viscous heating. Hence the viscous dissipation term in Eq. (4.3) can be discarded. Moreover, we assume no diffusion of species and therefore the species diffusion term is also absent in the conservation equation. The source term $\mathcal{S}_\mathbf{h} = 0$ as we do not have any volumetric heat source in our computational domain. Overall, the FLUENT solver computes for the variables ρ, u, p and T in the computational domain, using the conservation equations for mass, momentum and energy.

4.2.1. Transfer Function approach

For applying the transfer function approach, a step perturbation in the inlet velocity was chosen. The total velocity in the domain after the introduction of the step perturbation will be $u(t) = \bar{u} + u'(t)$, where $\bar{u}$ is the mean velocity at the inlet and $u'(t)$ is the step perturbation. The magnitude of the perturbation was chosen to be very small, as small as $|u'| = 5\%$ of $\bar{u}$. This is to avoid any nonlinearities in the system. The heat transfer occuring at the hex is recorded, and is given by $Q_h(t) = \bar{Q}_h + Q'_h(t)$. Here, $\bar{Q}_h$ is the mean heat absorption rate at the hex and Q'_h is the change in the heat absorption rate due to the velocity perturbation $u'(t)$.

When we apply a constant temperature condition at the hex surface, the heat flux to the wall from the fluid cell is computed as

$$q'_h = h_f\,(T_w - T_f)\,, \tag{4.4}$$

where q'_h is the local heat flux, h_f is the fluid-side local heat transfer coefficient, T_w is the wall temperature, T_f is the local fluid temperature. Q'_h is evaluated by integrating q'_h over the hex surface. The transient simulations give the time response of the hex

in terms of the heat absorbed at the hex. Figure 4.3 shows a sample time response (nondimensionalised) of the hex and the corresponding inlet velocity input (nondimensionalised). To relate the response of the hex to the velocity input, we convert the time data to their corresponding frequency responses through Fourier transformation i.e., $u'(t) \xrightarrow{FT} \hat{u}(\omega)$ and $Q'_h(t) \xrightarrow{FT} \hat{Q}_h(\omega)$. The heat exchanger transfer function (HTF) is then calculated using the equation given below.

$$\text{HTF} = \frac{\hat{Q}_h/\bar{Q}_h}{\hat{u}/\bar{u}} \,. \tag{4.5}$$

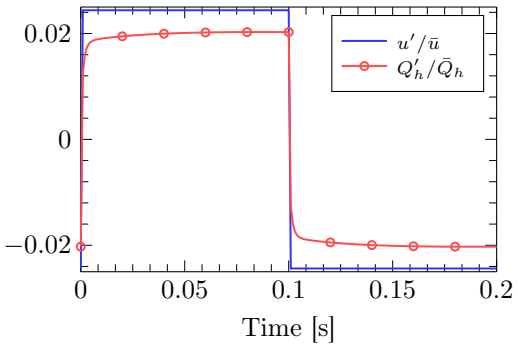

Figure 4.3: Profiles of input velocity perturbation and the resulting heat absorption rate fluctuation.

HTF is a complex quantity with both magnitude |HTF|, and phase Φ(HTF), and it depends on the flow field, geometry and frequency of the incoming perturbation. |HTF| is also referred to as the gain of HTF. Typical gain-phase plots of HTF of a hex are shown in Fig. 4.4 (a) and (b). The hex has diameter d = 3mm and open area ratio $\eta = 0.1$. The incoming velocities are $\bar{u} = 0.5,\ 1.0$ and 1.5 m/s. The gain-phase plots suggest that the hex acts like a low-pass filter i.e., the gain decreases with increasing frequency. The low-pass filter behaviour for a hex was also observed by Strobio Chen et al. (2015). They characterised the thermoacoustic behaviour of hex using fully compressible and weakly compressible numerical schemes in OpenFOAM®. For all values of the $\bar{u}$ considered in this study, it can be observed that the starting values of |HTF| is less than 1, and it decreases with increasing $\bar{u}$. This may be due to the thermal inertia present in the system.

Given the HTF, we can now construct a $\hat{Q} - \hat{u}$ relationship, similar to that of a heat source, from Eq. (4.5) as

$$\hat{Q}_h = \left\{ |\text{HTF}|\, e^{i\Phi(\text{HTF})} \right\} \frac{\hat{u}}{\bar{u}}\, \bar{Q}_h \,. \tag{4.6}$$

Therefore, it is necessary to obtain mathematical expressions for HTF.

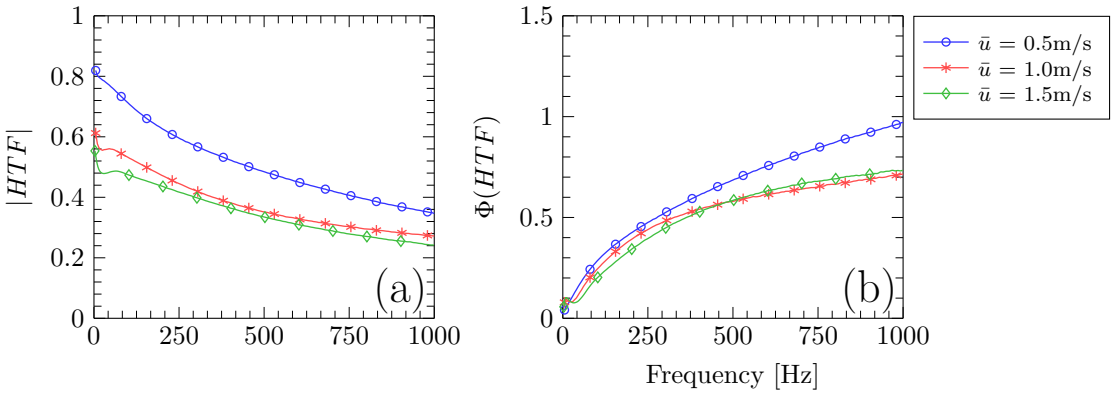

Figure 4.4: (a) |HTF| and (b) Φ(HTF) obtained from numerical simulations, for $d = 3$mm, $h_g = 0.3$mm and different mean velocities, $\bar{u}$.

4.2.2. Approximations to Transfer Functions

The mathematical expressions for the gain and phase of the HTF were obtained by assuming trial functions in the form of polynomials, and determining the coefficients of these trial functions using a constrained least squares approach (Lawson and Hanson, 1995). For the HTF shown in Fig. 4.5, we have assumed the following trial functions.

$$\log\left(|\text{HTF}|\right) = \begin{cases} a_0 + a_1 f + a_2 f^2 + a_3 f^3 & f \le f_p \\ b_0 + b_1 \sqrt{f} & f \ge f_p \end{cases} \tag{4.7}$$

$$\Phi\left(\text{HTF}\right) = \begin{cases} e_0 + e_1 f + e_2 f^2 + e_3 f^3 + e_4 f^4 & f \le f_p \\ g_0 + g_1 \sqrt{f} + g_2 f + g_3 \left(\sqrt{f}\right)^3 + g_4 f^2 & f \ge f_p \end{cases}, \tag{4.8}$$

where a_m, b_m, e_m and g_m are the coefficients to be determined. Constraints are imposed at the first frequency (f_0) and an intermediate frequency (f_p) values. Figures 4.5 (b) and (d) show the approximated |HTF| and Φ(HTF) for the simulated data shown alongside. Here, f_p is 500Hz for the approximation of |HTF| and 200Hz for the approximation of Φ(HTF). The form of the polynomials in Eqs.(4.7) and (4.8) and the

values for f_p were chosen through trial and error. Nevertheless, we can observe that except for a slight deviation in the initial slope of |HTF|, the approximated functions along with the f_p values accurately predict the simulated data. The full set of data for the simulations and their approximations are provided in Appendix B.

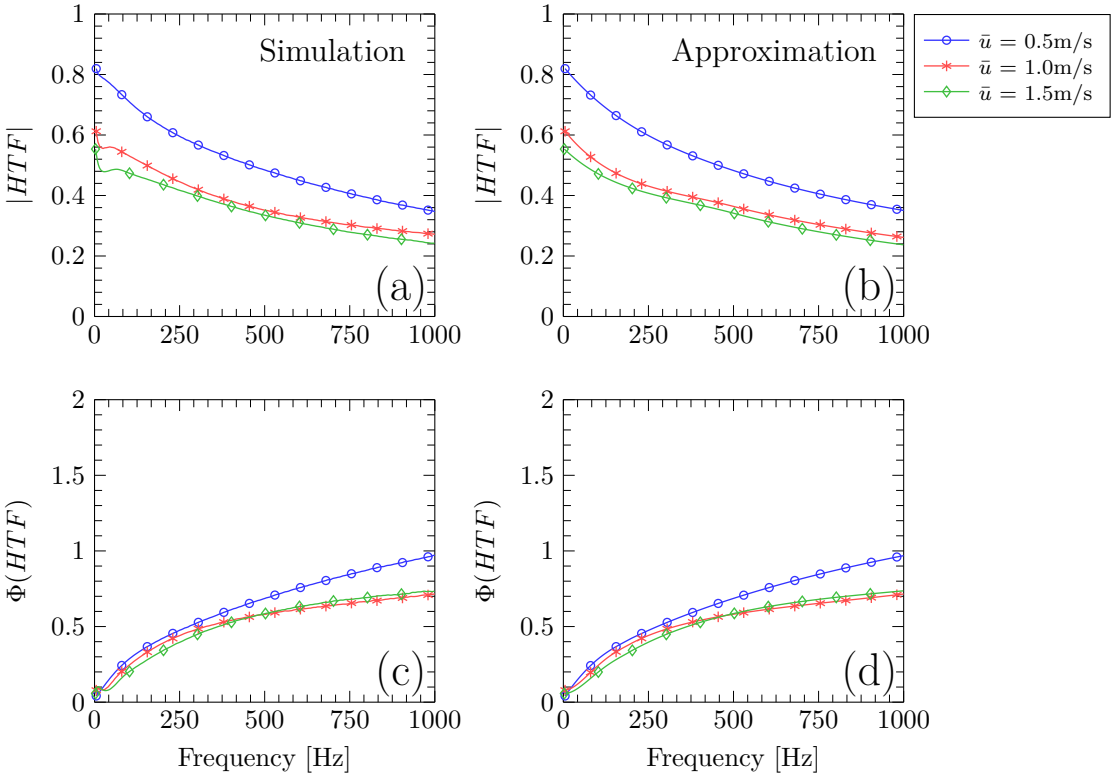

Figure 4.5: Comparison of |HTF| and Φ(HTF) obtained from numerical simulations ((a) and (c)) with their approximations ((b) and (d)), for $d = 3$mm, $h_g = 0.3$mm and different mean velocities, $\bar{u}$.

Substituting Eqs. (4.7) and (4.8) into Eq. (4.6) and taking $\hat{u}$ to be the acoustic velocity fluctuation upstream of $x = l_s$, we obtain,

$$\hat{Q}_h = \left(u_2^+ + u_2^-\right)\left(\bar{Q}_h/\bar{u}_2\right)\left\{|\text{HTF}|\, e^{i\Phi(\text{HTF})}\right\} \tag{4.9}$$

4.3. Theoretical and experimental modelling of acoustic scattering at hex

The acoustic scattering at the hex is modelled using a quasi-steady approach. In a steady flow, there are no temporal variations in the flow properties i.e., there are

no fluctuations about the mean values. In quasi-steady flow, the flow properties vary temporally. However, these variations occur over a large time scale (very low frequency variations) causing the flow to behave like an "*almost steady*" flow. Therefore, at any time instant, we can solve the for the scattering response as if the flow were steady, neglecting the influence of the fluctuations. Quasi-steady modelling was previously utilised by Ronneberger (1967) in studying the effect of subsonic mean flow on the aeroacoustic response of a stepwise expansion in a pipe or a sudden area expansion, and then by Hofmans et al. (2001b, 2003) and Durrieu et al. (2001) in studying the response of a diaphragm or a slit-plate in a pipe. Our geometry is similar to that studied by Hofmans (1998), except that we have an array of tubes.

To proceed with the modelling, we first simplify the geometry of the tube row by approximating it to two half cylinders placed within a duct (Fig. 4.6). The half cylinders are separated by a gap (h_g) and have a bias flow through the gap (u_g). This approximated geometry is widely used in the modelling of sound production and phonation (Vilain et al., 2004). The duct, then represents the wind pipe and the two half cylinders act as vocal chords. A bias flow through the gap between the half cylinders simulate voice production.

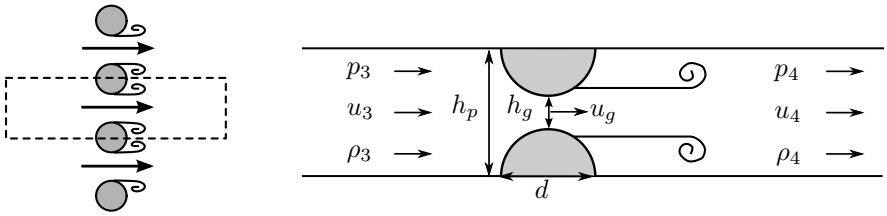

Figure 4.6: Tube row and its approximation

4.3.1. Theoretical modelling

We define the following non-dimensional quantities in order to conduct an order of magnitude analysis and to make some assumptions regarding the applicability of the quasi-steady model.

$$\text{Strouhal number} : St = \frac{f}{(u_g/r)} = \frac{\text{flow time scale}}{\text{acoustic time scale}} \tag{4.10}$$

$$\text{Helmholtz number} : He = \frac{h_p}{(c_3/f)} = \frac{\text{duct height}}{\text{wavelength}} \tag{4.11}$$

$$\text{Mach number} : M_3 = \frac{u_3}{c_3} = \frac{\text{flow speed}}{\text{speed of sound}} \tag{4.12}$$

where f is frequency of the acoustic wave, u_g is the flow velocity through the gap or the bias flow velocity, r is the radius of the cylinder, h_p is the duct height, c_3 is the speed of sound in region *3*, and u_3 is the incoming flow velocity. The assumptions used in the model are

- there is no temperature change across the tube row ($\bar{T}_3 = \bar{T}_4$), and the speed of sound is uniform across the regions *3* and *4* ($c_3 = c_4$),
- Strouhal number is a measure of the relevance of the unsteady effects in the flow. We assume $St \ll 1$ (low frequency), making the quasi-steady modelling a valid approach,
- Helmholtz number, which is a measure of the compactness of the source/sink region, is assumed to be very small i.e., $He \ll 1$. This means that the tube row is very compact compared to the acoustic wavelength, and that there are no phase changes to the acoustic quantities across the source/sink region,
- Mach number is a measure of the importance of the convection effects in the flow domain. In order to maintain a subsonic flow through the gap ($M_g < 1$), we have to restrict our analysis to very low incoming Mach numbers i.e., $M_3 \ll 1$,
- the flow within the duct (Fig. 4.7) is assumed to be inviscid and compressible (unless stated otherwise).
- the amplitude of the fluctuations in the bias flow is very small compared to the mean value. Hence there is no reverse flow through the gaps at any point. The bias flow is always from region *3* to region *4*.

Using these assumptions, we can now derive the expressions for the aeroacoustic response of the geometry with two half cylinders. Throughout this chapter, we refer to the tube row or its approximated geometry as '*sample*'.

Conservation Equations

The flow within the duct (Fig. 4.7) is divided into three regions: (a) *Region 3* – uniform flow upstream of the sample, (b) *Region j* – a compact source/sink region around the sample, where acoustic energy could be produced or dissipated due to vortex shedding, and (c) *Region 4* – uniform flow downstream of the sample. The flow, after passing through the gap (h_g) between the half cylinders, separates from the cylinder surfaces forming a jet. The cross sectional area of this jet is denoted by S_j. The duct cross sectional area is given by S_p.

The flow from upstream region into the jet is assumed to be isentropic and irrotational. Therefore, we can apply the continuity equation, the isentropic gas relation and the energy equation across regions *3* and *j*.

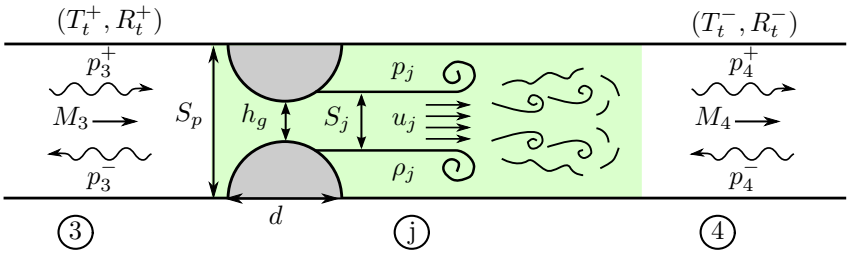

Figure 4.7: Schematic of the flow within the domain.

$$S_p \rho_3 u_3 = S_j \rho_j u_j \,, \tag{4.13}$$

$$\frac{p_3}{p_j} = \left(\frac{\rho_3}{\rho_j}\right)^{\gamma} \,, \tag{4.14}$$

$$\frac{1}{2}u_3^2 + \left(\frac{\gamma}{\gamma-1}\right)\frac{p_3}{\rho_3} = \frac{1}{2}u_j^2 + \left(\frac{\gamma}{\gamma-1}\right)\frac{p_j}{\rho_j} \,, \tag{4.15}$$

where S is the cross sectional area, ρ is the density, u is the velocity, p is the pressure, γ is the ratio of specific heats and the subscripts '3' and 'j' denote the upstream region and jet respectively.

Downstream of the jet, there is a turbulent mixing zone, where the jet kinetic energy is dissipated while some pressure recovery occurs. We have assumed the jet mixing zone to be very small and that all the relevant acoustical processes take place within this mixing zone. However, in reality, this may not always be true. After the mixing zone,

the flow becomes uniform again (*region 4*) and the flow is assumed to be adiabatic (no longer isentropic). We use the continuity and momentum equations to describe this region.

$$S_j \rho_j u_j = S_p \rho_4 u_4 \,, \tag{4.16}$$

$$S_p p_j + S_j \rho_j u_j^2 = S_p p_4 + S_p \rho_4 u_4^2 \,, \tag{4.17}$$

In our analysis, we have neglected the heat transfer, viscous and frictional losses at the walls. So, the conservation of energy in the flow gives

$$\frac{1}{2}u_3^2 + \left(\frac{\gamma}{\gamma-1}\right)\frac{p_3}{\rho_3} = \frac{1}{2}u_4^2 + \left(\frac{\gamma}{\gamma-1}\right)\frac{p_4}{\rho_4} \,. \tag{4.18}$$

However, we do take into account one important viscous flow effect: the flow separation on the cylinder surface. We focus on high Reynolds number flows ($Re > 8000$) and the viscous effects are confined to the thin boundary layers and shear layers. Therefore, the inviscid flow assumption holds throughout the flow. The flow separation location, which is required to evaluate the jet cross sectional area S_j, is found by solving the von Kármán equations using the Thwaites' method. The procedure for finding the separation location is given in Appendix C. This boundary layer method is valid when the boundary layer thickness, $\delta_{bl} \ll h_g$ i.e., $(u_g h_g/\nu)\,(h_g/r) \gg 1$, where ν is the kinematic viscosity. For $u_3 = 5\text{m/s}$, $(u_g h_g/\nu)\,(h_g/r) \approx 4000$. This confirms the validity of the boundary layer model.

Scattering Matrix

In order to account for the wave convection effects, we use total enthalpy as the acoustic variable (Hofmans et al., 2001b, 2003, Motheau et al., 2014), and it is defined as $H_i^{\pm} = p_i^{\pm}\,(1 \pm M_i)\,/\rho_i$. The scattering matrix relates the enthalpy perturbations upstream of the sample to the enthalpy perturbations downstream. The procedure followed in obtaining the scattering matrix is similar to that given in Hofmans (1998). As mentioned previously, the quasi-steady model described here is based on the model by Ronneberger (1967), who also took into account the entropy fluctuations convected by

the mean flow. But, we restrict ourselves to the case with no incoming entropy waves, and hence the entropy effects are not included in the scattering matrix.

To evaluate the scattering matrix, we split Eqs. (4.13) - (4.18) into two sets of equations: a non-linear set for the steady flow and a linearised set for the acoustic perturbations, containing both forward and backward travelling components of the wave. The steady flow equations are solved first and subsequently used in the equations for the acoustic perturbations. The full derivation of the scattering matrix is given in Appendix D. Once we obtain the scattering matrix, we can relate the incoming and outgoing acoustic perturbations, for a case with no incoming entropy as (Hofmans, 1998)

$$\begin{bmatrix}(1+M_4)\,p_4^+\\(1-M_3)\,p_3^-\end{bmatrix} = \begin{bmatrix}T_t^+ & R_t^-\\R_t^+ & T_t^-\end{bmatrix}\begin{bmatrix}(1+M_3)\,p_3^+\\(1-M_4)\,p_4^-\end{bmatrix}, \tag{4.19}$$

where M is the Mach number. p^+ and p^- denote the forward and backward travelling pressure waves, R and T denote the reflection and transmission coefficients of the sample and the superscripts '+' and '–' for R and T denote the upstream and downstream properties respectively. The subscript 't' stands for tube row. The '$\pm$' notation for the coefficients should not be mistaken with those used for the forward and backward travelling waves. The scattering matrix, in this case, is the matrix whose elements are $T_t^{\pm}$ and $R_t^{\pm}$.

To validate the quasi-steady theory against experimental results, we have chosen two samples: (1) *Sample 1* consisting of two half cylinders of diameter $d = 20$mm and separated by a gap height $h_g = 5$mm, and (2) *Sample 2* consisting of an array of tubes of diameter $d = 16$mm and $h_g = 4$mm. The theoretical results for these two samples are shown in Fig. 4.8 (a) and (b) respectively. We observe that the two plots are the same irrespective of the samples chosen. The significance of this result is that a scaling of the geometry is possible in terms of the open area ratio η. Both the samples have equal open area ratios of $\eta_1 = \eta_2 = 0.25$.

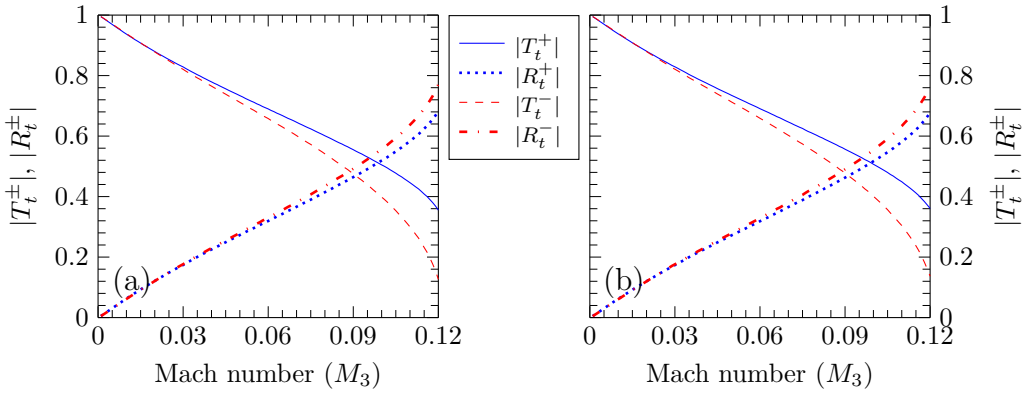

Figure 4.8: Quasi-steady model results for (a) $d = 20$mm, $h_g = 5$mm (*Sample 1*) and (b) $d = 16$mm, $h_g = 4$mm (*Sample 2*)

4.3.2. Experimental validation

The experiments were performed at the Marcus Wallenberg Laboratory for Sound and Vibration Research, KTH Royal Institute of Technology, Stockholm and the experimental setup is shown schematically in Fig. 4.9. It consisted of a long aluminium duct of rectangular cross-section (120mm × 25mm) and thickness 15mm. The samples were placed within the duct, one at a time. Acoustic excitation was provided by two pairs of loudspeakers placed near the upstream and downstream ends of the duct, far from the sample. In order to reduce the acoustic reflections, the duct was connected to an anechoic chamber at the upstream end and to a muffler in the downstream end. The pressure fluctuations were recorded using eight flush mounted microphones (1/4" pre-polarised condenser microphones by G.R.A.S. Type 40BD), four on either side of the sample. The microphones were all calibrated in gain and phase, relative to each other. This was done using a calibrator, where all the microphones were subjected to the same sound field. The flow velocity in the upstream end was measured using a static-pitot tube and a SWEMA3000 pressure transducer. Detailed explanation of the setup and measurement procedure can be found in Zhou (2015) and Peerlings (2015, 2017).

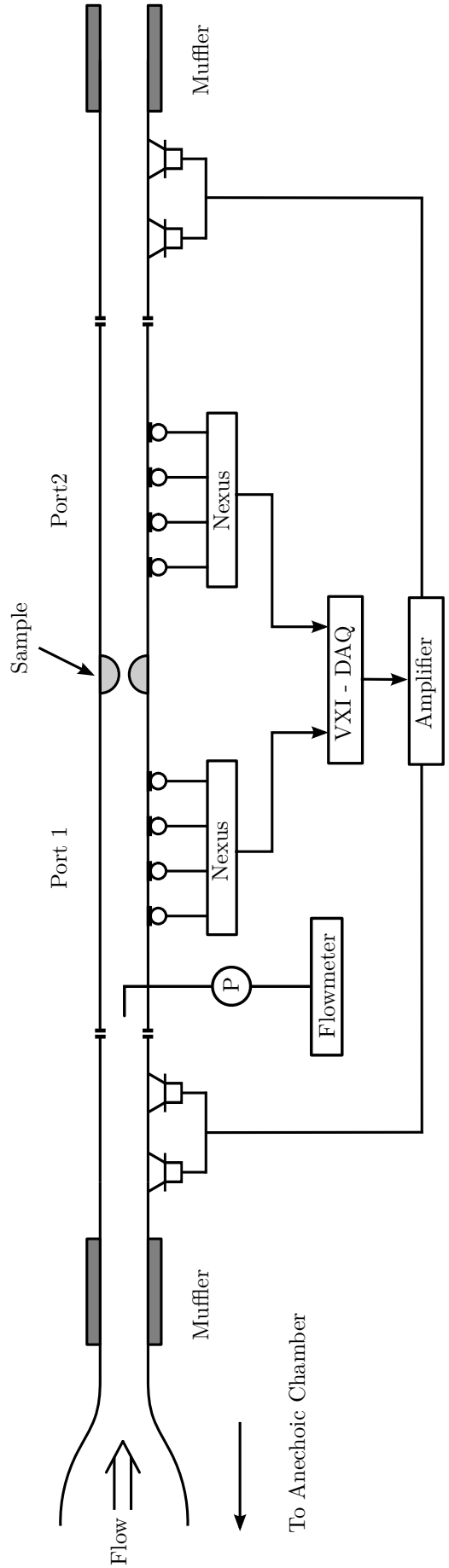

Figure 4.9: Schematic of the experimental setup

A two-port multi-microphone measurement technique (Jang and Ih, 1998, Peerlings, 2015) was used to obtain the pressure data. The acoustic pressure field within the duct can be written as a superposition of forward and backward travelling waves

$$p(x) = p^{+}\exp(ik^{+}x) + p^{-}\exp(-ik^{-}x) \tag{4.20}$$

where $p(x)$ is the measured complex pressure value at x and $p^{\pm}$ are the unknown pressure amplitudes. These unknown quantities are evaluated by measuring the pressure data at at least two positions. In our experiments, the measured data is obtained from four microphones, placed on either side of the sample. Using Eq. (4.20), the upstream and downstream pressure amplitudes can be evaluated as

$$\begin{bmatrix} \exp(ik^{+}x_{1,2}^{1}) & \exp(-ik^{-}x_{1,2}^{1}) \\ \exp(ik^{+}x_{1,2}^{2}) & \exp(-ik^{-}x_{1,2}^{2}) \\ \exp(ik^{+}x_{1,2}^{3}) & \exp(-ik^{-}x_{1,2}^{3}) \\ \exp(ik^{+}x_{1,2}^{4}) & \exp(-ik^{-}x_{1,2}^{4}) \end{bmatrix} \begin{bmatrix} p_{1,2}^{+} \\ p_{1,2}^{-} \end{bmatrix} = \begin{bmatrix} p(x_{1,2}^{1}) \\ p(x_{1,2}^{2}) \\ p(x_{1,2}^{3}) \\ p(x_{1,2}^{4}) \end{bmatrix}, \tag{4.21}$$

where the superscript of x denote the microphone position and the subscripts denote the port i.e., subscript 1 denotes port 1 or the upstream region and subscript 2 denotes port 2 or the downstream region. The overdetermined system in Eq. (4.21) is solved using pseudo-matrix inversion to obtain the unknown pressure amplitudes $p_{1,2}^{+}$ and $p_{1,2}^{-}$.

The scattering matrix, given by

$$\begin{bmatrix} p_2^{+} \\ p_1^{-} \end{bmatrix} = \begin{bmatrix} T_t^{+} & R_t^{-} \\ R_t^{+} & T_t^{-} \end{bmatrix} \begin{bmatrix} p_1^{+} \\ p_2^{-} \end{bmatrix}, \tag{4.22}$$

is determined from the measurements of two independent pressure fields. The independent tests are created by applying an upstream excitation (denoted by A) and a downstream excitation (denoted by B) resulting in the system of equations given in Eq. (4.23), which can be solved to extract the transmission and reflection coefficients.

$$\begin{bmatrix} p_2^{+A} & p_2^{+B} \\ p_1^{-A} & p_1^{-B} \end{bmatrix} = \begin{bmatrix} T_t^{+} & R_t^{-} \\ R_t^{+} & T_t^{-} \end{bmatrix} \begin{bmatrix} p_1^{+A} & p_1^{+B} \\ p_2^{-A} & p_2^{-B} \end{bmatrix} \tag{4.23}$$

Stepped sine excitations in the range 100 –1000 Hz were used in the measurements. We conducted experiments for both the samples and also for the conditions of *with* and *without* flow. The *without* flow experiments were conducted to validate the mea-

surements (and measurement procedure) with the theory devised by Huang and Heckl (1993). These results are provided in Appendix E. The results prove that the Huang and Heckl model, which is developed for an array of tubes, is also applicable to the approximated geometry of two half cylinders.

Next, we conducted experiments for the cases with *flow*. The aeroacoustic responses or the elements of the scattering matrix were measured for seven incoming velocities (u_3) around 5, 7.5, 9.5, 11.5, 13.5, 14.5 and 15.5m/s. Figures 4.10 and 4.11 show the measured $|T_t^{\pm}|$ and $|R_t^{\pm}|$ versus Strouhal number (St) for three velocities, for *Sample 1* and *Sample 2* respectively.

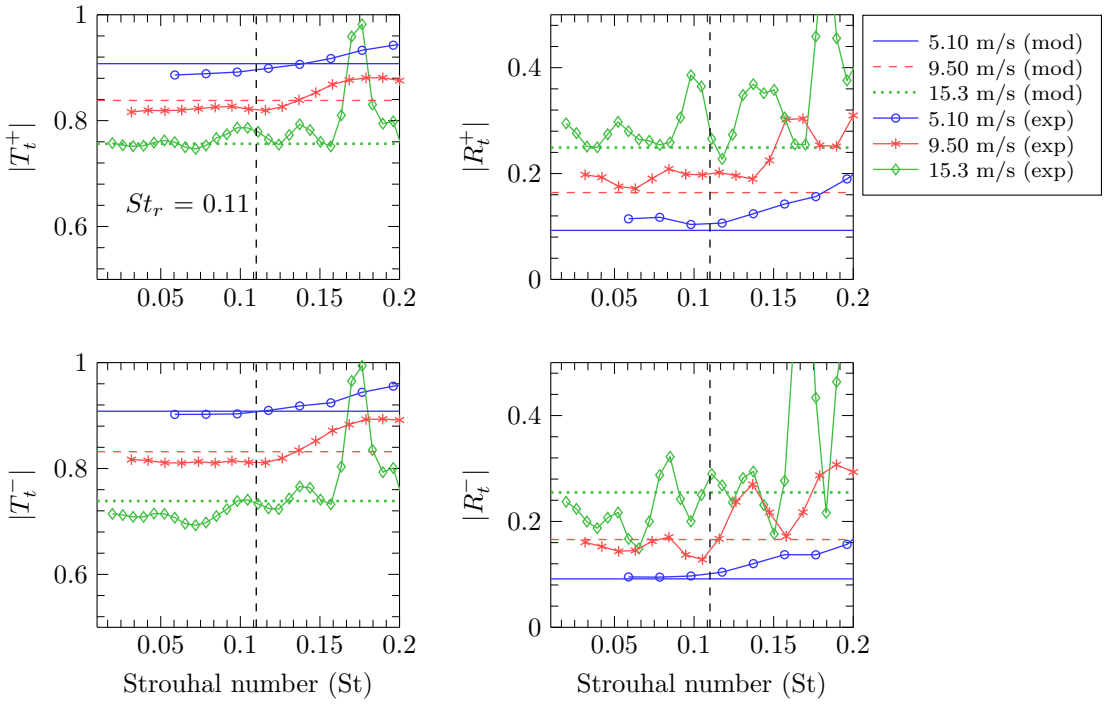

Figure 4.10: Measured and theoretical values for $|T_t^{\pm}|$ and $|R_t^{\pm}|$ vs. Strouhal number for *Sample 1*, and three velocities. The vertical broken line shows the Strouhal number limit till which the quasi-steady model is assumed to be valid.

We observe that the values for $|T_t^{\pm}|$ and $|R_t^{\pm}|$ are close to the theoretical values for low Strouhal numbers. Since neither the St limit to which the validity of the quasi-steady model holds nor the criterion for choosing such a limit are available, we assume (by visual inspection) $St_r = 0.11$ as the limit for *Sample 1* (Fig. 4.10). The Strouhal number used in the plots are based on the radius r of the cylinder i.e., $St_r = f/(u_g/r)$. The St_r limit for *Sample 2* can be obtained either through visual inspection or by scaling the St_r

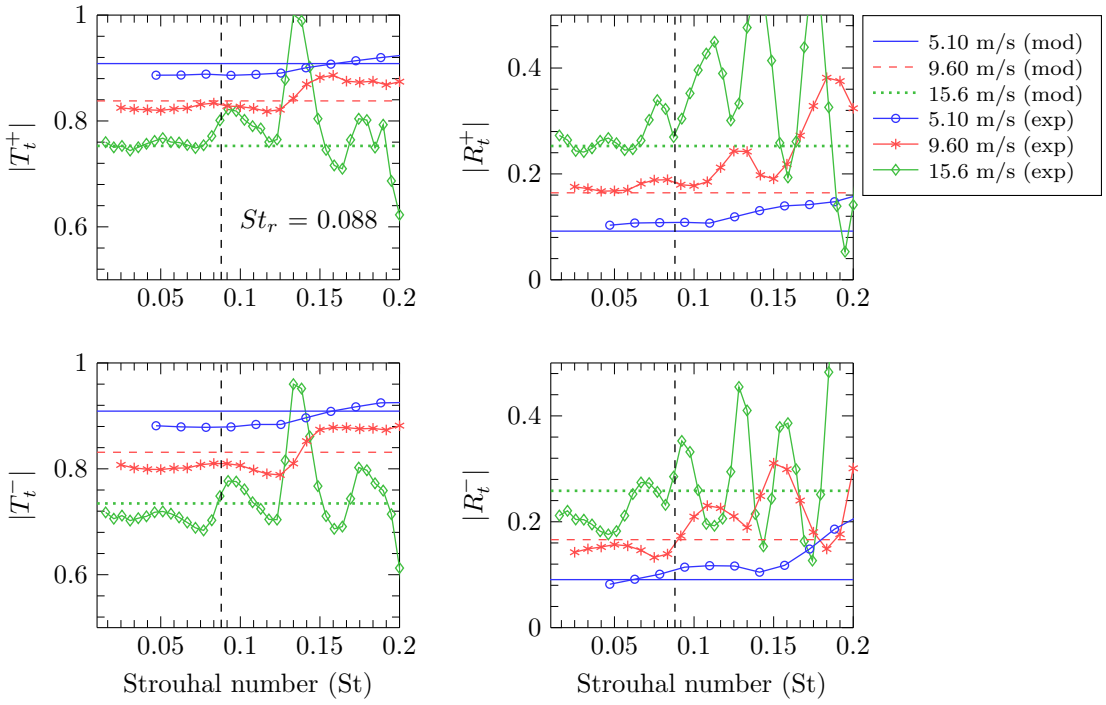

Figure 4.11: Measured and theoretical values for $|T_t^{\pm}|$ and $|R_t^{\pm}|$ vs. Strouhal number for *Sample 2*, and three velocities. The vertical broken line shows the Strouhal number limit till which the quasi-steady model is assumed to be valid.

limit of *Sample 1*. Assuming that for a particular incoming velocity, the frequency range where the quasi-steady model holds is the same for the two samples, we can write the ratio of Strouhal numbers as $St_{8mm}/St_{10mm} = 8/10$. This gives a value of $St_r = 0.088$ for Sample 2, as is also confirmed from visual inspection (Fig. 4.11). In order to have a better comparison with the theoretical results, we take $St_r = 0.11$ for *Sample 1* and $St_r = 0.088$ for *Sample 2*, and average the measurements over the frequency range [100 f_{lim}]Hz, where $f_{lim} = (St_r\ u_g)/r$ and $u_g = (S_p\ u_3)\,/S_g$, for the different values of u_3. The results are shown in Fig. 4.12. The lines —— , $\cdots\cdots$, – – and – · – represent the theory and the markers ($\circ$ and $\diamond$) represent the averaged values from measurements. The measurements show good agreement with theory, and we can conclude that the quasi-steady approach is adequate to describe the low-frequency and low-Mach number aeroacoustic response of an array of tubes as well as the approximated geometry.[1]

[1]The Huang and Heckl model is for $M_3 = 0$, whereas the quasi-steady model is valid for *low Mach numbers* and *low frequencies*. When comparing the two models, it can be noted that they are consistent i.e., for the case when $f = 0$ and $M_3 = 0$, $|T_t^{\pm}| \to 1$ and $|R_t^{\pm}| \to 0$, for both the models.

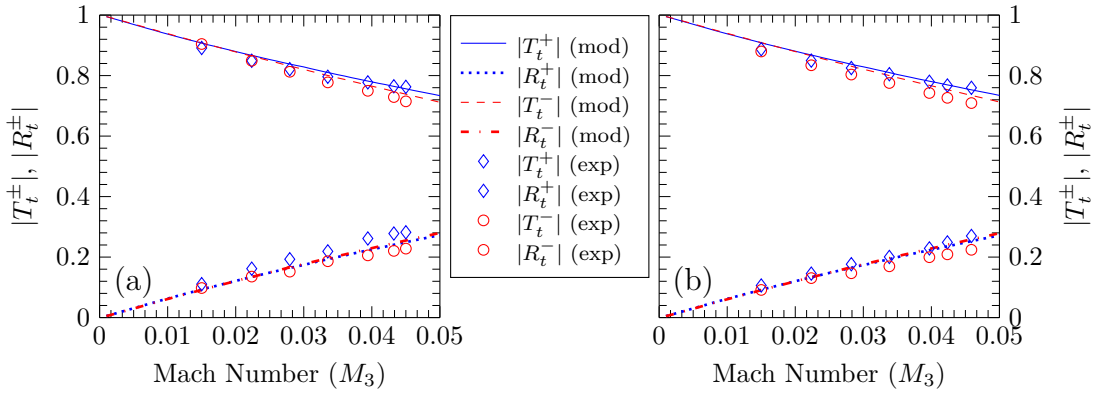

Figure 4.12: Measurements for (a) $d = 20$mm, $h_g = 5$mm (Sample 1) and (b) $d = 16$mm, $h_g = 4$mm (Sample 2)

4.3.3. Reasons for discrepancy between theoretical and measured results

The measured data deviates slightly from the theoretical values for those low Strouhal numbers that are less than the limit mentioned in the previous section. Some of the factors that can cause these deviations are as follows

(1) We observed that the incoming velocity was not constant throughout the experiments. This can alter the measured results and cause it to deviate from the theoretical values.

(2) The aeroacoustic response of the geometry considered is very sensitive to the changes in the gap height h_g. This is because the changes in the gap height indirectly affects the jet cross sectional area and the flow through the gaps. If the gap height is uneven in the transverse direction (perpendicular to the flow), we get data that are significantly different from the theoretical values.

(3) In the theoretical computations, we have assumed the flow to separate from a fixed location on the cylinder surface. In reality, due to the unsteady incoming velocity, this is not always true in the case of measured data. The variations in the flow separation location can cause the measured values to deviate from theoretical predictions.

(4) The large deviations in the measured data for $|R_t^-|$ (when compared to theory), may be due to the highly unsteady turbulent flow downstream of the sample.

(5) We have not accounted for the *wall effects* in our quasi-steady model.

For Strouhal numbers greater than the limit, the measurements deviate significantly from the theoretical predictions i.e., the measurements are much higher than the theoretical values. This can be because of the possibility that at high frequencies, our assumption of the mixing zone being shorter than the acoustic wavelength, may not be valid. However, when we look at measured data with respect to the frequency, rather than the St_r, we can observe that by increasing the incoming velocities from 5.1m/s to 15.5m/s, we can actually extend the limit of validity of the quasi-steady model from close to 300Hz to around 1000Hz (Fig. 4.13 and 4.14). These frequency limit values can be calculated from the Strouhal number limits aforementioned.

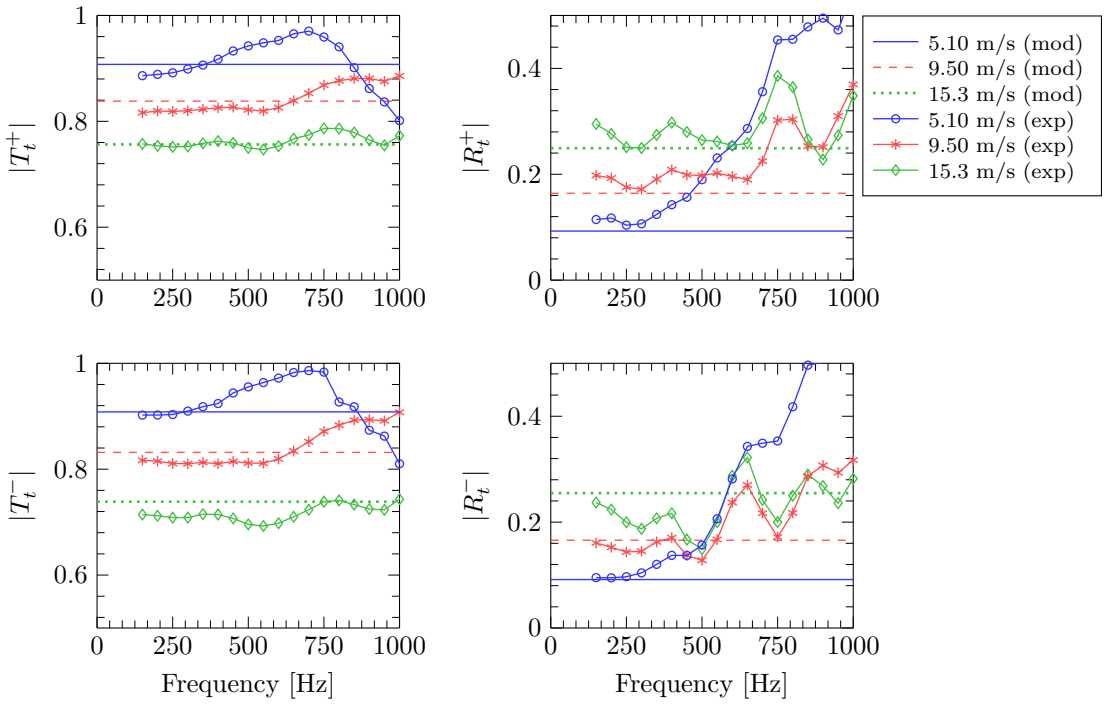

Figure 4.13: Measured and theoretical values for $|T_t^{\pm}|$ and $|R_t^{\pm}|$ vs. frequency for *Sample 1*, and three velocities

4.4. Total scattering matrix of hex

The total scattering matrix, $[\mathrm{SM}]_{hex}$, of the heat exchanger is obtained by using a network modelling approach. In this approach, the physical processes of heat transfer and acoustic scattering, occurring at the hex are treated as independent phenomena, sepa-

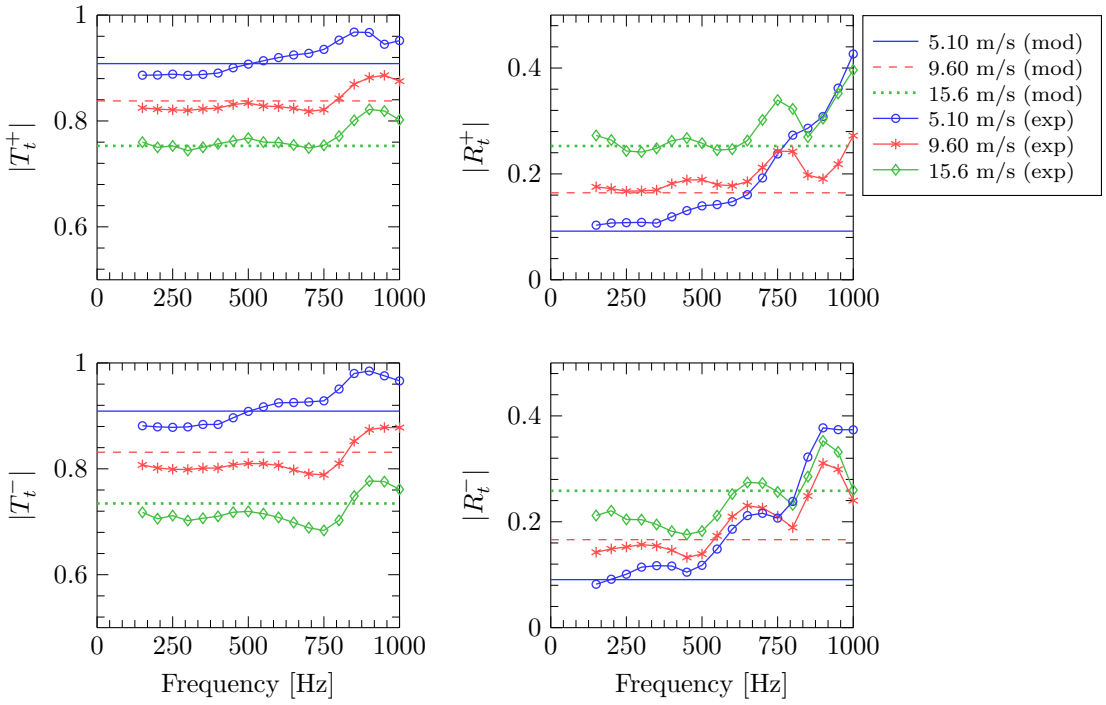

Figure 4.14: Measured and theoretical values for $|T_t^{\pm}|$ and $|R_t^{\pm}|$ vs. frequency for *Sample 2*, and three velocities

rated by an infinitesimally small distance Δx, as shown in Fig. 4.15. Each phenomenon is modelled as a frequency response, in the form of a two-input-two-output system that maps the outgoing acoustic pressure waves to the incoming acoustic pressure waves. This mapping is represented by the corresponding scattering matrix [SM]. Therefore, the total scattering matrix of the hex can be written as

$$\begin{bmatrix} p_4^+ \\ p_2^- \end{bmatrix} = \underbrace{\begin{bmatrix} T_{u\to d} & R_d \\ R_u & T_{d\to u} \end{bmatrix}}_{[\mathrm{SM}]_{hex}} \begin{bmatrix} p_2^+ \\ p_4^- \end{bmatrix} , \tag{4.24}$$

and the scattering matrices of the individual processes as

$$\begin{bmatrix} f_{2d} \\ p_2^- \end{bmatrix} = \underbrace{\begin{bmatrix} T_h^+ & R_h^- \\ R_h^+ & T_h^- \end{bmatrix}}_{[\mathrm{SM}]_{hs}} \begin{bmatrix} p_2^+ \\ g_{2d} \end{bmatrix} \tag{4.25}$$

for the heat sink, and

$$\begin{bmatrix} p_4^+ \\ g_{4u} \end{bmatrix} = \underbrace{\begin{bmatrix} T_t^+ & R_t^- \\ R_t^+ & T_t^- \end{bmatrix}}_{[\mathrm{SM}]_{tr}} \begin{bmatrix} f_{4u} \\ p_4^- \end{bmatrix} \tag{4.26}$$

for the tube row. Here f_{2d} and f_{4u} are the forward travelling waves downstream of heat sink and upstream of tube row respectively. Similarly, g_{2d} and g_{4u} are the backward travelling waves downstream of heat sink and upstream of tube row respectively.

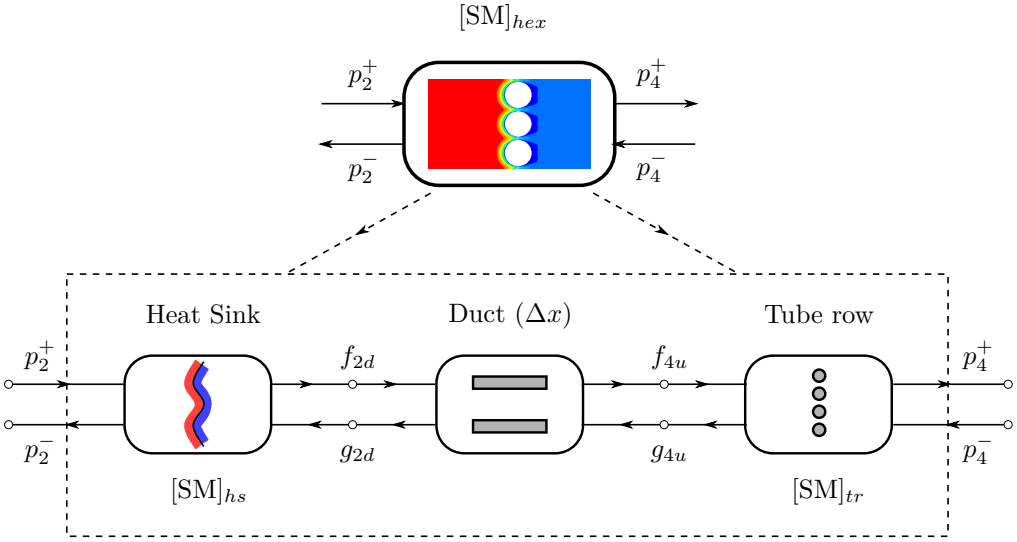

Figure 4.15: Schematic of the network modelling approach used on hex

The scattering matrix of the heat sink, $[\mathrm{SM}]_{hs}$, is obtained by matching the acoustic fields across the heat sink (Eqs. (3.18) and (3.21)) i.e.,

$$p_2^+ + p_2^- = f_{2d} + g_{2d} \qquad \text{(pressure continuity)} \tag{4.27}$$

$$\frac{1}{\rho_3 c_3}\left[f_{2d} - g_{2d}\right] - \frac{1}{\rho_2 c_2}\left[p_2^+ - p_2^-\right] = \frac{(\gamma-1)}{\rho_2 c_2^2 S}\hat{Q}_h \qquad \text{(velocity jump).} \tag{4.28}$$

Substituting Eq. (4.9) in Eq. (4.28), we obtain the velocity jump condition in terms of the approximated HTF as

$$f_{2d} - g_{2d} = \zeta_{32}\,(1+\alpha)\left[p_2^+ - p_2^-\right] \tag{4.29}$$

where

$$\zeta_{32} = \frac{\rho_3 c_3}{\rho_2 c_2} \qquad \text{and} \qquad \alpha = \frac{(\gamma-1)\,\bar{Q}_h\,\left\{|\mathrm{HTF}|\,e^{i\Phi(\mathrm{HTF})}\right\}}{(\rho_2 c_2^2 S)\,\bar{u}_2}. \tag{4.30, 4.31}$$

In our work, we name α as the *heat sink coefficient*. ζ_{32} is the ratio of impedances across the heat sink. $\zeta_{32} = 1$ for $\bar{T}_2 = \bar{T}_3$ and $\zeta_{32} > 1$ for $\bar{T}_2 > \bar{T}_3$. After some algebraic

manipulations involving Eqs. (4.27) - (4.31), we can derive the elements of $[\mathrm{SM}]_{hs}$ as

$$T_h^+ = \frac{2\,\zeta_{32}(1+\alpha)}{1+\zeta_{32}(1+\alpha)}; \qquad R_h^+ = \frac{\zeta_{32}(1+\alpha)-1}{1+\zeta_{32}(1+\alpha)}; \tag{4.32a, 4.32b}$$

$$T_h^- = \frac{2}{1+\zeta_{32}(1+\alpha)}; \qquad R_h^- = \frac{1-\zeta_{32}(1+\alpha)}{1+\zeta_{32}(1+\alpha)}; \tag{4.32c, 4.32d}$$

The scattering matrix of the tube row, $[\mathrm{SM}]_{tr}$, is found from the quasi-steady model (Eq. (4.19) and Appendix D) discussed in Section 4.3. The pressure field within the duct of length Δx is given by

$$f_{4u} = f_{2d} e^{(ik_3\Delta x)} \tag{4.33a}$$

$$g_{4u} = g_{2d} e^{(-ik_3\Delta x)} \tag{4.33b}$$

From Eqs. (4.25), (4.26) and (4.33), we can evaluate the elements of the total scattering matrix of the hex as (Strobio Chen et al., 2016)

$$T_{u\to d} = \frac{T_h^+\,T_t^+\,e^{(ik_3\Delta x)}}{1-R_h^-\,R_t^+\,e^{(2ik_3\Delta x)}}; \qquad R_u = R_h^+ + \frac{T_h^+\,T_h^-\,R_t^+\,e^{(2ik_3\Delta x)}}{1-R_h^-\,R_t^+\,e^{(2ik_3\Delta x)}}; \tag{4.34a, 4.34b}$$

$$T_{d\to u} = \frac{T_h^-\,T_t^-e^{(ik_3\Delta x)}}{1-R_h^-\,R_t^+\,e^{(2ik_3\Delta x)}}; \qquad R_d = R_t^- + \frac{T_t^+\,T_t^-\,e^{(2ik_3\Delta x)}}{1-R_h^-\,R_t^+\,e^{(2ik_3\Delta x)}}. \tag{4.34c, 4.34d}$$

In the limit $\Delta x \to 0$, the elements of the scattering matrix reduce to

$$T_{u\to d} = \frac{T_h^+\,T_t^+}{1-R_h^-\,R_t^+} = \frac{2\,\zeta_{32}(1+\alpha)\,T_t^+}{\left(1-R_t^+\right)+\zeta_{32}(1+\alpha)\left(1+R_t^+\right)} \tag{4.35a}$$

$$R_u = R_h^+ + \frac{T_h^+\,T_h^-\,R_t^+}{1-R_h^-\,R_t^+} = \frac{\left(R_t^+-1\right)+\zeta_{32}(1+\alpha)\left(1+R_t^+\right)}{\left(1-R_t^+\right)+\zeta_{32}(1+\alpha)\left(1+R_t^+\right)} \tag{4.35b}$$

$$T_{d\to u} = \frac{T_h^-\,T_t^-}{1-R_h^-\,R_t^+} = \frac{2\,T_t^-}{\left(1-R_t^+\right)+\zeta_{32}(1+\alpha)\left(1+R_t^+\right)} \tag{4.35c}$$

$$R_d = R_t^- + \frac{T_t^+\,T_t^-}{1-R_h^-\,R_t^+} = R_t^- + \frac{T_t^+\,T_t^-\,\left[1-\zeta_{32}(1+\alpha)\right]}{\left(1-R_t^+\right)+\zeta_{32}(1+\alpha)\left(1+R_t^+\right)} \tag{4.35d}$$

4.5. Acoustic properties of hex

From Eq. (4.35), we can infer that the total scattering property of the hex depends on

- α, which is influenced by the frequency of the incoming wave (f), the incoming velocity ($\bar{u}_2$) and the temperature jump across the hex ($\bar{T}_2 - \bar{T}_3$);
- $[\mathrm{SM}]_{tr}$, which is influenced by the hex tube diameter (d), open area ratio (η), the velocity in *Region 3* ($\bar{u}_3$); and
- ζ_{32}, which is a measure of the temperature jump across the hex.

Unfortunately, due to the limited data available for α, ζ_{32} and HTF from numerical simulations, it is not a straightforward task to study the influence of the above mentioned parameters on $[\mathrm{SM}]_{hex}$. So we study the effect of each of these parameters separately and attempt to draw simplifying assumptions about their influences.

4.5.1. Influence of heat sink coefficient (α)

To study the influence of α on $[\mathrm{SM}]_{hex}$, we plot the elements of the scattering matrix for the three velocities, by first assuming $\alpha = 0$ and then comparing it with the results obtained from numerical simulations, after considering non-zero α. These results are plotted in the Fig. 4.16. The solid markers are obtained from numerical simulations with $\alpha \neq 0$ and the curves are evaluated for $\alpha = 0$.

The results plotted show that the influence of α on the scattering elements is negligible. Therefore, for the purpose of parametric analysis, α can be neglected, leading to the simplification of Eq. (4.35) to

$$T_{u\to d} = \frac{2\,\zeta_{32}\,T_t^+}{\left(1 - R_t^+\right) + \zeta_{32}\left(1 + R_t^+\right)}, \tag{4.36a}$$

$$R_u = \frac{\left(R_t^+ - 1\right) + \zeta_{32}\left(1 + R_t^+\right)}{\left(1 - R_t^+\right) + \zeta_{32}\left(1 + R_t^+\right)}, \tag{4.36b}$$

$$T_{d\to u} = \frac{2\,T_t^-}{\left(1 - R_t^+\right) + \zeta_{32}\left(1 + R_t^+\right)}, \tag{4.36c}$$

$$R_d = R_t^- + \frac{T_t^+\,T_t^-\,\left(1 - \zeta_{32}\right)}{\left(1 - R_t^+\right) + \zeta_{32}\left(1 + R_t^+\right)}. \tag{4.36d}$$

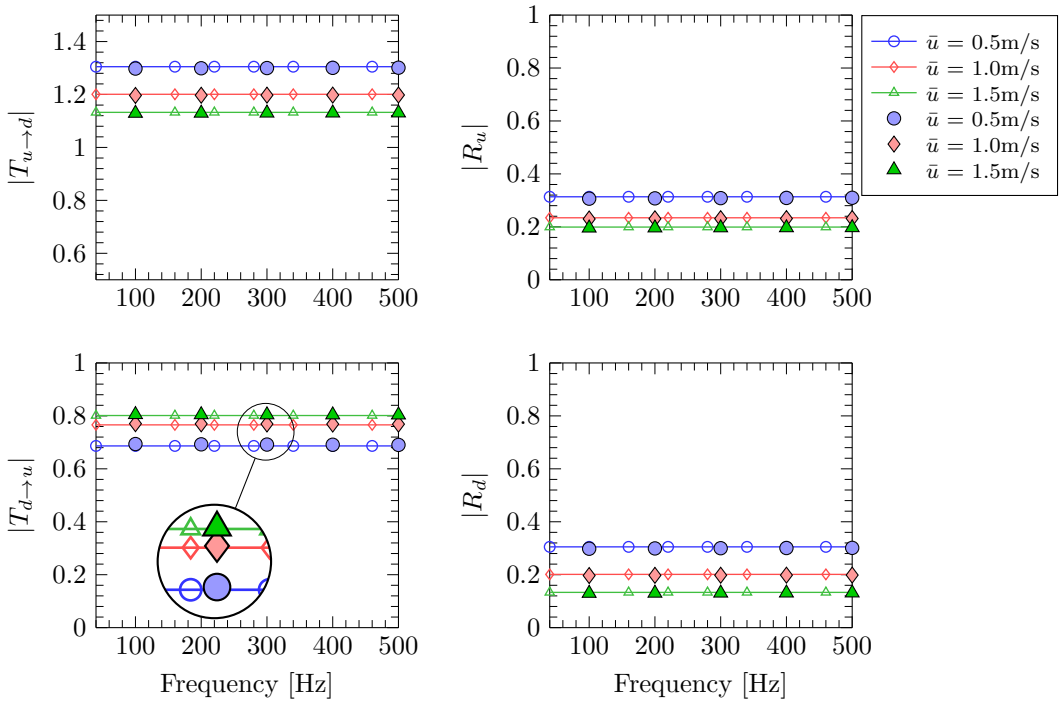

Figure 4.16: Variation of the elements of $[\mathrm{SM}]_{hex}$ as a function of frequency (f), for fixed velocities $\bar{u}$ (or $\bar{u}_2$), d = 3mm and η = 0.1. Solid markers indicate the results obtained by including α and curves indicate the results obtained by using $\alpha = 0$.

4.5.2. Influence of impedance ratio (ζ_{32})

The influence of ζ_{32} on the scattering properties of the hex is as shown in Fig. 4.17. The curves and markers are calculated for hex of d = 3mm, η = 0.1, f = 100Hz and $\bar{u}$ = 0.5, 1.0 and 1.5m/s. The solid markers indicate results from numerical simulations and the curves indicate those results when $\alpha = 0$ (Eq. (4.36)). As mentioned in the previous section, the value of the scattering matrix do not vary drastically due to the omission of α.

In the limit of $\alpha \to 0$, the acoustic matching conditions across the heat sink reduce to that of pressure continuity. Hence, the heat sink can be treated as an interface between the hot medium in *Region 2* and the cold medium in *Region 3*. There is a sudden change in the impedance across the heat sink which causes increasing values (> 1) for $|T_{u\to d}|$ as ζ_{32} is increased. Also, R_d becomes increasingly negative as ζ_{32} is increased, and this causes the trend reversal in $|R_d|$ compared to $|R_u|$. When $\bar{T}_2 = \bar{T}_3 =$

1500K, $\zeta_{32} = 1$ and the results for the scattering matrix coincide with the quasi-steady results obtained for this configuration.

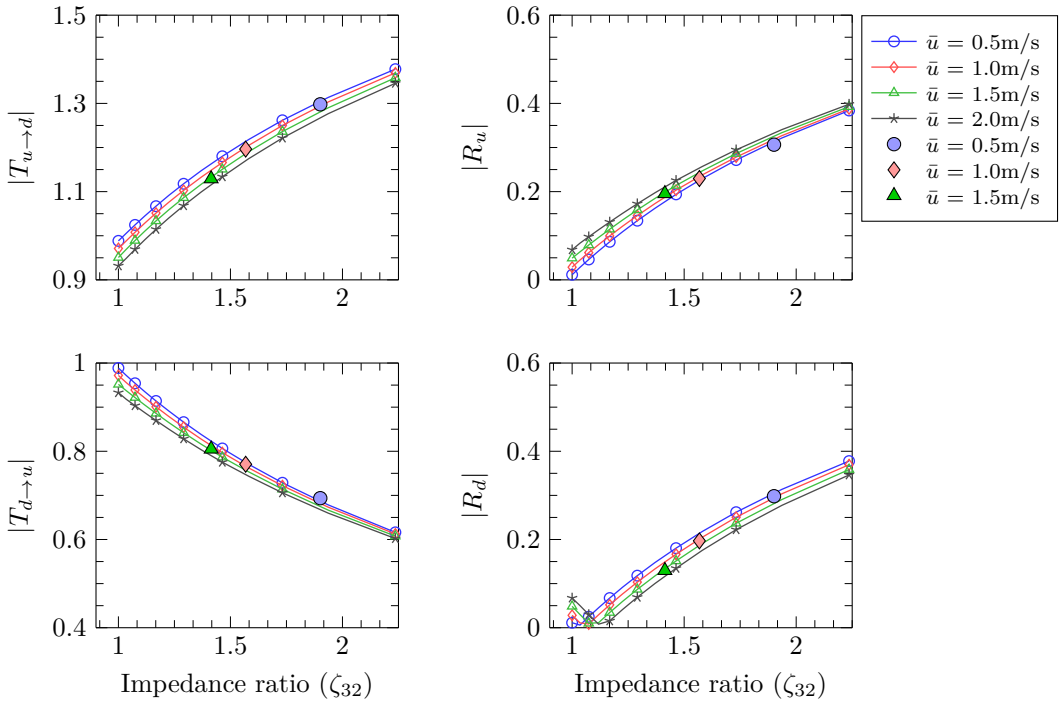

Figure 4.17: Variation of the elements of $[\mathrm{SM}]_{hex}$ as a function of ζ_{32}, for fixed velocities $\bar{u}$ (or $\bar{u}_2$), $f = 100$Hz, $d = 3$mm and $\eta = 0.1$. Solid markers indicate the results obtained by including α and curves indicate the results obtained by using $\alpha = 0$.

From numerical simulations, it is evident that $\bar{T}_3$, and subsequently ζ_{32}, vary with the incoming velocity $\bar{u}_2$ (or $\bar{u}$), for a given geometry of tube row (d and η) (Fig. 4.17). The $\bar{T}_3$ and the corresponding ζ_{32} values obtained from the numerical simulations, for $d = 3$mm, $\eta = 0.1$ and $\bar{T}_2 = 1500$K are shown in Table 4.1.

Table 4.1: $\bar{T}_3$ and ζ_{32} for $d = 3$mm and $\eta = 0.1$, evaluated from numerical simulations

$\bar{u}_2$ [m/s]	$\bar{T}_3$ [K]	ζ_{32}
0.5	415	1.899
1.0	610	1.567
1.5	750	1.412

However, due to insufficient data from the numerical simulations to correlate the variation of ζ_{32} with the variation in $\bar{u}_2$, we do not delve into the coupling between $\bar{u}_2$ and ζ_{32}. Instead, for the purpose of parametric analysis, we assume a constant tem-

perature of $\bar{T}_3 = 400$K ($\zeta_{32} = 1.936$) across the hex. Therefore, the set of assumptions used in the parametric analysis are

- The influence of α is ignored i.e., $\alpha = 0$
- The variation of ζ_{32} with respect to $\bar{u}_2$ is ignored for the purpose of parametric analysis
- The values of $\bar{T}_3$ and ζ_{32} used in the parametric analysis are 400K and 1.936, respectively

4.5.3. Influence of frequency (f)

Since α is neglected, it is expected that $[\mathrm{SM}]_{hex}$ will not exhibit an explicit dependence on frequency, at least in the frequency range where quasi-steady model holds. This is observed in Fig. 4.18, where the curves denote the results obtained using Eq. (4.36). The curves are calculated for hex of $d = 3$mm, $\eta = 0.1$, $\bar{T}_2 = 1500K$, $\bar{T}_3 = 400K$, $\zeta_{32} = 1.936$ and $\bar{u}_2 = 0.5$, 1.0, 1.5 and 2.0m/s. The magnitudes of the continuous curves remain as constants for the frequency range considered, indicating a quasi-steady response. $|T_{u\to d}|$ and $|T_{d\to u}|$ decrease with increasing $\bar{u}$, while $|R_u|$ increases with increasing $\bar{u}$. Again, these observations are in accordance with the quasi-steady results (Fig. 4.8). However, $|R_d|$ behaves in a manner contrary to the quasi-steady results. It shows a decreasing trend with increasing $\bar{u}$. Also, $|T_{u\to d}| > 1$. The latter observations are caused by the temperature jump across the heat sink as discussed in Section 4.5.2.

Similar results were obtained by Strobio Chen et al. (2016), where the scattering matrix of the hex was evaluated numerically using OpenFOAM®. The transmission and reflection coefficients were evaluated for the acoustic velocity, and this resulted in $|T_{u\to d}|$ being less than 1 and $|T_{d\to u}|$ being greater than 1.

4.5.4. Influence of mean flow velocity ($\bar{u}_2$)

The influence of the mean flow velocity on $[\mathrm{SM}]_{hex}$ is plotted in Fig. 4.19. The curves are calculated for hex of $d = 3$mm, $\eta = 0.1$, $\bar{T}_2 = 1500K$, $\bar{T}_3 = 400K$, $\zeta_{32} = 1.936$ and

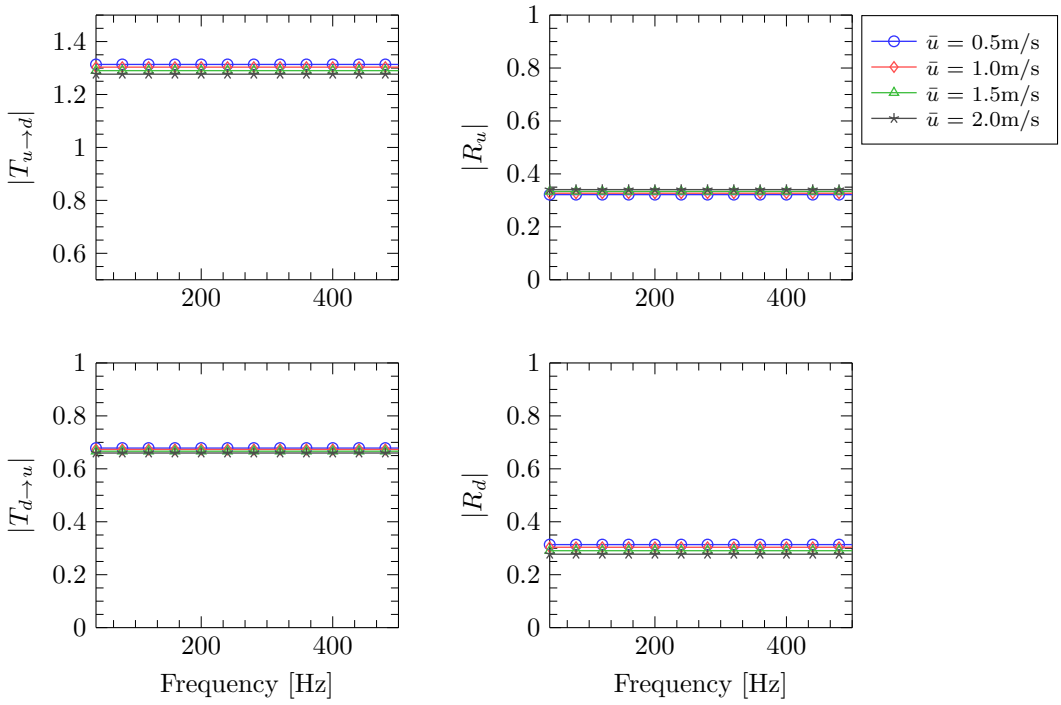

Figure 4.18: Variation of the elements of $[\mathrm{SM}]_{hex}$ as a function of frequency (f), for fixed velocities $\bar{u}$ (or $\bar{u}_2$), d = 3mm, $\eta = 0.1$ and $\zeta_{32} = 1.936$ when $\bar{T}_3$ = 400K. The curves are obtained using Eq. (4.36).

f = 100, 200, 300 and 400Hz. The quasi-steady nature of the scattering behaviour is very much evident in the plots, as the results for the different frequencies considered, all collapse onto one another. The observations are the same as those mentioned in the previous sections. $|T_{u\to d}|$, $|T_{d\to u}|$ and $|R_u|$ all behave in accordance to the trends shown in the quasi-steady results, whereas $|R_d|$ exhibits an opposite trend which can be attributed to the temperature jump due to the heat sink.

4.5.5. Influence of open area ratio (η)

The open area ratio $\eta = h_g/d$ is a measure for the transparency of the hex. For a fixed hex diameter and for small values of η, there is less transmission and more reflection across the hex. For large values of η, again for a fixed hex diameter, the hex tube row becomes increasingly acoustically transparent ($|T_t^{\pm}| \to 1$ and $|R_t^{\pm}| \to 0$) and the behaviour of the scattering matrix tends to that of a case where there is only a heat sink i.e., $|T_{u\to d}| \to 1.32$, $|T_{d\to u}| \to 0.68$, $|R_u| \to 0.32$ and $|R_d| \to 0.32$. This behaviour

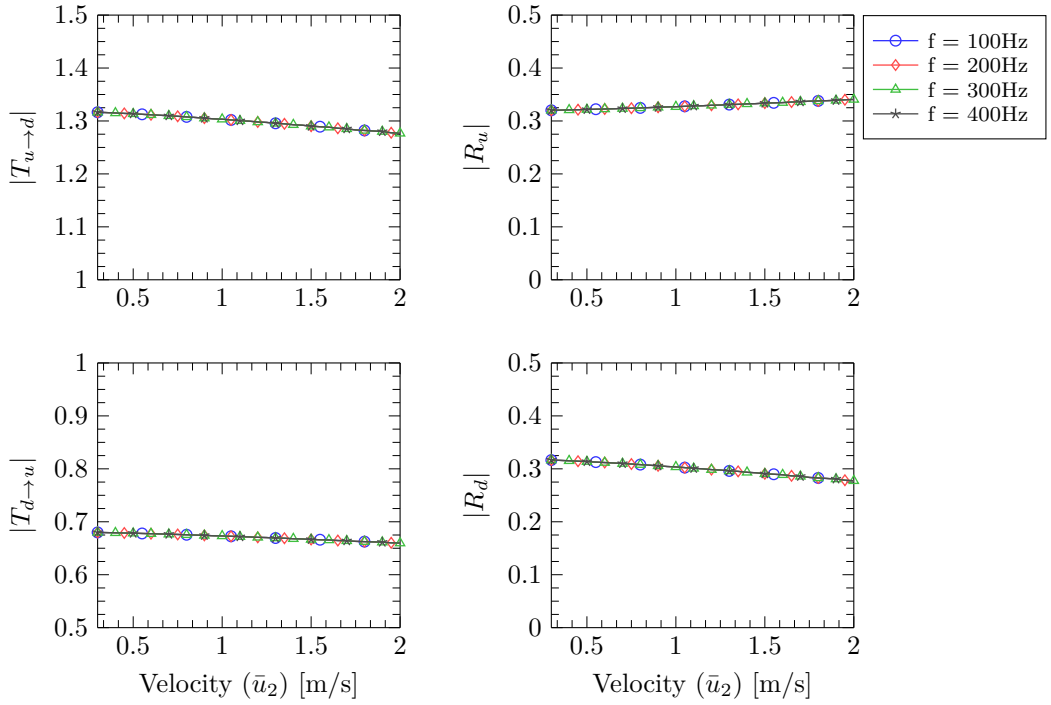

Figure 4.19: Variation of the elements of $[\mathrm{SM}]_{hex}$ as a function of the incoming velocity ($\bar{u}_2$), for fixed frequencies, $d = 3$mm, $\eta = 0.1$ and $\zeta_{32} = 1.936$ when $\bar{T}_3 = 400$K. The curves are obtained using Eq. (4.36).

is shown in Fig. 4.20. The curves are calculated for hex of $d = 3$mm, $f = 100$Hz, $\bar{T}_2 = 1500K$, $\bar{T}_3 = 400K$, $\zeta_{32} = 1.936$ and $\bar{u}_2 = 0.5$, 1.0, 1.5 and 2.0m/s.

4.5.6. Influence of hex tube diameter (d)

It can be observed from Fig. 4.21 that the acoustic response of the hex do not vary beyond a certain (hex) diameter value. This behaviour can be attributed to the quasi-steady nature of the response as well as the hydrodynamic flow field present. Since the mean flow velocity and the open area ratio are maintained as constants for the different diameters considered, one can easily deduce the dynamic similarity in the hydrodynamics involving the different diameters. This is particularly true for the larger diameters. For small diameters, the influence of the boundary layer on the hydrodynamic flow field around the hex tube is non-negligible. Hence the acoustic response is slightly varied. In addition to this, due to the quasi-steady nature of the influence of frequency on the scattering properties, there exists a sort of scaling

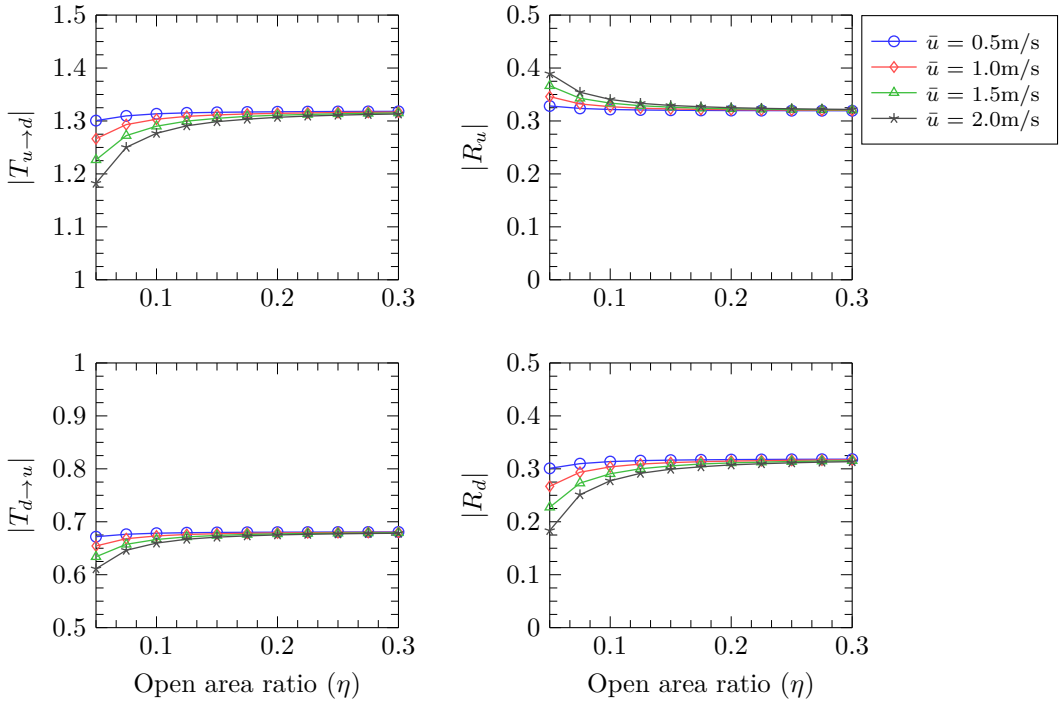

Figure 4.20: Variation of the elements of $[\mathrm{SM}]_{hex}$ as a function of open area ratio (η), for fixed velocities $\bar{u}$ (or $\bar{u}_2$), f = 100Hz, d = 3mm and $\zeta_{32} = 1.936$ when $\bar{T}_3 = 400$K. The curves are obtained using Eq. (4.36).

between the hex tube geometry and the acoustic wavelength. This may also give rise to the *pseudo-steady* behaviour of the scattering matrix as d is varied. The curves are calculated for hex of $\eta = 0.1$, f = 100Hz, $\bar{T}_2 = 1500K$, $\bar{T}_3 = 400K$, $\zeta_{32} = 1.936$ and $\bar{u}_2$ = 0.5, 1.0, 1.5 and 2.0m/s.

4.6. Conclusions

Heat exchangers are integral to heat generation systems like domestic boilers. The hex is housed within the combustion chamber, along with the heat source, leading to thermoacoustic interaction between the two components. Therefore, there arises the need to model the thermoacoustic response of the hex, to external velocity fluctuations. In the case of the heat source, the thermoacoustic response was modelled as the interaction between the heat release rate fluctuations and the upstream velocity fluctuations. However, in the case of hex, there are two physical processes occurring at the hex that needs to be modelled. The first process is the heat absorption at the hex (heat sink),

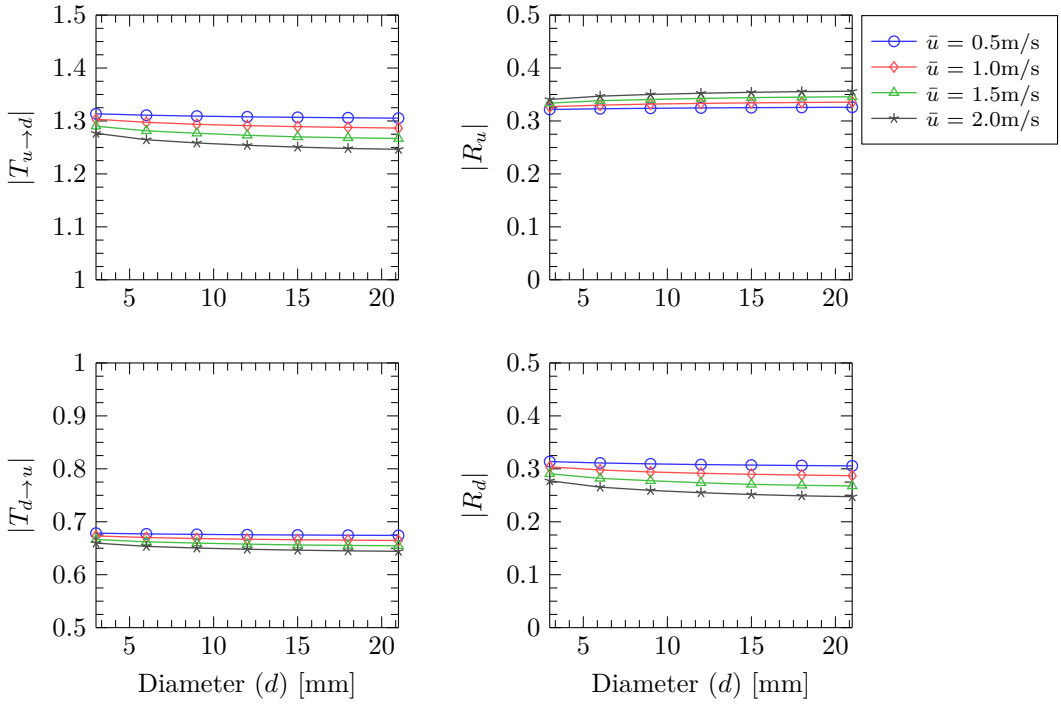

Figure 4.21: Variation of the elements of $[\mathrm{SM}]_{hex}$ as a function of hex diameter (d), for fixed velocities $\bar{u}$ (or $\bar{u}_2$), $f = 100$Hz, $\eta = 0.1$ and $\zeta_{32} = 1.936$ when $\bar{T}_3 = 400$K. The curves are obtained using Eq. (4.36).

and the second process is the acoustic scattering at the hex due to the tube row. For ease of analysis, we treat these two processes as independent processes, separated by an infinitesimal distance Δx. The heat transfer response (HTF) or the heat absorption rate law at the heat sink is evaluated through numerical simulations and subsequent curve fitting methods, and the acoustic response of the tube row is modelled through a quasi-steady approach.

Once the heat transfer response and the quasi-steady response of the heat sink and tube row respectively, are modelled, the total scattering response of the hex is calculated by letting $\Delta x \to 0$. Conducting a parametric study on the thermoacoustic response of hex to changes in the system parameters showed that the response of hex depended greatly on the mean flow velocity ($\bar{u}_2$), the frequency of the incident acoustic wave (f), the impedance ratio (ζ_{32}) across the heat sink and the geometry of the tube row (d and η).

Chapter 5

Cavity-backed Heat Exchanger

This chapter deals with the acoustic response of a cavity-backed hex, represented by the effective reflection coefficient. Studies conducted on cavity-backed slit-plates with bias flow have shown that such a configuration can act as a good sound absorber due to the vortex dissipation present within the cavity. Since the underlying hydrodynamics and loss mechanisms are the same for a cavity-backed slit-plate with bias flow and a cavity-backed hex in cross-flow, it is plausible that the latter can also act as a sound absorber. In order to quantify the absorbing efficiency of the cavity-backed hex, a variable called absorption coefficient is introduced. The aim is to maximise this absorption coefficient by varying the system parameters. This is accomplished by conducting a parametric analysis and by deducing the possible solutions for better absorption.

5.1. Introduction

In the modelled configuration of the combustion system, the hex and the heat source are placed within the outer casing of the combustor. Owing to the axisymmetric nature of the system, the outer casing can be simulated as a rigid backing plate, downstream of the hex, as shown in Fig. 5.1. The distance between the hex and the backing plate is

called the cavity length, l_c, and this new element in the system i.e., the cavity backing, acts as an added acoustic resonator. In the previous chapter, we modelled the hex as a combination of a heat sink and an acoustic scatterer, taking into account the vortex dissipation, viscous, thermal, and turbulent losses. These loss mechanisms, along with the resonating effect of the cavity, can be utilised to attenuate sound passing through the hex tube row.

There is a vast amount of literature available on the mechanism of sound absorption by vortex shedding induced by orifices, slit-plates and nozzle exits. In one such work, Surendran and Heckl (2016, 2017) have treated the hex tube row as an array of thin sharp-edged rods with rectangular cross sections, which can be treated as a slit-plate. The presence of a steady flow through the gaps between the rods induces vortex shedding and consequently sound absorption, which they have utilised to suppress thermoacoustic instability.

The effective reflection coefficient, R_L, of a cavity-backed hex is derived in Section 5.2, followed by the introduction of a quantity known as the absorption coefficient Δ_L, which indicates the absorbing efficiency of the cavity-backed hex. In Section 5.3, the influence of cavity backing on R_L and Δ_L is discussed. A parametric analysis on the influence of the various system parameters like mean flow velocity, incident frequency of the acoustic wave, impedance ratio across the hex and hex tube row geometry, on R_L and Δ_L is undertaken in Section 5.4. The aim of this analysis is to identify those system parameters that will maximise the sound absorbing capability of the cavity-backed hex.

5.2. Cavity-backed hex

The reflection coefficient R_L at $x = L$ is the effective reflection coefficient of the hex and the cavity backing. It is the ratio of the reflected pressure wave p_2^- to the incident wave p_2^+. Using Eq. (4.24) and the reflection coefficient of R_p at $x = L + l_c$ i.e.,

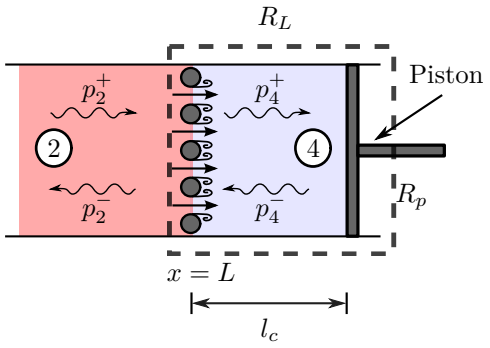

Figure 5.1: Schematic of cavity-backed hex. Here, R_L is the effective reflection coefficient at $x = L$.

$p_4^- = R_p\, e^{(2ik_4 l_c)}\, p_4^+$, we can derive the effective reflection coefficient as (Surendran and Heckl, 2014)

$$R_L = R_u + \frac{T_{d\to u}\, T_{u\to d}\, R_p\, e^{2ik_4 l_c}}{1 - R_d\, R_p\, e^{2ik_4 l_c}}, \tag{5.1}$$

Special cases are $R_p = 1$ (piston) and $R_p = -1$ (open end).

To quantify the damping property of the cavity-backed hex configuration, we introduce a quantity known as the absorption coefficient (Δ_L), which is the ratio of the acoustic energy absorbed or dissipated by the cavity-backed hex to the incident acoustic energy. It is defined as

$$\Delta_L = 1 - |R_L|^2. \tag{5.2}$$

Δ_L can take two extreme values, 1 or 0, depending on the reflection behaviour of the cavity-backed hex. In one case, $|R_L| = 1$ indicates that the cavity-backed hex may behave as a closed end ($R_L = 1$) or as an open end ($R_L =$ -1), leading to no absorption i.e., $\Delta_L = 0$ of the incident sound. In the other case, $|R_L| = 0$ indicates an anechoic condition and there will be maximum absorption of the incident sound i.e., $\Delta_L = 1$. So, for the cavity-backed hex to be an efficient acoustic damper, Δ_L must be maximised.

To this end, a parametric analysis is conducted to evaluate the influence of different system parameters on $|R_L|$ and Δ_L. This will shed more light on the usability of some of these parameters to maximise Δ_L, which is a measure of the acoustic damping associated with the cavity-backed hex. The influence of the cavity backing is discussed

in Section 5.3 and results for the parametric study are provided in Section 5.4. The parametric study is carried out using the assumptions listed in Section 4.5.2.

5.3. Cavity backing and resonance

It can be confirmed from Eq. (5.1) that in addition to the acoustic scattering properties of the hex, the cavity length (l_c) also influences the effective reflection and absorption properties of the cavity-backed hex. Here, the cavity backing can act as an additional resonator, causing resonance or anti-resonance, depending on the downstream reflection coefficient R_p.

Studies conducted on slit-plates backed by a rigid plate ($R_p = 1$) have shown that for an incident acoustic wave of frequency f, there will be maximum absorption if the cavity length $l_c = c_4/(4f)$ (Dowling and Hughes, 1992), where c_4 is the speed of sound inside the cavity. Similarly, for the cavity-backed hex, it can be observed from Fig. 5.2(b) that for a particular frequency, the maximum absorption is experienced for that l_c value which is equal to the quarter wavelength of the incident frequency. The absorption can be enhanced if $\bar{u}_2$ is increased, as mentioned in Section 5.4.2. $|R_L|$, on the other hand, exhibits a trend opposite to that of Δ_L. It decreases while Δ_L increases and vice versa. A maximum for $|R_L|$ indicates resonance behaviour, and a minimum for $|R_L|$ indicates an anti-resonance behaviour. In the latter situation, the cavity-backed hex acts as a near-anechoic end and is favoured for acoustic damping. The plots given in Fig. 5.2 are for $R_p = 1$, with frequencies $f = 100$, 200, 300 and 400Hz, $d = 3$mm, $\eta = 0.1$, $\bar{u}_2 = 2.0$m/s and $\zeta_{32} = 1.936$.

The behaviour of the hex with an open ended backing (R_p = -1) is shown in Fig. 5.3. Here, $|R_L|$ has minimum or Δ_L has maximum when $l_c = c_4/(2f)$. Again, resonance behaviour of cavity-backed hex is exhibited when $|R_L|$ is maximum and anti-resonance behaviour is exhibited when $|R_L|$ is minimum. The results are plotted for $f = 100$, 200, 300 and 400Hz, $d = 3$mm, $\eta = 0.1$, $\bar{u}_2 = 2.0$m/s and $\zeta_{32} = 1.936$.

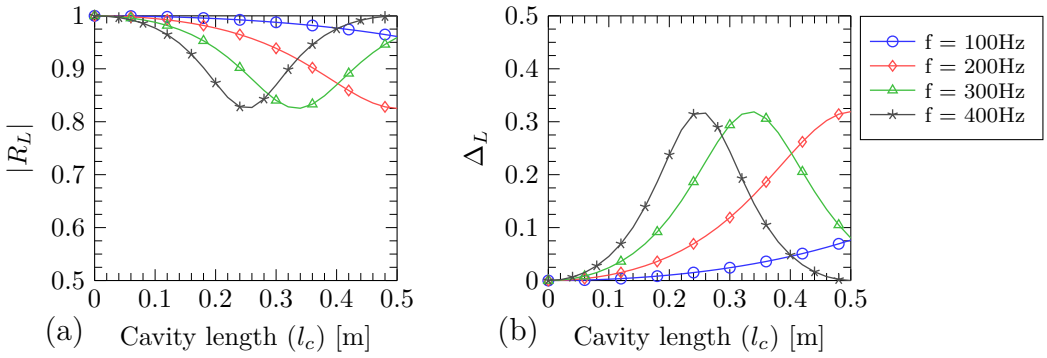

Figure 5.2: Variation of $|R_L|$ and Δ_L as functions of the cavity length (l_c), for fixed frequencies, $d = 3$mm, $\eta = 0.1$, $\zeta_{32} = 1.936$, $R_p = 1$ and $\bar{u}_2 = 2.0$m/s.

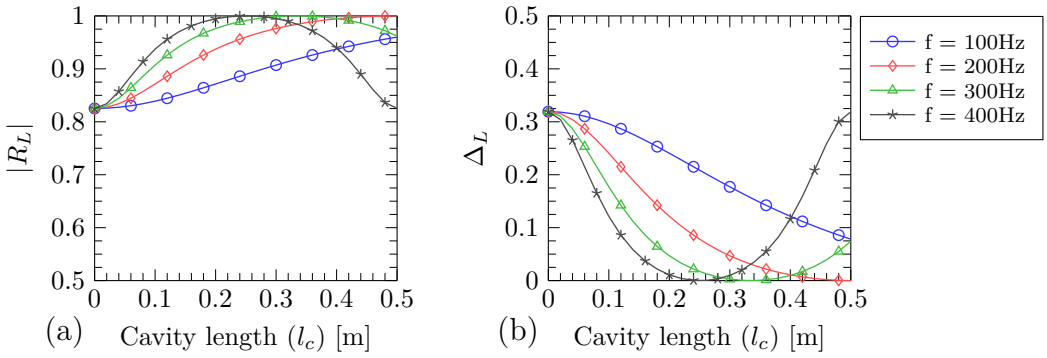

Figure 5.3: Variation of $|R_L|$ and Δ_L as functions of the cavity length (l_c), for fixed frequencies, $d = 3$mm, $\eta = 0.1$, $\zeta_{32} = 1.936$, $R_p =$ -1 and $\bar{u}_2 = 2.0$m/s.

5.4. Acoustic properties of cavity-backed hex

To study the influence of various system parameters on the acoustic properties or the acoustic response of a cavity-backed hex with rigid backing ($R_p = 1$), we have substituted the modified expressions for $T_{u\to d}$, $T_{d\to u}$, R_u and R_d (Eq. (4.36)) in Eqs. (5.1) and (5.2). Similar to the analysis done in the previous chapter, we conduct a parametric study to understand the influence of the system parameters like the frequency of the incident wave, the incoming velocity and the geometry of the hex tube row, which includes the tube diameter and the open area ratio.

5.4.1. Influence of frequency (f)

The influence of frequency on the reflection and absorption coefficients of a cavity-backed hex are shown in Fig. 5.4. Unlike the quasi-steady behaviour of the hex on its own (Fig. 4.18), the inclusion of a cavity has drastically changed the acoustic response. It can be observed that $|R_L|$ decreases with increasing f, reaches a minimum and then increases, whereas Δ_L increases with increasing f, reaches a maximum and then decreases. The depth of the minimum in $|R_L|$ and the height of the maximum in Δ_L are both increased as the flow velocity is increased. Also, these minimal and maximal values in $|R_L|$ and Δ_L respectively, fall in the same frequency range for the various velocities considered. This shows that for a given l_c, d, η and ζ_{32}, the damping associated with the frequencies in a particular range can be enhanced by increasing $\bar{u}$. For the plots in Fig. 5.4, $l_c = 0.25$m, $d = 3$mm, $\eta = 0.1$ and $\zeta_{32} = 1.936$.

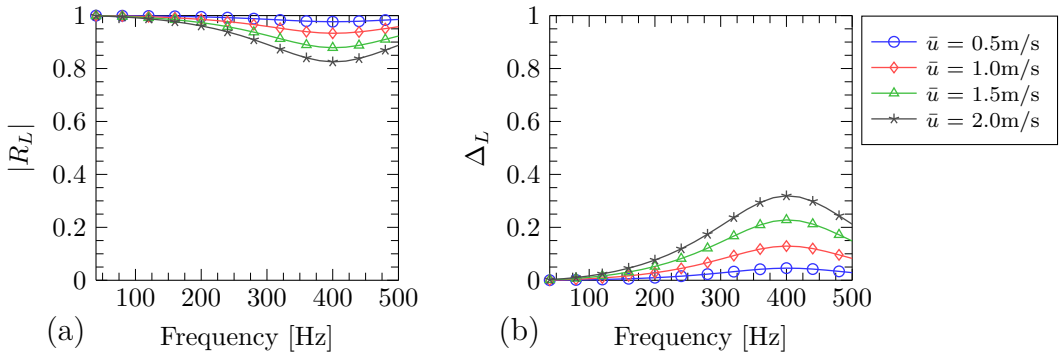

Figure 5.4: Variation of $|R_L|$ and Δ_L as functions of frequency (f), for fixed velocities $\bar{u}$ (or $\bar{u}_2$), $d = 3$mm, $\eta = 0.1$, $\zeta_{32} = 1.936$ and $l_c = 0.25$m.

5.4.2. Influence of mean flow velocity ($\bar{u}_2$)

Figure 5.5 shows the variation of $|R_L|$, Δ_L and the real part of R_L denoted by $\Re(R_L)$, as functions of the mean flow velocity, for four fixed frequencies: $f = 100$, 200, 300 and 400Hz, $d = 3$mm, $\eta = 0.1$, $l_c = 0.25$m and $\zeta_{32} = 1.936$. From Fig. 5.5(a), we can observe that for increasing values of $\bar{u}$, $|R_L|$ decreases, except for the frequency of 400Hz. For $f = 400$Hz, it can be observed that for increasing values of $\bar{u}$, $|R_L|$ decreases, reaches a minimum and then increases. Such a trend will be exhibited by other frequencies

(f = 100, 200 and 300Hz) if $\bar{u}_2$ is increased further (not shown in the plot). On the other hand, in Fig. 5.5(b), Δ_L increases with increasing $\bar{u}_2$, attains a maximum and then decreases, for f = 400Hz. This trend will be exhibited by other frequencies, if $\bar{u}_2$ is increased further.

One may, by intuition, expect that an increase in $\bar{u}_2$ indicates an increase in the perceived *blockage* experienced by the flow (due to compressibility and boundary layer effects), leading to an increase in the effective reflection i.e., increasing $\bar{u}_2$ should lead to increasing reflection for all $\bar{u}_2$. However, this trend is not shown in Fig. 5.5(a), but the real part of R_L depicts this trend (Fig. 5.5(c)). The presence of cavity causes R_L to have values between -1 (open end) and +1 (closed end). For some frequencies like 100Hz, the cavity-backed hex behaves like a rigid or an almost rigid end with $R_L > 0$ and close to +1. For other frequencies like 400Hz, whose peaks in Δ_L are close to 1, the increase in $\bar{u}_2$ causes R_L to start out as an open termination (R_L close to -1), and then gradually proceeds to an almost closed termination (R_L tending to 1). At a critical velocity, for a given frequency, R_L becomes 0 causing the cavity-backed hex to behave as an anechoic end. This condition favours the maximum absorption of the incident sound.

5.4.3. Influence of open area ratio (η)

As mentioned in Section 4.5.5, increasing η causes the hex tube row to be acoustically transparent, and the only other components then to influence the acoustic response would be the heat sink and the backing plate. This effect is shown in Fig. 5.6, where the influence of η on $|R_L|$ and Δ_L are shown for $\bar{u}_2$ = 0.5, 1.0, 1.5 and 2.0m/s, d = 3mm, f = 100Hz, l_c = 0.25m and ζ_{32} = 1.936. As η increases, $|R_L|$ increases and tends to +1, due to the influence of the backing cavity, and Δ_L decreases due to the decreased interaction between the acoustics and the shear layers downstream of the hex. Again, as $\bar{u}$ increases, $|R_L|$ decreases and Δ_L increases, for a given η.

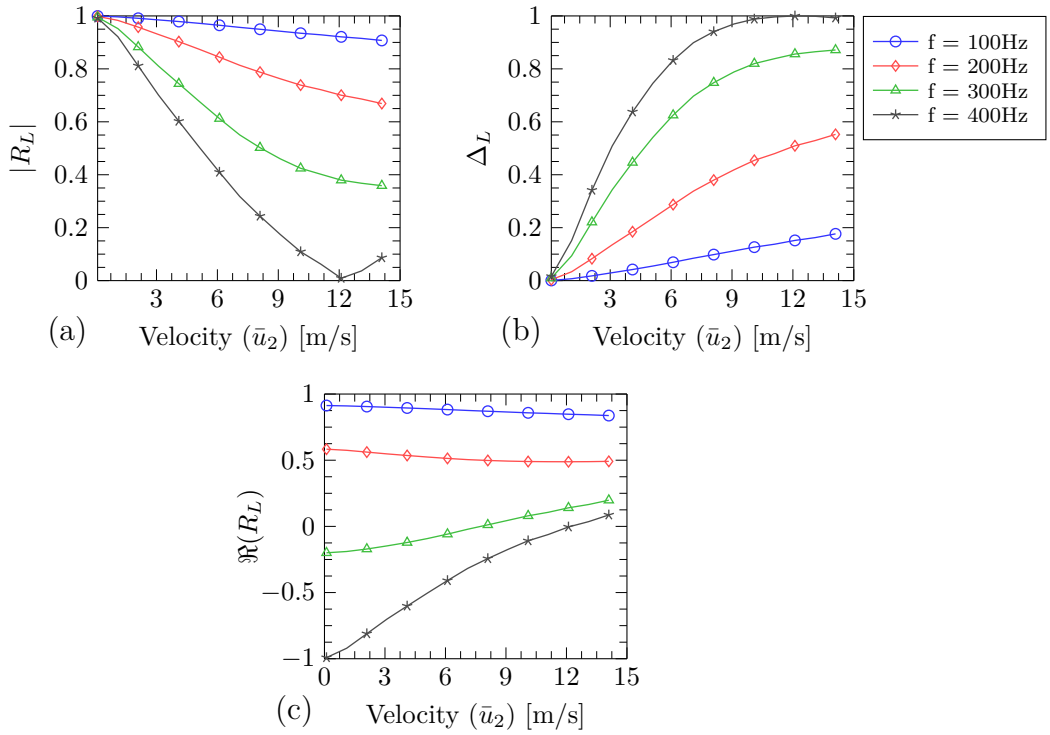

Figure 5.5: Variation of $|R_L|$, Δ_L and $\Re(R_L)$ as functions of the mean flow velocity ($\bar{u}_2$), for fixed frequencies, $d = 3$mm, $\eta = 0.1$, $\zeta_{32} = 1.936$ and $l_c = 0.25$m.

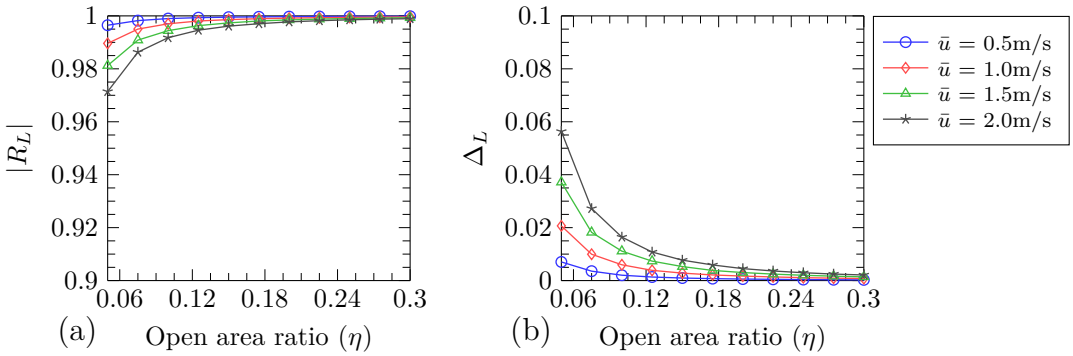

Figure 5.6: Variation of $|R_L|$ and Δ_L as functions of open area ratio (η), for fixed velocities $\bar{u}$ (or $\bar{u}_2$), $f = 100$Hz, $d = 3$mm, $\zeta_{32} = 1.936$ and $l_c = 0.25$m.

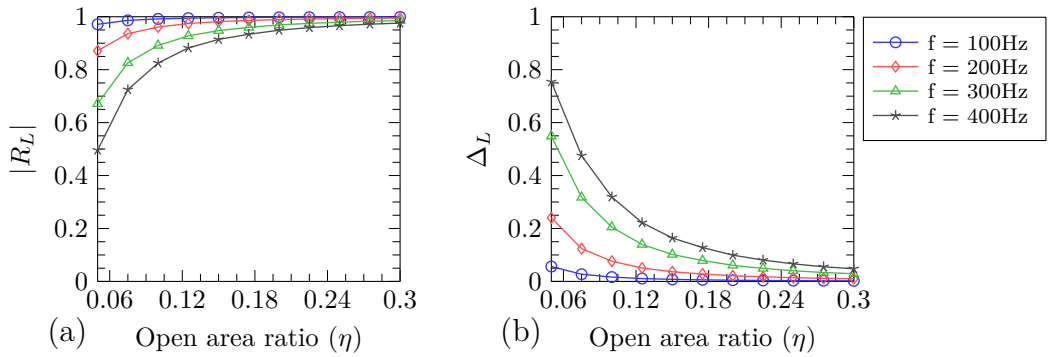

Figure 5.7: Variation of $|R_L|$ and Δ_L as functions of open area ratio (η), for fixed frequencies, $\bar{u}_2 = 2.0$m/s, $d = 3$mm, $\zeta_{32} = 1.936$ and $l_c = 0.25$m.

There is also a significant influence of frequency (Fig. 5.7). For certain frequencies the absorption is large. Δ_L increases with increasing f, reaches a maximum and decreases (as observed in Fig. 5.4). Therefore, from Figs. 5.6 and 5.7, it can be deduced that small values of η and large values of $\bar{u}_2$ enhances the absorption at the cavity-backed hex, for certain frequency ranges. However, small η values are not always recommended due to the boundary layer and flow compressibility effects. For large velocities through the gaps between the hex tubes, there may be triggering of hydrodynamic instabilities that are not favourable. Hence η must be chosen carefully to avoid undesired effects.

5.4.4. Influence of hex tube diameter (d)

Similar to the acoustic response of a hex tube in isolation (Section 4.5.6), the acoustic response of a cavity-backed hex also exhibits an almost *steady* response with respect to the increasing hex tube diameter. In Fig. 5.8, the variations of $|R_L|$ and Δ_L for fixed velocities: $\bar{u}_2 = 0.5$, 1.0, 1.5 and 2.0m/s and $f = 100$Hz are shown, whereas in Fig. 5.9, the variations of $|R_L|$ and Δ_L for fixed frequencies: $f = 100$, 200, 300 and 400Hz and $\bar{u}_2 = 2.0$m/s are shown. In both the figures, $\eta = 0.1$, $l_c = 0.25$m and $\zeta_{32} = 1.936$. As discussed previously, $\bar{u}$ and f also affect the influence of the hex tube diameter on $|R_L|$ and Δ_L. As $\bar{u}_2$ increases, $|R_L|$ decreases and Δ_L increases (Fig. 5.8). In the case of frequency, Δ_L is larger for frequencies like 300 and 400Hz, whereas it is very small for 100Hz. The opposite behaviour is exhibited by $|R_L|$ (Fig. 5.9).

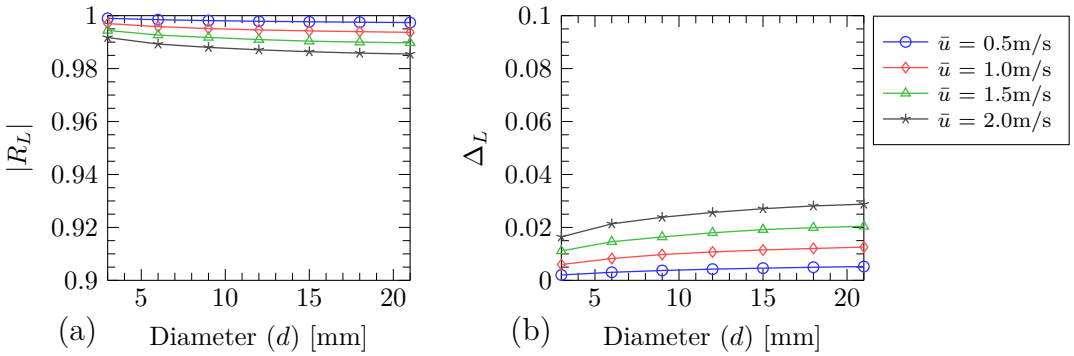

Figure 5.8: Variation of $|R_L|$ and Δ_L as functions of hex diameter (d), for fixed velocities $\bar{u}$ (or $\bar{u}_2$), $f = 100$Hz, $\eta = 0.1$, $\zeta_{32} = 1.936$ and $l_c = 0.25$m.

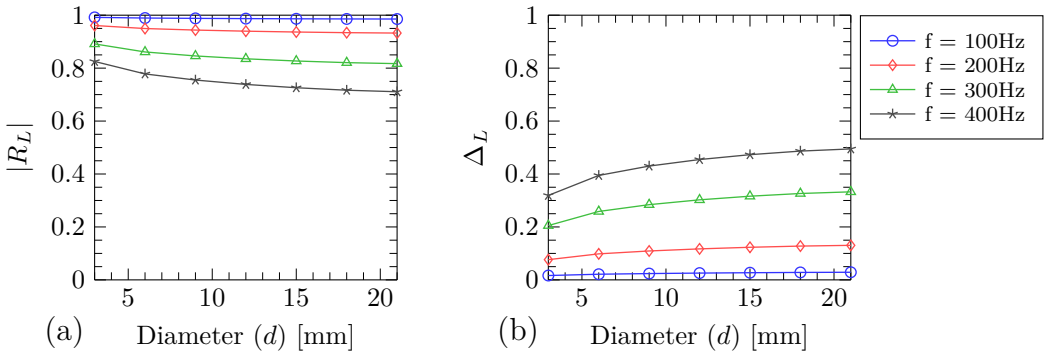

Figure 5.9: Variation of $|R_L|$ and Δ_L as functions of hex diameter (d), for fixed frequencies, $\bar{u}_2 = 2.0$m/s, $\eta = 0.1$, $\zeta_{32} = 1.936$ and $l_c = 0.25$m.

5.5. Conclusions

For a given combustor configuration, with fixed hex geometry (d and η) and temperature jumps across the heat source and the hex (ζ_{32}), that is undergoing a thermoacoustic instability, the frequency (f) of the acoustic waves propagating within the combustor will be the eigenfrequencies of the system. These eigenfrequencies are dependent on the system boundary conditions, namely the inlet and outlet reflection coefficients, R_0 and R_L. Hence, to stabilise an already unstable eigenmode of the combustor, we can vary R_L in such a way that there is maximum absorption of the sound waves propagating within the combustor. From the parametric analysis conducted, we can conclude that for a given hex geometry (d and η) and operating conditions like ζ_{32} and the probable eigenfrequency range, Δ_L can be maximised by varying the cavity length l_c and the mean flow velocity $\bar{u}_2$. For sufficiently large values of $\bar{u}_2$ and $l_c = c_4/(4f)$ or $l_c = c_4/(2f)$ depending on R_p, we can even achieve complete absorption of the incident sound. This attenuation property of the cavity-backed hex is utilised for suppression of thermoacoustic instability, as will be discussed in Chapter 6.

Chapter 6

Stability Analysis

In this chapter, we conduct the stability analysis on the idealised combustion system having a hex near the closed downstream end. Stability analysis is conducted for the first mode of the combustor, using the classical eigenvalue method. The combustor, in the absence of hex, is a quarter-wave resonator with a heat source, whose first mode is always unstable. We observe that the introduction of the hex with varying mean flow velocity, $\bar{u}$, and varying cavity length, l_c, modifies the stability behaviour of the combustion system. The stability maps are constructed in the $l_c - l_f$ plane. It is observed that increasing $\bar{u}$ and increasing l_c tends to stabilise the combustor. Influence of additional system parameters like hex tube diameter, d, open area ratio, η, and frequency, f, are also included in the stability analysis.

6.1. Introduction

Stability analysis of the combustor configuration (Fig. 2.2) considered in this thesis is carried out through the use of stability maps that depict the stable and unstable regimes of the combustor for different parameters or operating conditions. These maps can be obtained analytically (Heckl and Kosztin, 2013, Surendran et al., 2016b), nu-

merically (Wieczorek, 2010) or even experimentally (Rigas et al., 2016).

In stability analysis, we look at the response of the combustion system to perturbations in system parameters or system variables. For a combustion system, these perturbations could be in pressure, velocity, equivalence ratio etc. If the combustion system returns to its original state, after being perturbed, then it is termed a *stable* system, and if it does not return to its initial state, then it is termed an *unstable* system.

The stability behaviour may also be classified as *linear* or *non-linear* depending on the influence of the perturbation amplitudes. A linear stability analysis is undertaken if the perturbation amplitudes are very small and the system responds to only the first order term in the perturbation amplitude. If the perturbation amplitudes are high such that the higher order (non-linear) terms are non-negligible, a non-linear stability analysis has to be undertaken. A stable system (linear or non-linear) is characterised by decaying amplitudes as shown in Fig. 6.1(a). Here, the blue curve denotes the response ($y(t)$) of a non-linearly stable system and the red curve denotes the envelope of the response for a linearly stable system (exponential decay). An unstable system (linear) is characterised by the exponentially growing amplitudes as shown by the red curve in Fig. 6.1(b). In practical systems, the exponential growth is followed by a saturation in the amplitude, leading to a limit cycle [1] (blue curve in Fig. 6.1(b)). A limit cycle is characterised by high amplitude oscillations of specific frequencies.

In this thesis, we provide linear descriptions for the responses of the heat source and hex, and therefore we perform a linear stability analysis of the combustion system considered. This means that the solution we obtain will give either an exponential decay or an exponential growth in the amplitude of the response variable, but not limit cycle amplitudes. In the context of thermoacoustic instabilities, there is a coupling between Q' and p', where Q' is modelled as a function of the acoustic velocity fluctuation u',

[1] Inclusion of non-linear terms in the description of the heat source or hex can lead to the prediction of limit cycle behaviour. However, such an analysis is beyond the scope of this work, detailed discussions on non-linear behaviour of combustion systems is not included in the thesis.

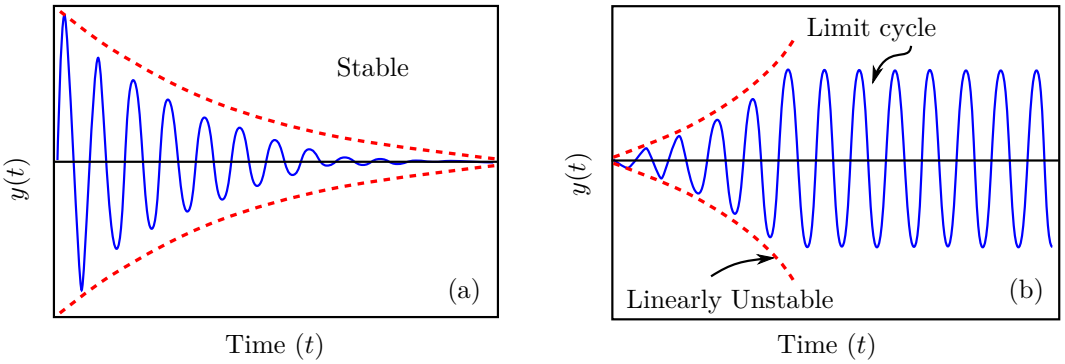

Figure 6.1: Schematic of typical time response of a system undergoing (a) stable oscillations, and (b) unstable oscillations, in the variable $y(t)$.

as discussed in Section 3.4. Here, u' is the perturbed variable and p' is the response variable.

6.2. Eigenvalue Method

There are several methods adopted by researchers to determine analytically, the stability behaviour of a system. Some methods like the Green's function approach (Bigongiari and Heckl, 2016, Heckl, 2015) or the system identification approach are used for analysis in time-domain, whereas methods like the classical eigenvalue method (Heckl, 1988, 2013) or Galerkin methods are used in frequency-domain analysis. In our analysis, we have described the combustion system in the frequency domain, and hence we use the classical eigenvalue method to predict the eigenfrequencies of the combustion system, and to construct the stability maps.

The prefix *eigen-* (German) means *self, own* or *characteristic*, and the *eigenfrequency* of a system is the frequency that belongs to the system i.e., the frequency at which the system oscillates when perturbed. We can evaluate the eigenfrequencies of a system by formulating the characteristic equation (from a system of homogeneous equations), and subsequently solving it to get its roots. This approach is applied to our combustor to determine the complex eigenfrequencies and the corresponding growth rates of the different eigenmodes present in the combustor. It is the growth rate that indicates the stability of the combustor considered.

6.2.1. Boundary and jump conditions

The combustion system shown in Fig. 2.2 can now be reduced to a configuration consisting of a duct which is open at one end ($R_0 = -1$ at $x = 0$) and having a reflection coefficient of R_L at the other end ($x = L$). R_L is the effective or combined reflection coefficient of the cavity-backed hex. The heat source is located at a distance of $x = l_f$ from the open end.

When formulating the characteristic equation for our combustor configuration, we make use of the acoustic matching or jump conditions (Eqs. (3.18) and (3.21)) given in Chapter 3, along with the following boundary conditions.

At $x = 0$,

$$p_1^+ = R_0\, p_1^-, \tag{6.1}$$

At $x = L$,

$$p_2^- = R_L\, p_2^+, \tag{6.2}$$

6.2.2. Methodology

Equations (3.18), (3.21), (6.1) and (6.2) can now be written in the form of a matrix equation as

$$[Y(\Omega)] \begin{bmatrix} p_1^+ \\ p_1^- \\ p_2^+ \\ p_2^- \end{bmatrix} = \begin{bmatrix} 0 \\ 0 \\ 0 \\ 0 \end{bmatrix}, \tag{6.3}$$

with matrix

$$[Y(\Omega)] = \begin{bmatrix} e^{-i\frac{\Omega}{c_1}l_f} & -R_0\, e^{i\frac{\Omega}{c_1}l_f} & 0 & 0 \\ 0 & 0 & R_L\, e^{i\frac{\Omega}{c_2}(L-l_f)} & e^{-i\frac{\Omega}{c_2}(L-l_f)} \\ 1 & 1 & -1 & -1 \\ -\left(1+\beta\, e^{i\Omega\tau}\right) & \left(1+\beta\, e^{i\Omega\tau}\right) & \zeta_{12} & -\zeta_{12} \end{bmatrix}, \tag{6.4}$$

where $\beta = (n_1(\gamma-1)) / (S\bar{\rho}_1 c_1^2)$ and $\zeta_{12} = (\bar{\rho}_1 c_1) / (\bar{\rho}_2 c_2)$. Here we have assumed a simple time-lag model (Eq. (3.12)) for the heat source.

6.2.3. Growth rate determination

The characteristic equation, det $Y(\Omega) = 0$ i.e.,

$$\begin{aligned}\left(1+\beta e^{i\Omega\tau}\right)\Big[&-R_L\, e^{(-i\frac{\Omega}{c_1}l_f)}\, e^{(i\frac{\Omega}{c_2}(L-l_f))} - e^{(-i\frac{\Omega}{c_1}l_f)}\, e^{(-i\frac{\Omega}{c_2}(L-l_f))} + \\ &R_0\, R_L\, e^{(i\frac{\Omega}{c_1}l_f)}\, e^{(i\frac{\Omega}{c_2}(L-l_f))} + R_0\, e^{(i\frac{\Omega}{c_1}l_f)}\, e^{(-i\frac{\Omega}{c_2}(L-l_f))}\Big] \\ +\,\zeta_{12}&\Big[R_L\, e^{(-i\frac{\Omega}{c_1}l_f)}\, e^{(i\frac{\Omega}{c_2}(L-l_f))} - R_0\, e^{(i\frac{\Omega}{c_1}l_f)}\, e^{(-i\frac{\Omega}{c_2}(L-l_f))}\Big] \\ -\,\zeta_{12}&\Big[e^{(-i\frac{\Omega}{c_1}l_f)}\, e^{(-i\frac{\Omega}{c_2}(L-l_f))} - R_0\, R_L\, e^{(i\frac{\Omega}{c_1}l_f)}\, e^{(i\frac{\Omega}{c_2}(L-l_f))}\Big] = 0, \end{aligned} \tag{6.5}$$

is solved numerically by Newton-Raphson method or bisection method. The solution, Ω, is a complex quantity of the form $\Omega_m = \omega_m + i\delta_m$, whose real part, ω_m, gives the natural frequency of the mode m, and the imaginary part, δ_m, gives the growth rate. The stability of the mode is determined from the sign of δ_m. Positive δ_m indicates instability and negative δ_m indicates stability.

6.3. Stability maps for various combustor properties

From Eq. (6.5), we can deduce that the parameters which influence the stability of the combustor are: the properties of the medium inside the duct ($\bar{\rho}_{1,2}$, $c_{1,2}$, $\bar{T}_{1,2}$), the duct length (L), the location of the heat source (l_f), the reflection coefficients at the boundaries (R_0 and R_L), the time-lag (τ), and the heat source coupling coefficient (n_1). In addition to these parameters, cavity length (l_c), hex dimensions (d and η) and mean flow velocity ($\bar{u}$) in *Region 2* have indirect influence through R_L (Eq. (5.1)). The R_L also takes into account the influence of the heat sink coefficient (α) and the impedance ratio (ζ_{32}) (using Eq. (4.35) in Eq. (5.1)). In this section, we examine the influence of some of these parameters on the stability of the combustion system.

The stability maps are constructed in the cavity length (l_c) - heat source location (l_f) plane, where the *grey* regions indicate instability and the *white* regions indicate

stability. Stability of any mode is determined from the sign of its growth rate, as mentioned in the previous section. In our study, we look at the stability of the first mode of the combustion system whose properties are listed in Table 6.1. The cold region is assumed to be at $\bar{T}_1 = 340$K with a speed of sound of $c_1 = 370.7$m/s, and the hot region is assumed to be at $\bar{T}_2 = 1500$K with a speed of sound of $c_2 = 778.63$m/s. The duct length L is assumed to be 1m and the heat source coupling coefficient $n_1 = 187$kg m/s^2. The time-lag, $\tau = 0.15\times10^{-3}$s, is chosen such that it is much smaller than the fundamental time periods encountered in the stability analysis. A conservative estimate of the time period range calculated from the stability map is $[\ 5.12 \quad 11.95\ ] \times 10^{-3}$s.

Table 6.1: Properties of the combustion system.

Property	Value
$\bar{T}_1$ [K]	340
c_1 [m/s]	370.7
$\bar{\rho}_1$ [kg/m^3]	1.2
$\bar{T}_2$ [K]	1500
c_2 [m/s]	778.63
$\bar{\rho}_2$ [kg/m^3]	0.27
L [m]	1
S [m^2]	0.0025
n_1 [kg m/s^2]	187
τ [s]	0.15×10^{-3}
l_f [m]	$[\ 0 \cdots L\ ]$
l_c [m]	$[\ 0 \cdots L/2\ ]$

Firstly, we construct the stability map for mode 1 of the combustor containing only the heat source and no hex, as shown in Fig. 6.2(a). We can observe that the system is unstable for the range of values of l_c and l_f considered. This behaviour can be explained in terms of the mode shape of the wave within the resonator. In the absence of the heat exchanger, the combustor configuration is essentially a quarter-wave resonator with a heat source at $x = l_f$. An increase in cavity length (l_c) effectively adds to the

resonator length, L. The total length of the resonator will now be $(L + l_c)$. The first mode shape of the quarter-wave resonator will be, as the name suggests, a quarter wave with a node at $x = 0$ and a maximum at $x = (L + l_c)$. From the Rayleigh criterion, we can conclude this unstable behaviour of the first mode of the resonator, regardless of the cavity length and heat source location considered. Figure 6.2(b) depicts the eigenfrequency range of the combustion system for the range of values of l_c and l_f considered.

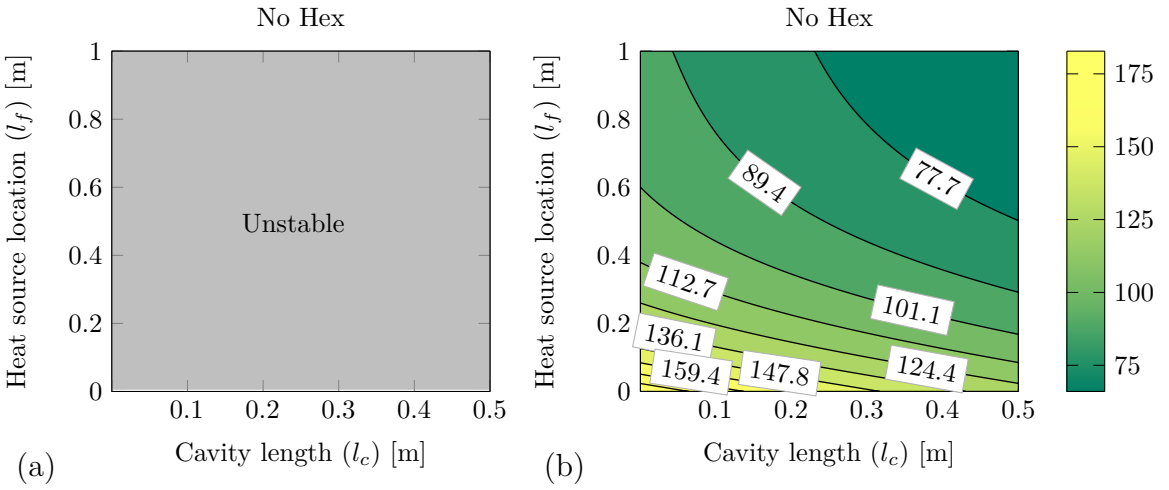

Figure 6.2: (a) Stability maps obtained for the case without hex and bias flow, and (b) contour map for the eigenfrequencies, ω_1 (in Hz) encountered. The properties of the system are given in Table 6.1.

Next, we introduce the heat exchanger with bias flow into the system. The influence of the hex on the stability behaviour of the combustion system can be explained in terms of the parametric analysis given in Chapter 5. An increase in the absorption coefficient, Δ_L is favoured for thermoacoustic instability control because this helps in breaking the feedback loop existing between the acoustic pressure fluctuations and the heat release rate fluctuations. The stability maps are constructed for $\bar{u} = 0.5$, 1.0 and 1.5m/s, since the numerical simulations for HTF are evaluated only for these velocities. The various $\bar{T}_3$ and ζ_{32} values used for constructing the stability maps are given in Table 6.2.

Table 6.2: $\bar{T}_3$ and ζ_{32} evaluated from numerical simulations.

d [mm]	η	$\bar{u}$ [m/s]	$\bar{T}_3$ [K]	ζ_{32}
3	0.1	0.5	415	1.901
		1.0	610	1.568
		1.5	750	1.414
	0.2	0.5	556	1.642
		1.0	798	1.371
		1.5	925	1.273
5	0.1	0.5	550	1.651
		1.0	790	1.378
		1.5	917	1.279
	0.2	0.5	735	1.429
		1.0	958	1.251
		1.5	1060	1.190

6.3.1. Influence of frequency (f)

Since we calculate the eigenfrequency of the combustion system, frequency cannot be considered as one of the system parameters. However, from Fig. 6.2, we can infer that the increasing l_f values corresponds to the decreasing values of f. Recalling from Section 5.4.1 that for a given $\bar{u}$, d, η, l_c and ζ_{32}, an increase in f favours the increase in Δ_L, for the frequency range [70 200]Hz. This observation translates to the increase of stability as l_f is decreased.

6.3.2. Influence of cavity length (l_c)

In terms of the influence of the cavity length, from the results given in Section 5.3, we can conclude that for the given eigenfrequency range and for a given l_c value, higher frequencies will have relatively higher Δ_L compared to the lower frequencies. This augments the effect of l_f on the stability. Also, for the range of eigenfrequencies considered, Δ_L increases as l_c increases. Combining the effects of l_f (or f) and l_c, we expect the stable regions to start appearing from the *right bottom* corner of the

stability map. The expected trend for increasing stable regions is shown in Fig. 6.3. This map also includes the effect of the mean flow velocity, as will be discussed in the next section.

6.3.3. Influence of mean flow velocity ($\bar{u}$)

In Section 5.4.2, we have concluded that an increase in $\bar{u}$ increases the Δ_L and in turn the damping of the unstable mode. Therefore, the stable regions in the stability map increases with increasing $\bar{u}$. This trend is indicated by the arrow along the diagonal in Fig. 6.3. Therefore, from the parametric analysis, we can expect the overall stability of the combustion system in the $l_f - l_c$ plane, to increase as $\bar{u}$ increases, starting at the right bottom corner. The stability maps constructed for the *base case* with $d = 3$mm, $\eta = 0.1$ and $\bar{u} = 0.5$, 1.0 and 1.5m/s, shown in Fig. 6.4, confirms our expected trend for stability growth. Also, there is a range of cavity lengths for a given $\bar{u}$ value where the system is stable irrespective of l_f. This stability and the range of l_c values can be improved further, by increasing $\bar{u}$.

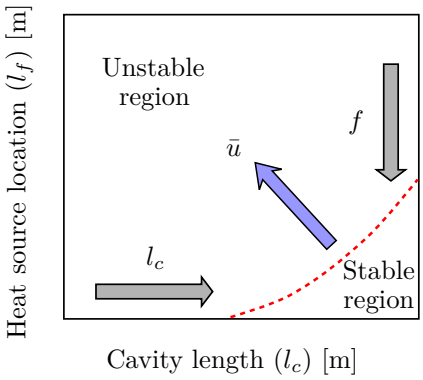

Figure 6.3: Expected trend for increase in stability, as l_c, l_f and $\bar{u}$ vary.

6.3.4. Influence of impedance ratios (ζ)

The jump in temperature ($\bar{T}$) or the jump in impedance ratio (ζ) occurs at two locations within the combustion system: (1) ζ_{32} at the hex location $x = L$, and (2) ζ_{12} at the heat source location $x = l_f$.

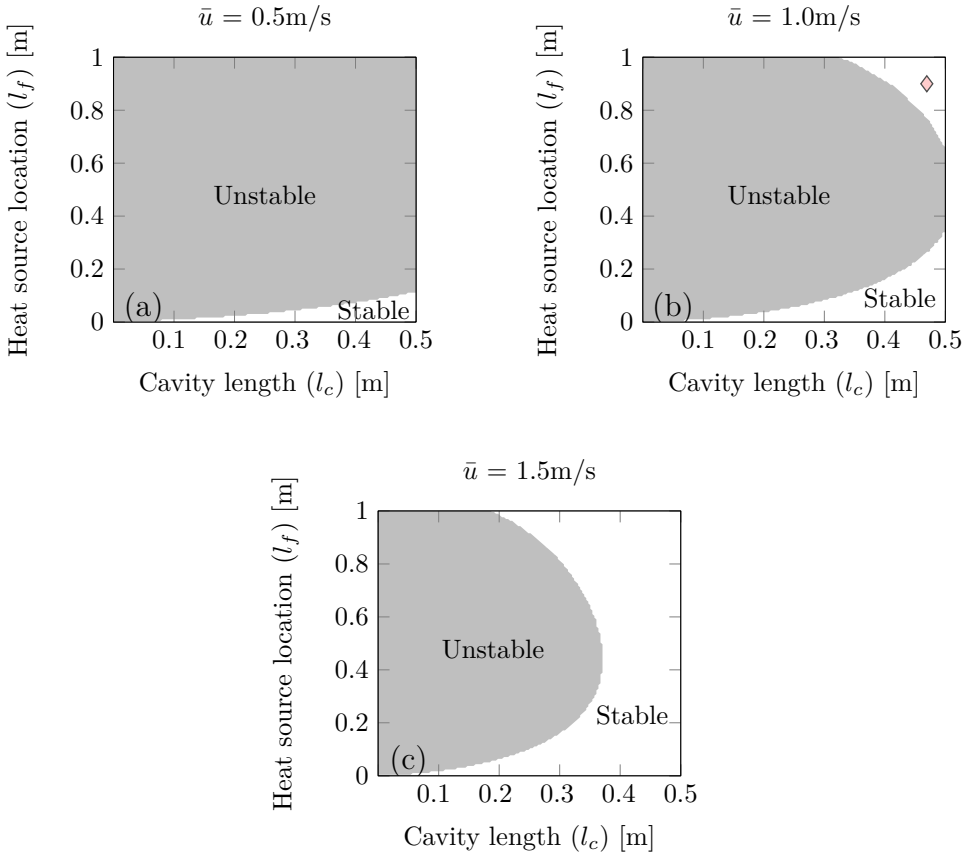

Figure 6.4: Stability maps obtained for d = 3mm, η = 0.1 and incoming velocity of (a) $\bar{u}$ = 0.5m/s, (b) $\bar{u}$ = 1.0m/s and (c) $\bar{u}$ = 1.5m/s.

ζ_{32} at the hex location $x = L$

The influence of ζ_{32} on Δ_L is shown in Fig. 6.5, for $d = 3$mm, $\eta = 0.1$ and for different mean velocities and frequencies considered in the stability maps. The increase in Δ_L for increasing $\bar{u}$ and f (for a given ζ_{32}) can be confirmed from the curves plotted. In terms of the effect of ζ_{32} on Δ_L, given a $\bar{u}$ and a f, it can be observed that there is very small variation in Δ_L, as ζ_{32} varies. This effectively means that for a given f, a comparison of Δ_L values across different $\bar{u}$ values is possible, regardless of the influence of ζ_{32}. This also translates to the fact that though ζ_{32} is different in each of the stability maps plotted in Fig. 6.4(a)-(c), a comparison of the stability behaviour is still possible, excluding the influence of ζ_{32}.

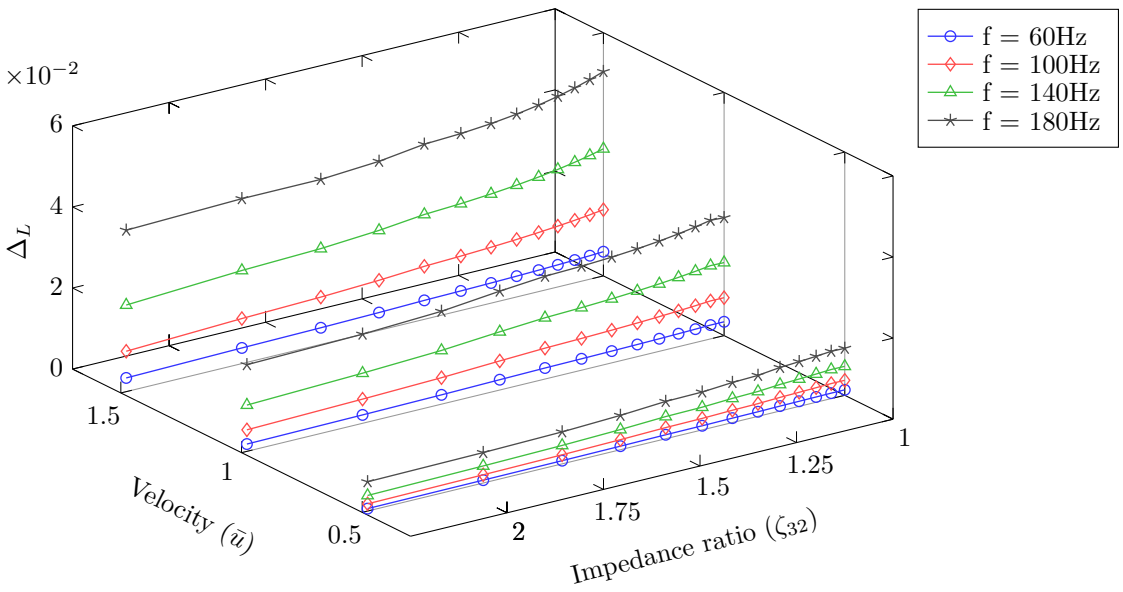

Figure 6.5: Variation of Δ_L with impedance ratio (ζ_{32}) and mean velocity ($\bar{u}$) for $d = 3$mm, $\eta = 0.1$, $l_c = 0.25$m and frequencies $f = 60$, 100, 140 and 180Hz.

ζ_{12} at the heat source location $x = l_f$

The parametric analysis conducted in Chapters 4 and 5 are associated with the influence of system parameters on the behaviour of hex without and with backing, respectively. Such an analysis excludes the influence of the temperature jump across the heat source (ζ_{12}). Temperature jump introduces jump in the speed of sound and consequently the wavelength and the phase difference between Q' and p'. The mode shape and the phase

difference is also modified by the variation in R_L at the downstream end. Such a phase shift can stabilise or destabilise the combustion system, depending on R_L as well as the position of the heat source within the system (Bigongiari and Heckl, 2016). The stable region marked with '$\diamond$' in Fig. 6.4(b) is believed to be caused by this influence of the temperature jump, in addition to the stabilising effect of increasing $\bar{u}$.

6.3.5. Influence of hex tube diameter (d)

The influence of the hex tube diameter on the stability of the combustion system is studied by increasing d from 3mm to 5mm. The stability maps, thus obtained are shown in Fig. 6.6. It can be observed that the stable regions in the stability maps are significantly larger than those shown in Fig. 6.4. This behaviour is in accordance with the parametric analysis in Section 5.4.4, where Δ_L is slightly larger for $d = 5$mm when compared to that for $d = 3$mm. Again, the influence of $\bar{u}$, l_c and f are as expected.

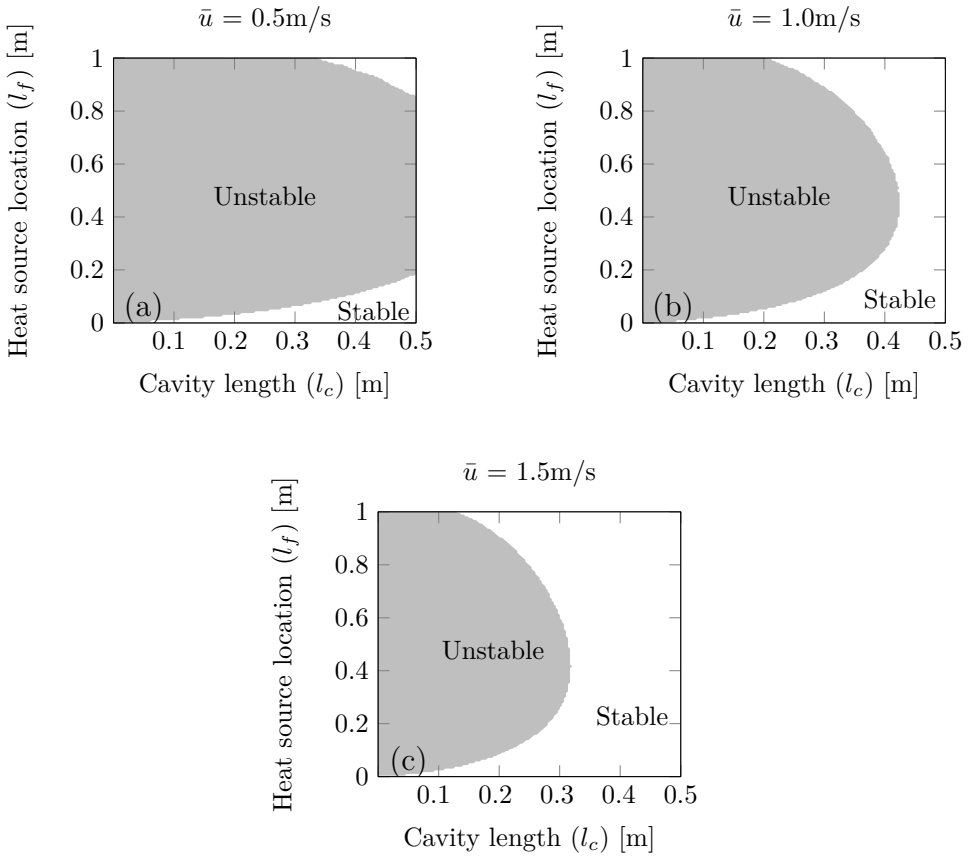

Figure 6.6: Stability maps obtained for $d = 5$mm, $\eta = 0.1$ and mean velocity of (a) $\bar{u} = 0.5$m/s, (b) $\bar{u} = 1.0$m/s and (c) $\bar{u} = 1.5$m/s.

6.3.6. Influence of open area ratio (η)

Now, the stability maps are constructed for hex geometry with a larger open area ratio, and are shown in Fig. 6.7 where $d = 3$mm and $\eta = 0.2$. From the discussion in Section 5.4.3, we expect less absorption for higher η values. This will manifest as a reduction in the stable regions compared to Fig. 6.4. The dashed line in the stability map in Fig. 6.7(a) indicates the boundary between the stable and unstable regions given in Fig. 6.4(a).

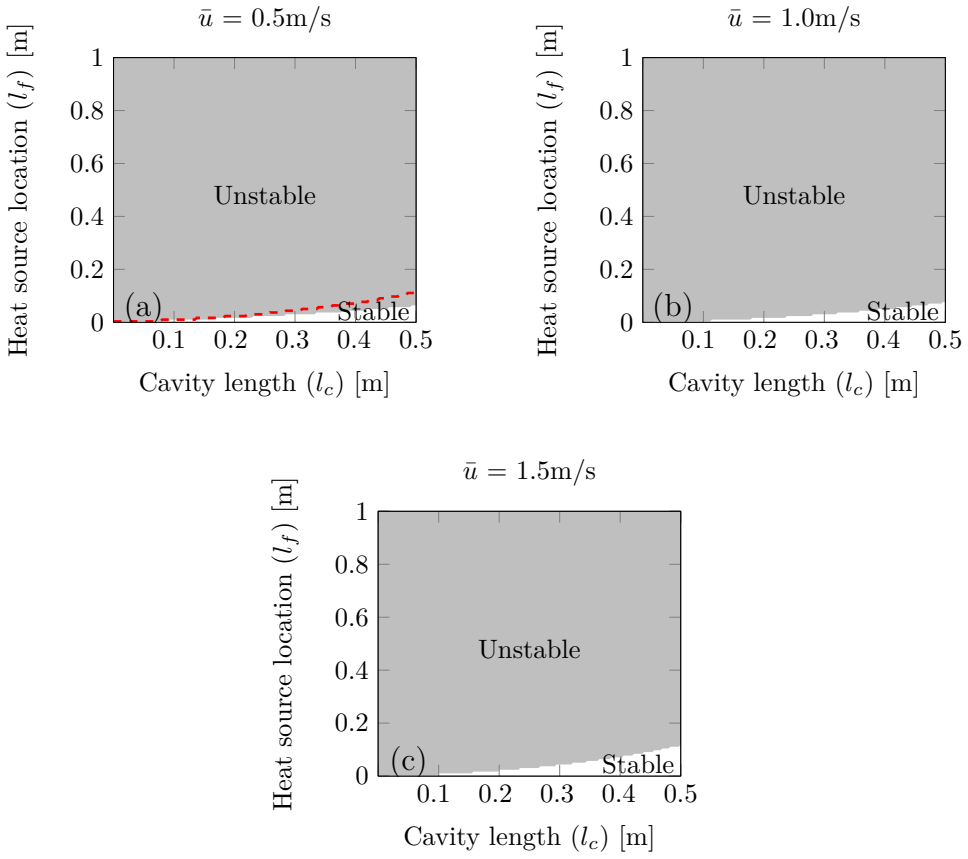

Figure 6.7: Stability maps obtained for $d = 3$mm, $\eta = 0.2$ and incoming velocity of (a) $\bar{u} = 0.5$m/s, (b) $\bar{u} = 1.0$m/s and (c) $\bar{u} = 1.5$m/s. Dashed lines indicate the boundary between the stable and unstable regions shown in Fig. 6.4(a).

Again, the influence of $\bar{u}$ and l_c remain the same. Increase in both $\bar{u}$ and l_c tend to stabilise the system, even though the increase in stability due to the increase in $\bar{u}$ is insubstantial compared to that shown in Fig. 6.4. This slight increase in stability can

be explained through the plots given in Fig. 6.8, where the variation of Δ_L is plotted for $f = 100$Hz, $\bar{u} = 0.5$, 1.0 and 1.5m/s, against the variation in η and ζ_{32}. As discussed previously, the influence of ζ_{32} can be neglected in this analysis. We can observe that at $\eta = 0.2$, the increase in $\bar{u}$ corresponds to a very small increase in Δ_L, compared to the increase at $\eta = 0.1$. This causes the similarity in the stability maps obtained for $\eta = 0.2$, even after increasing $\bar{u}$.

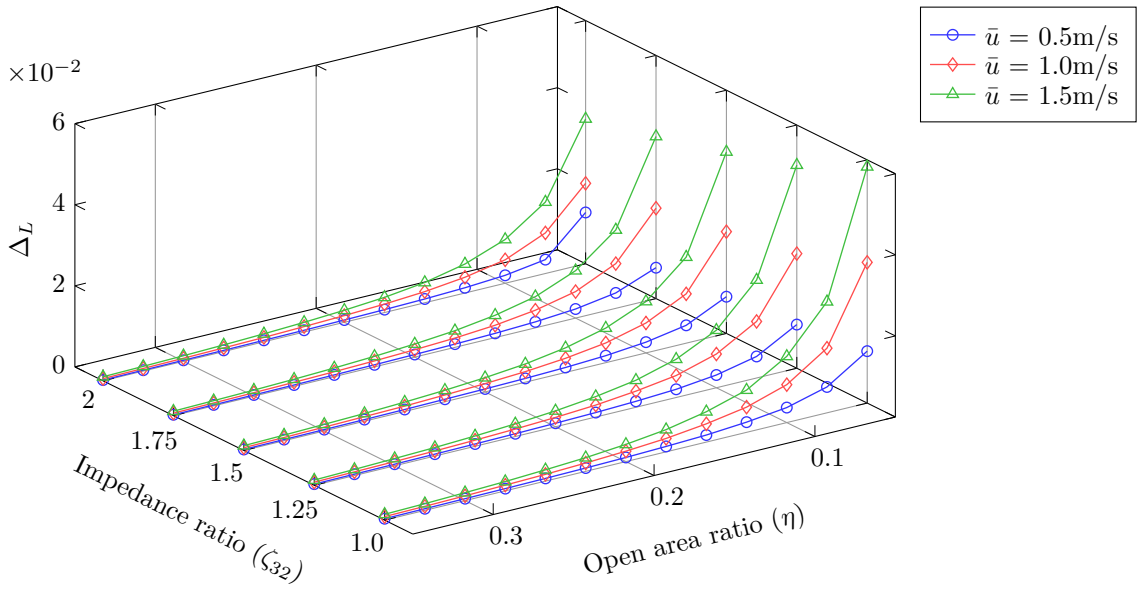

Figure 6.8: Variation of Δ_L with open area ratio (η) and impedance ratio (ζ_{32}) for $d = 3$mm, $l_c = 0.25$m, $f = 100$Hz and mean velocities $\bar{u} = 0.5$, 1.0 and 1.5m/s.

But the stability of the combustion system can be improved by increasing d. Such a situation is portrayed in Fig. 6.9, where the stability maps are given for $d = 5$mm, $\eta = 0.2$ and $\bar{u} = 0.5$, 1.0 and 1.5m/s. The stable regions are found to be larger for $\bar{u} = 1.5$m/s when compared to that for $\bar{u} = 0.5$m/s. The stability maps for $d = 5$mm and $\eta = 0.2$ also confirms all the expected trends discussed so far. The stabilising effect of increasing hex tube diameter is evident from Figs. 6.7 and 6.9. Also, the destabilising effect of open area ratio can be observed from comparing Figs. 6.6 and 6.9.

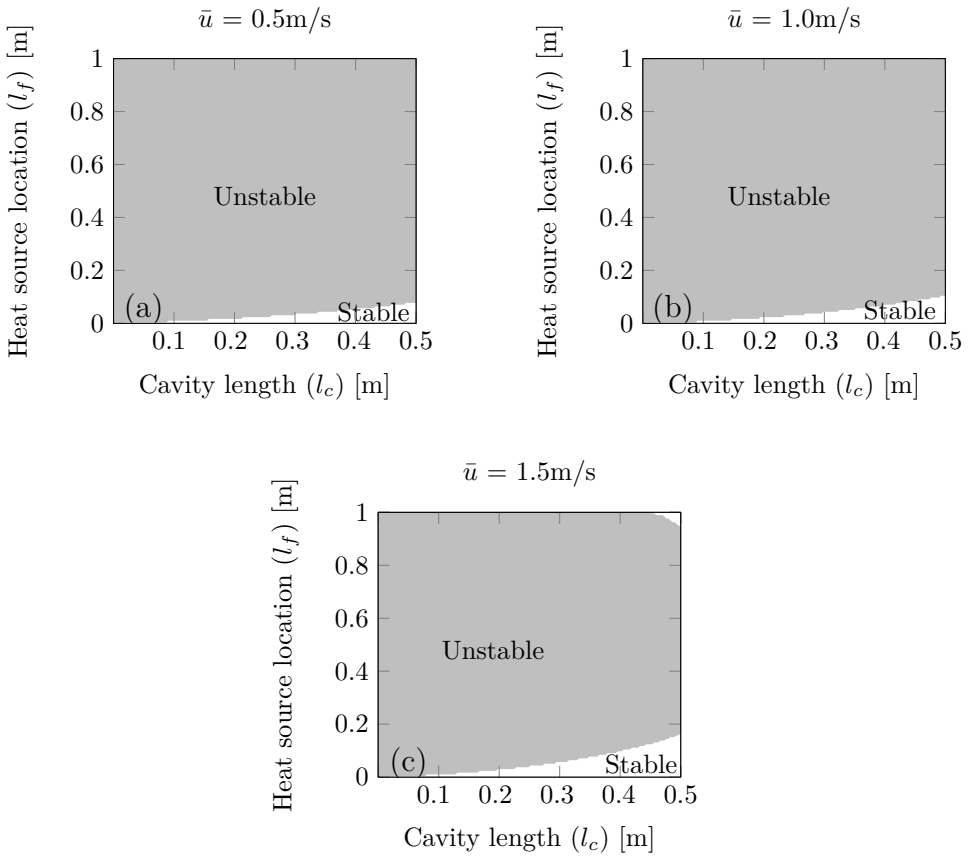

Figure 6.9: Stability maps obtained for $d = 5$mm, $\eta = 0.2$ and incoming velocity of (a) $\bar{u} = 0.5$m/s, (b) $\bar{u} = 1.0$m/s and (c) $\bar{u} = 1.5$m/s.

6.4. Conclusions

The linear stability analysis of an idealised combustion system with hex is carried out by taking into account the heat absorption and the acoustic scattering at the hex. Using the classical eigenvalue method, the complex eigenfrequencies (Ω_m) of the system are evaluated, by finding the complex roots of the characteristic equation. The real part of Ω_m (ω_m) denotes the natural frequency of the concerned mode, and the imaginary part (δ_m) denotes the growth rate. The sign of the growth rate is an indicator of the stability of the concerned mode, which in our study is the first mode.

The stability maps are constructed in the $l_c - l_f$ plane, and the analysis begins with an already unstable first mode of the combustor (without hex). The combustor, in the absence of the hex, is essentially a quarter-wave resonator with a heat source, whose first mode is always unstable. When hex is introduced near the rigid downstream end,

it acts an acoustic absorber whose reflective (R_L) and absorptive (Δ_L) properties can be varied. These properties depend on the different system parameters like $\bar{u}$, l_c, f, d and η. The aim is to stabilise the system by independently varying one of these parameters, while maintaining the other parameters as constants. From the stability maps generated, it can be concluded that increasing $\bar{u}$, l_c, d or f (in terms of l_f) tend to stabilise the system, whereas increasing η tends to destabilise it.

Nevertheless, for an unstable mode (first mode) of the combustion system with fixed geometry (d and η) for the hex, it has been observed that varying $\bar{u}$ and l_c can bring about stability.

Chapter 7

Conclusions

7.1. Summary and Conclusions

The need for clean and efficient power generation units have increased the demand for lean premixed combustion. Consequently, these combustions units become susceptible to combustion instabilities or thermoacoustic instabilities. These instabilities are characterised by high amplitude self-excited and low frequency pressure oscillations that can cause structural vibrations, unsteady thermal loading and in extreme cases, severe structural damage to the system.

Combustion instability is a consequence of the existence of a positive feedback loop between the heat release rate fluctuations Q' and the pressure fluctuations p'. In order to suppress and control the instability, the feedback loop between Q' and p' needs to be broken, by means of active or passive control strategies. We focus on passive methods to control instability. Typically in passive control, additional damping devices like acoustic resonators or acoustic liners with bias flow are included in the combustion unit to control instabilities.

Unfortunately, these passive devices are generally bulky and difficult to accommodate into small power generation units like domestic boilers, that are compact in size. However, domestic boilers have heat exchangers housed within the combustion chamber, along with the flame. Heat exchangers are periodic structures that consist of arrays

of tubes in cross flow. Studies conducted previously by researchers on tube arrays have shown that these structures can effectively dampen acoustic oscillations.

With this insight, the aim of the present work is to investigate the viability of using heat exchangers as passive control components. One of the main advantages of using heat exchanger to passively control instability is that they are an integral part of the combustion system and therefore is already present within the system. In other words, no extra provision is needed for accommodating them in the combustion system.

To this end, we simplify the complex boiler system to its basic components: the burner, the heat exchanger (hex) and the outer casing. These components can be modelled as a compact heat source within a quarter-wave resonator, with an array of tubes representing the hex placed near the closed end of the resonator. There is jump in the temperature ($\bar{T}$) and the speed of sound (c), across both heat source and hex. The heat source is modelled using a time-lag law, where the heat release rate fluctuations at the heat source location is dependent on the time-lagged acoustic velocity fluctuations. The main focus of the present work is in modelling the hex and subsequently utilising this model in the stability predictions of the complete combustion system.

Heat exchangers serve two purposes in our study: (1) they absorb the heat from the flame, and (2) they also dissipate the acoustic fluctuations incident on them. As there is limited literature available on the analytical modelling aspects of heat exchangers, we model the total acoustic scattering behaviour of hex by splitting the above mentioned physical processes into two individual processes that are separated by an infinitesimally small distance Δx. The heat transfer at the hex is computed numerically in FLUENT® to obtain a Heat exchanger Transfer Function (HTF), that relates the nondimensionalised heat absorption rate fluctuations to the nondimensionlised velocity fluctuations. Next, the acoustic scattering at the hex is evaluated analytically by employing a quasi-steady approach. The quasi-steady model was also verified experimentally, where two samples of different dimensions were tested. The quasi-steady model approximates the

tube row to a simplified geometry of two half cylinders separated by a gap. Experimental verification of an approximated geometry (d = 20mm) and a tube row (d = 16mm) proved the applicability of quasi-steady model to describe the acoustic scattering properties of tube rows.

From the HTF and the quasi-steady model, an expression for the total scattering matrix, in the limit $\Delta x \to 0$, of the hex was derived. This matrix depended on the heat sink coefficient (α), the impedance ratio across the hex (ζ_{32}), the geometry of hex tube row (d and η), the mean flow velocity ($\bar{u}$) and the frequency of the incident acoustic wave (f). α and ζ_{32} were calculated from FLUENT® results. Upon inspection, it was observed that α had very little influence on the scattering behaviour of hex, at least in the f and $\bar{u}$ ranges considered. In the combustion system configuration studied, the hex is placed near the closed end of the resonator. The influence of cavity length (l_c) is therefore an important aspect of the model description. A parametric analysis was conducted to determine the influence of each of the aforementioned parameters, namely $\bar{u}$, l_c, f, d and η, on the scattering properties of the hex.

The information thus obtained was then utilised in the linear stability predictions of the combustor. The stability maps were obtained through classical eigenvalue method, where the complex eigenfrequencies (Ω) of the first eigenmode of the system were evaluated for different system parameters. The stability behaviour is characterised by the growth rate of the eigenmode ($\delta_1 = \Im(\Omega_1)$). To understand the influence of hex on the stability, we began the analysis by constructing the stability map for the combustor *sans* hex. This essentially makes the combustor a quarter-wave resonator with a heat source, and its first mode is always unstable irrespective of the values for l_c and l_f. Next, a hex with cross flow was introduced into the system. By varying different parameters, especially $\bar{u}$ and l_c, we were able to obtain stable regions for the full range of l_f values considered. The salient results from our stability analysis are:

(1) We observed that the unstable mode of the combustor can be passively controlled to a large extent by varying the mean flow velocity $\bar{u}$ and the cavity length l_c.

(2) For an already unstable mode, an increase in velocity tends to stabilise it.

(3) Similarly, for the rigid downstream end condition ($R_p = 1$), an increase in the cavity length favoured stability.

(4) Eventhough, frequency cannot be treated as a parameter, the variation in the heat source location l_f manifested as a variation in the eigenfrequencies in the stability maps i.e., as l_f decreased, the $\omega_1 = \Re(\Omega_1)$ increased, and this favours stability.

(5) There was also an increase in the stability behaviour as the hex diameter (d) was increased.

(6) However, the increase in the open area ratio (η) had a destabilising effect. This is plausible due to the reduced interaction between the acoustic fluctuations and the shed vortices, downstream of the hex.

(7) Nevertheless, we were able to stabilise an unstable mode of the combustion system by varying system parameters like $\bar{u}$, l_c, d, η and f (through l_f).

(8) It should, however, be noted that the stabilising/destabilising trends provided in the thesis are valid only for the prescribed range of parameters. This range and the expected influence of the system parameters on the stability behaviour can be determined by conducting a parametric analysis.

The practical implications of our findings are promising. It improves the design flexibility of domestic boilers and opens the door to new designs for efficient, clean and reliable boilers and other compact power generation units. To summarise the work presesnted in this thesis, a schematic of the same is provided in Fig. 7.1.

7.2. Scope for future work

Our study is a first step in understanding the complex stability behaviour of domestic boilers. Several modifications and improvements to our analysis are possible, in order to have better instability predictions. Some of them are listed below.

(1) We have assumed an idealised combustion system with no losses and the heat source was modelled as a simple $n - \tau$ law. These assumptions can be relaxed to include losses at the duct walls (viscous and thermal). The time-lag law can be replaced with an experimentally measured FTF.

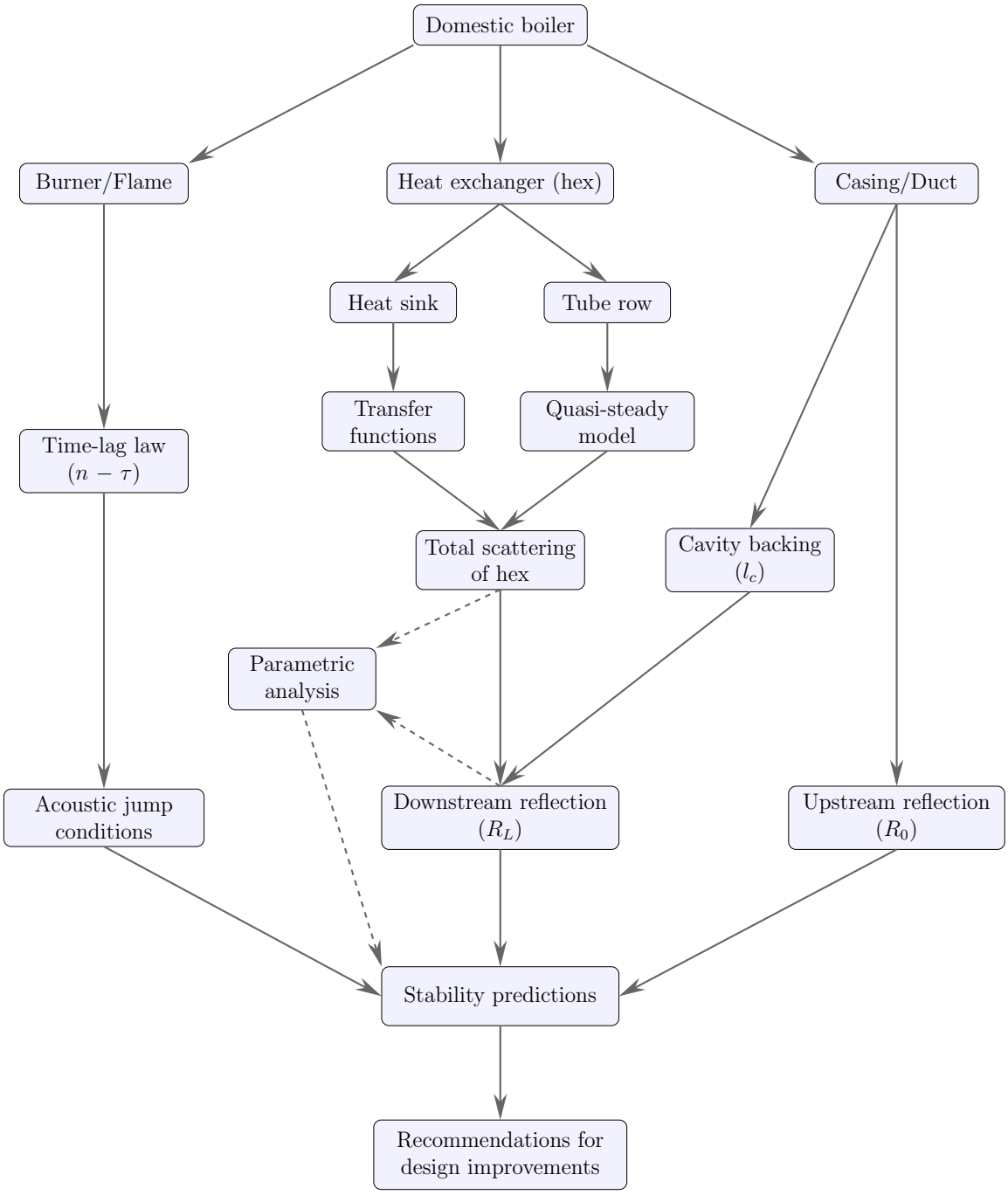

Figure 7.1: Thesis in a nutshell

(2) We could improve the heat exchanger modelling by verifying the total scattering matrix with numerical simulations or experiments.

(3) The quasi-steady model that we currently employ to obtain the acoustic scattering at the hex lacks phase information. It is worthy to look into the effects of phase differences at boundaries like the cavity-backed hex, as they could influence the stability behaviour.

(4) Currently, the information regarding the heat transfer at the hex and the flow properties after the hex is obtained from numerical simulations. This restricts our analysis as we could not look into the influence of the heat sink and the tube row, as independent entities. It would be an interesting study to decouple these processes and look at the stability behaviour of the combustion system. This could open up new possibilities in designing better and efficient passive control strategies.

(5) One of the shortcomings in our analysis is the relying on numerical simulations to obtain the HTF. It would be beneficial to either derive HTFs from analytical modelling of heat transfer process at the hex (similar to King's law for flow over hot wire) or obtain empirical relations from existing datasets in literature.

(6) In our analysis, we have only looked at the influence of a handful of parameters. There are other parameters that significantly affect the stability behaviour. One such parameter is the impedance ratio (ζ). The impedance ratio across the heat source can be viewed as the heating power of the burner and the impedance ratio across the hex is a measure of the absorption capacity of the hex. Hence, these parameters and their influences are also important aspects that needs attention in future analysis.

(7) We have undertaken a linear stability analysis. However, most practical systems perform in the non-linear regime. Therefore, it will be more practical to undertake a non-linear stability analysis by including FDFs (amplitude dependent FTFs).

(8) Finally, our analytical model is based on a highly idealised combustion system. Our findings act as guidelines for possible design modifications. In order to validate our model, the results obtained need to be compared with either experimental data or with high fidelity simulation data subject to fewer assumptions and from more realistic boiler configurations. At present, we lack such a database. Hence, through the present work, we lay the groundwork for future PhD topics like the high fidelity simulations of domestic boiler systems or the experimental validation of our findings in realistic boilers.

Appendix A

List of Publications

Conference Proceedings

Surendran, A. and **Heckl, M. A.** (**2017**), "Linear and nonlinear stability predictions for a domestic boiler with a heat exchanger for passive instability control", submitted to *The 24th International Congress on Sound and Vibration*, July, London, United Kingdom.

Surendran, A., **Heckl, M. A.**, **Hosseini, N.** and **Teerling, O. J.** (**2016**b), "Use of heat exchanger for passive control of combustion instabilities", in *The 23rd International Congress on Sound and Vibration*, July, Athens, Greece.

Abstract: One of the major concerns in the operability of power generation systems is their susceptibility to combustion instabilities. In this work, we aim to examine the effective use of heat exchangers, an integral component in any power generation system, to passively control combustion instability. The combustor is modelled as a quarter-wave resonator (1-D, open at one end, closed at the other) with a compact heat source within, which follows time lag law for heat release. The heat exchanger (hex) is modelled as an array of tubes with bias flow and is placed near the closed end of the resonator, causing it to behave like a cavity-backed slit plate: an effective acoustic absorber. For simplicity and ease of analysis, we treat the physical processes of heat transfer and acoustic scattering occurring at the hex as two individual processes separated by an infinitesimal distance. The aeroacoustic response of the tube array is modelled using a quasi-steady approach and the heat transfer across the hex is modelled by assuming it

to be a heat sink. Unsteady numerical simulations were carried out to obtain the heat exchanger transfer function (HTF), which is the response of the heat transfer at hex to upstream velocity perturbations. Combining the aeroacoustic response and the HTF, in the limit of the infinitesimal distance between these processes tending to zero, gives the net influence of the hex. Other parameters of interest are the heat source location and the cavity length (the distance between the tube array and the closed end). We then construct stability maps for the first resonant mode of the aforementioned combustor configuration, for various parameter combinations. Preliminary observations show that stability can be achieved for a wide range of parameters.

Contributions from co-authors: This conference paper is an outcome of my secondment at Bekaert Combustion Technology BV, Assen, The Netherlands. The aim of the secondment was to obtain the heat exchanger transfer functions (HTF) from numerical computations, using FLUENT®. My secondment at Bekaert was supervised by Dr. O. J. Teerling. Mr. Naseh Hosseini, TANGO ESR based at Bekaert, helped me with the setting up and performing of the numerical simulations. The paper was written by me under the supervision of Prof. Maria Heckl and the co-authors contributed in the revisions of the paper.

Surendran, A., **Heckl, M. A.**, **Boij, S.**, **Bodén, H.** and **Hirschberg, A.** (**2016**a), "Aeroacoustic response of an array of tubes with bias-flow", in *The 23rd International Congress on Sound and Vibration*, July, Athens, Greece.

Abstract: Heat exchanger tube bundles, consisting of tube arrays in cross flows, are vital in the efficient working of power generation systems. If sound propagates through these bundles, it can lead to resonance or acoustic attenuation, and thereby affecting the working of the power generation unit. Therefore, it is important to study the aeroacoustics of tube rows. The aim of the present work is to experimentally validate the quasi-steady compressible model developed to study the aeroacoustic response of an array of tubes with bias flow. In order to accomplish this, the array of tubes is approximated by a geometry consisting of two half cylinders separated by a gap and having a bias flow through the gap. Firstly, the case with no flow is considered and the experimental results for the reflection and transmission coefficients are compared against the analytical expressions developed by Huang and Heckl (Huang and Heckl, 1993, Acustica 78, 191-200). Then

the cases with flow are considered. A quasi-steady subsonic compressible model is developed to predict the reflection and transmission coefficients, valid for low Strouhal numbers, with the additional assumption of small Helmholtz number and low Mach numbers. This model is validated against the experimental results for the transmission and reflection coefficients. A two-port multi-microphone measurement technique is used to obtain the pressure data and a subsequent wave decomposition is utilised to extract the transmission and reflection coefficients. The results show good agreement with theory for various Mach numbers, in the low Strouhal number regime.

Contributions from co-authors: This conference paper is an outcome of my secondment at KTH, Stockholm, Sweden. The aim of the secondment was to experimentally validate the quasi-steady model developed at Keele. The quasi-steady was developed with helpful inputs from Prof. Avraham Hirschberg of TU Eindhoven, The Netherlands. My secondment at KTH was jointly supervised by Prof. Maria Heckl, and Prof. Hans Bodén and Dr. Susann Boij from KTH. The paper was written by me under the supervision of Prof. Maria Heckl and the co-authors contributed in the revisions of the paper.

Surendran, A. and **Heckl, M. A.** (**2016**), "Passive instability control by a heat exchanger in a combustor with non-uniform temperature", in *Thermoacoustic Instabilities in Gas Turbines and Rocket Engines: Industry meets Academia*, GTRE-022, Munich, Germany.

Abstract: Thermoacoustic instabilities, caused by the feedback between unsteady heat release and pressure perturbations, are characterised by large amplitude pressure oscillations. These oscillations, if unchecked and uncontrolled, pose a great threat to combustion systems. One strategy to mitigate them is by the use of cavity backed acoustic liners (perforated plates). In this study, we consider a generic combustor configuration: a quarter-wave resonator (1-D, one end open and the other end closed) containing a compact heat source and heat exchanger tube row. The aim is to use the heat exchanger tube row as the acoustic damper. The heat exchanger tubes are simulated using an array of thin rods with rectangular cross-section and having a bias flow through the gaps between the rods. When placed near the closed end of the resonator, these rods behave like a cavity-backed slit-plate/an acoustic liner. We derive the characteristic equation for the

complex eigenfrequencies of this set-up. From the growth rates (imaginary parts of the eigenfrequencies), we construct stability maps for various system parameter combinations. Preliminary results show that increasing the bias flow through the slits tends to stabilise the system.

Surendran, A. and **Heckl, M. A.** (**2015**), "Passive instability control by using a heat exchanger as acoustic sink", in *The 22nd International Congress on Sound and Vibration*, July, Florence, Italy.

Abstract: The aim of the present work is to investigate whether a combustion instability can be controlled by a passive method utilising a heat exchanger, which is an integral part of many combustion systems. We consider a generic configuration: a quarter-wave resonator (1-D, one end open and the other end closed) containing a compact heat source whose heat release follows a time-lag law. An array of rods inside the resonator simulates the heat exchanger tubes; a mean flow is also present. If the array of rods is placed near the closed end of the resonator, it behaves much like a cavity-backed orifice plate - a setup, which is commonly used as sound absorber in room acoustics. The temperature and the speed of sound are assumed to be uniform throughout the resonator. The array of rods is modelled as a slit-plate with known acoustic reflection and transmission coefficients; these coefficients depend on the frequency, Mach number, slit spacing and open-area ratio. Additional parameters of interest are the cavity length (distance of the slit-plate from the closed end) and the heat source location. Heat transfer between the rods and the surrounding fluid is ignored. The resonant frequencies and their growth rates are evaluated from the characteristic equation, derived for this configuration. Stability maps are constructed for various parameter combinations. It turns out that stability can be achieved for a wide range of parameters.

Surendran, A. and **Heckl, M. A.** (**2014**), "Analytical study of a Rijke tube with heat exchanger", in *The 21st International Congress on Sound and Vibration*, Beijing, China.

Abstract: Combustion systems are often integrated with heat exchangers to increase their efficiency and prolonged use. The thermo-acoustic instabilities in combustion systems had been the subject of research for over two decades. These instabilities occur due to the existence of feedback between

the unsteady heat release rate and acoustic oscillations. The aim of this paper is to study how a tube row simulating a heat exchanger affects the stability behaviour. The setup is modelled as a Rijke tube. The upstream end is open and the downstream end is a row of tubes backed by a cavity. The speed of sound is assumed to be constant throughout the duct. The reflection coefficient of the downstream end of the duct depends on the cavity length, tube row properties and the resonant frequency of the system. The resonant frequency of the system is evaluated from the characteristic equation, developed from the boundary conditions at the tube ends and the heat source. The acoustic waves are assumed to be one-dimensional, with the heat source obeying the $n - \tau$ model for heat release rate. The parameters of interest in this study are: cavity length (l_c) and the radius of the heat exchanger tubes (a). Stability maps involving the growth rate of the acoustic oscillations in the system show the unstable/stable behaviour of the combustion system.

Peer-reviewed Journals

Surendran, A. and **Heckl, M. A.**, "Passive instability control by a heat exchanger in a combustor with nonuniform temperature", *International Journal of Spray and Combustion Dynamics*, Prepublished May, 1, 2017.
DOI: 10.1177/1756827717695282.

Abstract: Thermoacoustic instabilities, caused by the feedback between unsteady heat release and acoustic pressure perturbations, are characterised by large-amplitude pressure oscillations. These oscillations, if uncontrolled, pose a threat to the integrity of combustion systems. One strategy to mitigate them is by installing cavity-backed perforated plates with bias flow into the combustion chamber. In this study, we consider a generic combustor configuration: a 1-D tube (with open and/or closed ends) containing a compact heat source and a heat exchanger tube row. The idea is to use the heat exchanger tube row as a device (analogously to a cavity-backed perforated plate) to manipulate the downstream end condition. We simulate the row of heat exchanger tubes by a slit plate with bias flow. We derive the characteristic equation for the complex eigenfrequencies of this set-up. From the growth rates (imaginary parts of the eigenfrequencies), we construct stability maps for various system parameter combinations. The results, obtained for the first two modes of the system, show that by varying

the cavity length or the bias flow velocity through the slits, we can stabilise a previously unstable combustion system.

Surendran, A., **Heckl, M. A.**, **Hosseini, N.** and **Teerling, O. J.**, "Passive control of instabilities in combustion systems with heat exchanger", submitted to *International Journal of Spray and Combustion Dynamics* (under revision).

Surendran, A., **Heckl, M. A.**, **Peerlings, L.**, **Boij, S.**, **Bodén, H.** and **Hirschberg, A.**, "Aeroacoustic response of an array of tubes with and without bias flow", under preparation to be submitted to *Journal of Sound and Vibration*.

Original Research Article

International journal of spray and combustion dynamics

International Journal of Spray and Combustion Dynamics
0(0) 1–14

DOI: 10.1177/1756827717695282
journals.sagepub.com/home/scd
SAGE

Passive instability control by a heat exchanger in a combustor with nonuniform temperature

Aswathy Surendran and Maria A Heckl

Abstract

Thermoacoustic instabilities, caused by the feedback between unsteady heat release and acoustic pressure perturbations, are characterised by large-amplitude pressure oscillations. These oscillations, if uncontrolled, pose a threat to the integrity of combustion systems. One strategy to mitigate them is by installing cavity-backed perforated plates with bias flow into the combustion chamber. In this study, we consider a generic combustor configuration: a one-dimentional tube (with open and/or closed ends) containing a compact heat source and a heat exchanger tube row. The idea is to use the heat exchanger tube row as a device (analogously to a cavity-backed perforated plate) to manipulate the downstream end condition. We simulate the row of heat exchanger tubes by a slit-plate with bias flow. We derive the characteristic equation for the complex eigenfrequencies of this set-up. From the growth rates (imaginary parts of the eigenfrequencies), we construct stability maps for various system parameter combinations. The results, obtained for the first two modes of the system, show that by varying the cavity length or the bias flow velocity through the slits, we can stabilise a previously unstable combustion system.

Keywords

Thermoacoustic instabilities, control of instability, stability analysis, heat exchangers, orifice plates

Date received: 30 September 2016; accepted: 24 January 2017

1 Introduction

When a heat source like a flame or a heated gauze is placed within an acoustic resonator, there may be an interaction between the heat release fluctuations and the acoustic pressure fluctuations, which forms a positive feedback loop leading to high-amplitude oscillations. This effect has been observed in combustion systems and is known as thermoacoustic instability. If uncontrolled, high-pressure loads occur, leading to excessive vibrations of mechanical parts, and in extreme cases, to catastrophic hardware damage.[1] It is therefore important to develop mitigation strategies to prevent these instabilities.

Combustion systems that are prone to thermoacoustic instabilities are gas turbine engines, rocket motors, afterburners, furnaces and domestic heaters. There is a large variety of designs. Some of them include heat exchangers, and such combustion systems are the topic of this paper. Heat exchangers are periodic structures that consist of arrays of tubes in a cross flow. If sound passes through an array of tubes, it is attenuated due to viscous, thermal and turbulent losses. We aim to utilise this attenuation property of tube arrays to control thermoacoustic instabilities. To this end, we consider an idealised combustion system: the combustion chamber is one-dimensional, the flame is compact and the heat exchanger is a row of narrow sharp-edged rods with rectangular cross-section. Effectively, we treat the heat exchanger as a slit-plate with bias flow.

Slit-plates and, more commonly, orifice plates with a mean flow through the holes (bias flow) are widely used as sound absorbers. A summary of the key contributions to this research topic can be found in the study by

School of Chemical and Physical Sciences, Keele University, Staffordshire, UK

Corresponding author:
Maria A Heckl, Keele University, Staffordshire ST5 5BG, UK.
Email: m.a.heckl@keele.ac.uk

Munjal.[2] Generic applications are presented by Davies.[3] The sound absorption of a perforated plate with bias flow can be enhanced greatly by a cavity backing.[4–6]

The idea that a cavity-backed perforated plate can be used in a combustion system to control thermocoustic instabilities was first realised experimentally by Tran et al.[7,8] They implemented a cavity-backed perforated plate at the upstream end of a swirl burner and achieved control by suitable choice of cavity length. Tran's work was continued by Scarpato et al.[9,10] who investigated the role of the Strouhal number on the absorption mechanism of the cavity-backed perforated plate.

A model corresponding to Tran's setup was developed by Heckl and Kosztin,[11] who predicted that control can be achieved for a wide range of cavity lengths. They modelled the flame dynamics by a generic time-lag law and also examined the effectiveness of the control for different time-lags.

Much is known about the damping mechanism of perforated plates with bias flow. When a sound wave hits such a plate, hydrodynamic effects come into play which affect the reflection, transmission and damping of the sound wave. A physically intuitive and experimentally validated model has been developed by Hofmans et al.[12] and Durrieu et al.[13] for a single orifice (both circular and slit-shaped). Their work provides physical insight, which will be valuable for understanding the results in our paper. Below is a summary of their relevant findings.

At the orifice, a free jet is formed by flow separation. The cross-sectional area of the jet is smaller than that of the orifice (vena contracta). One can imagine the orifice as partially blocked by this hydrodynamic effect. Downstream of the orifice, the jet becomes unstable; vortices form and are swept downstream.

The blockage has a strong effect on the acoustic reflection and transmission. The magnitude of the reflection coefficient increases with Mach number, while its phase remains zero. Thus, the orifice behaves like a partially reflective rigid wall. The vortex generation is responsible for the sound absorption, as initially proposed theoretically by Howe.[14] The absorption first increases with Mach number, then reaches a maximum and decreases for higher Mach numbers.

The acoustic behaviour of a perforated plate can be manipulated in a big way by backing it with a cavity. The cavity acts like an acoustic resonator, and as such, it can amplify or damp acoustic waves that enter it. The combination of a perforated plate with bias flow and a backing cavity has been found to become anechoic for certain frequencies and flow Mach numbers.[4,5,6]

For our purpose of describing a heat exchanger as a perforated plate, we are particularly interested in plates with slit-shaped perforations. A comprehensive analytical model for such plates (with and without cavity backing) was produced by Dowling and Hughes.[15] They used the Kutta condition to derive expressions for the reflection and transmission coefficient of the slit-plate. The key parameters in their model are Strouhal number, bias flow Mach number, open area ratio and cavity length.

In this paper, we present a model for an idealised combustion system, which consists of a one-dimensional tube with a compact flame and a jump in mean temperature across the flame or heat source. The upstream end of the tube is open, and the downstream end is formed by a slit-plate, a certain distance upstream of the tube end, which may be open or closed. Surendran and Heckl[16] have already developed a theoretical model for such a combustion system and have shown that the slit-plate with bias flow is an effective method to passively control thermoacoustic instabilities. The present study extends this work in the following ways:

- Instead of the basic $n-\tau$ law, we use an extended (and more versatile) time-lag law to describe the heat source.
- We included a temperature jump at the heat source, rather than assuming a uniform temperature throughout the tube. This assumption of a temperature jump makes the combustor more realistic and close to real situations.
- We examined a wider range of boundary conditions at the downstream tube end.

We begin our analysis with the description of the combustion system and its associated modelling aspects in Section 2. In Section 3, we look at the influence of system parameters on the acoustic properties of the slit-plate and then proceed to the stability predictions (Section 4) for various system parameters, using an eigenvalue method.

2 Description of model

The combustion system studied is as shown in Figure 1. It consists of a quarter-wave resonator, open at the

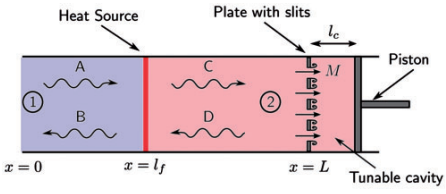

Figure 1. Schematic of the combustion system.

upstream end ($x = 0$) and having a reflection coefficient $R_0 = -1$. The heat source is located at a distance l_f from the upstream end, dividing the resonator into two regions: a cold upstream region (Region 1) and a hot downstream region (Region 2). The speeds of sound ($c_{1,2}$) and mean temperatures ($T_{1,2}$) are uniform in both regions. The slit-plate simulating the heat exchanger is located at $x = L$. The slit-plate has a bias flow through the gaps, denoted by its Mach number, M. The downstream end of the resonator may be open or closed. In the case of closed end, the downstream extremity is equipped with a rigid piston, enabling us to vary the distance between the slit-plate and the piston. In any case, the distance between the slit-plate and the downstream end is referred to as the cavity length (l_c).

2.1 Acoustic field

The acoustic field within the combustor is modelled as one-dimensional acoustic waves propagating perpendicular to the rods (normal incidence), as shown in Figure 1. For the present study, we ignore the heat transfer between the rods and the surrounding fluid, i.e., air. The acoustic pressure and velocity fields inside the resonator are,

Region 1 (cold):

$$\hat{p}_1(x) = Ae^{ik_1(x-l_f)} + Be^{-ik_1(x-l_f)} \quad 0 < x < l_f \tag{1}$$

$$\hat{u}_1(x) = \frac{1}{\rho_1 c_1}\left\{Ae^{ik_1(x-l_f)} - Be^{-ik_1(x-l_f)}\right\} \quad 0 < x < l_f \tag{2}$$

Region 2 (hot):

$$\hat{p}_2(x) = Ce^{ik_2(x-l_f)} + De^{-ik_2(x-l_f)} \quad l_f < x < L \tag{3}$$

$$\hat{u}_2(x) = \frac{1}{\rho_2 c_2}\left\{Ce^{ik_2(x-l_f)} - De^{-ik_2(x-l_f)}\right\} \quad l_f < x < L \tag{4}$$

where $\hat{p}$ and $\hat{u}$ are the acoustic pressure and acoustic velocity, respectively (the $\hat{}$ indicates that they are frequency-domain quantities), and A, B, C and D are the pressure amplitudes to be determined. The subscripts 1 and 2 indicate the cold and hot regions respectively within the resonator, and $k_{1,2} = \omega/c_{1,2}$ is the wave number. The factor of $e^{-i\omega t}$ is omitted throughout the analysis.

2.2 Generic heat release law

The heat source is assumed to be compact, planar and confined to an infinitesimally thin region at $x = l_f$. For the heat release rate ($\hat{Q}$), we have adopted the generic heat release law by Heckl and Kosztin,[11] where the heat release rate depends on both the instantaneous velocity fluctuations $u(t)$ as well as the time-lagged velocity fluctuations $u(t-\tau)$ at the location l_f. It is given by

$$\hat{Q}(\omega) = \alpha\left[n_1\hat{u}(l_f)e^{i\omega\tau} - n_0\hat{u}(l_f)\right] \tag{5}$$

or using Equation (2), by

$$\hat{Q}(\omega) = \frac{\alpha(A-B)}{\rho_1 c_1}\left[n_1 e^{i\omega\tau} - n_0\right] \tag{6}$$

where α is a factor relating the local and global heat release rates, and n_1 and n_0 are non-dimensional coefficients called coupling coefficients.

2.3 Cavity backed slit-plate

The heat exchanger is modelled as an array of thin rods, spaced a distance d apart and having rectangular cross-sections (Figure 2). Therefore, we can treat this array as a plate with slits of width $2s$. A pressure difference across the slit-plate creates a bias flow of Mach number M through the slits, causing vortex shedding. In the model by Dowling and Hughes,[15] the transmission and reflection coefficients of a slit-plate with bias flow were derived as

$$T_{sp} = \rho\omega\dot{V}/(kd) \tag{7}$$

$$R_{sp} = 1 - \rho\omega\dot{V}/(kd) \tag{8}$$

with

$$\frac{\rho\omega\dot{V}}{kd} = \frac{i\pi\nu/(2\kappa sM)}{i\pi\nu/(2\kappa sM) - \ln(\pi\nu) + \ln 2/\Phi} \tag{9}$$

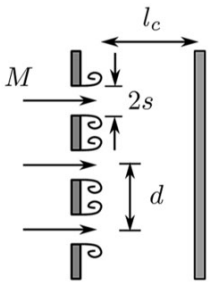

Figure 2. Geometry of the slit-plate.

and

$$\Phi = 1 - \frac{1}{\kappa s \ln 2} \times \left\{ \frac{\pi I_0(\kappa s) e^{-\kappa s} + 2i \sinh(\kappa s) K_0(\kappa s)}{\pi e^{-\kappa s}\left[I_1(\kappa s) + \frac{I_0(\kappa s)}{\kappa s \ln 2} \right] + 2i \sinh(\kappa s)\left[\frac{K_0(\kappa s)}{\kappa s \ln 2} - K_1(\kappa s) \right]} \right\} \tag{10}$$

The subscript sp refers to slit-plate and $\dot{V}$ is the perturbation volume flux through the slit. $\nu = 2s/d$ is the open area ratio, $\kappa s = \omega s/U$ is the Strouhal number, U is the bias flow velocity and I_m and K_m are the modified Bessel functions of order m. Equations (7)–(10) are valid for $s/d \ll 1$ and $d \ll \lambda$, where λ is the wavelength of the incident wave. Further details can be found in the study by Dowling and Hughes.[15] The tube end backing the plate is at a distance l_c from the slit-plate. The effective reflection coefficient, R_L, of the cavity-backed slit-plate is given by Surendran and Heckl[16]

$$R_L = R_{sp} + \frac{R_p T_{sp}^2 e^{2ik_2 l_c}}{1 - R_p R_{sp} e^{2ik_2 l_c}} \tag{11}$$

where R_p is the reflection coefficient at the downstream end of the tube. $R_p = 1$, if the end is closed and $R_p = -1$, if it is open.

3 Acoustic properties of the cavity-backed slit-plate

We describe the acoustic energy loss at the slit-plate by the absorption coefficient Δ_{sp}, given by

$$\Delta_{sp} = 1 - |T_{sp}|^2 - |R_{sp}|^2 \tag{12}$$

In analogy with this, we write the absorption coefficient of the slit-plate with cavity backing as

$$\Delta_L = 1 - |R_L|^2 \tag{13}$$

Δ_{sp} and Δ_L are a measure of the acoustic energy (relative to the incident energy) that is dissipated.

From equations (7)–(13), we can observe that these coefficients depend on the following parameters: bias flow Mach number (M), frequency of the wave (ω), cavity length (l_c) and open area ratio (ν). We investigate the influence of these parameters in the following four sections, both for the slit-plate in isolation and for the cavity-backed slit-plate.

3.1 Influence of Mach number

Figure 3 shows the reflection coefficient (magnitude and phase) and absorption coefficient for a slit-plate in isolation (Figure 3(a), (b), (c)) and for a cavity-backed slit-plate (Figure 3(d), (e), (f)), as function of Mach number for three fixed frequency values: $f = 60$, 120 and 170 Hz. The open area ratio in these figures is 0.1 and the cavity length is 0.5 m.

We observe from Figure 3(a) and (b) that the slit-plate behaves like a partially reflective solid wall ($|R_{sp}| < 1$, $\measuredangle R_{sp} = 0$). As the Mach number increases, the reflectivity increases, while the phase remains zero. This effect has been observed before.[12,13] It is a consequence of the vena contracta effect and boundary layer associated with the bias flow, which increasingly blocks the slits as M increases. Figure 3(c) shows the absorption coefficient Δ_{sp}: it increases initially with M and reaches a maximum of 0.5. The absorption is due to

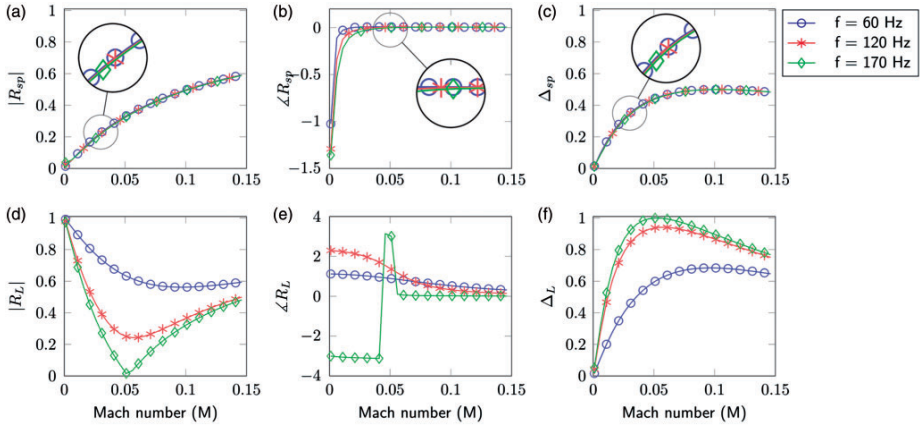

Figure 3. Reflection coefficient and absorption coefficient of slit-plate ((a)–(c)) and cavity-backed slit-plate ((d)–(f)) as a function of Mach number, for fixed frequency values and $\nu = 0.1$. For (d)–(f), $l_c = 0.5$ m.

vortices being generated at the downstream slit edges and swept away by the mean flow.[12,13] The reflection and absorption coefficients are weakly dependent on frequency. The zoomed-in plots show this weak dependence on frequency.

The results for the cavity-backed slit-plate are quite different. There is now a pronounced dependence on frequency (see Figure 3(d), (e), (f)). The cavity is an acoustic resonator, which acts like a tube with two closed ends (one of them partially reflective). For the case shown here ($l_c = 0.5$ m), it has an anti-resonance (i.e. a quarter wavelength in the cavity) at the frequency 170 Hz. At this frequency, the reflection coefficient R_L varies widely. It reaches values close to zero for Mach numbers around 0.05, and its phase jumps from $-\pi$ to 0. At this point, the absorption coefficient becomes 1, and the cavity-backed slit-plate behaves like an anechoic end.[15]

3.2 Influence of frequency

The influence of frequency on the reflection and absorption coefficients of both slit-plate and cavity-backed slit-plate is shown in Figure 4. The open area ratio is 0.1 and the cavity length is 0.5 m. The slit-plate on its own behaves largely independently of frequency, while the cavity-backed slit-plate shows a strong dependence. As in the previous section, we observe anechoic behaviour for frequencies near 170 Hz at $M = 0.05$. The behaviour is near-anechoic for a substantial range around this frequency: $|R_L| < 0.2$ in the range between 130 Hz and 200 Hz.

3.3 Influence of cavity length

Since the anechoic behaviour of the cavity-backed slit-plate is associated with the anti-resonance in the cavity, it is expected that the cavity length has a strong influence. This is indeed the case as can be seen from Figure 5(a), (b) and (c). The frequency values shown are $f = 60$, 120 and 170 Hz, the Mach number is 0.05 and the open area ratio is 0.1. At $l_c = 0$, the slit-plate and the backing wall coincide, effectively forming a rigid wall with complete reflection ($|R_L| = 1$) and no absorption ($\Delta_L = 0$). As l_c increases, $|R_L|$ decreases from 1, attains a minimum and then increases to 1 (Figure 5(a)). At this second maximum, l_c is equal to half the wavelength, and the cavity is at resonance. This alternating behaviour of decreasing and increasing $|R_L|$ continues with increasing l_c. At the same time, Δ_L also alternates, reaching maxima of 1 where $|R_L|$ has minima.

Again, the range where near-anechoic behaviour prevails is quite large: for example, for $f = 120$ Hz, $|R_L| < 0.2$ in the l_c range between 0.6 m and 0.9 m.

3.4 Influence of open area ratio

The open area ratio $\nu = 2s/d$ is a measure for the transparency of the slit-plate. Hence, as ν increases, we expect the slit-plate on its own to become acoustically less reflective and less absorbing. Figure 6(a) and (c) confirms this (for the frequency 170 Hz). The Mach number dependence is also shown in Figure 6. We observe that the phase of R_{sp} is strongly affected by it (see Figure 6(b)): for low M ($M = 0.001$), $\angle R_{sp} = -\pi$, while for higher M ($M = 0.005$, 0.1), $\angle R_{sp} = 0$. This

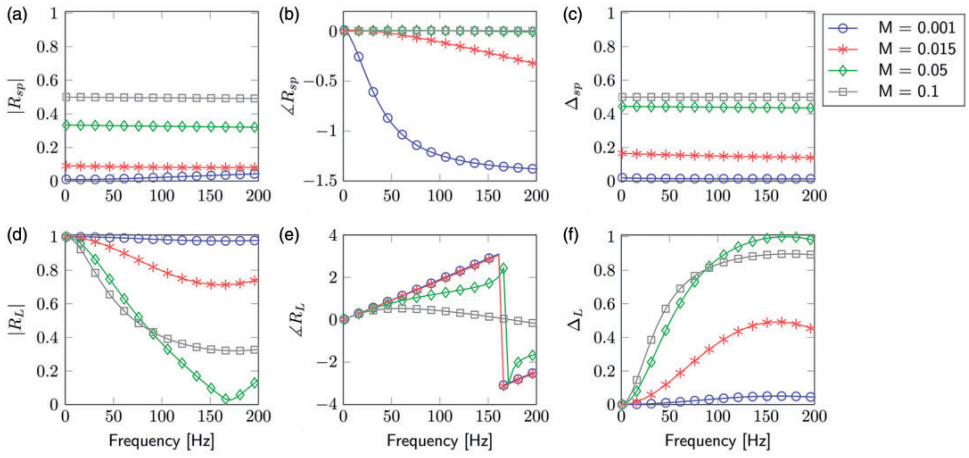

Figure 4. Reflection coefficient and absorption coefficient of slit-plate ((a)–(c)) and cavity-backed slit-plate ((d)–(f)) as a function of frequency, for fixed Mach numbers and $\nu = 0.1$. For (d)–(f), $l_c = 0.5$ m.

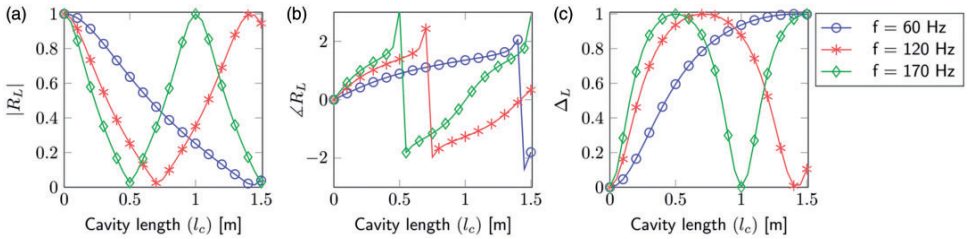

Figure 5. Reflection coefficient ((a)–(b)) and absorption coefficient ((c)) of cavity-backed slit-plate, as a function of cavity length, for fixed frequencies, $M = 0.05$ and $\nu = 0.1$.

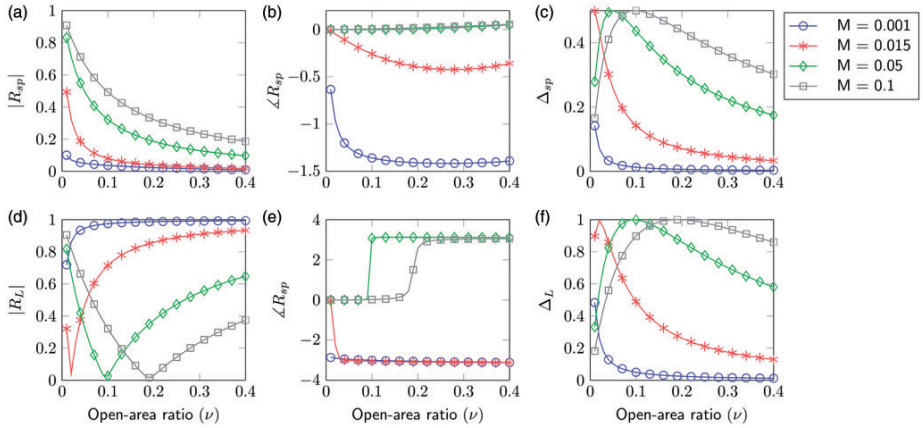

Figure 6. Reflection coefficient and absorption coefficient of slit-plate ((a)–(c)) and cavity-backed slit-plate ((d)–(f)) as a function of open area ratio, for fixed Mach numbers and $f = 170$ Hz. For (d)–(f), $l_c = 0.5$ m.

can again be explained by the hydrodynamic blockage effects (vena contracta and boundary layer) mentioned in Section 3.1. As a result, the slit-plate in isolation behaves like an increasingly reflective rigid wall as the Mach number increases; also its ability to absorb weakens as ν increases because less vortex shedding occurs.

The consequences for the cavity-backed slit-plate are shown in Figure 6(d), (e), (f), again for the case $f = 170$ Hz and $l_c = 0.5$ m. Except for the lowest Mach number ($M = 0.001$), $|R_L|$ decreases for small ν values, reaches a minimum and then steadily increases. At the minimum, $\measuredangle R_L$ jumps from 0 to $\pm\pi$, and Δ_L reaches the optimal value of 1. The width of the minimum of $|R_L|$ and maximum of Δ_L is again conveniently wide, as is the case for the parameters examined in the previous three sections.

3.5 Influence of open-end cavity

We also considered the case of a cavity bounded by an open end (rather than a closed end) at $x = L + l_c$ and investigated the dependence on the parameters M, f, l_c and ν. The results (not shown) are very similar: $|R_L|$ has a minimum when the cavity is at anti-resonance; this now happens when the cavity length is equal to half a wavelength. The optimal values for M, f, l_c and ν change, but $|R_L|$ is still close to 0 and Δ_L is still close to 1 in a large parameter range.

In summary, for a given f, the absorption coefficient of a cavity-backed slit-plate can be maximised if we choose the appropriate l_c, ν and M. In the case of a combustor with an unstable mode, the frequency of the unstable mode is known. Therefore, given a fixed slit-plate dimension, we aim to stabilise the combustor by choosing the appropriate bias flow Mach number, M, and cavity length, l_c.

4 Stability predictions

For stability predictions, we make use of the eigenvalue method,[17] which is instrumental in obtaining the growth rates of different modes in the system. In the

present work, we restrict ourselves to the first and second modes of the combustor.

4.1 Boundary and jump conditions

The unknowns in our system are the four pressure amplitudes A, B, C and D. Therefore, we need four homogeneous equations, obtained from the following boundary and jump conditions.

At $x = 0$:

$$Ae^{-ik_1 l_f} = R_0 Be^{ik_1 l_f} \tag{14}$$

At $x = L$:

$$De^{-ik_2(L-l_f)} = R_L Ce^{ik_2(L-l_f)} \tag{15}$$

R_0 and R_L are the reflection coefficients at $x = 0$ and $x = L$, respectively.

Across the heat source ($x = l_f$), we assume continuity of pressure,

$$A + B = C + D \tag{16}$$

and a velocity jump generated by the heat source[18]

$$-\frac{(A-B)}{\rho_1 c_1} + \frac{(C-D)}{\rho_2 c_2} = \frac{(\gamma-1)}{\rho_1 c_1^2 S}\hat{Q}(l_f) \tag{17}$$

where S is the cross-sectional area of the duct and γ is the ratio of the specific heat capacities.

4.2 Eigenfrequencies and growth rates

Equations (14)–(17) can be rearranged in matrix form to yield:

$$[Y(\Omega)]\begin{bmatrix} A \\ B \\ C \\ D \end{bmatrix} = \begin{bmatrix} 0 \\ 0 \\ 0 \\ 0 \end{bmatrix} \tag{18}$$

with

$$Y(\Omega) = \begin{bmatrix} e^{-i\frac{\Omega}{c_1}l_f} & -R_0 e^{i\frac{\Omega}{c_1}l_f} & 0 & 0 \\ 0 & 0 & R_L e^{i\frac{\Omega}{c_2}(L-l_f)} & -e^{-i\frac{\Omega}{c_2}(L-l_f)} \\ 1 & 1 & -1 & -1 \\ \left(-1-\beta_1 e^{i\Omega\tau}+\beta_0\right) & \left(1+\beta_1 e^{i\Omega\tau}-\beta_0\right) & \zeta & -\zeta \end{bmatrix} \tag{19}$$

where $\beta_{0,1} = \left(\alpha n_{0,1}(\gamma-1)\right)/\left(S\rho_1 c_1^2\right)$ is a quantity proportional to the coupling coefficients and $\zeta = (\rho_1 c_1)/(\rho_2 c_2)$ is the ratio of the specific impedances.

Solution of the characteristic equation, $\det Y(\Omega) = 0$, using the Newton Raphson or bisection method, gives us the eigenfrequencies of the system. The solution $\Omega_m = \omega_m + i\delta_m$ is a complex quantity where ω_m denotes the natural frequency of the mode m and δ_m its growth rate. Positive δ_m indicates instability and negative δ_m indicates stability.

4.3 Stability maps – closed end

From equation (19), one can infer that the parameters which affect the stability of the combustor are: the properties of the medium inside the duct ($\rho_{1,2}$, $c_{1,2}$, $T_{1,2}$), the duct length (L), the location of the heat source (l_f), the reflection coefficients at the boundaries (R_0 and R_L), the time-lag (τ) and the heat release rate law properties (α and $n_{0,1}$). In addition to these parameters, cavity length (l_c), slit-plate dimensions (d and v) and bias flow Mach number (M) have an indirect influence through R_L. Here, we consider the influence of the following three parameters: cavity length, heat source location and bias flow Mach number.

The stability maps are constructed in the cavity length (l_c) – heat source location (l_f) plane, where the *grey* regions indicate instability and the *white* regions indicate stability. Stability of any mode is determined from the sign of its growth rate, as mentioned in the previous section. In our study, we look at the stability of the first two modes of the system. The cold region is assumed to be at room temperature ($T_1 = 288\,\mathrm{K}$) and the hot region is assumed to be at $T_2 = 1288\,\mathrm{K}$. The duct length L is assumed to be 1 m, duct cross-section S is assumed to be $0.05 \times 0.05\ \mathrm{m}^2$ and the heat release rate law properties are taken as constants: $\alpha = 120$ kg m/s^2, $n_1 = 1.2$, $n_0 = 0.2$ and $\tau = 0.15 \times 10^{-3}$ s. Table 1 shows the range of the conservative estimates of the time periods for the first and second eigenmodes. We can observe that the time-lag chosen in our analysis is much smaller than the fundamental periods encountered in the stability analysis. The complete list of system parameters used in the forthcoming analysis is given in Table 2.

Firstly, we construct the stability map for mode 1 of a quarter-wave resonator containing only a heat source and no slit-plate, for two temperature distributions: $T_1 = T_2 = 288\,\mathrm{K}$ (Figure 7 (a)) and $T_1 = 288\,\mathrm{K}$, $T_2 = 1288\mathrm{K}$ (Figure 7(b)). We observe from the plots that the system is unstable for the range of values of l_c and l_f considered. This behaviour can be explained in terms of the mode shape of the wave within the resonator. In the absence of the slit-plate, an increase in cavity length (l_c) effectively adds to the duct length, L. The total length of the resonator will now be $(L + l_c)$. The first mode shape of the quarter-wave resonator will be, as the name suggests, a quarter wave with a node at $x = 0$ and a maximum at $x = (L + l_c)$. From the Rayleigh criterion, we can conclude this instability behaviour of the first mode of the resonator, regardless of the cavity length and heat source location considered.

Table 1. Range of time periods of the eigenfrequencies in the stability maps.

Mode	Temperature distribution	Time period range
1	$T_1 = 288$ K, $T_2 = 1288$ K	$[5.6 \ldots 16.6] \times 10^{-3}$ s
2	$T_1 = 288$ K, $T_2 = 1288$ K	$[1.4 \ldots 5.2] \times 10^{-3}$ s

Table 2. List of system parameters used.

Parameter	Notation	Value
Temperature [K]	$\boldsymbol{T_1}$	288
	$\boldsymbol{T_2}$	1288
Density [kg/m^3]	ρ_1	1.2
	ρ_2	0.268
Speed of sound [m/s]	$\boldsymbol{c_1}$	341
	$\boldsymbol{c_2}$	721.5
Duct length [m]	L	1
Cross-sectional area [m^2]	$\boldsymbol{S}$	0.0025
Cavity length [m]	$\boldsymbol{l_c}$	$[0 \cdots \boldsymbol{L}/2]$
Heat source location [m]	$\boldsymbol{l_f}$	$[0 \cdots \boldsymbol{L}]$
Time-lag law parameters	α [kg m/s^2]	120
	$\boldsymbol{n_1}$	1.2
	$\boldsymbol{n_0}$	0.2
	τ [s]	0.15×10^{-3}
Slit-plate	$\boldsymbol{d}$ [m]	0.02
	ν	0.1

Next, we introduce a slit-plate with bias flow into the system. The slit dimensions are $d = 0.02\,\mathrm{m}$ and $\nu = 0.1$. The present study is an extension to the work by Surendran and Heckl,[19] where they investigated the effect of the bias flow Mach number M and cavity length on the stability of a quarter-wave resonator with a heat source obeying the simple $n - \tau$ law. They observed that the stability of the first mode increased with increasing M. Figure 8 shows the stability maps obtained for the current resonator configuration with uniform temperature distribution and generic heat release law. In this study also, the stability maps exhibit trends similar to those reported by Surendran and Heckl.[19] At very low M, the unstable region is larger compared to the stable region (Figure 8(a)). As we increase M, the stable region increases (Figure 8(b) and (c)). We also get a range of l_c values where the resonator is stable, irrespective of the location of the heat source.

The influence of l_c and M on the stability of the combustor can be explained through the contour plot of ω_1, the real part of the complex eigenfrequency Ω_1, as shown in Figure 9. The contours vary in the range ~55–85 Hz, and correspond to mode 1 of the combustor with $T_1 = T_2 = 288\,\mathrm{K}$. The eigenfrequencies decrease with increasing l_c and from Figure 5(c), we can conclude that for a given bias flow M, an acoustic wave of 55 Hz with $\boldsymbol{l_c} = 0.5\,\mathrm{m}$ has higher absorption

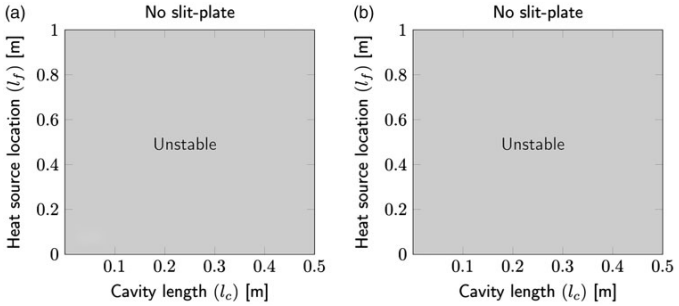

Figure 7. Stability map for mode 1 without slit-plate and bias flow with (a) $T_1 = T_2 = 288$ K and (b) $T_1 = 288$ K and $T_2 = 1288$ K.

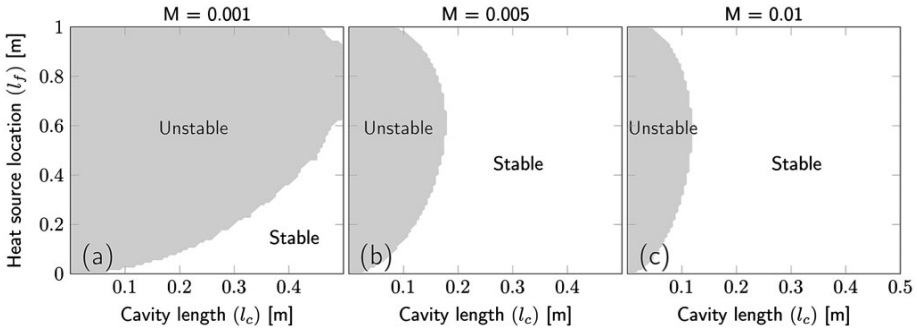

Figure 8. Stability maps for mode 1 and different Mach numbers (a) $M = 0.001$, (b) $M = 0.005$ and (c) $M = 0.01$, for a combustor with $T_1 = T_2 = 288$K.

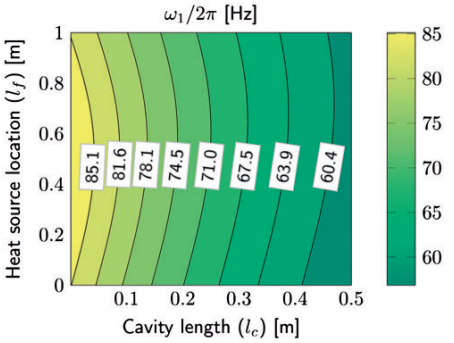

Figure 9. Eigenfrequency ($\omega_1/2\pi$) (Hz) contour for mode 1 of the combustor with $T_1 = T_2 = 288$ K.

than a wave of 80 Hz with $l_c = 0.1$ m. The influence of bias flow M is shown in Figure 3(f). For a given frequency and l_c, the absorption increases with increasing M. Combining these effects, we can explain the stability maps shown in Figure 8. The combustor starts to stabilise for higher l_c, and the stable regions grow as we increase the bias flow M.

As a step further to our study, we also incorporated a temperature jump across the heat source ($T_1 = 288$ K and $T_2 = 1288$ K). The stability maps, again constructed in the l_f –l_c plane for three Mach numbers: $M = 0.001$, 0.005 and 0.01, are given in Figure 10. Comparison of Figure 10 and Figure 8 shows that having a hot region or temperature nonuniformity within the combustor tends to de-stabilise it, i.e., the unstable regions are larger. But in this case also, we can extend the stable regions of the system by increasing M. Hence, it is still possible to find a cavity length and Mach number that stabilises the combustion system.

Similar stability maps can also be constructed for the second mode of the resonator. Here also, we start with the no slit-plate case. Figure 11(a) and (b) shows the stability maps for the second mode when we have uniform and nonuniform temperature distribution, respectively. The stability maps are as expected. In the second mode, we have three-quarters of a wave within the combustor and as the heat source changes its position from the inlet towards the slit-plate, we get constructive and destructive interaction between the heat release rate fluctuations and the acoustic pressure fluctuations leading to alternating stable and unstable regions. In Figure 11(a), the small unstable region near $l_c = 0.5$ m for $l_f = [0.5 \cdots 1]$ m is caused by non-convergence of the numerical method used. Ideally, this region should also be stable.

Now, we introduce the slit-plate with the bias flow. Figure 12 shows the stability maps for mode 2 of the combustor with uniform temperature distribution and Figure 13 shows the stability maps when there is nonuniform temperature distribution. We observe that the unstable regions get fragmented and slowly turn into stable regions as we increase M. The effect of Mach number is similar for both the temperature distributions. Again, we are able to find ranges for the Mach number and cavity length that could stabilise the already unstable modes of the combustor. In Figure 12(a) also, the small region near $l_c = 0.5$ m for $l_f = [0 \cdots 1]$ m should have been stable. But this unstable region is caused by non-convergence of the numerical method used.

4.4 Stability maps – open end

In this section, we look at the stability maps for the resonator with open ends. The stability maps are again constructed in the cavity length (l_c) – heat source location (l_f) plane. The properties of the system are the same as those given in the previous section. The cold region is assumed to be at room

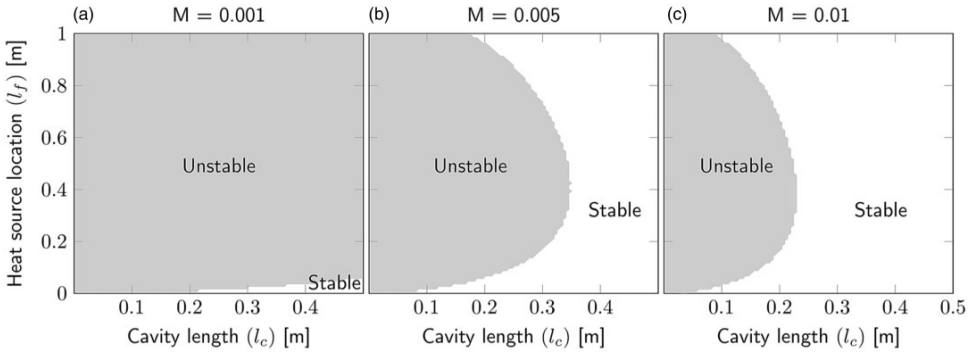

Figure 10. Stability maps for mode 1 and different Mach numbers (a) $M = 0.001$, (b) $M = 0.005$ and (c) $M = 0.01$, for a combustor with $T_1 = 288$ K and $T_2 = 1288$ K.

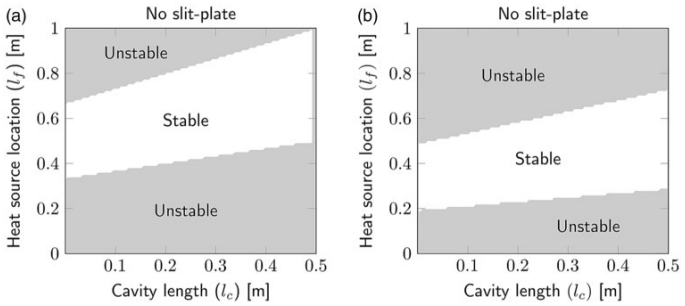

Figure 11. Stability map for mode 2, without slit-plate and bias flow with (a) $T_1 = T_2 = 288$ K and (b) $T_1 = 288$ K and $T_2 = 1288$ K.

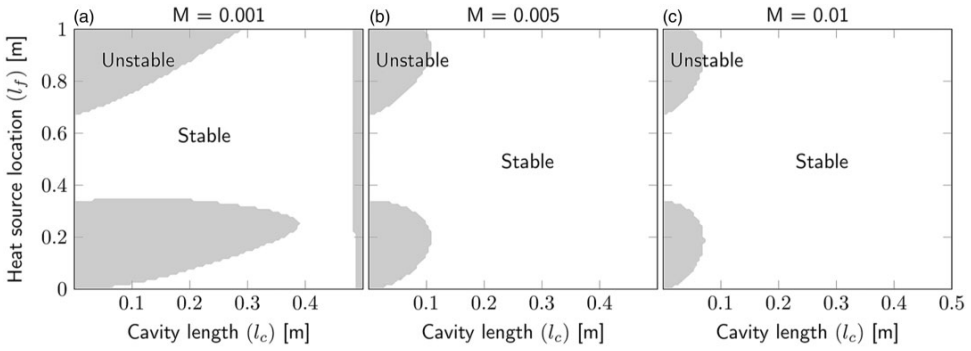

Figure 12. Stability maps for mode 2 and different Mach numbers (a) $M = 0.001$, (b) $M = 0.005$ and (c) $M = 0.01$, for a combustor with $T_1 = T_2 = 288$ K.

temperature ($T_1 = 288$ K) and the hot region is assumed to be at $T_2 = 1288$ K. The duct length L is assumed to be 1 m, the duct cross-section S is assumed to be 0.05×0.05 m^2 and the heat release rate law properties are taken as constants: $\alpha = 120$ kg m/s^2, $n_1 = 1.2$, $n_0 = 0.2$ and $\tau = 0.15 \times 10^{-3}$ s. Table 3 shows the range of the conservative estimates of the time periods for the first and second eigenmodes. The time-lag

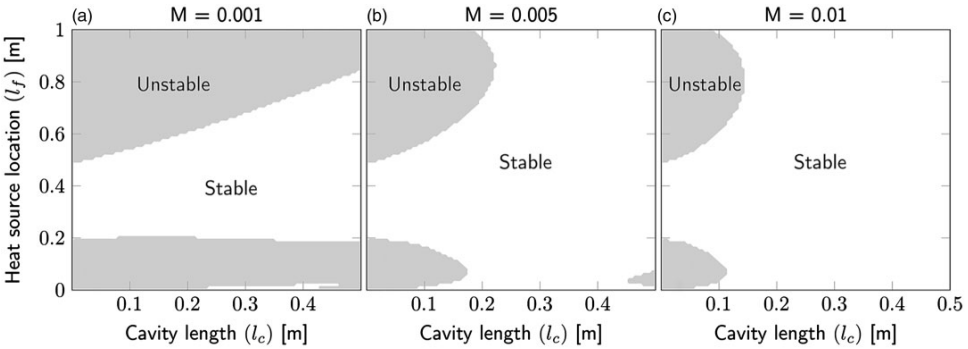

Figure 13. Stability maps for mode 2 and different Mach numbers (a) $M = 0.001$, (b) $M = 0.005$ and (c) $M = 0.01$, for a combustor with $T_1 = 288$ K and $T_2 = 1288$ K.

Table 3. Range of time periods of the eigenfrequencies in the stability maps.

Mode	Temperature distribution	Time period range
1	$T_1 = 288$ K, $T_2 = 1288$ K	$[2.7 \cdots 6.7] \times 10^{-3}$ s
2	$T_1 = 288$ K, $T_2 = 1288$ K	$[1.3 \cdots 3.5] \times 10^{-3}$ s

chosen is much smaller than the fundamental periods encountered in the stability analysis.

Like in the previous section, we start with the stability maps for the no slit-plate case. Figure 14 shows the stability maps for mode 1 of the resonator with no slit-plate, for uniform (Figure 14 (a)) and nonuniform (Figure 14 (b)) temperature distributions. The results obtained for the uniform temperature distribution (Figure 14 (a)) show that the resonator is stable when the heat source is placed in the lower half (downstream section) of the resonator. This is because the first mode shape within the resonator is half a wave with nodes at $x = 0$ and $x = (L + l_c)$, and using the Rayleigh criterion, we can deduce that the system will have a stable mode when the heat source is placed in the lower half of the resonator. When there is a temperature jump, we observe that the stable region is larger (Figure 14(b)), and this can be attributed to the frequency shift due to the temperature jump and the changes in the speed of sound. In other words, the presence of the heat source and the consequent temperature jump modifies the mode shape such that we get a constructive interference between acoustic pressure fluctuations and heat release rate fluctuations leading to stable behaviour.

The introduction of slit-plate with bias flow changes the stability behaviour significantly. Figures 15 and 16 show the stability maps for the resonator with uniform and nonuniform temperature distribution, respectively, after the inclusion of the slit-plate with bias flow. The Mach number M increases from plots (a) to (c), and we observe the increased stability of the resonator. Unlike the closed end case, in the open end situation, we get complete stability for higher M values (Figures 15 and 16(b) and (c)).

Finally, stability maps are also constructed for the second mode of the open end resonator. The no slit-plate cases for the two temperature distributions are shown in Figure 17(a) and (b). The alternating unstable and stable bands are due to the mode shape of the pressure wave and its interaction with the heat release rate fluctuations. In the second mode, we have a full wave within the combustor leading to alternating stable and unstable regions.

Figure 18 shows the stability maps for mode 2 of the combustor with uniform temperature distribution and Figure 19 shows the stability maps for the nonuniform temperature distribution. We observe that the unstable regions decrease as we increase M. The effect of Mach number is similar for both the temperature distributions. There is a wide range of cavity lengths that could stabilise the unstable mode of the resonator.

5 Summary and outlook

We presented a model for an idealised combustor with heat exchanger to predict its stability behaviour. The combustion system consisted of a one-dimensional tube with a compact flame and a mean temperature jump across the heat source. The heat exchanger is modelled as an array of thin sharp-edged rods with rectangular cross-sections. Hence, the heat exchanger was treated as a slit-plate. We also included a bias flow through the slits to enhance the sound absorption characteristic of the slit-plate. Instead of a simple $n - \tau$ law, we have used an extended version of the time-lag law to describe the heat source.

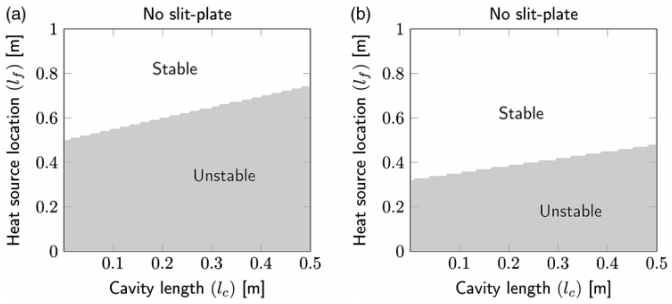

Figure 14. Stability map for mode 1 without slit-plate and bias flow with (a) $T_1 = T_2 = 288$ K and (b) $T_1 = 288$ K and $T_2 = 1288$ K.

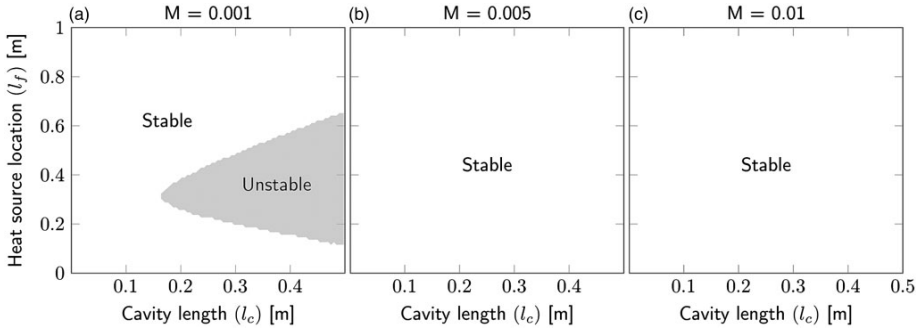

Figure 15. Stability maps for mode 1 and different Mach numbers (a) $M = 0.001$, (b) $M = 0.005$ and (c) $M = 0.01$, for a combustor with $T_1 = T_2 = 288$ K.

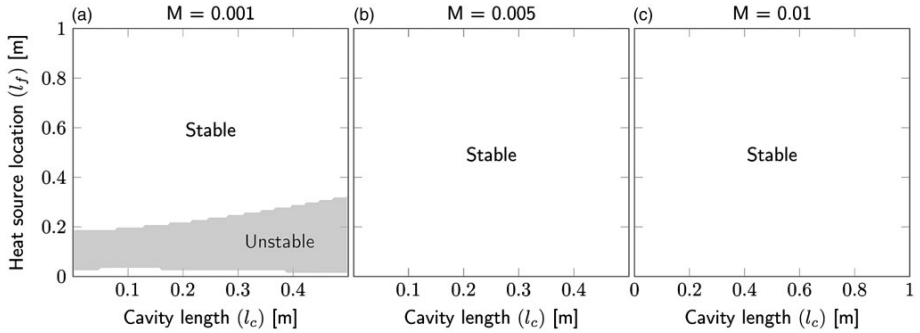

Figure 16. Stability maps for mode 1 and different Mach numbers (a) $M = 0.001$, (b) $M = 0.005$ and (c) $M = 0.01$, for a combustor with $T_1 = 288$ K and $T_2 = 1288$ K.

Our model is applied to the idealised combustion system with tuneable downstream end condition, that is, by varying the aeroacoustic properties of the slit-plate backed by an open end or a rigid end, we can tune the downstream reflection coefficient. Stability maps constructed in the cavity length (l_c) – location of heat source (l_f) plane yield the following results:

- The unstable mode of a combustor can be controlled passively by a bias-flow slit-plate provided that the

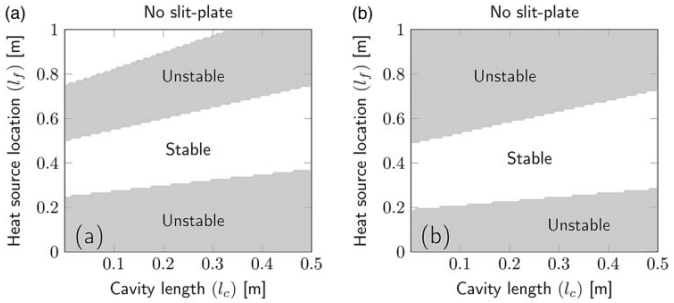

Figure 17. Stability map for mode 2 without slit-plate and bias flow with (a) $T_1 = T_2 = 288$ K and (b) $T_1 = 288$ K and $T_2 = 1288$ K.

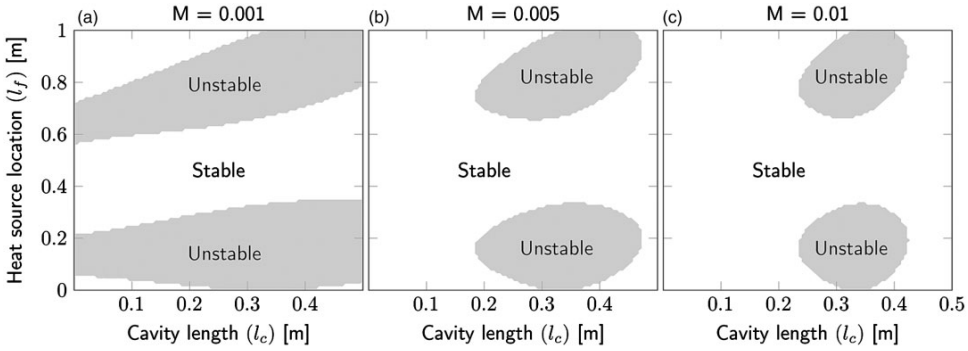

Figure 18. Stability maps for mode 2 and different Mach numbers (a) $M = 0.001$, (b) $M = 0.005$ and (c) $M = 0.01$, for a combustor with $T_1 = T_2 = 288$ K.

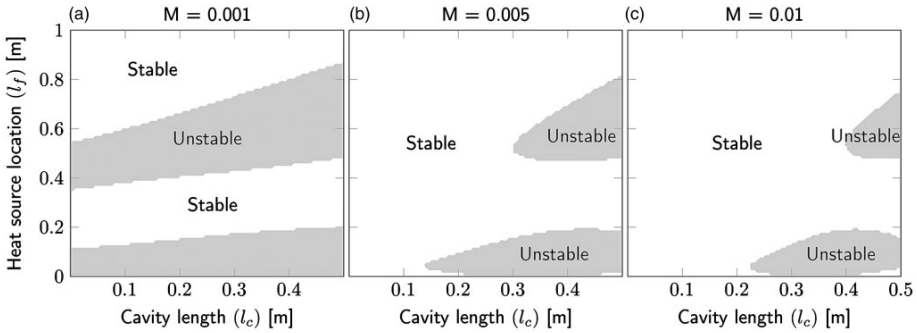

Figure 19. Stability maps for mode 2 and different Mach numbers (a) $M = 0.001$, (b) $M = 0.005$ and (c) $M = 0.01$, for a combustor with $T_1 = 288$ K and $T_2 = 1288$ K.

bias flow Mach number and the cavity length are chosen appropriately.

- For a particular unstable mode, an increase of the bias flow Mach number tends to enhance the stability of that mode.
- There is a wide range of cavity lengths, for fixed Mach number, that can be utilised to enhance the stability of the combustor,
- The temperature jump at the flame has a significant effect on the combustor's stability behaviour: it can

be stabilising or destabilising, and it is therefore important to include it in the model.

With our model, we are able to find a broad range of values for the bias flow Mach number and the cavity length that can be used to stabilise the already unstable modes of the combustion system considered. These findings have practical implications for combustion systems like domestic boilers. The need for clean and compact boilers makes it difficult for the inclusion of passive control components like quarter-wave resonators and Helmholtz resonators, that are generally bulky. In such situations, it is a viable alternative to use heat exchangers to control thermoacoustic instabilities.

In a domestic boiler, the heat exchanger is housed within the combustion chamber, along with the flame, and therefore there is no requirement for additional space. Our study shows that there is a wide range of values for l_c (distance between heat exchanger and combustion chamber end) and for M (Mach number of the flow through the gaps between the heat exchanger tubes) that stabilise a previously unstable combustion system. This form of passive instability control improves the design flexibility of domestic boilers, as no additional components are required. It opens the door for new designs of efficient and reliable boilers with reduced pollution of the environment.

Acknowledgements

The presented work is part of the Marie Curie Initial Training Network Thermo-acoustic and Aero-acoustic Nonlinearities in Green combustors with Orifice structures (TANGO). The authors are also thankful to Prof. Avraham Hirschberg, Technical University of Eindhoven, for the fruitful discussions on the acoustic behaviour of slit-plates in a duct.

Declaration of Conflicting Interests

The author(s) declared no potential conflicts of interest with respect to the research, authorship, and/or publication of this article.

Funding

The author(s) disclosed receipt of the following financial support for the research, authorship, and/or publication of this article: We gratefully acknowledge the financial support from the European Commission under call FP7-PEOPLE-ITN-2012.

References

1. Lieuwen TC and Yang V. *Combustion instabilities in gas turbine engines: operational experience, fundamental mechanisms, and modeling*. Reston, VA: American Institute of Aeronautics and Astronautics, Inc., 2005.
2. Munjal ML. *Acoustics of ducts and mufflers – with application to exhaust and ventilation system design*. New York: John Wiley and Sons Ltd., 1987.
3. Davies POAL. Practical flow duct acoustics. *J Sound Vib* 1988; 124: 91–115.
4. Ronneberger D. Experimentelle Untersuchungen zum akustischen Reflexionsfaktor von unstetigen Querschnittsänderungen in einem luftdurchströmten Rohr [Experimental investigations about the acoustic reflection coefficient of discontinuous changes of cross-section in tubes with air flow]. *Acustica* 1967; 19: 222–235.
5. Bechert DW. Sound absorption caused by vorticity shedding, demonstrated with a jet flow. *J Sound Vib* 1980; 70: 389–405.
6. Hughes IJ and Dowling AP. The absorption of sound by perforated linings. *J Fluid Mech* 1990; 218: 299–335.
7. Tran N, Ducruix S and Schuller T. Damping combustion instabilities with perforates at the premixer inlet of a swirled burner. *Proc Combust Inst* 2009; 32: 2917–2924.
8. Tran N, Ducruix S and Schuller T. Passive control of the inlet acoustic boundary of a swirled burner at high amplitude combustion instabilities. *ASME J Eng Gas Turb Power* 2009; 131: 051502/1–7.
9. Scarpato A, Tran N, Ducruix S, et al. Modeling the damping properties of perforated screens traversed by a bias flow and backed by a cavity at low Strouhal number. *J Sound Vib* 2012; 331: 276–290.
10. Scarpato A, Ducruix S and Schuller T. A comparison of the damping properties of perforated plates backed by a cavity operating at low and high Strouhal numbers. *Comptes Rendus Mécanique* 2013; 341: 161–170.
11. Heckl M and Kosztin B. Analysis and control of an unstable mode in a combustor with tuneable end condition. *Int J Spray Combust Dynam* 2013; 5: 243–272.
12. Hofmans GCJ, Boot RJJ, Durrieu PPJM, et al. Aeroacoustics response of a slit-shaped diaphragm in a pipe at low Helmholtz number, 1: Quasi-steady results. *J Sound Vib* 2001; 244: 35–56.
13. Durrieu P, Hofmans G, Ajello G, et al. Quasisteady aeroacoustic response of orifices. *J Acoust Soc Am* 2001; 110: 1859–1872.
14. Howe MS. On the theory of unsteady high Reynolds number flow through a circular aperture. *Proc Math Phys Eng Sci* 1979; 366: 205–223.
15. Dowling AP and Hughes IJ. Sound absorption by a screen with a regular array of slits. *J Sound Vib* 1992; 156: 387–405.
16. Surendran A and Heckl MA. Analytical study of a Rijke tube with heat exchanger. In: *The 21st international congress on sound and vibration*, Beijing, China, 13–17 July 2014.
17. Heckl MA. *Heat sources in acoustic resonators*. PhD Thesis, Emmanuel College, Cambridge, 1985.
18. Heckl MA. Active control of the noise from a Rijke tube. *J Sound Vib* 1988; 124: 117–133.
19. Surendran A and Heckl MA. Passive instability control by using a heat exchanger as acoustic sink. In: *The 22nd international congress on sound and vibration*, Florence, Italy, 12–16 July 2015.

Appendix B

Transfer Function Approximations

The mathematical approximations for HTF were obtained by assuming

$$\log\left(|\mathrm{HTF}|\right) = \begin{cases} a_0 + a_1 f + a_2 f^2 + a_3 f^3 & f \leq f_p \\ b_0 + b_1 \sqrt{f} & f \geq f_p \end{cases} \tag{B.1}$$

$$\Phi\left(\mathrm{HTF}\right) = \begin{cases} e_0 + e_1 f + e_2 f^2 + e_3 f^3 + e_4 f^4 & f \leq f_p \\ g_0 + g_1 \sqrt{f} + g_2 f + g_3 \left(\sqrt{f}\right)^3 + g_4 f^2 & f \geq f_p \end{cases}, \tag{B.2}$$

where $f_p = 500$Hz for $|HTF|$ and $f_p = 200$Hz for $\Phi(HTF)$. Simulations were conducted for diameters 3mm and 5mm, open area ratios 0.1 and 0.2, and inlet velocities 0.5, 1.0 and 1.5m/s. Open area ratio is the ratio between the gap height h_g and the tube diameter d. The complete set of data for the simulations and their approximations are included in this appendix.

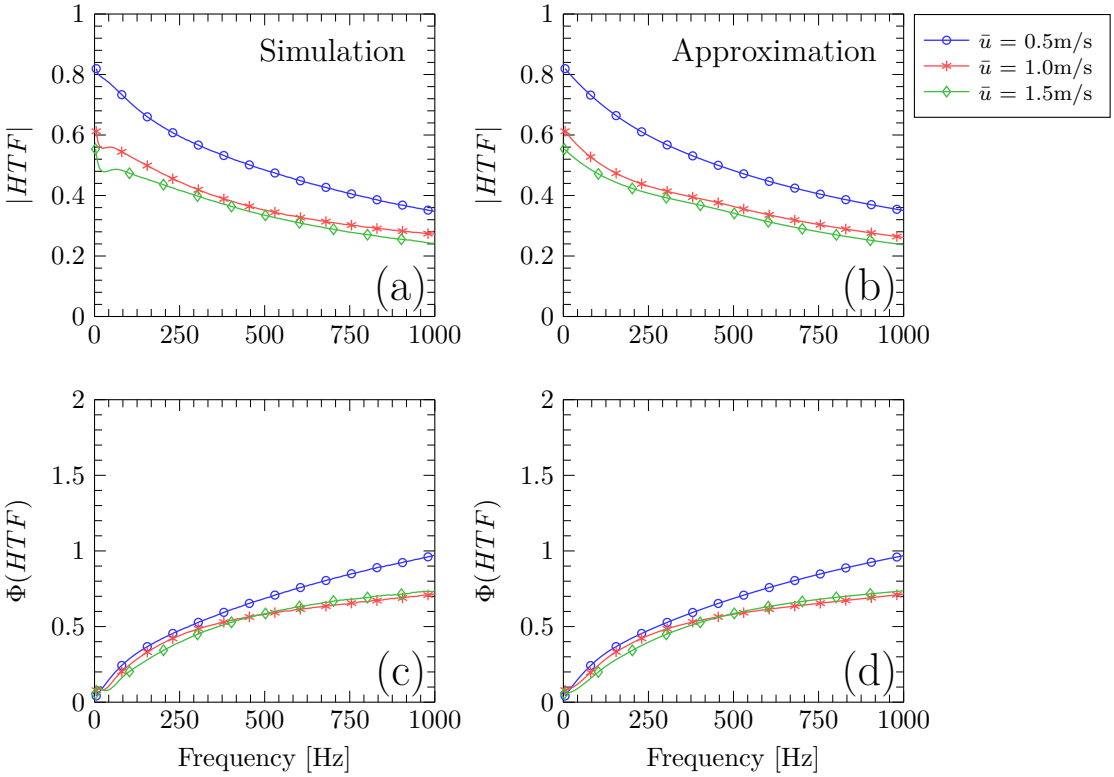

Figure B.1: Comparison of |HTF| and Φ(HTF) obtained from numerical simulations ((a) and (c)) with their approximations ((b) and (d)), for $d = 3$mm, $h_g = 0.3$mm and different mean velocities, $\bar{u}$.

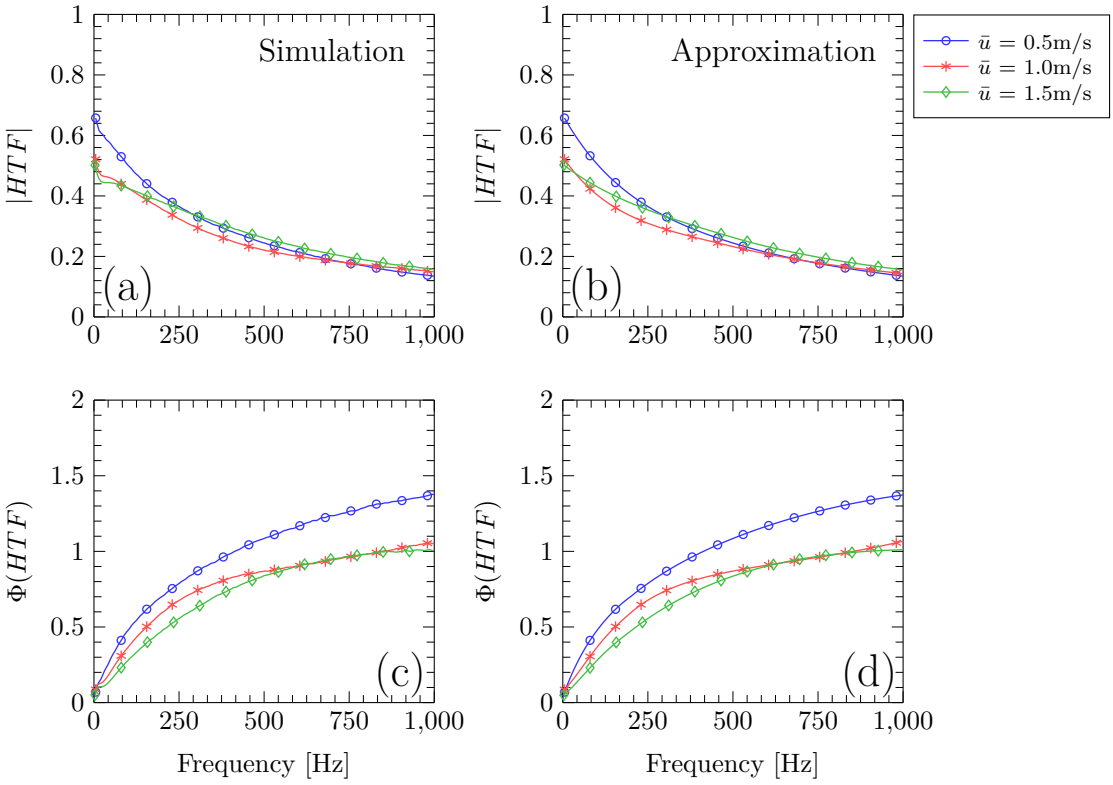

Figure B.2: Comparison of |HTF| and Φ(HTF) obtained from numerical simulations ((a) and (c)) with their approximations ((b) and (d)), for $d = 3$mm, $h_g = 0.6$mm and different mean velocities, $\bar{u}$.

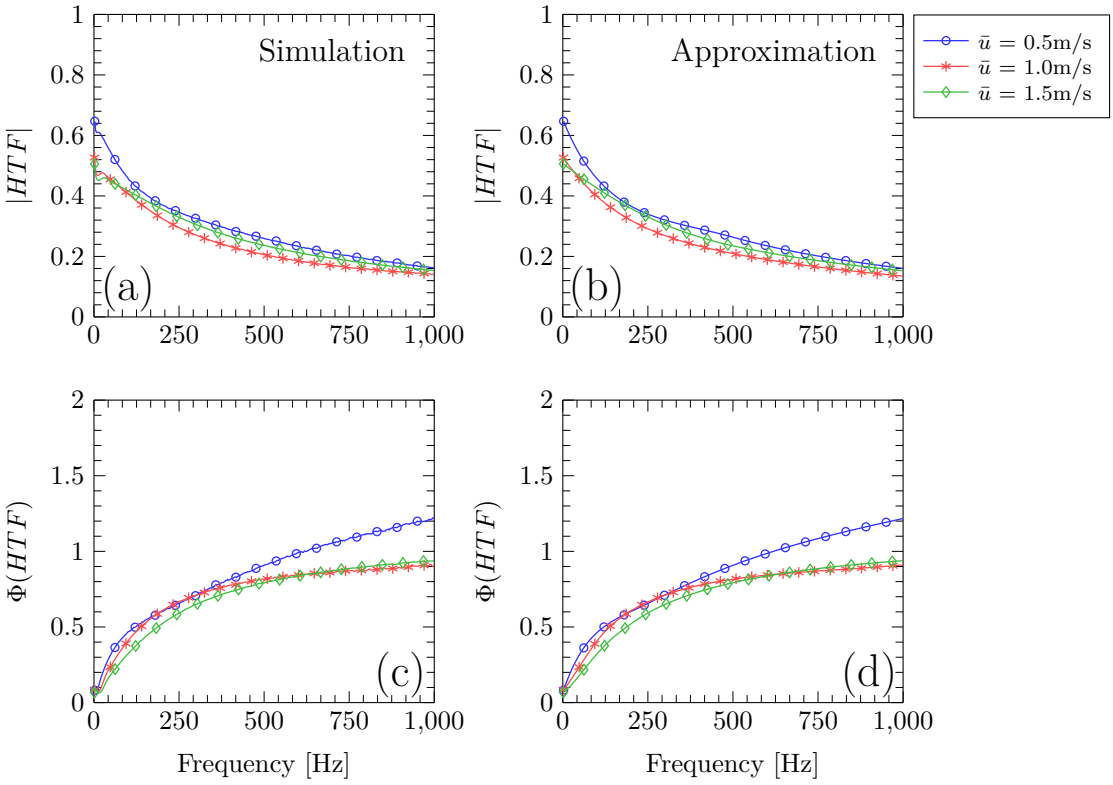

Figure B.3: Comparison of |HTF| and Φ(HTF) obtained from numerical simulations ((a) and (c)) with their approximations ((b) and (d)), for $d = 5$mm, $h_g = 0.5$mm and different mean velocities, $\bar{u}$.

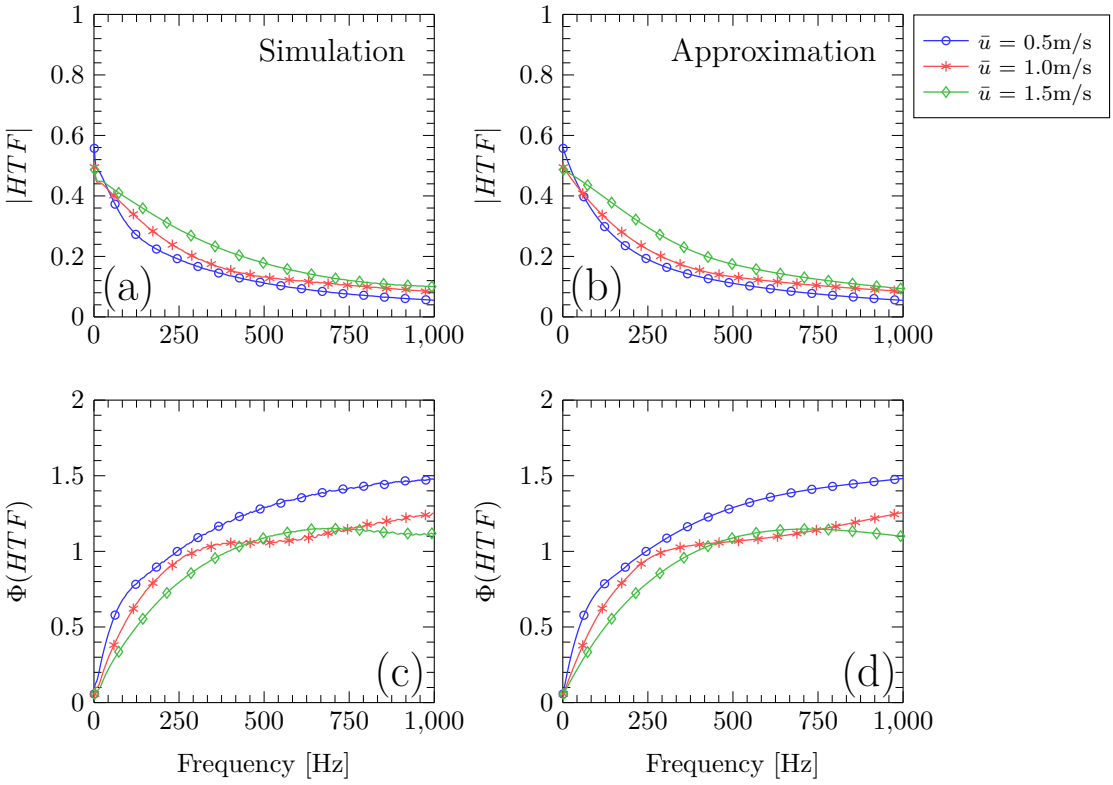

Figure B.4: Comparison of |HTF| and Φ(HTF) obtained from numerical simulations ((a) and (c)) with their approximations ((b) and (d)), for d = 5mm, h_g = 1mm and different mean velocities, $\bar{u}$.

Appendix C

Flow separation point calculation

In order to find the flow separation point on the cylinder, we start with the boundary layer equations (Schlichting, 1979). Consider a solid surface in a high Reynolds number flow as shown in the schematic in Fig. C.1. Very close to the solid surface we have the boundary layer where all the viscous effects are confined. The flow around the body can be divided into two : (1) the 1-D inviscid bulk or mean flow denoted by $U(x)$, and (2) the 2-D flow within the boundary layer, denoted by $\tilde{u}(x, y)$ and $\tilde{v}(x, y)$. Applying the conservation of mass and momentum to the bulk flow, we obtain

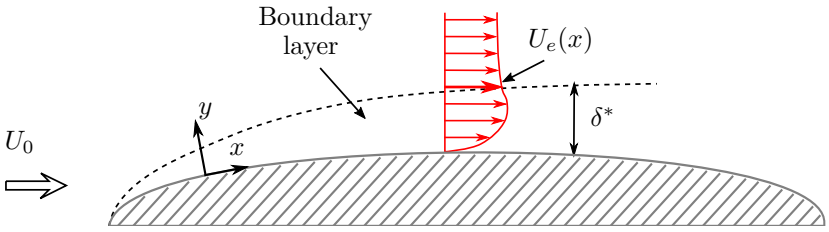

Figure C.1: Schematic of the boundary layer formed on a solid surface

$$\frac{\partial U}{\partial y} = 0, \tag{C.1}$$

$$\frac{\partial U}{\partial t} + U\frac{\partial U}{\partial x} = \frac{-1}{\rho}\frac{\partial P}{\partial x}, \tag{C.2}$$

$$0 = \frac{-1}{\rho}\frac{\partial P}{\partial y} \tag{C.3}$$

where P denotes the pressure field in the bulk flow. Similarly for the boundary layer flow, we get

$$\frac{\partial \tilde{u}}{\partial x} + \frac{\partial \tilde{v}}{\partial y} = 0, \tag{C.4}$$

$$\frac{\partial \tilde{u}}{\partial t} + \tilde{u}\frac{\partial \tilde{u}}{\partial x} + \tilde{v}\frac{\partial \tilde{u}}{\partial y} = \frac{-1}{\rho}\frac{\partial \tilde{p}}{\partial x} + \nu\frac{\partial^2 \tilde{u}}{\partial y^2}, \tag{C.5}$$

$$0 = \frac{-1}{\rho}\frac{\partial \tilde{p}}{\partial y} \tag{C.6}$$

where $\tilde{p}$ is the pressure field within the boundary layer, and ν is the kinematic viscosity of the fluid. Equations (C.4) - (C.6) form the so-called *Prandtl equations*. From Eqs. (C.3) and (C.6), we can infer that the pressure across the boundary layer, in the y direction is uniform. In other words, we can assume the pressure on the surface of the solid body to be equal to the pressure at the edge of the boundary layer. Therefore, from Eq. (C.2), we can calculate the pressure gradient at the edge of the boundary layer as

$$\frac{\partial P}{\partial x} = -\rho\frac{\partial U_e(x)}{\partial t} - \rho U_e(x)\frac{\partial U_e(x)}{\partial x}. \tag{C.7}$$

where $U_e(x)$ denotes the bulk flow velocity at the edge of the boundary layer. Equation (C.7) matches the outer bulk flow solution to the inner boundary layer solution.

C.1. von Kármán equation

Before deriving the von Kármán equation, we define two quantities to describe the boundary layer thickness.

1. *Displacement thickness* (δ^*) - This quantity can be interpreted as the distance by which the streamlines are displaced *inward* due to the presence of a boundary layer. It is defined as

$$\delta^*(x) = \int_0^\infty \left(1 - \frac{\tilde{u}}{U_e}\right) \mathrm{d}y \tag{C.8}$$

2. *Momentum thickness* (Θ) - This is a measure of the momentum loss, due to the presence of the boundary layer. This quantity is defined as

$$\Theta(x) = \int_0^\infty \frac{\tilde{u}}{U_e}\left(1 - \frac{\tilde{u}}{U_e}\right) \mathrm{d}y \tag{C.9}$$

The von Kármán equation is derived by combining Eqs. (C.5) and (C.7) along with the following boundary conditions

$$\tilde{u}(x,0) = 0 \qquad \text{(no slip at wall)}, \tag{C.10}$$
$$\tilde{v}(x,0) = 0 \qquad \text{(no flow through the wall)}, \tag{C.11}$$
$$\tilde{u}(x,\infty) = U_e(x) \qquad \text{(velocity matching at the edge)}, \tag{C.12}$$

and integrating along y. This will give us

$$\underbrace{\frac{\partial}{\partial t}\int_0^\infty U_e\left(1 - \frac{\tilde{u}}{U_e}\right)\mathrm{d}y}_{=\frac{\partial}{\partial t}(U_e\delta^*)} + \underbrace{\int_0^\infty \tilde{u}\frac{\partial}{\partial x}\left(U_e - \tilde{u}\right)\mathrm{d}y + \int_0^\infty \tilde{v}\frac{\partial}{\partial y}\left(U_e - \tilde{u}\right)\mathrm{d}y}_{=\frac{\partial}{\partial x}(U_e^2\Theta)} +$$
$$\underbrace{\frac{\mathrm{d}U_e}{\mathrm{d}x}\int_0^\infty U_e\left(1 - \frac{\tilde{u}}{U_e}\right)\mathrm{d}y}_{=\frac{\mathrm{d}U_e}{\mathrm{d}x}U_e\delta^*} = \underbrace{-\nu\int_0^\infty \frac{\partial^2\tilde{u}}{\partial y^2}\mathrm{d}y}_{=\frac{\tau_0}{\rho}}, \tag{C.13}$$

$$\frac{\partial}{\partial t}\left(U_e\delta^*\right) + U_e\delta^*\frac{\mathrm{d}U_e}{\mathrm{d}x} + \frac{\partial}{\partial x}\left(U_e^2\Theta\right) = \frac{\tau_0}{\rho}, \tag{C.14}$$

where τ_0 is the wall shear stress. Equation (C.14) is called the *unsteady von Kármán equation*.

C.2. Thwaites' Method

Thwaites (1949) (Kundu et al., 2012) developed an approximate solution to the von Kármán equation by using shape parameters that depend only on the shape of the velocity profile. These shape parameters are defined as,

$$\mathcal{H} = \frac{\delta^*}{\Theta} \qquad \text{and} \qquad \mathcal{T} = \frac{\Theta}{\nu U_e} = \frac{\tau_0}{\rho}. \tag{C.15, C.16}$$

The von Kármán equation (Eq. (C.14)) can now be written in terms of the only unknown variable Θ as,

$$\frac{\mathrm{d}}{\mathrm{d}x}\left(\frac{\Theta^2}{\nu}\right)+\frac{2}{U_e}\left[(\mathcal{H}+2)\frac{\mathrm{d}U_e}{\mathrm{d}x}\left(\frac{\Theta^2}{\nu}\right)-\mathcal{T}\right]=0. \tag{C.17}$$

Thwaites gave the following approximation to the shape parameters

$$2\,(\mathcal{H}+2)\,\lambda-2\mathcal{T}=6\lambda-0.45, \tag{C.18}$$

where $\lambda=\frac{\mathrm{d}U_e}{\mathrm{d}x}\frac{\Theta^2}{\nu}$. Substituting Eq.(C.18) in Eq. (C.17) and integrating it along the axial direction (x) gives us

$$\Theta^2=\frac{0.45\nu}{U_e^6(x)}\int_0^x U_e^5(\tilde{x})\mathrm{d}\tilde{x}+\frac{\Theta_0^2\,U_0^6}{U_e^6(x)}. \tag{C.19}$$

Here, $\tilde{x}$ is the integration variable and Θ_0 and U_0 are the values of Θ and U_e at $x=0$, respectively. If $x=0$ is a stagnation point, then $U_e=U_0=0$ and $\Theta=\Theta_0=0$. Once Θ is known, we can calculate λ and the shape parameters $\mathcal{H}$ and $\mathcal{T}$, from the table provided in Kundu et al. (2012). We can now use these parameters to find the flow separation location on the cylinder surface.

C.3. Flow separation location

Flow separation is the onset of flow reversal on the solid surface and the flow will no longer be attached to the surface. The schematic for a separated flow is shown in Fig. C.2. At the separation point S on the wall, the surface shear stress will go to zero. This implies that $(\partial u/\partial y)_{wall}=0$, or in terms of the shape parameter, $\mathcal{T}=0$. This will give the criterion for flow separation as $\lambda_S=-0.0992$.

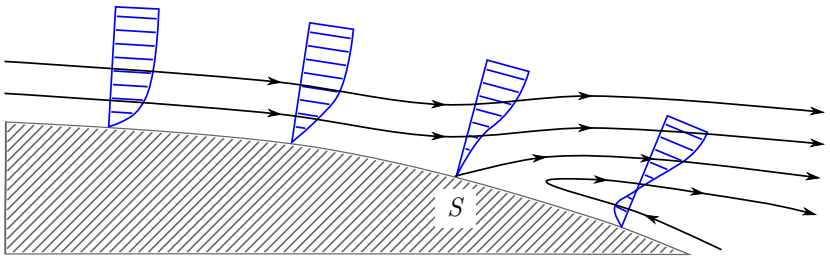

Figure C.2: Schematic of streamlines and velocity profiles near the flow separation point S

In order to find the separation location on the hex cylinder surface, we discretize the flow domain (Fig. C.3) into N divisions of interval Δx. The grid points are numbered sequentially and denoted by the subscript i. The algorithm for finding the grid point is as follows (Vilain et al., 2004):

1. Initialise $U_{e,1} = U_0$, $\Theta_1 = 0$, $\mathcal{H}_1 = 0$ and $\lambda_1 = 0$.

2. Evaluate

$$U_{e,i} = \frac{U_{e,1}\, h_1}{h_i - 2\,\mathcal{H}_{i-1}\,\Theta_{i-1}}, \tag{C.20}$$

$$\Theta_i = \sqrt{\frac{0.45\,\nu\,\Delta x \sum_{j=1}^{i} U_{e,j}^5}{U_{e,i}^6}}, \tag{C.21}$$

$$\lambda_i = \frac{\Theta_i^2}{\nu}\frac{U_{e,i} - U_{e,i-1}}{\Delta x}, \tag{C.22}$$

   where h_i is the height of the duct at any location x_i along the flow direction.

3. Once λ_i is known, evaluate $\mathcal{H}(\lambda_i)$ from the table

4. Using a relaxation scheme, iterate for $U_{e,i}$, Θ_i, λ_1 and $\mathcal{H}_i$, till they converge.

5. Check for flow separation by comparing the value of λ_i with λ_S.
   - If $\lambda_i \neq \lambda_S$, move to the next grid point and repeat steps 2 to 5.
   - If $\lambda_i = \lambda_S$, compute the location of separation for the corresponding x_i.

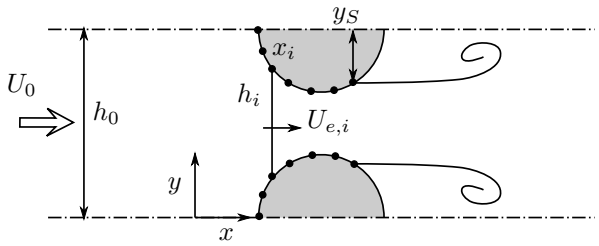

Figure C.3: Schematic of the discretised flow domain

C.3.1. Comparison with simulations

Steady simulations were conducted in FLUENT®, in order to evaluate the location of flow separation on the hex cylinder. The wall shear stress on the hex was recorded and the flow separation point was calculated by finding those points on the hex where wall shear stress was zero. The results obtained from simulations and their comparison with the results using Thwaites' method is shown in Table C.1. y_S is the ordinate of the separation location, measured from the centreline of the hex cylinder. The analytical approximations show good agreement with the simulated results.

Table C.1: Flow separation locations obtained from both FLUENT® simulations and Thwaites' method. y_S is calculated from the centreline of hex.

η	d [mm]	U_0 [m/s]	y_S [mm]	
			FLUENT®	Thwaites'
0.1	3	0.1	1.21	1.32
		0.2	1.349	1.366
		0.5	1.414	1.414
		1.0	1.436	1.437
		1.5	1.447	1.451
	5	0.1	2.213	2.264
		0.2	2.326	2.332
		0.5	2.384	2.391
		1.0	2.396	2.424
		1.5	2.397	2.437
0.2	3	0.1	1.161	1.221
		0.2	1.297	1.299
		0.5	1.374	1.366
		1.0	1.411	1.403
		1.5	1.424	1.421
	5	0.1	2.119	2.129
		0.2	2.241	2.235
		0.5	2.34	2.33
		1.0	2.373	2.378
		1.5	2.396	2.397

Appendix D

Derivation of Scattering Matrix

Following the procedure given in Hofmans (1998), we can linearise Eqs. (4.13) - (4.18) to get

$$S_p\left[\bar{\rho}_3 u_3' + \rho_3' \bar{u}_3\right] = S_j\left[\bar{\rho}_j u_j' + \rho_j' \bar{u}_j\right], \tag{D.1}$$

$$\left(\frac{\bar{p}_3}{\bar{p}_j}\right)\left[\frac{p_3'}{\bar{p}_3} - \frac{p_j'}{\bar{p}_j}\right] = \left(\frac{\bar{\rho}_3}{\bar{\rho}_j}\right)^{\gamma}\left[\frac{\gamma\rho_3'}{\bar{\rho}_3} - \frac{\gamma\rho_j'}{\bar{\rho}_j}\right], \tag{D.2}$$

$$\bar{u}_3 u_3' + \left(\frac{\gamma}{\gamma-1}\right)\left[\frac{\bar{p}_3}{\bar{\rho}_3}\right]\left[\frac{p_3'}{\bar{p}_3} - \frac{\rho_3'}{\bar{\rho}_3}\right] = \bar{u}_j u_j' + \left(\frac{\gamma}{\gamma-1}\right)\left[\frac{\bar{p}_j}{\bar{\rho}_j}\right]\left[\frac{p_j'}{\bar{p}_j} - \frac{\rho_j'}{\bar{\rho}_j}\right], \tag{D.3}$$

$$S_j\left[\bar{\rho}_j u_j' + \rho_j' \bar{u}_j\right] = S_p\left[\bar{\rho}_4 u_4' + \rho_4' \bar{u}_4\right], \tag{D.4}$$

$$S_p p_j' + S_j\left[\rho_j' \bar{u}_j + \bar{\rho}_j u_j'\right] = S_p\left[\rho_4' \bar{u}_4 + \bar{\rho}_4 u_4'\right], \tag{D.5}$$

and

$$\bar{u}_3 u_3' + \left(\frac{\gamma}{\gamma-1}\right)\left[\frac{\bar{p}_3}{\bar{\rho}_3}\right]\left[\frac{p_3'}{\bar{p}_3} - \frac{\rho_3'}{\bar{\rho}_3}\right] = \bar{u}_4 u_4' + \left(\frac{\gamma}{\gamma-1}\right)\left[\frac{\bar{p}_4}{\bar{\rho}_4}\right]\left[\frac{p_4'}{\bar{p}_4} - \frac{\rho_4'}{\bar{\rho}_4}\right]. \tag{D.6}$$

Applying continuity equation across *Regions 3* and *j*, we can evaluate

$$\bar{u}_j = \frac{S_p\ \bar{\rho}_3\ \bar{u}_3}{S_j\ \bar{\rho}_j}, \tag{D.7}$$

and using Eq. (D.1),we can get

$$u_j' = \frac{S_p\left[\bar{\rho}_3 u_3' + \rho_3' \bar{u}_3\right] - S_j \rho_j' \bar{u}_j}{S_j \bar{\rho}_j}. \tag{D.8}$$

Eliminating $\bar{u}_j$ and u_j' from the above equations, and combining Eqs. (D.1) and (D.4), we can reduce the equations to

$$\bar{\rho}_3 u_3' + \rho_3' \bar{u}_3 = \bar{\rho}_4 u_4' + \rho_4' \bar{u}_4, \tag{D.9}$$

$$\left(\frac{\bar{p}_3}{\bar{p}_j}\right)\left[\frac{p'_3}{\bar{p}_3}-\frac{p'_j}{\bar{p}_j}\right]=\left(\frac{\bar{\rho}_3}{\bar{\rho}_j}\right)^{\gamma}\left[\frac{\gamma\rho'_3}{\bar{\rho}_3}-\frac{\gamma\rho'_j}{\bar{\rho}_j}\right], \tag{D.10}$$

$$\bar{u}_3u'_3+\left(\frac{\gamma}{\gamma-1}\right)\left[\frac{\bar{p}_3}{\bar{\rho}_3}\right]\left[\frac{p'_3}{\bar{p}_3}-\frac{\rho'_3}{\bar{\rho}_3}\right]=\left(\frac{\mathcal{S}\bar{\rho}_3\bar{u}_3}{\bar{\rho}_j}\right)^2\left[\frac{u'_3}{\bar{u}_3}+\frac{\rho'_3}{\bar{\rho}_3}-\frac{\rho'_j}{\bar{\rho}_j}\right]+ \tag{D.11}$$

$$\left(\frac{\gamma}{\gamma-1}\right)\left[\frac{\bar{p}_j}{\bar{\rho}_j}\right]\left[\frac{p'_j}{\bar{p}_j}-\frac{\rho'_j}{\bar{\rho}_j}\right], \tag{D.12}$$

$$p'_j+\rho'_j\left(\frac{\mathcal{S}\bar{\rho}_3^2\bar{u}_3^2}{\bar{\rho}_j^2}\right)+2\bar{\rho}_j\left(\frac{\mathcal{S}\bar{\rho}_3^2\bar{u}_3^2}{\bar{\rho}_j^2}\right)\left[\frac{u'_3}{\bar{u}_3}+\frac{\rho'_3}{\bar{\rho}_3}-\frac{\rho'_j}{\bar{\rho}_j}\right]=p'_4+\rho'_4\bar{u}_4^2+2\bar{\rho}_4\bar{u}_4u'_4, \tag{D.13}$$

and

$$\bar{u}_3u'_3+\left(\frac{\gamma}{\gamma-1}\right)\left[\frac{\bar{p}_3}{\bar{\rho}_3}\right]\left[\frac{p'_3}{\bar{p}_3}-\frac{\rho'_3}{\bar{\rho}_3}\right]=\bar{u}_4u'_4+\left(\frac{\gamma}{\gamma-1}\right)\left[\frac{\bar{p}_4}{\bar{\rho}_4}\right]\left[\frac{p'_4}{\bar{p}_4}-\frac{\rho'_4}{\bar{\rho}_4}\right], \tag{D.14}$$

where $\mathcal{S}=S_p/S_j$.

We now substitute the acoustic quantities with their forward and backward travelling wave components as

$$p'_3=p_3^+ + p_3^- \qquad u'_3=\frac{p_3^+-p_3^-}{\rho_3c_3} \qquad \rho'_3=\frac{p_3^++p_3^-+\sigma_3}{c_3^2}$$

$$p'_4=p_4^+ + p_4^- \qquad u'_4=\frac{p_4^+-p_4^-}{\rho_4c_4} \qquad \rho'_4=\frac{p_4^++p_4^-+\sigma_4}{c_4^2}$$

$$\rho'_j=\frac{p'_j+\sigma_j}{c_j^2},$$

where σ denotes the entropy wave that is convected by the mean flow velocity. The scattering matrix derived here can relate the upstream and downstream entropy waves. The Eqs. (D.9) - (D.14) can be written in a matrix form, in terms of the total enthalpies and entropy waves as

$$\begin{bmatrix}\wp_{34}^{(\gamma-1)/2} & 1 & \wp_{34}^{(\gamma-1)/2}M_4\\ \wp_{34} & -1 & -\wp_{34}/(\gamma-1)\\ (1+M_4) & -C_2 & M_4^2\end{bmatrix}\begin{bmatrix}(1+M_4)p_4^+\\ (1-M_3)p_3^-\\ \sigma_4\end{bmatrix}=\begin{bmatrix}1 & \wp_{34}^{(\gamma-1)/2} & M_3\\ 1 & -\wp_{34} & -1/(\gamma-1)\\ C_1 & -1+M_4 & C_3\end{bmatrix}\times\begin{bmatrix}(1+M_3)p_3^+\\ (1-M_4)p_4^-\\ \sigma_3\end{bmatrix}, \tag{D.15}$$

where

$$C_1 = B_1 - (1 - A_1)\, B_3/A_3 \qquad A_1 = \mathcal{S}\ \wp_{3j}^2 M_3$$

$$C_2 = -B_1 - (1 + A_1)\, B_3/A_3 \qquad A_2 = \frac{-1}{\gamma - 1} - \mathcal{S}^2 \wp_{3j}^2 M_3^2 + \frac{\gamma}{\gamma - 1}\wp_{3j}^{1-\gamma}$$

$$C_3 = B_2 - A_2 B_3/A_3 \qquad A_3 = -\wp_{3j} + \mathcal{S}^2 \wp_{3j}^{\gamma+2} M_3^2$$

$$B_1 = 2\ \mathcal{S}\ \wp_{3j} M_3 \qquad \wp_{34} = \wp_{3j}/\wp_{4j}$$

$$B_2 = 2\ \mathcal{S}\ \wp_{3j} M_3^2 - \wp_{3j}^{-\gamma} \qquad \wp_{3j} = \bar{\rho}_3/\bar{\rho}_j$$

$$B_3 = 1 - \mathcal{S}\ \wp_{3j}^{1+\gamma} M_3^2 \qquad \wp_{4j} = \bar{\rho}_4/\bar{\rho}_j$$

Here $\wp_{3j}$, $\wp_{4j}$ and M_4 are unknown quantities that need to be evaluated. For a given M_3, $\wp_{3j}$ can be evaluated from Eqs. (4.13) and (4.15), by solving

$$M_3 = \sqrt{\frac{2}{\gamma - 1}} \sqrt{\frac{1 - \wp_{3j}^{1-\gamma}}{\mathcal{S}^2 \wp_{3j}^2 - 1}}. \tag{D.16}$$

The quantities $\wp_{4j}$ and M_4 are evaluated as follows

– The jet Mach number (M_j) is evaluated first, using Eq. (4.13) as

$$M_j = M_3\ \mathcal{S}\ \wp_{3j}^{(\gamma+1)/2} \tag{D.17}$$

– Next $\wp_{4j}$ is evaluated from Eq. (4.16) as

$$\wp_{4j} = \frac{M_j/M_4}{\mathcal{S} c_4/c_j} \tag{D.18}$$

– From Eqs. (4.16) and (4.17), we obtain

$$\frac{c_4}{c_j} = \frac{\mathcal{S} M_4}{M_j}\left[\frac{1 + \gamma \mathcal{S}^{-1} M_j^2}{1 + \gamma M_4^2}\right] \tag{D.19}$$

– We can relate M_4 and M_j using Eqs. (4.15) and (4.18) as

$$\frac{(\gamma - 1)}{2} M_j^2 + 1 = \left(\frac{c_4}{c_j}\right)^2 \left[\frac{\gamma - 1}{2} M_4^2 + 1\right] \tag{D.20}$$

Equation (D.20) is a quadratic function in M_4^2 which can be solved to obtain M_4, and consequently $\wp_{4j}$ and $\wp_{34}$. Once these quantities are evaluated, we can find the *Scattering Matrix* $[SM]$ as

$$\begin{bmatrix}(1+M_4)p_4^+\\(1-M_3)p_3^-\\ \sigma_4\end{bmatrix} = [SM]\begin{bmatrix}(1+M_3)p_3^+\\(1-M_4)p_4^-\\ \sigma_3\end{bmatrix}, \tag{D.21}$$

where

$$\begin{aligned}[SM] &= \begin{bmatrix}\wp_{34}^{(\gamma-1)/2} & 1 & \wp_{34}^{(\gamma-1)/2}M_4\\ \wp_{34} & -1 & -\wp_{34}/(\gamma-1)\\ (1+M_4) & -C_2 & M_4^2\end{bmatrix}^{-1} \quad \begin{bmatrix}1 & \wp_{34}^{(\gamma-1)/2} & M_3\\ 1 & -\wp_{34} & -1/(\gamma-1)\\ C_1 & -1+M_4 & C_3\end{bmatrix}\\ &= \begin{bmatrix}SM_{11} & SM_{12} & SM_{13}\\ SM_{21} & SM_{22} & SM_{23}\\ SM_{31} & SM_{32} & SM_{33}\end{bmatrix}.\end{aligned}$$

When there is no incoming entropy ($\sigma_3 = 0$), Eq. (D.21) reduces to

$$\begin{bmatrix}(1+M_4)\,p_4^+\\(1-M_3)\,p_3^-\end{bmatrix} = \begin{bmatrix}SM_{11} & SM_{12}\\ SM_{21} & SM_{22}\end{bmatrix}\begin{bmatrix}(1+M_3)\,p_3^+\\(1-M_4)\,p_4^-\end{bmatrix}. \tag{D.22}$$

Appendix E

Huang and Heckl model

Huang and Heckl (1993) used the grating theory, initially proposed by Twersky (1956, 1962), to obtain the expressions for the reflection and transmission coefficients of an array of circular tubes without bias flow (Fig. E.1).

The expressions for the transmitted and reflected pressure fields are found to be

$$p_t(r,\varphi) = \Psi_o e^{ik_o r\cos(\varphi-\varphi_o)} + \frac{2\Psi_o}{k_o h_p}\sum_{\nu=-\infty}^{\infty}\frac{1}{\cos\varphi_\nu}\sum_{n=-\infty}^{\infty}A_n e^{in\varphi_\nu + ik_o r\cos(\varphi-\varphi_o)}, \tag{E.1}$$

and

$$p_r(r,\varphi) = \frac{2\Psi_o}{k_o h_p}\sum_{\nu=-\infty}^{\infty}\frac{1}{\cos\varphi_\nu}\sum_{n=-\infty}^{\infty}A_n e^{in(\pi-\varphi_\nu) - ik_o r\cos(\varphi+\varphi_o)}. \tag{E.2}$$

ν is an integer which denotes the number of the scattered wave angle φ_ν and A_n is the multiple scattering coefficient of the tube row.

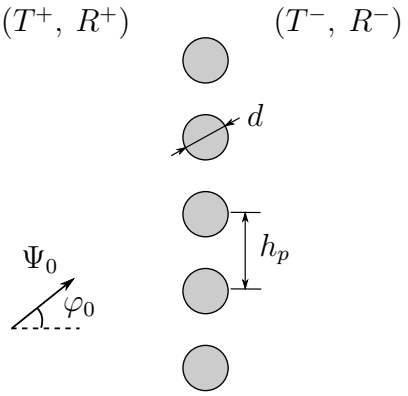

Figure E.1: Geometry of a tube row

The coefficient A_n is evaluated from (Twersky, 1962):

$$A_n = a_n \left(e^{-in\varphi_o} + \sum_{m=-\infty}^{\infty} A_m \, F_{n-m} \right), \tag{E.3}$$

where a_n is the scattering coefficient of a single tube and F_{n-m} is the Schlömilch series. F_{n-m} is a function of the incident angle φ_o and the ratio of the spacing to the wavelength (h_p/λ_o).The complete expression for the Schlömilch series is provided in the Appendix F.

For normal incidence of the pressure wave ($\varphi_o = 0$), the transmission and reflection coefficients, $T^{\pm}$ and $R^{\pm}$ are written as the ratio of the transmitted and reflected waves to the incident wave, respectively. Hence,

$$T^{\pm} = 1 + \frac{2}{k_o h_p} \sum_{n=-\infty}^{\infty} A_n \tag{E.4}$$

$$R^{\pm} = \frac{2}{k_o h_p} \sum_{n=-\infty}^{\infty} A_n \, e^{in\pi} \tag{E.5}$$

where the superscripts '+' and '–' denote the upstream and downstream properties, respectively.

E.1. Experimental results

We conducted experiments without mean flow in order to validate the experimental data with the theory. Figures E.2 - E.5 show the results obtained from experiments and theory, for the two samples considered: *Sample 1* - $d = 20$mm and $h_g = 5$mm, and *Sample 2* - $d = 16$mm and $h_g = 4$mm. There is very good agreement between the theory and measurements.

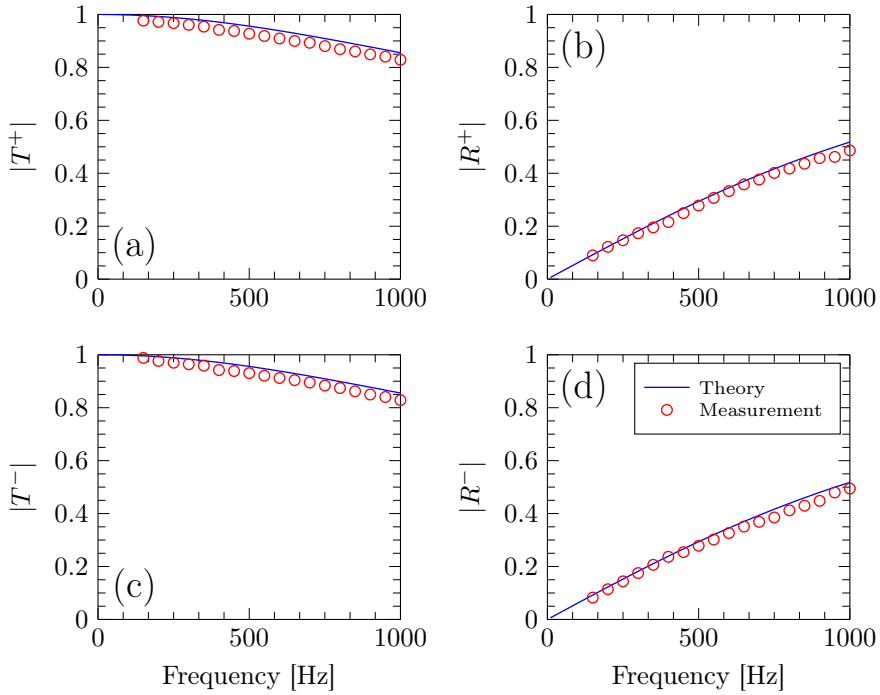

Figure E.2: Magnitude of transmission and reflection coefficients for Sample 1 with no bias flow.

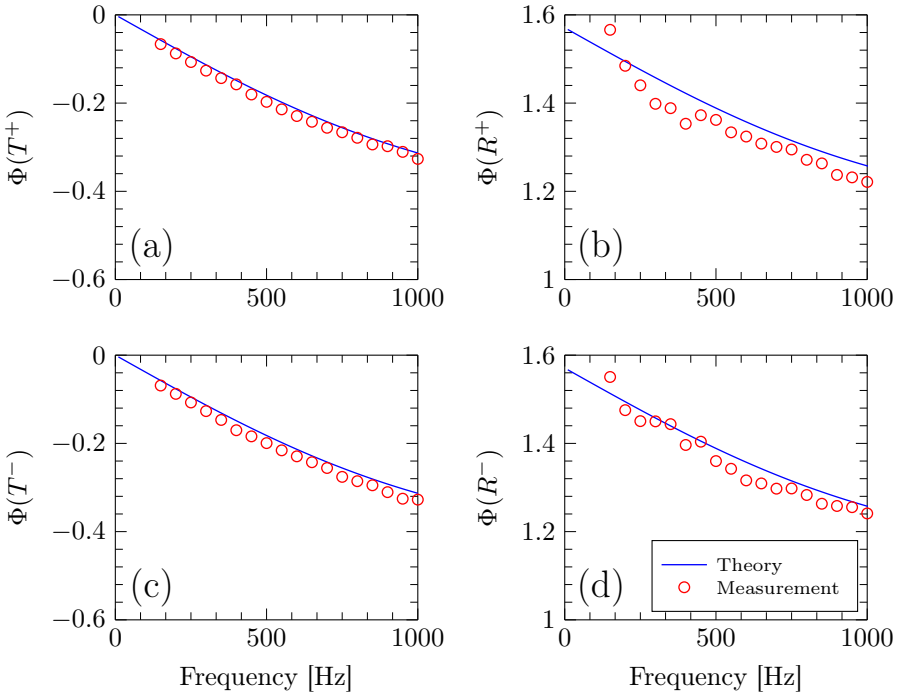

Figure E.3: Phase of transmission and reflection coefficients for Sample 1 with no bias flow.

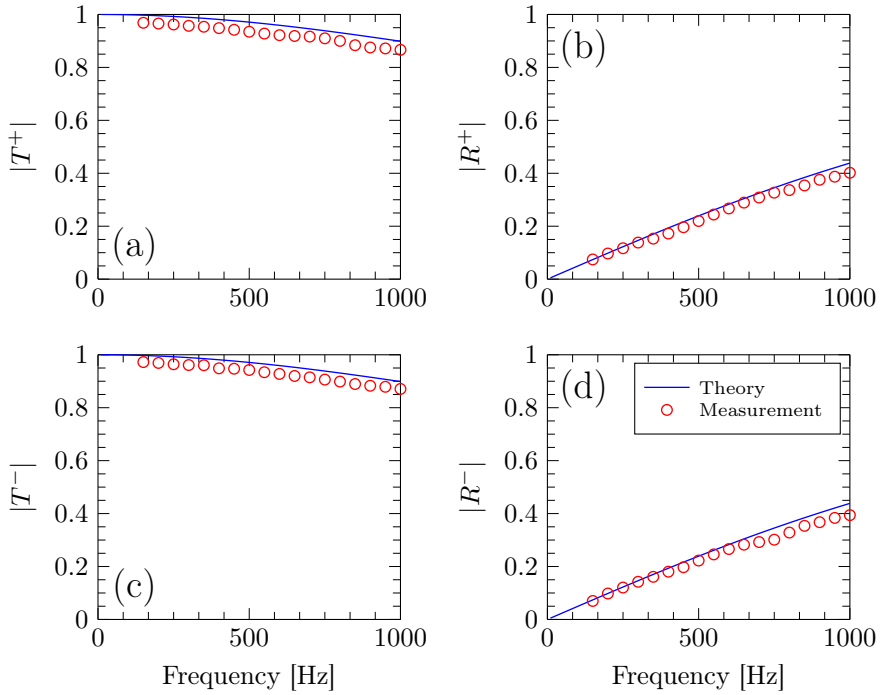

Figure E.4: Magnitude of transmission and reflection coefficients for Sample 2 with no bias flow.

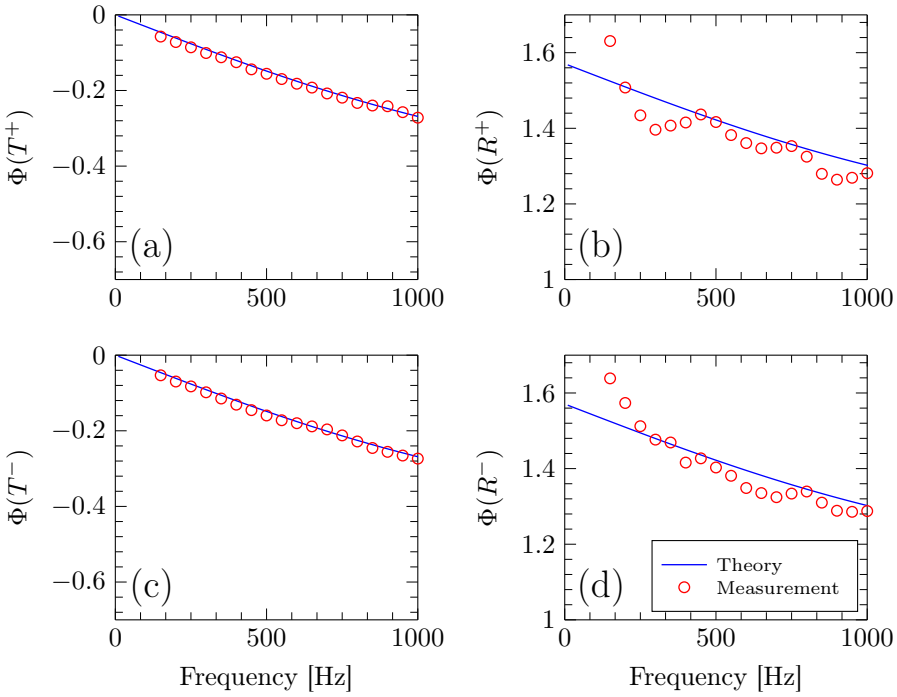

Figure E.5: Phase of transmission and reflection coefficients for Sample 2 with no bias flow.

Appendix F

Schlömilch Series

The expressions for Schlömilch series are taken from Twersky (1961, 1962).

$$F_{n-m} = \mathscr{R}_{n-m} + i\mathscr{I}_{n-m}, \tag{F.1}$$

where the subscript denotes the order of the series.

For *Zero-order*:

$$\mathscr{R}_0 = \frac{1}{\pi\Delta}\sum_{\nu=-\nu_-}^{\nu_+}\frac{1}{\cos\varphi_\nu} - 1,$$

$$\mathscr{I}_0 = -\frac{2}{\pi}\log\left(\frac{\gamma\Delta}{2}\right) + \frac{1}{\pi}\left[\sum_{\nu=1}^{\nu_+}\frac{1}{\nu} + \sum_{\nu=1}^{\nu_-}\frac{1}{\nu}\right] - \frac{1}{\pi}\left[\sum_{\nu=\nu_++1}^{\infty}\frac{1}{\Delta\sinh\theta_{\nu_+}} - \frac{1}{\nu}\right] - \frac{1}{\pi}\left[\sum_{\nu=\nu_-+1}^{\infty}\frac{1}{\Delta\sinh\theta_{\nu_-}} - \frac{1}{\nu}\right] \tag{F.2}$$

Even-order:

$$\mathscr{R}_{2N} = \frac{1}{\pi\Delta}\sum_{\nu=-\nu_-}^{\nu_+}\frac{\cos(2N\varphi_\nu)}{\cos\varphi_\nu} \tag{F.3}$$

$$\mathscr{I}_{2N} = \frac{1}{N\pi} + \frac{1}{\pi}\sum_{s=1}^{N}\frac{(-1)^s\,2^{2s}\,(N+s-1)!\,B_{2s}(\Delta\sin\varphi_0)}{(2s)!\,(N-s)!\,\Delta^{2s}} - \frac{1}{\pi\Delta}\left[\sum_{\nu=0}^{\nu_+}\frac{\sin(2N\varphi_\nu)}{\cos\varphi_\nu} - \sum_{\nu=-1}^{-\nu_-}\frac{\sin(2N\varphi_\nu)}{\cos\varphi_\nu}\right] - \frac{(-1)^N}{\pi\Delta}\left[\sum_{\nu=\nu_++1}^{\infty}\frac{e^{-2N\theta_{\nu_+}}}{\sinh\theta_{\nu_+}} + \sum_{\nu=\nu_-+1}^{\infty}\frac{e^{-2N\theta_{\nu_-}}}{\sinh\theta_{\nu_-}}\right] \tag{F.4}$$

Odd-order:

$$\mathscr{R}_{2N+1} = -\frac{i}{\pi\Delta}\sum_{\nu=\nu_-}^{\nu_+}\frac{\sin\left(2N+1\right)\varphi_\nu}{\cos\varphi_\nu} \tag{F.5}$$

$$\mathscr{I}_{2N+1} = -\frac{2i}{\pi}\sum_{s=0}^{N}\frac{(-1)^s\,2^{2s}\,(N+s)!\,B_{2s+1}\left(\Delta\sin\varphi_0\right)}{(2s+1)!\,(N-s)!\,\Delta 2s+1} - \frac{i}{\pi\Delta}\left[\sum_{\nu=0}^{\nu_+}\frac{\cos(2N+1)\varphi_\nu}{\cos\varphi_\nu} - \sum_{\nu=-1}^{-\nu_-}\frac{\cos(2N+1)\varphi_\nu}{\cos\varphi_\nu}\right] + \frac{i(-1)^N}{\pi\Delta}\left[\sum_{\nu=\nu_++1}^{\infty}\frac{e^{-(2N+1)\theta_{\nu_+}}}{\sinh\theta_{\nu_+}} - \sum_{\nu=\nu_-+1}^{\infty}\frac{e^{-(2N+1)\theta_{\nu_-}}}{\sinh\theta_{\nu_-}}\right] \tag{F.6}$$

Here, Δ is the ratio between the tube spacing h_p and the wavelength λ_0, γ is a numerical constant, equal to $\gamma = 1.781...$ and $B_n(x)$ is the Bernoulli number of order n and argument x. The expressions for $B_n(x)$ were taken from Abramowitz and Stegun (1972)

$$B_n(x) = -2\frac{n!}{(2\pi)^n}\sum_{k=1}^{\infty}\frac{\cos\left(2\pi kx - n\pi/2\right)}{k^n} \qquad \begin{matrix}(n>1, & 0\le x\le 1\\ n=1, & 0<x<1)\end{matrix} \tag{F.7}$$

$$(-1)^n\,B_n(-x) = B_n(x) + nx^{n-1} \qquad (n>0, \quad x<0) \tag{F.8}$$

$$B_n(x+1) - B_n(x) = nx^{n-1} \qquad (n>0, \quad x>1) \tag{F.9}$$

φ_ν, $\nu_\pm$ and $\theta_{\nu_\pm}$ are defined as:

$$\begin{aligned}\sin\varphi_\nu &= \sin\varphi_0 + \frac{2\pi\nu}{k_0 h_p}\\ \cos\varphi_\nu &= \begin{cases}\sqrt{1-\sin^2\varphi_\nu} & \text{for} \quad |\sin\varphi_\nu|\le 1\\ i\sqrt{1-\sin^2\varphi_\nu} & \text{for} \quad |\sin\varphi_\nu|>1\end{cases},\end{aligned} \tag{F.10}$$

$$\nu_\pm = \mathrm{INT}\left(\frac{h_p}{\lambda_0}\left(1\pm\sin\varphi_0\right)\right), \tag{F.11}$$

and

$$\cosh\theta_{\nu_\pm} = \frac{\nu}{\Delta} \pm \sin\theta_0, \tag{F.12}$$

where INT indicates the conversion of a real number to an integer.

References

Abramowitz, M. and **Stegun, I. A.** (**1972**), *Handbook of Mathematical Functions*, 9^{th} ed., Dover Publications, Inc., New York. [Cited on page 142.]

Andreini, A., **Facchini, B.**, **Giusti, A.** and **Turrini, F.** (**2014**), "Assessment of Flame Transfer Function Formulations for the Thermoacoustic Analysis of Lean Burn Aero-Engine Combustors", *Energy Procedia*, **45**: pp. 1422 – 1431. [Cited on page 35.]

ANSYS Inc. (**2013**), *ANSYS Fluent Theory Guide*, version 15.0 ed. [Cited on page 42.]

Bechert, D. W. (**1980**), "Sound absorption caused by vorticity shedding, demonstrated with a jet flow", *Journal of Sound and Vibration*, **70**(3): pp. 389–405. [Cited on page 8.]

Bigongiari, A. and **Heckl, M. A.** (**2016**), "A Green's function approach to the rapid prediction of thermoacoustic instabilities in combustors", *Journal of Fluid Mechanics*, **798**: pp. 970–996. [Cited on pages 82 and 91.]

Candel, S. M. (**1992**), "Combustion instabilities coupled by pressure waves and their active control", *Twenty-Fourth Symposium (International) on Combustion*, **24**(1): pp. 1277–1296. [Cited on page 5.]

Crocco, L. and **Cheng, S.** (**1956**), "Theory of combustion instability in liquid propellant rocket motors", *Tech. Rep. 8*, AGARDO-GRAPH by Butterworths Scientific Publications. [Cited on page 33.]

Culick, F. E. C. (**2006**), "Unsteady motions in combustion chambers for propulsion systems", *Tech. Rep. AG-AVT-039*, RTO AGARDograph by NATO. [Cited on pages ix, 4, 7, 8, and 37.]

Cummings, A. and **Eversman, W.** (**1983**), "High amplitude acoustic transmission through duct terminations : Theory", *Journal of Sound and Vibration*, **91**(4): pp. 503–518. [Cited on page 10.]

Dowling, A. P. and **Ffowcs Williams, J. E.** (**1983**), *Sound and Sources of Sound*, Ellis Horwood Limited. [Cited on page 6.]

Dowling, A. P. and **Hughes, I. J.** (**1992**), "Sound absorption by a screen with a regular array of slits", *Journal of Sound and Vibration*, **156**(3): pp. 387–405. [Cited on pages 9 and 73.]

Durrieu, P., **Hofmans, G.**, **Ajello, G.**, **Boot, R.**, **Aurégan, Y.**, **Hirschberg, A.** and **Peters, M. C. A. M.** (**2001**), "Quasisteady aero-acoustic response of orifices", *The Journal of the Acoustical Society of America*, **110**(4): pp. 1859–1872. [Cited on page 47.]

Eldredge, J., **Bodony, D.** and **Shoeybi, M.** (**2007**), "Numerical investigation of the acoustic behavior of a multi-perforated liner", in *13th AIAA/CEAS Aeroacoustics Conference*, Rome, Italy. [Cited on page 10.]

Eldredge, J. D. and **Dowling, A. P.** (**2003**), "The absorption of axial acoustic waves by a perforated liner with bias flow", *Journal of Fluid Mechanics*, **485**: pp. 307–335. [Cited on page 12.]

Flohr, P., **Paschereit, C. O.** and **Belluci, V.** (**2003**), "Steady CFD Analysis for Gas Turbine Burner Transfer Functions", in *41st AIAA Aerospace Sciences Meeting and Exhibit*, Reno, Nevada. [Cited on page 4.]

Glassman, I. and **Yetter, R. A.** (**2008**), *Combustion*, Academic Press Limited. [Cited on page 19.]

Han, X., **Li, J.** and **Morgans, A. S.** (**2015**), "Prediction of combustion instability limit cycle oscillations by combining flame describing function simulations with a thermoacoustic network model", *Combustion and Flame*, **162**(10): pp. 3632–3647. [Cited on page 4.]

Heckl, M. (**2015**), "A new perspective on the flame describing function of a matrix flame", *International Journal of Spray and Combustion Dynamics*, **7**(2): pp. 91–112. [Cited on page 82.]

Heckl, M. and **Kosztin, B.** (**2013**), "Analysis and control of an unstable mode in a combustor with tuneable end condition", *International Journal of Spray and Combustion Dynamics*, **5**(3): pp. 243–272. [Cited on pages 12, 33, and 80.]

Heckl, M. A. (**1988**), "Active control of the noise from a Rijke tube", *Journal of Sound and Vibration*, **124**(1): pp. 117–133. [Cited on page 82.]

Heckl, M. A. (**2013**), "Analytical model of nonlinear thermo-acoustic effects in a matrix burner", *Journal of Sound and Vibration*, **332**(17): pp. 4021–4036. [Cited on page 82.]

Hofmans, G., **Ranucci, M.**, **Ajello, G.**, **Auregan, Y.** and **Hirschberg, A.** (**2001**a), "Aeroacoustic response of a slit-shaped diaphragm in a pipe at low Helmholtz number, 2: Unsteady results", *Journal of Sound and Vibration*, **244**(1): pp. 57–77. [Cited on page 10.]

Hofmans, G. C. J. (**1998**), *Vortex Sound in Confined Flows*, Ph.D. thesis, Technische Universiteit Eindhoven. [Cited on pages 10, 47, 50, 51, and 133.]

Hofmans, G. C. J., **Boot, R. J. J.**, **Durrieu, P. P. J. M.**, **Auregan, Y.** and **Hirschberg, A.** (**2001**b), "Aeroacoustics response of a slit-shaped diaphragm in a pipe at low Helmholtz number, 1: Quasi-steady results", *Journal of Sound and Vibration*, **244**(1): pp. 35–56. [Cited on pages 10, 47, and 50.]

Hofmans, G. C. J., **Groot, G.**, **Ranucci, M.**, **Graziani, G.** and **Hirschberg, A.** (**2003**), "Unsteady flow through in-vitro models of the glottis", *The Journal of the Acoustical Society of America*, **113**(3): pp. 1658–1675. [Cited on pages 10, 47, and 50.]

Hosseini, N., **Kornilov, V.**, **Teerling, O. J.**, **Lopez Arteaga, I.** and **de Goey, L. P. H.** (**2015**), "Transfer function calculations of segregated elements in a simplified slit burner with heat exchanger", in *The 22nd International Congress on Sound and Vibration*, Florence, Italy. [Cited on page 41.]

Howe, M. S. (**1979**), "On the Theory of Unsteady High Reynolds Number Flow Through a Circular Aperture", *Proceedings of the Royal Society A: Mathematical, Physical and Engineering Sciences*, **366**: pp. 205–223. [Cited on page 9.]

Howe, M. S. (**1980**), "The influence of vortex shedding on the diffraction of sound by perforated screen", *Journal of Fluid Mechanics*, **97**(4): pp. 641–653. [Cited on page 9.]

Huang, X. Y. and **Heckl, M. A.** (**1993**), "Transmission and Dissipation of Sound Waves in Tube Bundles", *Acustica*, **78**(4): pp. 191 – 200. [Cited on pages 55 and 137.]

Huang, Y. and **Yang, V.** (**2009**), "Dynamics and stability of lean-premixed swirl-stabilized combustion", *Progress in Energy and Combustion Science*, **35**(4): pp. 293–364. [Cited on page 11.]

Hughes, I. J. and **Dowling, A. P.** (**1990**), "The absorption of sound by perforated linings", *Journal of Fluid Mechanics*, **218**: pp. 299 – 335. [Cited on page 9.]

Jaensch, S., **Merk, M.**, **Gopalakrishnan, E. A.**, **Bomberg, S.**, **Emmert, T.**, **Sujith, R. I.** and **Polifke, W.** (**2017**), "Hybrid CFD/low-order modeling of nonlinear thermoacoustic oscillations", *Proceedings of the Combustion Institute*, **36**(3): pp. 3827–3834. [Cited on page 4.]

Jang, S. and **Ih, J.** (**1998**), "On the multiple microphone method for measuring in-duct acoustic properties in the presence of mean flow", *The Journal of the Acoustical Society of America*, **103**(3): pp. 1520–1526. [Cited on page 54.]

Jing, X. and **Sun, X.** (**1999**), "Experimental investigations of perforated liners with bias flow", *The Journal of the Acoustical Society of America*, **106**(5): pp. 2436–2441. [Cited on page 9.]

King, L. V. (**1914**), "On the Convection of Heat from Small Cylinders in a Stream of Fluid: Determination of the Convection Constants of Small Platinum Wires with Applications to Hot-Wire Anemometry", *Philosophical Transactions of the Royal Society A*, **214**: pp. 373–432. [Cited on page 34.]

Kristiansen, U. R. and **Fahy, F. J.** (**1972**), "Scattering of Acoustic waves by an N-layer periodic grating", *Journal of Sound and Vibration*, **24**(3): pp. 315–335. [Cited on page 14.]

Kristiansen, U. R. and **Fahy, F. J.** (**1974**), "Sound propagation and Energy dissipation in flow through arrays of small scatterers", *Journal of Sound and Vibration*, **32**(2): pp. 189–198. [Cited on page 14.]

Kundu, P. K., **Cohen, I. M.** and **Dowling, D. R.** (**2012**), *Fluid Mechanics*, 5th ed., Elsevier Inc. [Cited on pages 129 and 130.]

Laera, D., **Ceglie, V.** and **Camporeale, S. M.** (**2016**), "Instability analysis of a full-scale lean-premized burner with a distributed flame describing function", in *Thermoacoustic Instabilities in Gas Turbines and Rocket Engines: Industry meets Academia*, GTRE-023, Munich, Germany. [Cited on page 4.]

Lahiri, C. (**2014**), *Acoustic performance of bias flow liners in gas turbine combustors*, Ph.D. thesis, Technische Universität Berlin. [Cited on page 10.]

Lahiri, C. and **Bake, F.** (**2017**), "A review of bias flow liners for acoustic damping in gas turbine combustors", *Journal of Sound and Vibration*, **400**: pp. 564–605. [Cited on page 10.]

Lawson, C. L. and **Hanson, R. J.** (**1995**), *Solving Least Squares Problems*, The Society for Industrial and Applied Mathematics. [Cited on page 45.]

Leppington, F. G. and **Levine, H.** (**1973**), "Reflexion and transmission at a plane screen with periodically arranged circular or elliptical apertures", *Journal of Fluid Mechanics*, **61**: pp. 109–127. [Cited on page 9.]

Lieuwen, T. and **Zinn, B. T.** (**1998**), "The role of equivalence ratio oscillations in driving combustion instabilities in low NO_x gas turbines", *Twenty-Seventh Symposium (International) on Combustion*, **27**(2): pp. 1809–1816. [Cited on page 30.]

Lieuwen, T. C. and **Yang, V.** (**2005**), *Combustion Instabilities in Gas Turbine Engines: Operational Experience, Fundamental Mechanisms, and Modeling*, vol. 210 of *Progress in Astronautics and Aeronautics*, American Institute of Aeronautics and Astronautics, Inc. [Cited on pages ix, 4, 7, 11, and 13.]

Lighthill, M. J. (**1954**), "The response of laminar skin friction and heat transfer to fluctuations in the stream velocity", *Proceedings of the Royal Society A: Mathematical, Physical and Engineering Sciences*, **224**(1156): pp. 1–23. [Cited on page 34.]

Lord Rayleigh (**1896**), *The Theory of Sound*, vol. II, 2nd ed., Dover Publications. [Cited on pages 25 and 26.]

McManus, K. R., **Poinsot, T.** and **Candel, S. M.** (**1993**), "A review of active control of combustion instabilities", *Progress in Energy and Combustion Sciences*, **19**(1): pp. 1–29. [Cited on pages 5, 29, and 30.]

Mendez, S. and **Eldredge, J. D.** (**2009**), "Acoustic modeling of perforated plates with bias flow for Large-Eddy Simulations", *Journal of Computational Physics*, **228**(13): pp. 4757–4772. [Cited on page 10.]

Monkewitz, P. A. (**1985**), "The response of Helmholtz resonators to external excitation. Part 2. Arrays of slit resonators", *Journal of Fluid Mechanics*, **156**: pp. 151–166. [Cited on page 9.]

Moran, M. J. and **Shapiro, H. N.** (**2004**), *Fundamentals of Engineering Thermodynamics*, 5th ed., John Wiley and Sons Inc. [Cited on page 28.]

Motheau, E., **Selle, L.** and **Nicoud, F.** (**2014**), "Accounting for convective effects in zero-Mach-number thermoacoustic models", *Journal of Sound and Vibration*, **333**(1): pp. 246–262. [Cited on page 50.]

Na, W. (**2015**), *Frequency Domail Linearized Navier-Stokes Equations Methodology for Aero-Acoustic and Thermoacoustic Simulations*, Licentiate thesis, Royal Institute of Technology, Stockholm. [Cited on page 10.]

Na, W., **Boij, S.** and **Efraimsson, G.** (**2016**), "Acoustic Characterization of a Hybrid Liner Consisting of Porous Material by Using A Unified Linearized Navier-Stokes Approach", in *22nd AIAA/CEAS Aeroacoustics Conference*, Lyon, France. [Cited on page 10.]

Noiray, N. (**2007**), *Linear and nonlinear analysis of combustion instabilities, application to multipoint injection systems and control strategies*, Ph.D. thesis, École Centrale Paris. [Cited on page 35.]

Peerlings, L. (**2015**), *Methods and techniques for precise and accurate in-duct aeroacoustic measurements : Application to the area expansion*, Licentiate thesis, Royal Institute of Technology, Stockholm. [Cited on pages 52 and 54.]

Peerlings, L. (**2017**), *Assessing precision and accuracy in acoustic scattering matrix measurements*, Ph.D. thesis, Royal Institute of Technology, Stockholm. [Cited on page 52.]

Poinsot, T. (**2013**), "Simulation methodologies and open questions for acoustic combustion instability studies", *Annual Research Briefs, Center for Turbulence Research, Standford University, Stanford, CA*: pp. 179–188. [Cited on page 4.]

Poinsot, T. (**2017**), "Prediction and control of combustion instabilities in real engines", *Proceedings of the Combustion Institute*, **36**(1): pp. 1–28. [Cited on pages ix, 4, and 5.]

Polifke, W. (**2010**), "Low-Order Analysis Tools for Aero- and Low-Order Analysis Tools for Aero- and Thermo-Acoustic Instabilities", in **Schram, C.** (Editor), *Advances in Aero-Acoustics and Thermo-Acoustics*, January 2011, Von Karman Institute for Fluid Dynamics, Brussels. [Cited on page 5.]

Polifke, W., **Poncet, A.**, **Paschereit, C. O.** and **Döbbeling, K.** (**2001**), "Reconstruction of acoustic transfer matrices by instationary computational fluid dynamics", *Journal of Sound and Vibration*, **245**(3): pp. 483–510. [Cited on page 4.]

Pope, S. B. (**2000**), *Turbulent Flows*, Cambridge University Press, Cambridge. [Cited on page 31.]

Quinn, M. C. and **Howe, M. S.** (**1984**), "The Influence of Mean Flow on the Acoustic Properties of a Tube Bank", *Proceedings of the Royal Society A: Mathematical, Physical and Engineering Sciences*, **396**(December): pp. 383–403. [Cited on page 14.]

Raun, R. L., **Beckstead, M. W.**, **Finlinson, J. C.** and **Brooks, K. P.** (**1993**), "A review of Rjke tubes, Rijke burners and related devices", *Progress in Energy and Combustion Sciences*, **19**: pp. 313–364. [Cited on page 2.]

Rehman, S. F. and **Eldredge, J. D.** (**2007**), "Numerical investigation of a bias-flow perforated liner for damping of thermoacoustic instabilities", in *ASME Turbo Expo 2007: Power for Land, Sea and Air*, Montreal, Canada. [Cited on page 12.]

Richardson, E. G. (**1922**), "The Theory of the Singing Flame", *Proceedings of the Physical Society of London*, **35**: pp. 47–54. [Cited on page 2.]

Rienstra, S. and **Hirschberg, A.** (**2014**), "An Introduction to Acoustics", *Tech. Rep. IWDE 92-06*, Eindhoven University of Technology. [Cited on page 21.]

Riess, P. (**1859**), "Das Anblasen offener Röhren durch eine Flamme", *Annalen der Physik und Chemie*, **108**(2): pp. 653–656. [Cited on page 25.]

Rigas, G., **Jamieson, N. P.**, **Li, L. K. B.** and **Juniper, M. P.** (**2016**), "Experimental sensitivity analysis and control of thermoacoustic systems", *Journal of Fluid Mechanics*, **787**: pp. R1 1–11. [Cited on page 81.]

Rijke, P. L. (**1859**), "Notice of a New Method of causing a Vibration of the Air contained in a Tube open at both ends", *The London, Edinburgh, and Dublin Philosophical Magazine and Journal of Science*, **XVII**(4): pp. 419–422. [Cited on page 25.]

Rolls-Royce (**1996**), *The jet engine*, 5th ed., Rolls-Royce plc, Derby, UK. [Cited on pages ix and 11.]

Ronneberger, D. (**1967**), "Experimentelle Untersuchungen zum akustischen Reflexionsfaktor von unstetigen Querschnittsänderungen in einem luftdurchströmten Rohr (Experimental Investigations about the Acoustic Reflection Coefficient of Discontinuous Changes of Cross-Section in Tubes with Air Flow)", *Acustica*, **19**: pp. 222 – 235. [Cited on pages 47 and 50.]

Salikuddin, M. and **Ahuja, K. K.** (**1983**), "Acoustic power dissipation on radiation through duct terminations: Experiments", *Journal of Sound and Vibration*, **91**(4): pp. 479–502. [Cited on page 10.]

Scarpato, A., **Ducruix, S.** and **Schuller, T.** (**2013**), "A comparison of the damping properties of perforated plates backed by a cavity operating at low and high Strouhal numbers", *Comptes Rendus Mécanique*, **341**(1-2): pp. 161–170. [Cited on page 12.]

Scarpato, A., **Tran, N.**, **Ducruix, S.** and **Schuller, T.** (**2012**), "Modeling the damping properties of perforated screens traversed by a bias flow and backed by a cavity at low Strouhal number", *Journal of Sound and Vibration*, **331**(2): pp. 276–290. [Cited on page 12.]

Schadow, K. C. and **Gutmark, E.** (**1992**), "Combustion instability related to vortex shedding in dump ccombustor and their passive control", *Progress in Energy and Combustion Science*, **18**: pp. 117–132. [Cited on page 31.]

Schlichting, H. (**1979**), *Boundary-Layer Theory*, 7th ed., McGraw-Hill Book Company. [Cited on page 127.]

Schuller, T., **Durox, D.** and **Candel, S.** (**2003**), "A unified model for the prediction of laminar flame transfer functions: comparisons between conical and V-flame dynamics", *Combustion and Flame*, **134**(1-2): pp. 21–34. [Cited on page 35.]

Selimefendigil, F., **Föller, S.** and **Polifke, W.** (**2012**), "Nonlinear identification of unsteady heat transfer of a cylinder in pulsating cross flow", *Computers and Fluids*, **53**(1): pp. 1–14. [Cited on page 35.]

Smits, J. M. A. and **Kosten, C. W.** (**1951**), "Sound absorption by slit resonators", *Acta Acustica united with Acustica*, **1**(3): pp. 114–122. [Cited on page 9.]

Sohn, C. H. and **Park, J. H.** (**2011**), "A comparative study on acoustic damping induced by half-wave, quarter-wave, and Helmholtz resonators", *Aerospace Science and Technology*, **15**(8): pp. 606–614. [Cited on page 7.]

Sondhauss, C. (**1850**), "Über die Schallschwingungen der Luft in erhitzten Glasröhren und in gedeckten Pfeifen von ungleicher Weite", *Annalen der Physik und Chemie*, **79**: pp. 1–34. [Cited on page 25.]

Stow, S. R. and **Dowling, A. P.** (**2009**), "A Time-Domain Network Model for Nonlinear Thermoacoustic Oscillations", *ASME Journal of Engineering for Gas Turbines and Power*, **131**(May 2009): pp. 031,502/1 – 10. [Cited on page 5.]

Strobio Chen, L., **Polifke, W.**, **Hosseini, N.**, **Teerling, O. J.**, **Lopez Arteaga, I.**, **Kornilov, V.** and **de Goey, P.** (**2016**), "Acoustic scattering behaviour of a 2D flame with heat exchanger in cross-flow", in *The 23rd International Congress on Sound and Vibration*, July, Athens, Greece. [Cited on pages 61 and 65.]

Strobio Chen, L., **Witte, A.** and **Polifke, W.** (**2015**), "Thermo-acoustic characterization of a heat exchanger in cross flow using compressible and weakly compressible

numerical simulation", in *The 22nd International Congress on Sound and Vibration*, July, Florence, Italy. [Cited on page 44.]

Surendran, A. and **Heckl, M. A.** (**2014**), "Analytical study of a Rijke tube with heat exchanger", in *The 21st International Congress on Sound and Vibration*, Beijing, China. [Cited on page 72.]

Surendran, A. and **Heckl, M. A.** (**2015**), "Passive instability control by using a heat exchanger as acoustic sink", in *The 22nd International Congress on Sound and Vibration*, July, Florence, Italy. [Cited on page 16.]

Surendran, A. and **Heckl, M. A.** (**2016**), "Passive instability control by a heat exchanger in a combustor with non-uniform temperature", in *Thermoacoustic Instabilities in Gas Turbines and Rocket Engines: Industry meets Academia*, GTRE-022, Munich, Germany. [Cited on pages 16 and 71.]

Surendran, A. and **Heckl, M. A.** (**2017**), "Passive instability control by a heat exchanger in a combustor with nonuniform temperature", *International Journal of Spray and Combustion Dynamics*, **0**(0). [Cited on pages 16 and 71.]

Surendran, A., **Heckl, M. A.**, **Boij, S.**, **Bodén, H.** and **Hirschberg, A.** (**2016**a), "Aeroacoustic response of an array of tubes with bias-flow", in *The 23rd International Congress on Sound and Vibration*, July, Athens, Greece. [Cited on page 16.]

Surendran, A., **Heckl, M. A.**, **Hosseini, N.** and **Teerling, O. J.** (**2016**b), "Use of heat exchanger for passive control of combustion instabilities", in *The 23rd International Congress on Sound and Vibration*, July, Athens, Greece. [Cited on pages 16 and 80.]

Tam, C., **Kurbatskii, K.**, **Ahuja, K.** and **Gaeta Jr., R.** (**2001**), "A numerical and experimental investigation of the dissipation mechanisms of resonant acoustic liners", *Journal of Sound and Vibration*, **245**(3): pp. 545–557. [Cited on page 11.]

Tam, C. K. W., **Ju, H.**, **Jones, M. G.**, **Watson, W. R.** and **Parrott, T. L.** (**2005**), "A computational and experimental study of slit resonators", *Journal of Sound and Vibration*, **284**: pp. 947–984. [Cited on page 10.]

Tam, C. K. W., **Ju, H.**, **Jones, M. G.**, **Watson, W. R.** and **Parrott, T. L.** (**2010**), "A computational and experimental study of resonators in three dimensions", *Journal of Sound and Vibration*, **329**: pp. 5164–5193. [Cited on page 10.]

Tay-Wo Chong, L. and **Polifke, W.** (**2012**), "LES-based study of the influence of thermal boundary condition and combustor confinement on premix flame transfer functions", in *Proceedings of ASME Turbo Expo 2012*, Copenhagen, Denmark. [Cited on page 4.]

Tran, N., **Ducruix, S.** and **Schuller, T.** (**2009**a), "Damping combustion instabilities with perforates at the premixer inlet of a swirled burner", *Proceedings of the Combustion Institute*, **32**(2): pp. 2917–2924. [Cited on page 12.]

Tran, N., **Ducruix, S.** and **Schuller, T.** (**2009**b), "Passive Control of the Inlet Acoustic Boundary of a Swirled Burner at High Amplitude Combustion Instabilities", *ASME Journal of Engineering for Gas Turbines and Power*, **131**(5 - 051502): pp. 1–7. [Cited on page 12.]

Twersky, V. (**1956**), "On the Scattering of Waves by an Infinite Grating", *IRE Transactions on Antennas and Propagation*, **4**: pp. 330–345. [Cited on page 137.]

Twersky, V. (**1961**), "Elementary function representations of Schlömilch series", *Archive for Rational Mechanics and Analysis*, **8**(1): pp. 323 – 332. [Cited on page 141.]

Twersky, V. (**1962**), "On Scattering of Waves by the Infinite Grating of Circular Cylinders", *IRE Transactions on Antennas and Propagation*, **10**: pp. 737–765. [Cited on pages 137, 138, and 141.]

Vilain, C. E., **Pelorson, X.**, **Fraysse, C.**, **Deverge, M.**, **Hirschberg, A.** and **Willems, J.** (**2004**), "Experimental validation of a quasi-steady theory for the flow

through the glottis", *Journal of Sound and Vibration*, **276**: pp. 475–490. [Cited on pages 47 and 131.]

Wieczorek, K. (**2010**), *Numerical study of Mach number effects on combustion instability*, Ph.D. thesis, University of Montpellier. [Cited on page 81.]

Zhang, Q. and **Bodony, D. J.** (**2012**), "Numerical investigation and modelling of acoustically excited flow through a circular orifice backed by a hexagonal cavity", *Journal of Fluid Mechanics*, **693**: pp. 367–401. [Cited on page 10.]

Zhao, D. and **Li, X. Y.** (**2015**), "A review of acoustic dampers applied to combustion chambers in aerospace industry", *Progress in Aerospace Sciences*, **74**: pp. 114–130. [Cited on page 7.]

Zhao, D., **Morgans, A. S.** and **Dowling, A. P.** (**2011**), "Tuned Passive Control of Acoustic Damping of Perforated Liners", *AIAA Journal*, **49**(4): pp. 725–734. [Cited on page 12.]

Zhou, L. (**2015**), *Acoustic characterization of orifices and perforated liners with flow and high-level acoustic excitation*, Ph.D. thesis, KTH Royal Institute of Technology, Stockholm. [Cited on page 52.]

Zhou, L. and **Bodén, H.** (**2014**), "Experimental investigation of an in-duct orifice with bias flow under medium and high level acoustic excitation", *International Journal of Spray and Combustion Dynamics*, **6**(3): pp. 267–292. [Cited on page 11.]